Evaluation of the Influence of Aeration on the Discharge Capacity and Flow Induced Vibrations of Piano Key Weir Spillways

by
Jaretha Lombaard

Thesis presented in partial fulfilment of the requirements for the degree of Masters of Engineering in the Faculty of Engineering at Stellenbosch University

Supervisor: Prof Gerrit R. Basson

March 2020

DECLARATION

By submitting this thesis, I declare that the entirety of the work contained therein is my own original work, that I am the sole author thereof (unless to the extent explicitly otherwise stated), that reproduction and publication thereof by Stellenbosch University will not infringe any third party rights and that I have not previously in its entirety or in part submitted it for obtaining any qualification.

Name: Jaretha Lombaard

Date: March 2020

ABSTRACT

A Piano Key Weir (PKW) spillway is a popular option for increasing the discharge capacity of existing dams due to its high discharge efficiency compared to linear and traditional labyrinth weirs, as well as its small structural footprint. Thinner elements of a PKW, such as the sidewalls, may be susceptible to flow induced vibrations (FIVs) and subsequent structural fatigue and/or cause significant noise disturbance to the environment when the PKW is spilling. Previous PKW hydraulic model studies have observed that vibrations that occur in the PKW structure disappear by artificially aerating the air cavity behind the overflow nappe.

A physical hydraulic model study of PKWs was conducted at Stellenbosch University to evaluate the influence of artificial aeration on the discharge capacity, the overall hydraulic behaviour and the FIVs, specifically nappe oscillations. Two physical hydraulic models were constructed – one large-scale half key model, constructed from structural steel, and one smaller scale multi-key model, constructed from timber. Both models were constructed with the option of introducing air to the air cavity behind the overflow nappe via two different sizes of aeration pipes

The study found that PKWs are indeed self-aerating, especially for higher headwater levels. Artificially aerating the air cavity behind the nappe slightly increases the discharge efficiency at lower headwater levels and has an overall stabilising effect on the pressure fluctuations in this air cavity.

Pressure fluctuations in the air cavity occur over all ranges of headwater levels tested and increased in magnitude with the increase in headwater level. At lower headwater levels, these pressure fluctuations and FIVs were mainly caused by vortex shedding which were induced by the upstream flow conditions around the upstream overhang of the PKW. These vortices presented itself as swirls of flow that were passed over the sidewall. At higher headwater levels, the fluctuations could be attributed to the flow dynamics in the outlet key as it became drowned. In both cases, aeration had a limited effect on the pressure fluctuations. Nappe oscillations, as a type of FIV, only occurred at very low headwater levels. These oscillations reduced in intensity when the nappe air cavity was aerated but disappeared when the nappe was broken or split. As indicated by other studies, the latter observation confirmed that the air cavity only functions as an amplifier of the pressure fluctuations.

The sidewall vibrations appeared to be excited by the air pressure fluctuations as a result of the aforementioned vortex shedding. Although there was some correlation between the excitation frequencies and natural frequencies of the sidewall, the vibration amplitudes were relatively low and none of the mode shapes were such that resonant behaviour of the PKW

sidewall would occur. Artificial aeration had no effect on the vibration frequencies of the PKW sidewall or the intensity thereof for the flow ranges tested.

OPSOMMING

‘n Klavierklawerkeerwal (KKK) oorloop is ‘n gewilde keuse om die oorloopkapasiteit van bestaande damme te verhoog weens hul hoë deurstromingdoeltreffendheid in vergelyking met lineêre of tradisionele saagtandkeerwalle, asook hul klein strukturele voetspoorarea.

Dunner elemente van ‘n KKK, soos die symure, mag vatbaar wees vir vloei-geïnduseerde vibrasies (VIV) en daaropvolgende strukturele vermoeidheid en/of omgewings-geraasversteuring wanneer die KKK oorloop. Vorige KKK fisiese hidrouliese modelstudies het waargeneem dat vibrasies wat in die KKK-struktuur voorkom verdwyn wanneer die lugholte agter die oorloopnappe kunsmatig belug word.

Fisiese hidrouliese modelstudies is by Stellenbosch Universiteit uitgevoer om die invloed van kunsmatige belugting op die oorloopkapasiteit, die algemene hidrouliese gedrag en die VIV te evalueer. Twee fisiese hidrouliese modelle is gebou – een grootskaal halwe klawer model, gebou uit strukturele metaal, en een kleinskaal multi-klawer model, gebou met hout. Beide modelle is gebou met die keuse om lug toe te dien na die lugholte agter die oorloopnappe met behulp van belugtingspype. Die studie het bevind dat KKKe vanself belug word, veral vir hoë oorloopwatervlakke. Die deurlatingsdoeltreffendheid neem effens toe as die lugholte agter die nappe kunsmatig belug word onder lae vloeitoestande. Kunsmatige belugting het ook ‘n algemene stabiliseringseffek op die lugdrukvariasie in hierdie lugholte.

Die lugdruk in die lugholte fluktueer vir alle getoetsde oorloopwatervlakke en neem toe met die toename in die oorloopwatervlak. Vir lae oorloopwatervlakke word die drukfluktuasies meestal veroorsaak deur werwelstorting wat ook ‘n tipe VIV is. Hierdie werwelstortings word veroorsaak deur die vloei toestande rondom die stroomopoorhang van die KKK en kom voor as dikker kolkende vloeistrome wat bo-oor die symuur se kruin vloei. Vir hoër oorloopwatervlakke kan die drukfluktuasies toegeskryf word aan die vloei dinamika in die uitlaatklawer soos wat dit oorstroom word. In beide gevalle het kunsmatige belugting ‘n beperkte invloed op die drukfluktuasies gehad. Nappe-ossillasies, as 'n VIV, kom slegs voor tydens baie lae oorloopwatervlakke. Die intensiteit van hierdie ossillasies verlaag wanneer die lugholte belug word en verdwyn heeltemal wanneer die nappe gebreek of gesplit word. Soos aangedui in ander studies, bevestig die laasgenoemde waarneming dat die lugholte slegs as 'n versterker van die ossillasies funksioneer.

Dit blyk dat die symuurvibrasies opgewek word deur die drukfluktuasies as gevolg van die werwelafwerping wat ontstaan stroomop van die KKK. Alhoewel daar 'n mate van korrelasie bestaan tussen die opwekkingsfrekwensies en natuurlike frekwensies van die symuur, is die vibrasie-amplitudes relatief laag en word geen van die vibrasie modus vorms in so 'n mate bevoordeel dat dit die resonante gedrag van die KKK-symuur sal aktiveer nie. Kunsmatige

belugting het geen effek op die vibrasiefrekwensies van die KKK-symuur of die intensiteit daarvan vir die deurstromings wat getoets is nie.

ACKNOWLEDGEMENTS

I would like to express my sincere gratitude to the following people and organisations for their support, assistance, guidance, patience and advice:

- My supervisor Prof Basson for his all-round support and granting me the opportunity;
- Frank Denys for the opportunity to conduct a parallel study on the same physical hydraulic models, his guidance, assistance, patience and motivation, which without, this study would have not been possible.
- Mr. Johan Nieuwoudt, Mr. Iliyaaz Williams and Mr. Marvin Lindoor at Stellenbosch University Hydraulic Laboratory, for their assistance and hard work during the construction and testing of the models;
- AECOM, as well as my supervisors at AECOM, for the financial support and granting me the time needed to complete this thesis.
- Roelof Schoeman for the assistance with computer programming language.
- My family, friends and colleagues for the continuous support and motivation.
- Pieter Schoeman for always being by my side, supporting, encouraging and keeping me positive throughout.

TABLE OF CONTENTS

LIST OF FIGURES

LIST OF TABLES

LIST OF ABBREVIATIONS, UNITS AND SYMBOLS

ABBREVIATIONS

PKW	Piano Key Weir
FSL	Full Supply Level
FIV	Flow Induced Vibrations
3D	Three Dimensional
EIE	Extraneously-Induced Excitation
MIE	Movement Induced Excitation
IIE	Instability-Induced Excitations
FFT	Fast Fourier Transform
PVC	Polyvinyl Chloride
PSD	Power Spectral Density
ICOLD	International Commission on Large Dams
EDF	*Electricité de France*
CFD	Computational Fluid Dynamic
DC	Direct Current

UNITS

mm	Millimetre
mA	Milliampere
A	Ampere
Ω	Ohm
V	Volt
m^3/s	Cubic meters per second
l/s	Litres per second
Pa	Pascal
m	Metre
Hz	Hertz
m/s	Metre per second
s	Second
m/m	Metre fall per metre distance
N	Newton
Nm	Newton metres
m^2	Square metres
m^2/s	Square metres per second
GPa	Gigapascal

SYMBOLS OR VARIABLES

A	Cross-sectional area	m^2
B_b	Weir base length	m
B_i	Overhang length of inlet key	m
B_o	Overhang length of outlet key	m
C_d	Discharge coefficient	–
$C_{d,L}$	Discharge coefficient related to weir length	–
$C_{d,W}$	Discharge coefficient related to weir width	–
Ch	Cauchy number	–
C_s	Standard weir discharge coefficient	–
c_s	Speed of sound (343 m/s)	m/s
d	Falling jet height	m
d_b	Flow depth at the brink of a step	m
df	Frequency resolution	Hz
d_p	Flow depth in the pool beneath the nappe	m
E	Young's modulus	GPa
Eu	Euler number	–
F	Force	N
f	Frequency	Hz
Fr	Froude	–
f_s	Sampling frequency	Hz
g	Gravitational acceleration (9.81 m/s^2)	m/s^2
H	Overflow depth	m
H	Measured pressure head	m
h	Piezometric head	m
H/P	Overflow depth ratio	–
H_d	Design upstream water head	m
H_{max}	Maximum pressure head limit of transmitter	m
H_{min}	Minimum pressure head limit of transmitter	m
h_n	Nappe thickness	m
H_T	Total upstream water head	m
I	Moment of inertia	10^6 m^4
I_{max}	Maximum current output of transmitter	A
I_{min}	Minimum current output of transmitter	A
K_{Wi}	Influence of flow velocity	–
K_{Wo}	Side crest length decrease induced by outlet key flow and side nappe interference	–
L	Weir length (along crest)	m
L	Characteristic length	m
L_u	Developed length of one PKW unit	m

M	Momentum	Nm
Ma	Mach number	–
N	Number of samples	–
n	Developed length ratio	–
N_u	Number of PKW units	–
p	Pressure	Pa
P	Weir height	m
P_d	Dam height below PKW base	m
P_e	Mean weir height along sidewall	m
P_i	Height of inlet entrance measured from PKW crest	m
P_m	Wall height measured from the intersection of sloped bases of adjacent keys	m
p_n	Nappe perimeter	m
P_o	Height of outlet exit measured from PKW crest	m
q	Specific Discharge	$m^3/s/m$
Q	Discharge	m^3/s
Q_{air}	Nappe aeration	m^3/s
Q_P or Q_{PKW}	Piano key weir discharge	m^3/s
q_s	Linear water flow overflowing inlet keys and sidewalls	m^3/s
Q_s	Linear (sharp crested) weir discharge	m^3/s
R	Resistance of transmitter	Ω
r	Discharge enhancement ratio	–
Re	Reynolds number	–
R_o	Outlet key parapet wall height	m
S_i	Slope of inlet key apron	m/m
S_o	Slope of outlet key apron	m/m
St	Strouhal number	–
T	Time	s
T_s	Wall thickness	m
V	Characteristic velocity	m/s
v	Kinematic viscosity (≈ 1.13 x 10^{-6} m^2/s for water)	m^2/s
V_{atm}	Voltage reading of atmospheric hydrostatic pressure	V
V_i	Jet speed at impact	m/s
V_m	Minimum velocity required to entrain air (assumed as 1.1 m/s)	m/s
W	Linear weir width	m
We	Weber number	–]
W_i	Width of inlet key	m
W_o	Width of outlet key	m
W_u	Width of a PKW unit (one inlet + two half outlets)	m
α and β	Characterise influence of inlet key slope	–

ΔP	Pressure losses	Pa
λ	Scaling factor	–
ρ	Density	kg/m^3
σ	Surface tension ($\approx$ 0.073 N/m for water)	N/m
ω	Circular frequency	radians/s
x	Measured voltage reading	V

1. INTRODUCTION

1.1 BACKGROUND

Piano Key Weirs, often referred to as PK weirs or PKWs, were first developed in the late 1990s and early 2000s as an improvement of the well-known labyrinth weir spillways. Due to their better hydraulic performance and higher cost effectiveness compared to the general labyrinth weir spillways, piano key weirs (further referred to in this document as PKWs), have become an increasingly popular spillway option for new dams and also especially for dam safety improvement and rehabilitation of existing dams (Schleiss, 2011).

PKWs have been successfully constructed in several countries including France, India, Australia, Sri Lanka, Vietnam, Switzerland and Algeria. The first South African PKW was recently installed at the existing Hazelmere Dam to increase the reservoir storage and the spillway discharge capacity. The installation of a PKW at the existing Tzaneen Dam is also due to start soon (van Deventer *et. al*, 2015) (Mabela, 2017) (Chemaly, 2017).

The hydraulic behaviour of PKWs is highly complex due to its three-dimensional (3D) nature (Leite Ribeiro *et. al*, 2012). The static hydraulic behaviour of PKWs is now well understood, thanks to the several parametric studies undertaken during the past ten years (Anderson & Tullis, 2011) (Erpicum *et al.* 2014) (Machiels *et al.*, 2014) (Kabiri-Samani & Javaheri, 2012). The transient behaviour of PKWs is not so well understood and is the subject of several on-going studies.

One of the main concerns identified by the previous studies is the presence of oscillating negative pressures behind the overflow nappe, the potential of these oscillations causing structural vibrations and the effect of artificially aerating the overflow nappe (Leite Ribeiro *et al.*, 2007) (Erpicum, *et al*., 2013a).

Furthermore, although PKWs have showed that they are naturally aerated, the majority of PKWs installed to date include aeration pipes below the downstream overhang of the inlet key. The added benefit of artificially aerating the nappe, and the influence on the stability of the structure, have not yet been investigated in detail (Laugier *et al.*, 2013).

1.2 OBJECTIVES AND SCOPE

The main objectives of this study were to investigate, by means of physical hydraulic model studies, the effect on the discharge capacity of artificially aerating the air cavity behind the overflow nappe of a PKW, the overall hydraulic behaviour and Flow Induced Vibrations (FIV), specifically nappe oscillations. The effect of different aeration pipe sizes installed under the overflow nappe on the aforementioned was also investigated.

The FIV investigated in this study was limited to nappe oscillations and was focussed on whether introducing artificial aeration to the air cavity behind the nappe has any effect on these oscillations. Attention was also given to the vortex shedding (also a FIV) that occurs around the upstream overhang of the outlet key and which can potentially impact nappe oscillations. The study does not aim to identify the mechanisms that initiate the nappe oscillations.

The study only aimed to identify whether there is a relationship between structural vibrations, nappe oscillations and artificial aeration and did not focus on the structural or hydro-elastic behaviour of PKWs as such or whether the potential excitation forces can activate any of the PKW sidewall modal shapes and cause resonant behaviour. These are briefly discussed in this study.

Artificial aeration was limited to aeration pipes installed under the inlet key overhang. No other form of aeration was evaluated.

1.3 METHODOLOGY

A literature review was conducted on the geometry and hydraulic characteristics of PKWs, FIV and aeration of hydraulic overflow structures. Two physical hydraulic models were designed and constructed at the Hydraulics Laboratory of the Stellenbosch University, South Africa, as part of a parallel study conducted by Denys (2019). These two physical hydraulic models were also utilized for this study. The purpose of the first model, constructed from timber at a scale of 1:7.5, was to evaluate the overall behaviour of PKWs with and without artificial aeration. The second model, constructed from steel at a scale of 1:2.73, was to evaluate specifically the vibrations of the thin walled PKW elements. Different discharges (or flow magnitudes) and aeration conditions were evaluated. Experimental data, including flow discharge, flow surface profiles, pressures, air flow and vibration data, were collected and evaluated according to the objectives of the study. The literature review, experimental setup and findings of the experimental investigation are recorded in this thesis.

The parallel study by Denys (2019) focused in depth on the hydrodynamics and transient flow behaviour of PKWs, as well as on the interaction between the flow and thin-walled structural elements of PKWs.

1.4 THESIS OUTLINE

This thesis contains the following sections:

- **Section 2** provides a literature review on the geometry and types of PKWs, the flow characteristics, and discharge capacity and design criteria for PKWs;
- **Section 3** provides an overview of FIV, with specific focus on instability induced vibrations likely to occur at PKWs;
- **Section 4** discusses aeration of overflow nappes and the aerations systems and designs implemented on PKWs to date.
- **Section 5** describes the experimental setup, including a description of the physical hydraulic model scale and layout, the measuring equipment and techniques used to record data, the experimental procedures followed, and the scenarios evaluated;
- **Section 6** provides the results of the experiments, as well as a discussion of the results;
- **Section 7** provides a summary of the main findings and conclusions with regard to the results obtained from the physical hydraulic model; and
- **Section 8** provides recommendations for further evaluation of FIV and aeration systems of PKWs, as well as recommendations for future PKW projects.
- **Appendices A to D** include additional information on PKW hydraulics, physical hydraulic modelling and the experimental setup, and results.

2. OVERVIEW OF PIANO KEY WEIRS AND HYDRAULIC CHARACTERISTICS

2.1 INTRODUCTION

A spillway is a structure that provides the controlled release of water from a water body, usually a dam or reservoir, generally into a downstream river area. Adequate spillway capacity is essential to ensure the safe release of surplus and flood water that cannot be contained within the reservoir or storage of the dam above the Full Supply Level (FSL). A spillway mainly comprises of the following components (USBR, 1987):

- **Entrance channel** which directs water from the reservoir towards the control structure;
- **Control structure** which regulates the flow discharging from the reservoir. The control can be uncontrolled or controlled and generally consist of a weir type structure and mechanical equipment such as radial gates.
- **Discharge channel** which conveys the flow from the control structure. The dimensions of the discharge channel are mainly governed by hydraulic requirements.
- **Terminal structure** which returns flow to the river after dissipating excess energy to prevent scour or erosion of the dam wall, dam foundation and downstream river banks and damage to adjacent structures. Typical terminal structures include ski jumps, roller buckets and stilling basins.

Approximately one third of all dam failures is due to inadequate spillway capacity (Schleiss, 2011). Many dam improvement programmes for increasing the flood discharge capacity, as well as the storage capacity, involve the installation of mechanical gates. These gates are vulnerable to failure if not adequately maintained or operated, and as such are generally avoided in Africa (Lempérière, *et al.*, 2013).

Various types of ungated (or uncontrolled) spillways exist and are selected based on the role of the dam, topography, geology, dam type, hydrology and the reliability of dam operation and maintenance. Typical spillway types include (Sharma & Sharma, 1992):

- Free over-fall or straight drop spillway;
- Ogee or overflow spillway;
- Chute spillway;
- Side channel spillway;
- Bywash spillway;
- Labyrinth weir spillway; and
- PKW spillway.

A significant amount of research has gone into the improvement of ungated or free overflow structures to increase the spillway capacity. The discharge capacity of an ungated or free overflow crest spillway is directly proportional to the length of the overflow crest for a given upstream head, given that the downstream chute and channel have enough conveyance capacity (Schleiss, 2011).

Due to its generally zig-zag layout in plan, and thus longer effective overflow length, labyrinth spillways (**Figure 2.1**) can discharge large flows at lower headwater levels compared to linear overflow spillways (Crookston & Tullis, 2013). This makes labyrinth weirs a popular spillway choice for dams where the spillway width or flood surcharge space is limited (Lux & Hinchliff, 1985). Labyrinth spillways are also widely used in existing dams to increase the storage capacity and flood discharge capacity due to their low cost compared to gated spillways and increased discharge capacity for a given headwater level and reduced required width. Furthermore, labyrinth weirs also serve as protection structures for canals and run-of-river hydroelectric plants, as well as energy dissipating structures to aerate or de-aerate flow to meet downstream water quality requirements (Schleiss, 2011).

One drawback of a labyrinth spillway is that it is not suitable for increasing the discharge or storage capacity of most existing concrete gravity dams, as a labyrinth spillway requires a considerably flat area, i.e. large footprint (Lempérière & Ouamane, 2003).

Figure 2.1: Labyrinth weir spillway, Dog River Dam, Georgia (Paxson *et al.*, 2011)

The PKW is a relatively new spillway development, which originated from traditional labyrinth weirs in the late 1990s and early 2000s as part of investigations by Hydrocoop in France and the University of Briska in Algeria (Lempérière & Ouamane, 2003).

A PKW (**Figure 2.2**) has an alternating rectangular plan layout, which has the added benefit of sloped bases which guide flow over and away from the crest and further increases the discharge capacity compared with a labyrinth weir (Denys, 2015). Based on more than 50 hydraulic tests by Hydrocoop, a PKW can accommodate specific flows of up to 100 $m^3/s/m$ and may be up to four times more efficient than an ogee crested weir for a similar headwater and weir width (Lempérière & Ouamane, 2003). Compared to labyrinth weirs, the discharge capacity of a PKW can be 10% higher for a similar headwater level and crest footprint (Anderson & Tullis, 2011).

Figure 2.3 shows a typical PKW, referred to as a Type A PKW due to its symmetrical upstream and downstream overhangs. This type of PKW forms the focus of this study.

Figure 2.2: PKW spillway construction of Gloriettes Dam, France (ICOLD Technical Committee on Hydraulics for Dams, 2016)

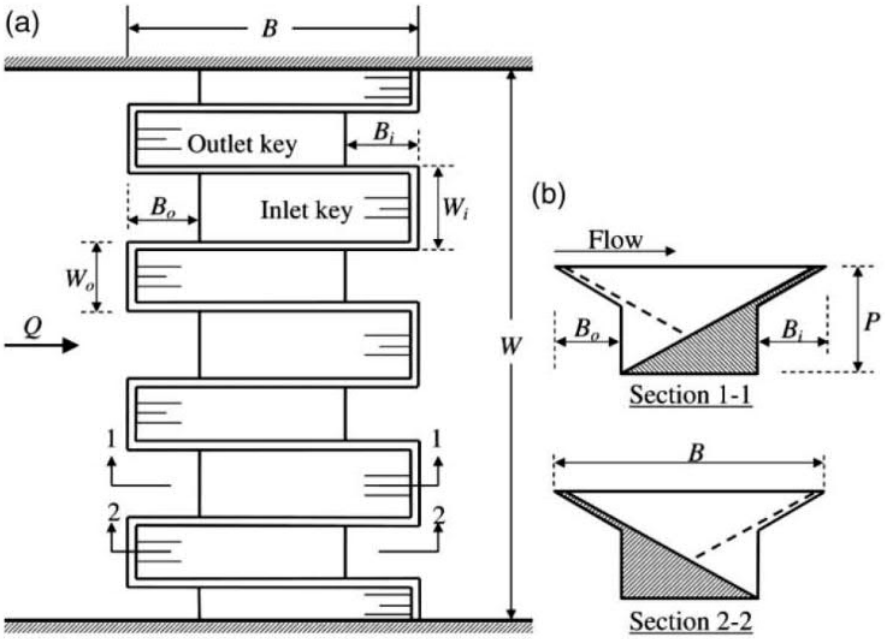

Figure 2.3: Plan view (a) and cross-sections (b) of typical PKW (Kabiri-Samani & Javaheri, 2012)

Due to the sloped bases, the foundation footprint of a PKW is much smaller compared to a labyrinth spillway and allows the spillway to be installed where foundation space is limited, e.g. at concrete gravity dams. These characteristics make the PKW an attractive and economical option for increasing the spillway capacity of existing dams (Schleiss, 2011). Paxson, *et al*. (2013) concluded that PKWs can provide an ideal and unique solution for increasing the discharge and storage capacity of existing dams compared to gated spillways and labyrinth weirs.

The first PKW was installed at the Golours Dam in France in 2006. Since then, several PKWs have been constructed. According to the World Register of Piano Key Weirs (PKW 2017), by 2017 30 PKWs had been successfully installed in ten countries around the world (**Figure 2.4**), the majority of which were installed on existing dams to increase the discharge capacity. In South Africa, the existing Hazelmere Dam was raised by means of a PKW (construction recently completed) and construction to raise the existing Tzaneen Dam with a modified PKW started recently (van Deventer, *et al.*, 2015) (Mabela, 2017) (Chemaly, 2017).

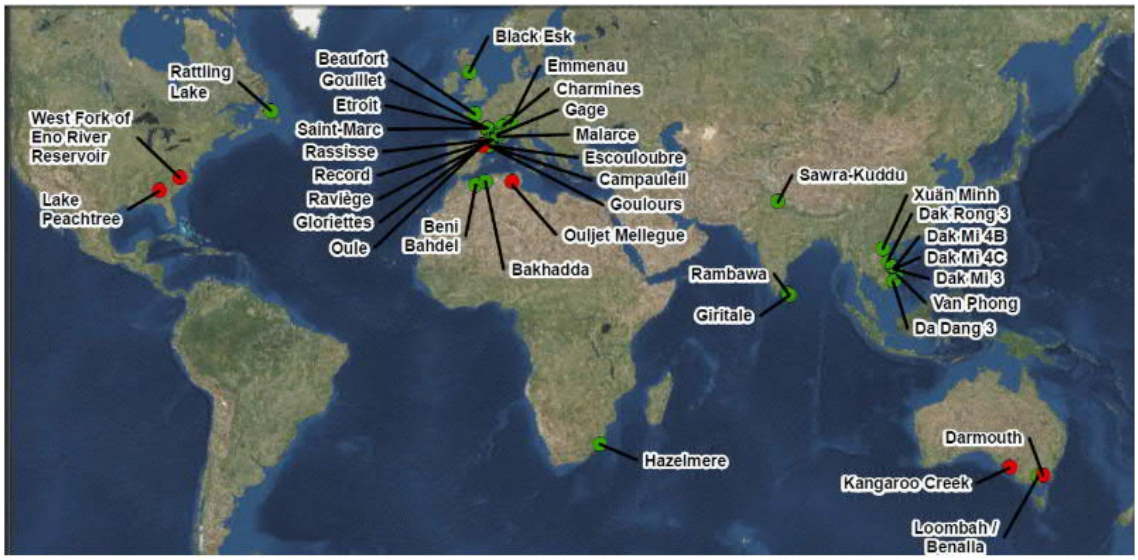

Figure 2.4: Location of constructed PKWs around the world (PKW 2017)

It should be noted that the discharge efficiency of both labyrinth and PKW spillways are optimum only for lower upstream heads and can start to behave as a linear spillway at high heads (Schleiss, 2011).

2.2 GEOMETRY AND TYPES OF PIANO KEY WEIRS

2.2.1 Overview of Piano Key Weir geometry

The plan layout of a PKW consists of repeating rectangular profiles, referred to as cycles or units. The rectangular keys (or profiles) have alternating sloped bases in the upstream and downstream directions, which create up-and downstream overhangs. Flank walls or sidewalls between keys are vertical. The layout represents piano keys – hence the name. These cycles can follow a straight axis, curved axis or even a circular axis as is the case at the Black Esk Dam, Scotland (Ackers, *et al.*, 2013).

The inlet key refers to the key of which the base has a positive slope in the downstream direction and the outlet key has a negative base slope in the downstream direction. A PKW-unit or cycle refers to one complete inlet key with sidewalls and two halves of outlet keys on either side of the inlet key (Machiels, *et al.*, 2014).

As previously mentioned, PKWs have several parameters that influence their hydraulic behaviour. Pralong *et al.* (2011a) developed a standardized terminology for the fundamental geometrical parameters that have the most influence on the hydraulic performance of a PKW. These parameters are illustrated in **Figure 2.5** and **Figure 2.6** and are summarised in **Table 2.1**. Subscript "*i*" refers to parameters associated with the inlet key and subscript "*o*" refers to the outlet key parameters.

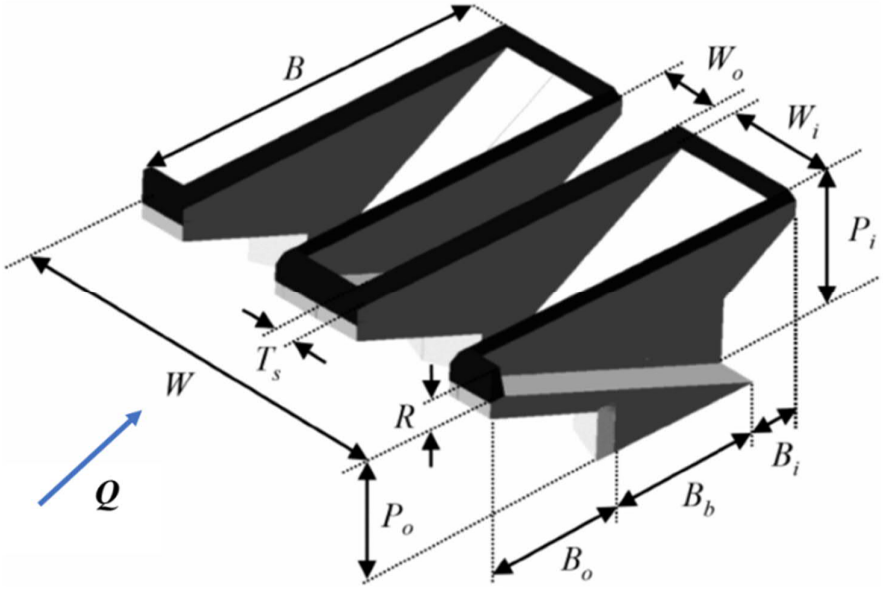

Figure 2.5: 3D illustration of the fundamental geometrical parameters of a PKW (Pralong, et al., 2011a)

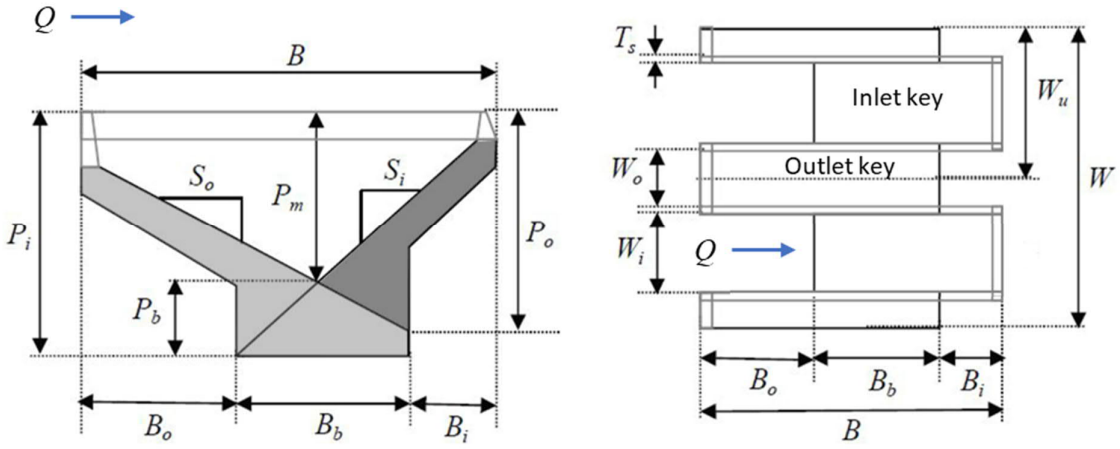

Figure 2.6: Cross-sectional (left) and plan view (right) illustration of the fundamental geometrical parameters of a PKW (Pralong, *et al.*, 2011a)

2.2.2 Types of Piano Key Weirs

PKWs have been classified into four types, depending on the upstream and downstream overhangs, namely Type A, Type B, Type C and Type D. Type A is considered the typical PKW and incorporates both upstream and downstream overhangs. Type B incorporates only upstream overhangs, whereas Type C incorporates only downstream overhangs. Type D has no overhangs. The types are illustrated in **Figure 2.7** and **Figure 2.8**.

Table 2.1: Fundamental geometrical parameters (Pralong, *et al.*, 2011a)

Parameter	Definition
B	Upstream-downstream length of PKW, $B = B_b + B_i + B_o$ (m)
B_b	Base length of PKW footing (m)
B_i, B_o	Downstream (inlet key) / Upstream (outlet key) overhang length (m)
C_{dW}	Discharge coefficient related to total width, where $Q = C_{dW} W \sqrt{2gH^3}$
H_T	Total head over crest upstream of weir, $H_T = h + V^2/2g$ (m)
L	Total developed length along overflowing crest axis (m)
L_u	Developed length of one PKW unit, $L_u = W_i + W_o + 2T_s + 2B_h$ (m)
n	Developed length ratio or magnification ratio, n = L/W
N_u	Number of PKW units
P_i, P_o	Height of the inlet entrance / outlet exit measured from PKW crest (m)
Q	Discharge (m^3/s)
q	Specific discharge ($m^3/s/m$)
R_o	Outlet key parapet wall height (m)
S_i, S_o	Slope of the inlet/outlet key apron (m/m)
T_s	Sidewall thickness (m)
W	Total linear width of the PKW (m)
W_i, W_o	Width of the inlet/outlet key (wall to wall) (m)
W_u	Width of a PKW unit (one inlet + two half outlets), $W_u = W_i + W_o + 2T_s$ (m)

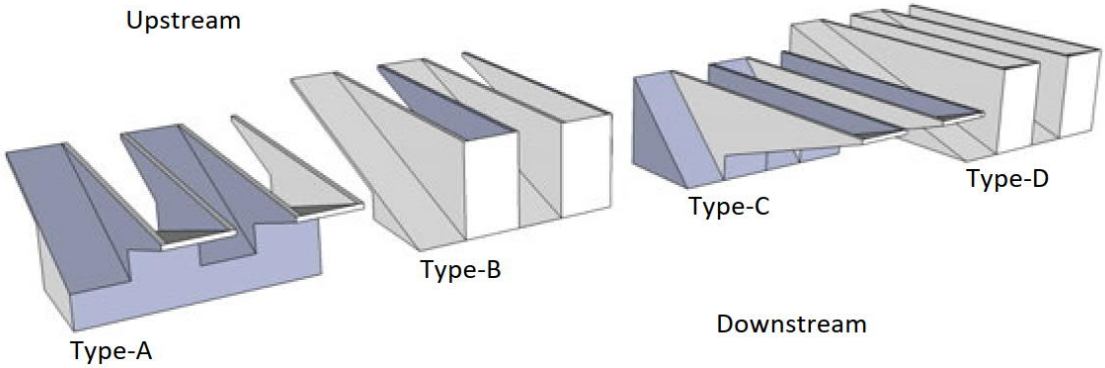

Figure 2.7: 3D schematic of PKW types (Erpicum, *et al.*, 2013)

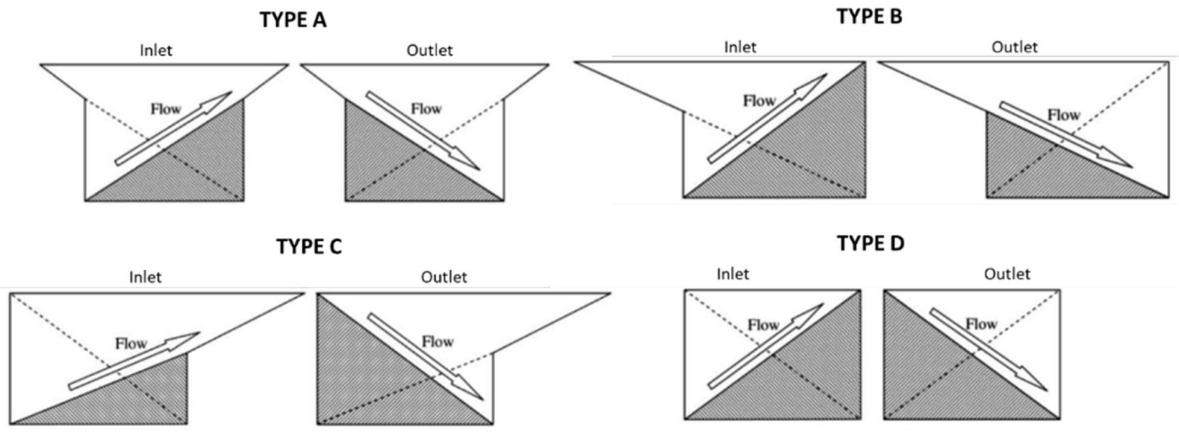

Figure 2.8: Cross-sectional schematics of PKW types (adapted from (Kabiri-Samani & Javaheri, 2012)

The use of the different types mainly depends on the specific discharge required and whether it is incorporated into an existing dam or a new dam. The overhangs on both the upstream and downstream sides make the Type A PKW structure essentially self-balancing and favourable for precast concrete elements. The overhangs do not necessarily have to be symmetrical. The Type A PWK can economically accommodate specific discharges of up to 20 $m^3/s/m$ (Schleiss, 2011). This type is mostly implemented in existing gravity dams to increase the spillway capacity.

According to Schleiss (2011), the Type B PKW can accommodate specific discharges up to 100 $m^3/s/m$ due to the smaller structural loads. According to Pralong *et al.* (2011), Type B PKWs have shown to have only a slightly higher discharge capacity compared to Type A (approximately 3% higher discharge capacity for the same headwater level). However, studies by Circero *et al.* (2016) have shown that Type B is 5 to 15 % more efficient in terms of discharge capacity than a Type A, depending on the dam height below the PKW base, P_d. These results are consistent with the first PKW experimental results of Ouamane & Lempérière (2006). This is due to the upstream overhangs creating a larger flow area and wetted perimeter, and slightly less energy losses in the inlet key. Type B PKWs are not as balanced as Type A and are thus mainly considered only for application in new dams where these can be fully designed into the dam superstructure with the required support mechanisms.

Type C PKWs provide no additional hydraulic performance benefit, except for better management of large pieces of floating debris (Lempérière, *et al.*, 2011). Type D PKWs are basically improved classic labyrinth weirs and beneficial where a wider footprint is required due to foundation conditions, e.g. alluvial rivers (Lempérière, *et al.*, 2011).

As previously mentioned, this study focusses only on Type A PWKs.

2.3 FLOW CHARACTERISTICS

To understand the effects of different PKW geometrical parameters and hydraulic behaviour, one needs to understand the unique and complex three-dimensional flow regime. The basic principle of PKW flow is that flow converges into the inlet key and diverges away from the outlet key (Machiels, 2012).

2.3.1 Inlet and outlet flow characteristics

The flow paths via a PKW are illustrated by Safarzadeh & Noroozi (2017) in **Figure 2.9**. The "near bed flow" diverts at the base of the upstream overhang of the outlet key into one of the adjacent inlet keys. The upward sloped base of the inlet key then forces the flow upward and over the downstream transverse crest of the inlet key. At middle depth, the flow approaching the outlet key also diverges underneath the upstream overhang into the inlet keys and converges with the flow approaching the inlet keys. This flow is then forced upward and discharged mainly over the lateral sidewall crests. Near the surface, the flow approaching the outlet key flows directly over the upstream transverse crest. At the corners of the outlet key crest, the flow over the crest converges with the flow from the lateral crests creating small standing waves. The near surface flow approaching the inlet key diverges towards the lateral crests and discharges (Safarzadeh & Noroozi, 2017).

Due to the higher flow inertia in the longitudinal (downstream) direction for high heads, more flow discharges over the downstream crest of the inlet key than the lateral crests. The portion of flow over the outlet key upstream crest remains constant irrespective of upstream head (Schleiss, 2011) (Machiels, *et al.*, 2011).

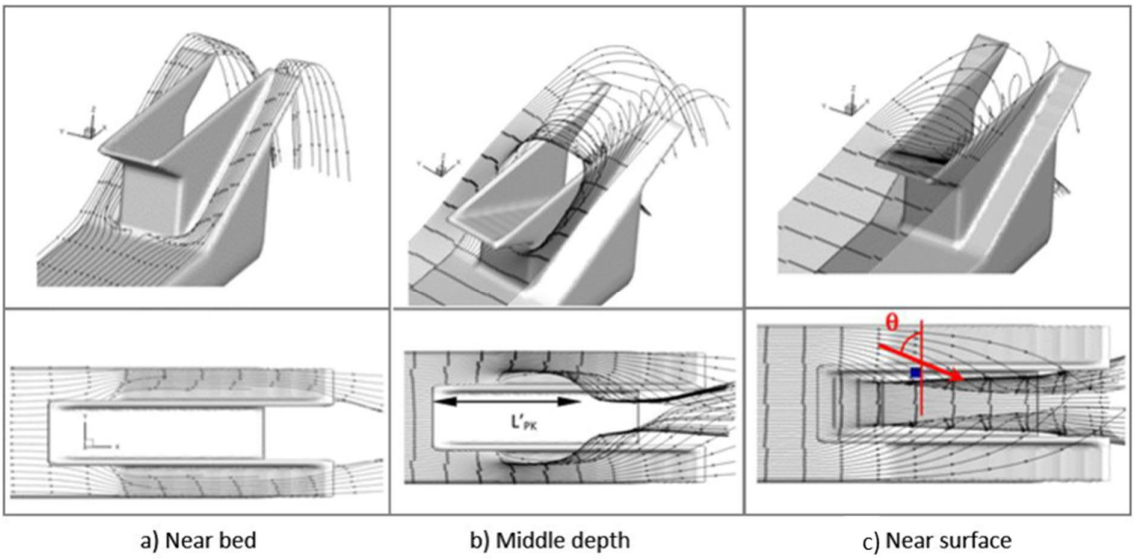

Figure 2.9: PKW flow lines at different depths (Safarzadeh & Noroozi, 2017)

It should be noted that only a very small portion of the flow discharges over the outlet key crest. Approximately 90% of all flow entering the inlet key is from flow diverged from below the upstream overhang of the outlet key where a stagnation pressure zone forms (Pralong, *et al.*, 2011) (Blancher, *et al*., 2011). As the flow changes direction and diverges around the 90° corner of the outlet key upstream overhang, a shear boundary layer forms and causes a separation bubble (recirculation zone) to develop. The flow in this area is unstable and results in vortex shedding and FIV (Denys, 2018). The effect of this separation bubble can be reduced by placing a "nose" under the upstream overhang of the outlet key (refer to **Section 2.4.3**).

Under unsubmerged conditions, the flow will fall freely over the lateral crests of the inlet key into the outlet key as a continuous nappe. The downward sloping base of the outlet key will guide the collected discharged flow downstream of the PKW under supercritical conditions. A hydraulic jump, as shown in **Figure 2.10 (a)**, will form either in the outlet key or downstream if the tail water depth is sufficient (Kabiri-Samani & Javaheri, 2012).

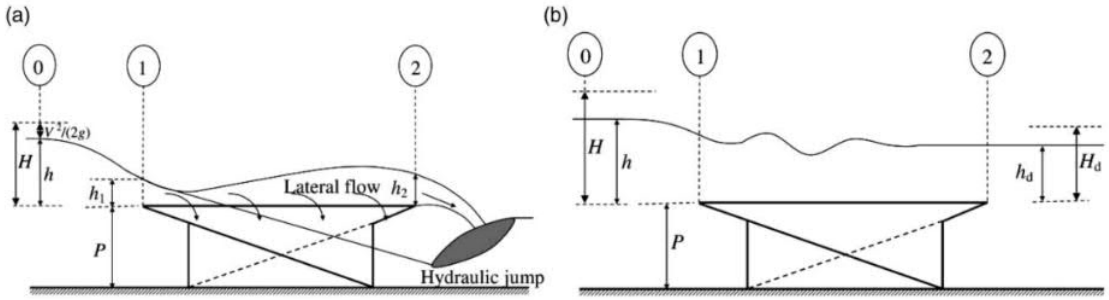

Figure 2.10: Hydraulic aspects of PKW flow for (a) free, (b) submerged weir flow (Kabiri-Samani & Javaheri, 2012)

Due to the flows ability to change direction at low approach velocities and momentum, flow will discharge perpendicularly over the transverse and lateral crests under low head conditions. This allows the PKW to act as a long linear weir over a shorter total width, and hence the increased discharge capacity. However, as the upstream head increases, the velocity and momentum increase and cause the flow to deviate from the previously perpendicular direction. This causes more flow convergence within the limited flow area, resulting in higher flow velocities, higher energy losses and consequently lower discharge efficiencies (Machiels, 2012). In the case of very high heads, the discharge capacity of a PKW becomes limited by the ability of the outlet key to collect and discharge flow to downstream without becoming locally submerged (Machiels, *et al.,* 2014).

As the head increases, a critical flow section moves from the downstream crest upstream into the inlet key causing an rippled free surface profile as shown in **Figure 2.10 (b)** and **Figure 2.11**. As the head increases, the convergence of flow in the inlet key and the recirculation zones along the lateral walls increase. This results in a reduced cross-sectional area and

increased flow velocities until the flow becomes supercritical. The control section then moves upstream where the flow depth is larger, and ultimately reduces the discharge capacity (Machiels, *et al.*, 2011). The pressure profiles in the inlet key remain close to hydrostatic pressure irrespective of the headwater depth (Erpicum, *et al.*, 2012).

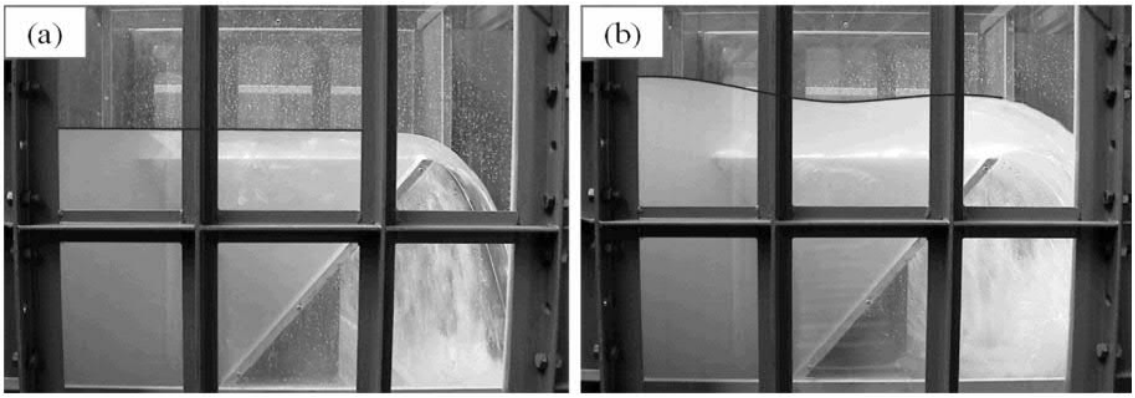

Figure 2.11: Free surface profiles for low and high heads of H/P (a) 0.15 and (b) 0.35 (Machiels, *et al.*, 2011)

2.3.2 Nappe characteristics

The nappe refers to the jet of water that passes over a weir structure. The behaviour of the nappe should be considered during the design of weirs and spillways to ensure optimum hydraulic performance, as well as to account for flow-induced vibrations, pressure fluctuations, noise and flow surging (Falvey, 1980). The hydraulic performance is influenced by the geometry of the weir, as well as the aeration condition of the nappe (Crookston & Tullis, 2013).

In case of a PKW, the flow over the lateral and downstream inlet key crest forms a continuous curtain with an enclosed air pocket (Denys, *et al.*, 2017), i.e. a nappe. The nappe thickness is dictated by the overflow location along the crest and hence the fall height. At higher flows or for narrow outlet keys, the flows from opposite lateral crests may collide, but do not have a significant effect on the discharge efficiency if free flow conditions are adhered to (Machiels, 2012).

Three typical nappe behaviours are observed for PKWs (unsubmerged conditions) and can all occur simultaneously at different locations along the lateral crests for a specific flow (Machiels, *et al.*, 2011) (Machiels, *et al.*, 2009). These behaviours are summarised below (Johnson, 2000) and illustrated in **Figure 2.12**:

- A **clinging nappe** occurs at low heads or velocities when there is no air beneath the nappe and it clings to the crest and the downstream wall of the structure.
- At higher heads, a **depressed or leaping nappe** occurs when the nappe starts to pull away from the wall but remains in contact with the downstream end of the crest.

Generally, the pressure below the nappe is negative and is only partially ventilated or aerated.

- A **free or springing nappe** occurs at even higher heads when the nappe detaches from the upstream edge of the crest. The nappe is characterised by atmospheric pressure underneath the nappe, generally obtained by ventilating a weir.

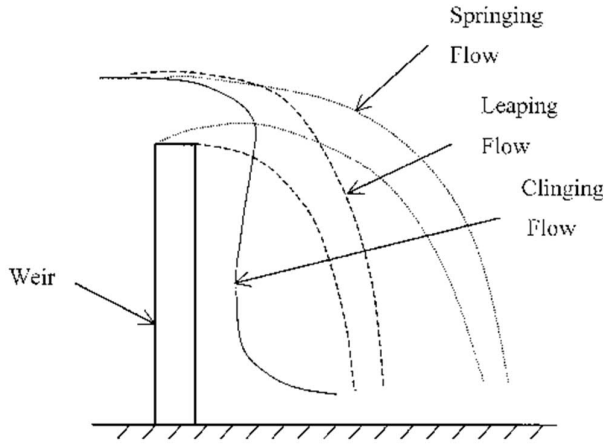

Figure 2.12: Nappe behaviour classification (Johnson, 2000)

The transitions from clinging to leaping and then to springing are dictated by the crest width and headwater depth. Based on experimental studies by Machiels *et al.* (2009) (2011) and Karbiri-Samani & Javaheri (2012), the leaping nappe remains attached to the lateral crest for very low heads (H/P ≤ 0.05) and then starts to spring free (springing nappe), detaching from the crest, over ¾ of the length of the lateral crest for H/P ≈ 0.1 (**Figure 2.13** and **Figure 2.14**). The same principle applies to the downstream crest of the inlet key. The nappe transitions from leaping to springing for slightly higher heads until it becomes fully aerated at H/P = 0.15 to 0.2. At even higher heads, the nappes discharging from the lateral crests interact and form a single nappe, ultimately reducing the discharge efficiency (Kabiri-Samani & Javaheri, 2012).

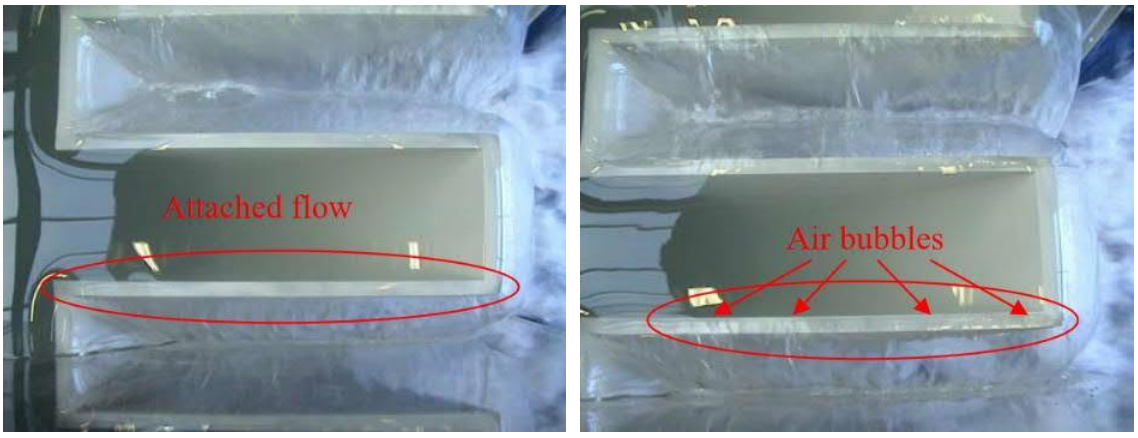

Figure 2.13: Transition from partially clinging (left) to springing nappe (right) on the inlet key downstream crest (Machiels, *et al.*, 2009)

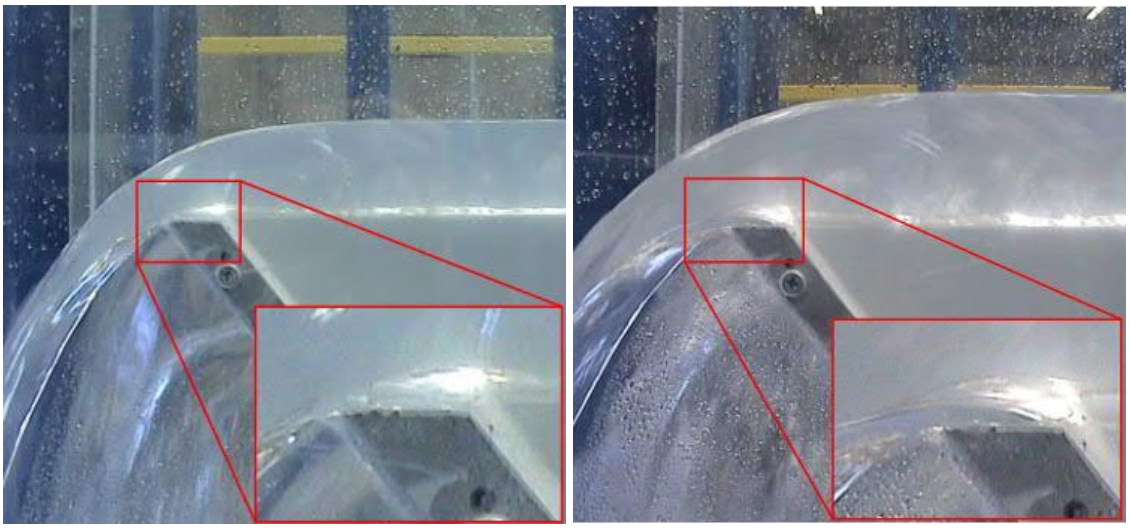

Figure 2.14: Transition from partially clinging (left) to springing nappe (right) on the inlet key downstream crest (Machiels, *et al.*, 2009)

At the upstream crest, the nappe transitions from completely clinging to fully aerated as the head increases (**Figure 2.15**) – highlighting the importance of the outlet key slope on the nappe behaviour (Machiels, *et al.*, 2011) (Kabiri-Samani & Javaheri, 2012).

Figure 2.15: Transition from clinging (left) to springing nappe (right) on the outlet key upstream crest (Machiels, *et al.*, 2009)

Table 2.2 summarises the nappe behaviour for different head ratios as studied by Machiels *et al.* (2009) (2011) and Karbiri-Samani & Javaheri (2012).

Table 2.2: Flow regimes and nappe characteristics for PKWs (adapted from Mehboudi, *et al.*, 2017)

Flow condition		Reference	Flow	Interference wedge
Nappe *Cavity beneath the falling nappe appears*	Clinging	Machiels *et al.* (2011)	$H/P < 0.05$	Either does not form or does not decrease the discharge coefficient
		Kabiri-Samani & Javaheri (2012)	$H/P < 0.05$	
	Leaping/ Depressed	Machiels *et al.* (2011)	$0.09 < H/P < 0.10$	
		Kabiri-Samani & Javaheri (2012)	$0.05 < H/P < 0.10$	
	Springing/ Free	Machiels *et al.* (2011)	$0.11 < H/P < 0.12$	
		Kabiri-Samani & Javaheri (2012)	$0.10 < H/P < 0.15$	
Transition *Cavity beneath the falling nappe starts disappearing*		Kabiri-Samani & Javaheri (2012)	$0.15 < H/P < 0.2$	Form and occupies almost 50% of outlet ramp area
Suppressed *Cavity beneath the falling nappe completely disappears*		Kabiri-Samani & Javaheri (2012)	$H/P > 0.2$	Form and occupies almost 100% of outlet ramp area

In general, as the nappe over a spillway structure transitions from clinging to free, the discharge coefficient decreases. In the case of a PKW, the discharge coefficient increases as the head increases until the nappe behaviour transitions from leaping to springing along the lateral crest (**Figure 2.16** – area a). The discharge coefficient stabilises with increase in head (**Figure 2.16** – area b and c) until the downstream nappe becomes springing, where-after the discharge coefficient gradually decreases with increase in head (**Figure 2.16** – area d) (Machiels, *et al.*, 2011). The variation in the discharge coefficient in areas b and c (**Figure 2.16**), is due to the combined effects of the free nappe developing on the lateral crest (decreasing the coefficient), the downstream crest depressed nappe and the clinging nappe on the upstream crest (increasing the coefficient for higher heads).

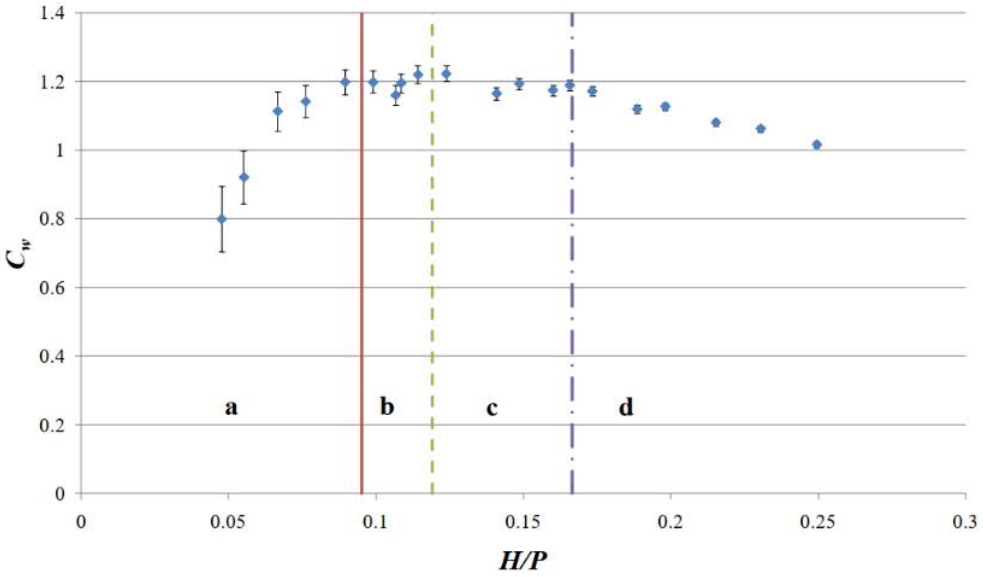

Figure 2.16: Variation of discharge coefficient in relation to nappe behaviour (Machiels, *et al.*, 2011)

The nappe behaviour with regard to FIV and aeration is discussed in more detail in **Section 3** and **Section 4**.

2.4 DISCHARGE CAPACITY AND DESIGN CRITERIA

2.4.1 Overview

Due to their layout, the effective overflow lengths of PKWs are much longer than for linear weirs and as such have higher discharge capacities compared to linear weirs operating at the same headwater depth and same linear widths. Furthermore, the sloped bases guide flow over and away from the crests which further increases the discharge capacities compared to labyrinth weirs.

PKWs can accommodate specific flows up to 100 $m^3/s/m$ if optimally designed, however, the associated geometrical design is not necessarily the most economical to construct. PKWs with specific flows of 20 $m^3/s/m$ to 40 $m^3/s/m$ are more practical and economical. Nonetheless, the discharge capacity is two to four times higher than for an ogee-crested linear spillway with the same headwater level and linear width (Denys, 2015).

The hydraulics of a PKW are significantly complicated by the three-dimensional nature of the flow and many parameters influence the discharge capacity. A substantial number of experiments have been carried out since 2003 to establish general applicable design criteria and to evaluate the hydraulic behaviour of PKWs. In most cases, PKWs have been designed making use of physical hydraulic models to predict the discharge rating curves and behaviour (Schleiss, 2011) (Denys, 2015).

2.4.2 Discharge capacity

The discharge over a PKW adheres to free surface flow conditions, and thus the discharge, Q, is relative to the upstream head, H (ICOLD Technical Committee on Hydraulics for Dams, 2016):

$$Q \propto \sqrt{2gH^3} \qquad \textbf{2-1}$$

Where:

- Q Discharge (m^3/s)
- g Gravitational acceleration (m^{-2}/s)
- H Upstream head (m)

The discharge of a PKW can either be expressed in terms of the developed crest length or the total width of the weir together with the respective discharge coefficients (Leite Ribeiro, *et al.*, 2009) (Leite Ribeiro, *et al.*, 2012a) (Leite Ribeiro*, et al.*, 2012):

$$Q_P = C_{d,W} W \sqrt{2gH_T{}^3} \qquad \textbf{2-2}$$

$$Q_P = C_{d,L} L \sqrt{2gH_T{}^3} \qquad \textbf{2-3}$$

Where:

- Q_P Discharge of PKW (m^3/s)
- $C_{d,W}$, $C_{d,L}$ Discharge coefficient
- W Total weir width (m)
- L Total developed weir length (m)
- H_T Total upstream head (m)

The other specific PKW parameters are combined into the discharge coefficient, depending on which method is followed. In the case of Equation 2-3, the effective crest length decreases with increasing head due to submergence (ICOLD Technical Committee on Hydraulics for Dams, 2016).

A second approach is to compare the discharge capacity of a PKW to that of a standard linear weir (sharp crested weir or ogee weir) at the same overflow head by means of an enhancement or relative discharge ratio (Leite Ribeiro, *et al.*, 2012a) (Leite Ribeiro*, et al.*, 2012).

$$r = \frac{Q_P}{Q_s} = \frac{C_{d,W} W \sqrt{2gH_T{}^3}}{C_s W \sqrt{2gH_T{}^3}} = \frac{C_{dW}}{C_s} \quad \textbf{2-4}$$

$$r = \frac{Q_P}{Q_s} = \frac{C_{d,L} L \sqrt{2gH_T{}^3}}{C_s W \sqrt{2gH_T{}^3}} = \frac{C_{P,L} L}{C_s W} \quad \textbf{2-5}$$

Where:

r	Enhancement ratio
Q_P	PKW discharge (m^3/s)
Q_S	Standard weir discharge (m^3/s)
$C_{d,W}$, $C_{d,L,}$ C_s	Discharge coefficients
W	Total weir width (m)
L	Total developed weir length (m)
H_T	Total upstream head (m)

In the case of sharp crested weirs, the C_s value is 0.42 (Hager & Schleiss, 2009) and in the case of ogee-crested weirs, the C_s value changes according to the deviation of the considered head from the design head (Erpicum, *et al.*, 2014). However, account should be taken depending of which standard weir type has been used when interpreting the results using the enhancement ratio. **Figure 2.17** shows the comparison of the discharge per unit width for a PKW compared to an ogee crested weir, as well as the associated enhancement ratio.

The relevant discharge coefficients or enhancement ratio is generally estimated by means of physical or numerical modelling and expressed as a function of H/P (Schleiss, 2011).

Blancher *et al.* (2011), as well as Anderson & Tullis (2011) amongst many others, evaluated the increase in the discharge capacity, as well as discharge coefficients, of a PKW compared to labyrinth and linear weirs using numerical analysis validated by physical models (**Figure 2.18** and **Figure 2.19**). The results indicated that the hydraulic performance of a basic Type A PKW is 10 to 20% more efficient than an equivalent rectangular shaped labyrinth. However, the discharge efficiency of both PKWs and labyrinth weirs decreases as the headwater increases. This coincides with the fact that labyrinths and PKWs are most efficient at lower heads and start acting as linear weirs for high heads.

The various studies of the hydraulic behaviour and structural optimisation, have contributed significantly to the increase in the discharge efficiency of PKWs. With reference to **Figure 2.20**, the more recently constructed PKWs have much higher specific discharges compared to the first PKWs.

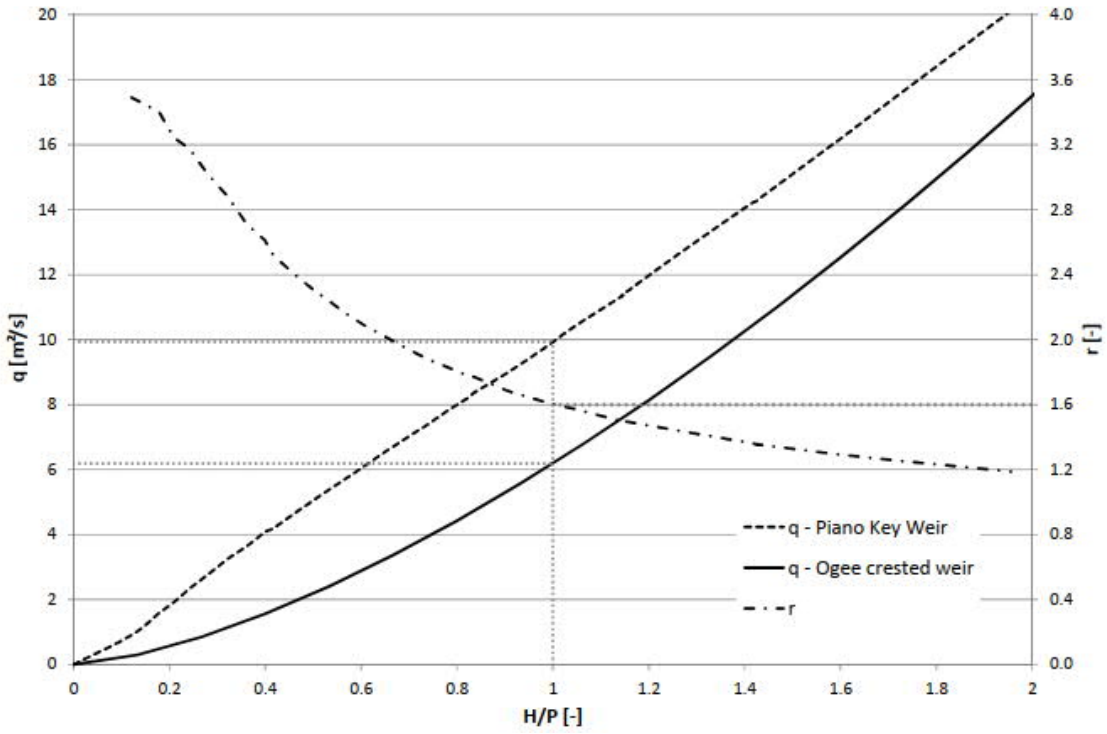

Figure 2.17: Comparison of unit discharge for PKW and ogee crested weir (Erpicum, *et al.*, 2013)

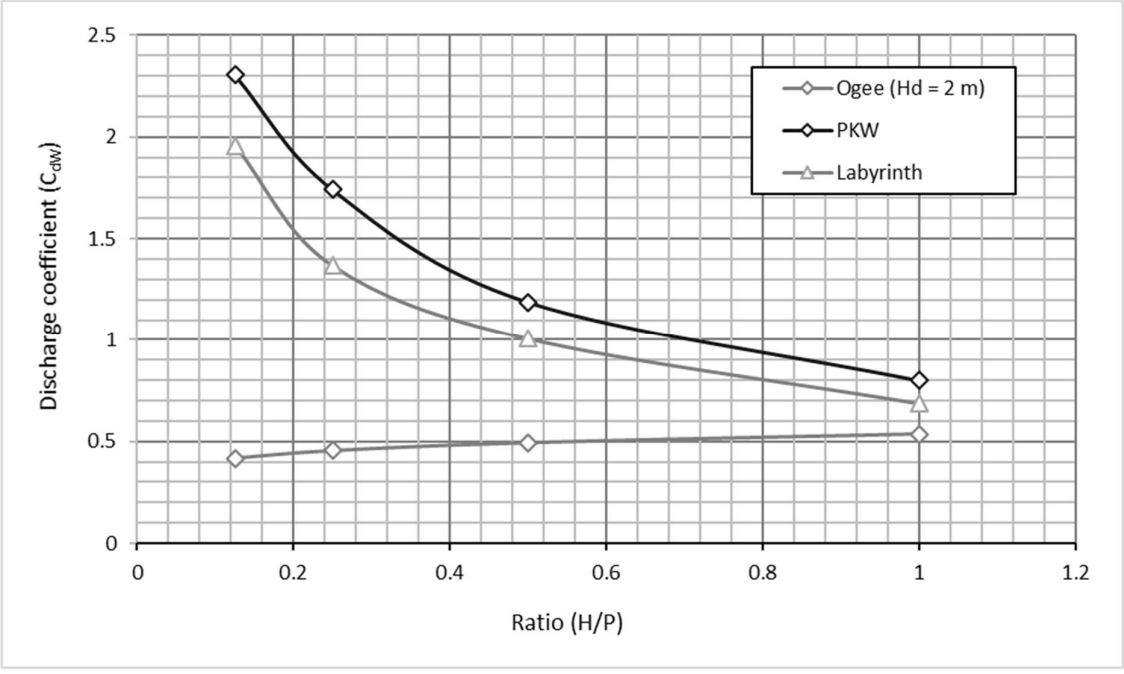

Figure 2.18: Comparison of discharge coefficients of linear, labyrinth and PKW spillways (Blancher, *et al.*, 2011)

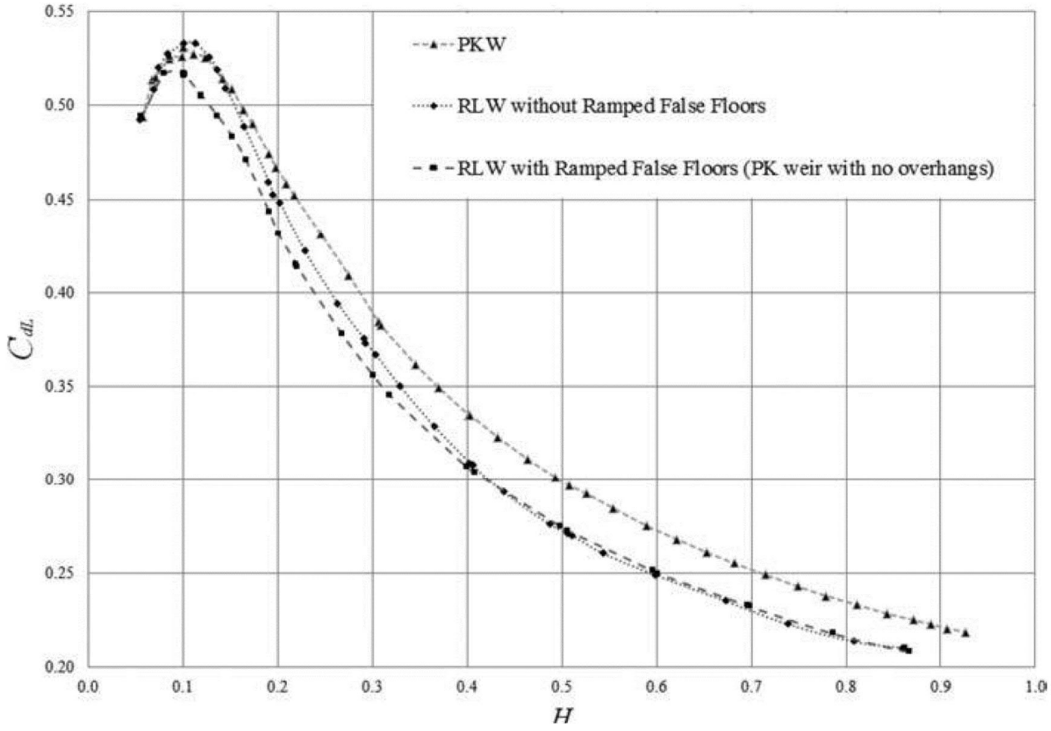

Figure 2.19: Comparison of discharge coefficients of labyrinth and PKW spillways (Anderson & Tullis, 2011)

Note: RLW = Rectangular labyrinth weir

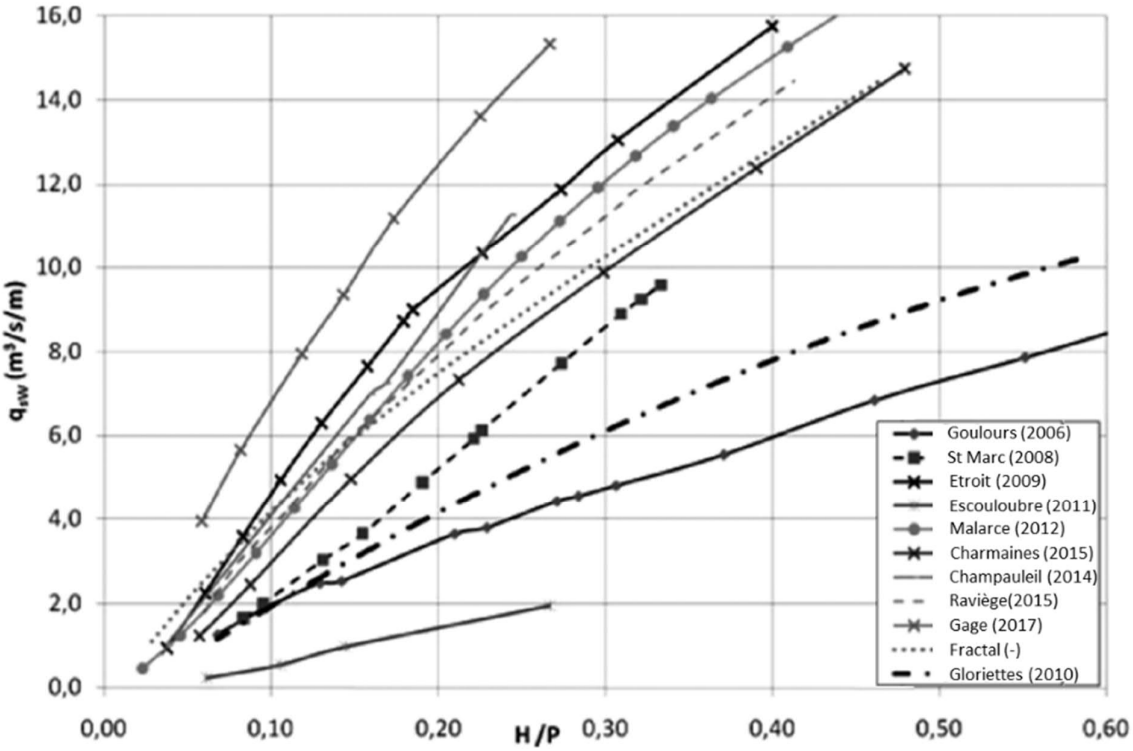

Figure 2.20: Specific discharge vs H/P for constructed PKW (Laugier, *et al.*, 2013)

2.4.3 Factors affecting the discharge efficiency

Several studies have been undertaken to determine the effect of the various geometrical parameters on the discharge capacity of PKWs.

The dominant geometrical parameters affecting the discharge efficiency are:

- The developed crest length, L;
- The total weir width, W;
- The upstream head, H_T; and
- The upstream weir height, P_i.

These parameters can be summarised as dimensionless ratios L/W and H_T/P_i and can be used to empirically determine the discharge capacity of PKWs with an 83% accuracy (Leite Ribeiro, *et al.*, 2013). Although other parameters also play a role on the discharge efficiency, their individual effects are generally less than 5% (Denys, 2019). These other parameters include the key height P, the inlet to outlet key ratios W_i/W_o and the overhang ratios B_i/B_o (Erpicum, *et al.*, 2014). A single set of optimal values for the parameters, however, does not exist and depends on the combination of the parameters.

The discharge per PKW unit, given that the units and approach conditions are identical, is not sensitive to number of PKW units (Leite Ribeiro, Pfister, Boillat, Schleiss, & Laugier , 2012b).

The different factors affecting the discharge efficiency and how these factors affect the discharge efficiency is discussed in detail in **Appendix A**. The factors can be summarised as follows:

- **Crest length magnification ratio (L/W):** The L/W ratio for most PKWs installed to date ranges from 4 to 8, however, a ratio of 5 seems to be the most cost effective and has been implemented in most existing PKWs (Lempérière, *et al.*, 2011) (Leite Ribeiro, *et al.*, 2013).
- **Head to weir height ratio, (H_T/P_i):** The efficiency of a PKW reduces as the head increases and the PKW starts behaving like a linear weir. Most PKWs implemented to date have a H_T/P_i ratio of 0.3 (highest 0.8) at the maximum design flow rate (Leite Ribeiro, *et al.*, 2013).
- **Key height to unit width ratio (P/W_u):** The optimum key height to unit width ratio, P/W_u, is approximately 1.33 for PKWs with standard L/W ratios equal to 5 (Machiels, *et al.*, 2014). However, a P/W_u ratio of 0.5 is considered a more economical design, especially for dam rehabilitation projects (Machiels, 2012). For “low” PKW heights, where $P/W_u < 1$, the discharge capacity increases as the head increases. For “high” PKWs (P/W_u), the discharge capacity becomes virtually independent of the PKW height.

- **Inlet and outlet key widths (W_i and W_o):** A higher inlet to outlet key ratio W_i/W_o results in higher discharge efficiency (Le Doucen, *et al.*, 2009). The optimum ratio is between 1.25 and 1.6 (Machiels, *et al.*, 2014), however, ratios of between 1.0 and 1.5 have been generally used in PKW prototypes (Leite Ribeiro, *et al.*, 2013).
- **Overhang lengths ratio, B_o/B_i and sidewall angles:** Hydraulic model studies showed that the discharge efficiency of PKW models with only an upstream overhang (Type B) is 12% more than models with symmetrical overhangs. According to Erpicum *et al.* (2014) and Machiels (2014) a B_o/B_i ratio of 3 yields the highest discharge efficiency for high PKWs with an L/W ratio equal to 5, except for very low heads. Hydraulic model studies by Electricité de France (EDF) indicated that the discharge efficiency of a PKW with a sidewall angle of 5° and wider inlet key compared to outlet key ($W_i>W_o$), is 5% to 20% more efficient than a Type A PKW with the same L/W ratio at lower heads (Circero, *et al.*, 2013).
- **Wall thickness and crest shape:** According to Blancher *et al.* (2011), as well as Laugier *et al.* (2013), thicker walls can reduce the discharge efficiency by 10% to 15% for a specific discharge. However, one should consider the practicality of constructing thin walled elements. Half-round or quarter-round upstream crests on the lateral walls, compared to flat crests, can increase the discharge efficiency of PKWs at low heads by up to 20%, however, the gain in efficiency reduces as the head increases above H/P > 0.3 (Circero, *et al.*, 2016).
- **Parapet walls:** Several studies have shown that placing a parapet wall on the upstream crest of the outlet key increases the discharge efficiency of PKWs (Vermeulen, *et al.*, 2011) (Machiels, *et al.*, 2013a). Parapet walls on the downstream crest of the inlet key have a marginal effect on the discharge efficiency.
- **Nose under upstream overhang of outlet key:** Adding a “nose” under the upstream overhang of the outlet key has been shown to streamline the approach flow into the inlet key, reduce energy losses and vortex shedding, and ultimately increases the PKW discharge efficiency (Denys, 2015).
- **Submergence and tail water level:** PKWs are generally installed on top of dams and therefore not affected by submergence (ICOLD Technical Committee on Hydraulics for Dams, 2016). If in-channel or in-river PKWs are submerged they are not significantly influenced and can operate under higher efficiency for submerged conditions compared to other weir types, due to their unique flow patterns (Schleiss, 2011).

- **Debris and drift wood:** PKWs have been found to be relatively insensitive to floating debris – washing most debris downstream during larger flows and if not, still retains 75% to 80% of their discharge capacity (Pfister, *et al.*, 2013).

2.4.4 Hydraulic design equations for a Type A Piano Key Weir

The design of PKWs is complicated by the large number of parameters affecting the discharge efficiency. However, several rating curve formulae have been developed for specific sets of geometrical characteristics based on experimental data.

Lempérière (2009) used Equation 2-6 to determine the specific discharge for a given design with geometrical dimensions relative to the wall height, P_m (measured from the intersection of sloped bases of adjacent keys - refer to **Figure 2.6**) and for headwater levels in the range of $0.4P_m$ to $2P_m$. This equation assumes that the head-discharge relationship is linear. The equation compared well with physical model results (error ± 2%) of the given design. However, for other geometries significant errors resulted and it was evident that the head-discharge relationship is slightly parabolic. These findings supported the need for the inclusion of other parameters into the equation (Anderson & Tullis, 2011).

$$q = 4.3\ h\sqrt{P_m} \qquad \textbf{2-6}$$

Where:

q Specific discharge ($m^3/s/m$)

h Piezometric head (m), for range $0.4P_m$ to $2P_m$

P_m Wall height measured from the intersection of sloped bases of adjacent keys (m).

Three general methodologies for Type A PKWs have been developed by Kabiri-Samani & Javaheri (2012), Leite Ribeiro *et al.* (2012a) and Machiels (2012). for specific parameter ranges. A summary of the specific geometrical ranges is included in **Table 2.3** as compared by Pfsiter & Schleiss (2013). The individual equations are only applicable to the geometrical limits in the table and must be respected when deriving rating curves.

Table 2.3: Geometrical limits of general equations for A-type PKWs (Pfister & Schleiss, 2013)

Equation	L/W	H/P	W_i/W_o	B/P	B_i/B, B_o/B
Kabiri-Samani & Javaheri (2012)	2.5 to 7.0	0.1 to 0.6	0.33 to 1.22	1.0 to 2.5	0.00 to 0.26
Leite Ribeiro et al. (2012a)	3.0 to 7.0	0.1 to 2.8	0.50 to 2.00	1.5 to 4.6	0.20 to 0.40
Machiels (2012)	4.2 to 5.0	0.1 to 5.0	0.50 to 2.00	1.0 to 6.0	0.29 to 0.33

a) Kabiri-Samani & Javaheri (2012)

Kabiri-Samani & Javaheri conducted 600 scaled physical hydraulic model tests for Type A, B and C PKWs for both free flow and submerged flow conditions. The rating curve is based on the general ogee equation (Equation 2-7).

$$Q = \frac{2}{3} C_d W \sqrt{2g\, H_t{}^3} \qquad \textbf{2-7}$$

Where:

- Q Discharge (m^3/s)
- C_d Discharge coefficient
- W Channel width (m)
- g Gravity acceleration (m/s^2)
- H_T Total upstream water head (m)

The discharge coefficient, C_d, for free flow conditions was derived as a function of the associated geometrical parameters, and is expressed as:

$$C_d = \left[0.212 \left(\frac{H}{P}\right)^{-0.675} \left(\frac{L}{W}\right)^{0.377} \left(\frac{W_i}{W_o}\right)^{0.426} \left(\frac{B}{P}\right)^{0.306} e^{1.504\frac{B_o}{B} + 0.093\frac{B_i}{B}}\right] + 0.606 \qquad \textbf{2-8}$$

** Refer to **Table 2.1** for notations.*

b) Leite Ribeiro et al. (2012a)

Leite Ribeiro et al. (2012a) followed the principle of comparing the discharge capacity of a PKW to that of a linear sharp crested weir, i.e. a relative discharge ratio, *r*. Physical hydraulic model studies were conducted for 49 different Type A PKW geometries, and free flow conditions without tail water submergence.

The relative discharge ratio can be expressed as:

$$r = \frac{Q_{PKW}}{Q_s} = \frac{Q_{PKW}}{0.42W\sqrt{2g{H_T}^3}} \quad \textbf{2-9}$$

Where:

Q_{PKW} PKW discharge (m^3/s)
Q_s Linear sharp crested weir discharge (m^3/s)
W Channel width (m)
g Gravity acceleration (m/s^2)
H_T Total upstream water head (m)

As discussed under **Section 2.4.3**, the PKW discharge efficiency, and therefore the relative discharge ratio, is primarily influenced by the developed crest length L, the total weir width W, the upstream head H_T and the upstream weir height, P_i. Secondary parameters include inlet to outlet key width ratio (W_i/W_o), inlet to outlet key height ratio (P_i/P_o), relative overhang length (B_i+B_o)/B, and relative parapet wall height (R_o/P_o). The relative discharge ratio can therefore be expressed as:

$$r = 1 + 0.24\left(\frac{(L-W)P_i}{WH}\right)^{0.9} wpba \quad \textbf{2-10}$$

Where:

$$w = \left(\frac{W_i}{W_o}\right)^{0.5}$$

$$p = \left(\frac{P_o}{P_i}\right)^{0.25}$$

$$b = \left(0.3 + \frac{B_o+B_i}{B}\right)^{-0.5}$$

$$a = 1 + \left(\frac{R_o}{P_o}\right)^2$$

** Refer to **Table 2.1** for notations.*

c) Machiels (2012)

Machiels (2012) did extensive research on the influence of serval parameters on the discharge efficiency of PKWs under free flow conditions. Flows ranged between 13 to 400 l/s/m. He expressed the unit discharge formula as the sum of the discharge over the downstream overhang (subscript *d)*, upstream overhang (subscript *u)* and the lateral side crests (subscript *s)*, using the following equations:

$$q = \frac{Q_{PKW}}{W} = q_u \frac{W_o}{W_u} + q_d \frac{W_i}{W_u} + q_s \frac{2B}{W_u} K_{Wi} K_{Wo} \quad \text{2-11}$$

$$q_u = 0.374 \left(1 + \frac{1}{1000H + 1.6}\right)\left(1 + 0.5\left(\frac{H}{H + P_T}\right)^2\right)\sqrt{2gH^3} \quad \text{2-12}$$

$$q_d = 0.445\left(1 + \frac{1}{1000H + 1.6}\right)\left(1 + 0.5\left(\frac{H}{H + P}\right)^2\right)\sqrt{2gH^3} \quad \text{2-13}$$

$$q_s = 0.41\left(1 + \frac{1}{833H + 1.6}\right)\left(1 + 0.5\left(\frac{0.833H}{0.833H + P_e}\right)^2\right)\left(\frac{P_e + \beta}{(0.833H + P_e)^{\alpha} + \beta}\right)\sqrt{2gH^3} \quad \text{2-14}$$

Where:

W_u Unit width, W_i+W_o+2T (m)

P_T Total upstream height $P_T = P + P_d$ (m)

P Height of PKW (m)

P_d Dam height below PKW (m)

P_e Mean weir height along sidewall (m)

$$P_e = P_T \frac{B_o}{B} + \frac{P}{2}\left(1 - \frac{B_o}{B}\right) \quad \text{2-15}$$

α and β Characterise influence of inlet key slope

$$\alpha = \frac{0.7}{S_i{}^2} - \frac{3.58}{S_i} + 7.55 \text{ and } \beta = 0.029e^{-\frac{1.446}{S_i}} \quad \text{2-16}$$

S_i Inlet key slope $S_i = \frac{P}{B - B_o}$

K_{Wi} Influence of flow velocity

$$K_{Wi} = 1 - \frac{\gamma}{\gamma + W_i{}^2} \text{ and } \gamma = -0.0038\frac{W_i}{W_o} + 0.0055 \quad \text{2-17}$$

K_{Wo} Side crest length decrease induced by outlet key flow and side nappe interference.

$H/W_o \leq L_1$	$K_{Wo} = 1$
$L_1 \leq H/W_o \leq L_2$	$K_{Wo} = \frac{2}{(L_2 - L_1)^3}\left(\frac{H}{W_o}\right)^3 - \frac{3(L_2 - L_1)}{(L_2 - L_1)^3}\left(\frac{H}{W_o}\right)^2 + \frac{6L_2L_1}{(L_2 - L_1)^3}\frac{H}{W_o} + \frac{L_2{}^2(L_2 - 3L_1)}{(L_2 - L_1)^3}$
$H/W_o \geq L_2$	$K_{Wo} = 0$

2-18

** Refer to **Table 2.1** for notations not defined above.*

This analytical formulation showed a unit discharge accuracy of 15% when compared with data from physical hydraulic model studies for a wide range of geometrical parameters (Machiels, *et al.*, 2013).

d) Comparison of design equations

Pfsiter & Schleiss (2013) compared the rating curves of the three methodologies for a hypothetical Type A PKW, defined according to the relevant parameter limits given in **Table 2.3**. The following characteristics/parameters were applied:

$W = 100$ m	$B_i = B_o = 2.00$ m
$P_d = 30$ m	$W_u = W_i + W_o + 2T_S = 4.00$ m,
$Q_D = 2500$ m3/s	$N = W/W_u = 25$,
$B = 8.00$ m,	$L = W + (2NB) = 500$ m,
$P = P_i = P_o = 5.00$ m	$L/W = 5.00$,
$T_S = 0.35$ m	$B/P = 1.60$,
$R = 0$ m (without parapet walls),	$W_i/W_o = 1.20$,
$W_i = 1.80$ m	$B_i/B = B_o/B = 0.25$,
$W_o = 1.50$ m	$S_i = S_o = 0.83$

As shown in **Figure 2.21**, the three methodologies give similar rating curve results, especially the methodologies followed by Kabiri-Samani & Javaheri (2012) and Leite Ribeiro *et al.* (2012a). The methodology followed by Machiels (2012) is more conservative. The comparison of these methodologies highlights the importance of applying the methodologies only within the geometrical ranges for which they have been validated. One parameter outside of the geometrical limits may result in a completely different rating curve (Machiels, *et al.*, 2013).

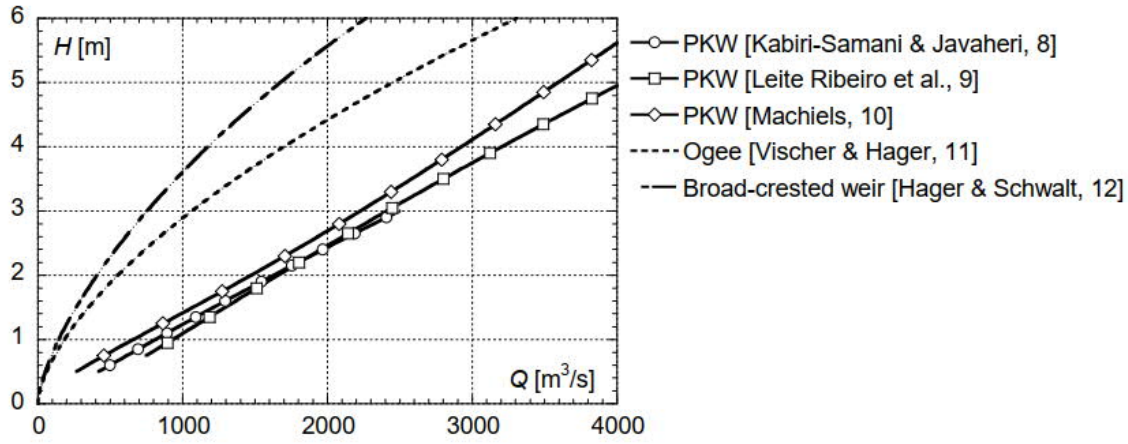

Figure 2.21: Comparison of rating curves for ogee crested weir, sharp crested weir and PKW (Pfister & Schleiss, 2013)

These methodologies do not consider economic optimisation. Nevertheless, these methodologies serve as useful tools for the preliminary design of PKWs. Pfister & Schleiss (2013) recommend that several equations should be considered during design, as well as

numerical or ideally physical modelling, if possible. Additional to the assurance of the PKW hydraulic behaviour, numerical or physical modelling can be useful to optimise the design.

e) Numerical modelling

Three-dimensional computational fluid dynamic (CFD) modelling has been used to investigate the hydraulic behaviour of PKWs, as well as for the preliminary design of many PKWs installed to date. These numerical models have been successfully validated with experimental data and show less than a 5% deviation in flow rates (Erpicum, *et al.*, 2012).

The HECE research group of the University of Liege developed WOLF1D-PKW, a one-dimensional numerical model, based on large scale physical model test results, aimed at predicting the discharge capacity of a PKW with a 10% accuracy. The model simulates flow over half a unit – half an inlet and half an outlet with lateral wall – for a given upstream discharge range (Erpicum, *et al.*, 2012). This WOLF1D-PKW model is available as a freeware on http://www.pk-weirs.ulg.ac.be.

Although CFD modelling can predict the hydraulic behaviour of PKWs to a high level of accuracy, it cannot accurately replicate all relevant flow characteristics, including downstream flow and energy dissipation. Therefore, ICOLD Bulletin 172 (2016) recommends that the final geometrical design of a PKW should be evaluated by means of a physical hydraulic model. The majority of the large PKWs implemented to date have been optimized and validated by physical hydraulic modelling.

3. FLOW INDUCED VIBRATIONS

3.1 OVERVIEW

The noise and vibrations that occur as a result of fluid flow are referred to as flow-induced vibrations (FIV). FIV result from the transfer of energy from pressure oscillations in a fluid to a system or structure in attempting to return to its equilibrium state after being deflected. The basic elements of FIV are (Naudasher & Rockwell, 2012) (Ausoni, 2009):

- **Body oscillations:** Either an elastic structure or a rigid structure that is elastically supported and which can deform or undergo angular movement;
- **Fluid oscillations:** A fluid mass that oscillates as a result of fluid compressibility or gravity; and
- **Source of excitation:** Source of vibration – discussed later.

FIV are apparent in all water related components, although all are not addressed to the same extent in hydraulic design. Body oscillations mainly occur in thin walled elements where the stiffness of the element is not sufficient to resist deflections, e.g. thin walled overflow structures, spillway gates and thin walled pipelines (Naudasher & Rockwell, 2012). Considering that PKWs are mainly constructed from rigid reinforced concrete, FIV are not generally addressed. However, with all free-fall overflow structures the fluid oscillation of the overflow nappe needs to be addressed (Falvey, 1980). Three general sources of excitation exist as described in Naudasher & Rockwell (2012):

- **Extraneously-induced excitation (EIE):** Random or periodic excitations, caused by fluctuating pressures and flow velocities, independent of flow instability caused by the structure itself and structural movement (generally associated with turbulence, waves, earthquakes etc.).
- **Movement induced excitation (MIE):** Excitations due to fluctuating forces arising from movements of a self-exciting oscillating body.
- **Instability-induced excitations (IIE):** Excitation due to the instability of flow and inherent to the flow created by the considered structure. IIE can be further classified based on the control mechanisms as flow-dynamic excitations, fluid-resonant excitation and fluid elastic excitation.

The FIV potentially applicable to PKWs relate to IIE and are further discussed in the following section and sub-sections.

3.2 INSTABILITY-INDUCED EXCITATIONS

The main source of IIE is a flow instability that results in flow oscillations if a certain threshold value of the flow velocity is exceeded, e.g. flows around or past a structure or obstruction resulting in the presence of vortex shedding, imposing shear layers, interface instabilities and swirling flow instabilities (Naudasher & Rockwell, 2012) (Denys, 2019). Energy is transferred from the flow to the instability and then back to the flow via a feedback loop. Two critical locations exist in the flow – one location being sensitive to disturbances, and the other being where new disturbances are self-generating. These new self-generating disturbances feed back to the sensitive location via the fluid (Falvey, 1980). The type and control (or amplification mechanism) exercised on the flow instability thus play major roles in IIE. The control mechanisms for IIE include (Naudasher & Rockwell, 2012) (Falvey, 1980):

- Flow-dynamic excitation: Function of flow dynamics;
- Fluid-resonant excitation: Function of flow dynamics and resonating fluid body (resonant element located in the feedback path); and
- Fluid-elastic excitation: Function of flow conditions and an elastic resonating structure.

Fluid-elastic or fluid-resonant are the most dangerous IIE control mechanisms as they can lock into the frequency of the body or fluid oscillator and result in a resonant response. Flow oscillations and the associated generated forces can become so intense, well correlated and concentrated around a specific frequency that large amplitude oscillations of the body or fluid can occur (Naudasher & Rockwell, 2012). It is therefore important to assess the possibility of resonance between the dominant frequencies of IIE and the natural frequency of the body or fluid oscillators (Naudasher & Rockwell, 2012).

IIE can be controlled or prevented by altering the geometry and or the flow dynamics by incorporating e.g. flow splitters, flow guides etc. (Naudasher & Rockwell, 2012).

The FIV potentially applicable to PKWs and further discussed in this study include (Denys, Basson, & Strasheim, 2017):

- Vortex shedding, as a result of the shear boundary layer and the separation bubble that forms as flow diverges around the corner of the outlet key upstream overhang into the inlet key.
- Nappe oscillations, as well as the dynamics and sub-atmospheric pressures of the air cavity that develop under the nappe.

The nappe oscillations form the focus of FIV investigations of this study.

3.2.1 Vortex shedding and flapping

Vortex shedding, and flapping can be simply described as the release of vortices from a separation bubble that develops as a result of flow around bluff geometric bodies. Vortex shedding occurs at higher frequencies, whereas flapping occurs at lower frequencies (Kiya & Sasaki, 1983). As vortices are shed, there is a drop in pressure in the separation bubble, which can cause FIV (Naudasher & Rockwell, 2012).

As a fluid flows around a bluff geometric body, a transfer of transverse momentum occurs and causes a free shear boundary to form and detach from the downstream edge of the body. The shear boundary reattaches itself to the body further downstream and develops a separation bubble (**Figure 3.1**). The location where the shear boundary reattaches is governed by the mass equilibrium of the separation bubble and upstream turbulence. This separation bubble consists of a low velocity recirculation zone. The flow in this area is continuously buffeted by the surrounding flow and therefore highly dynamic and unstable (Naudasher & Rockwell, 2012) (Denys, 2018).

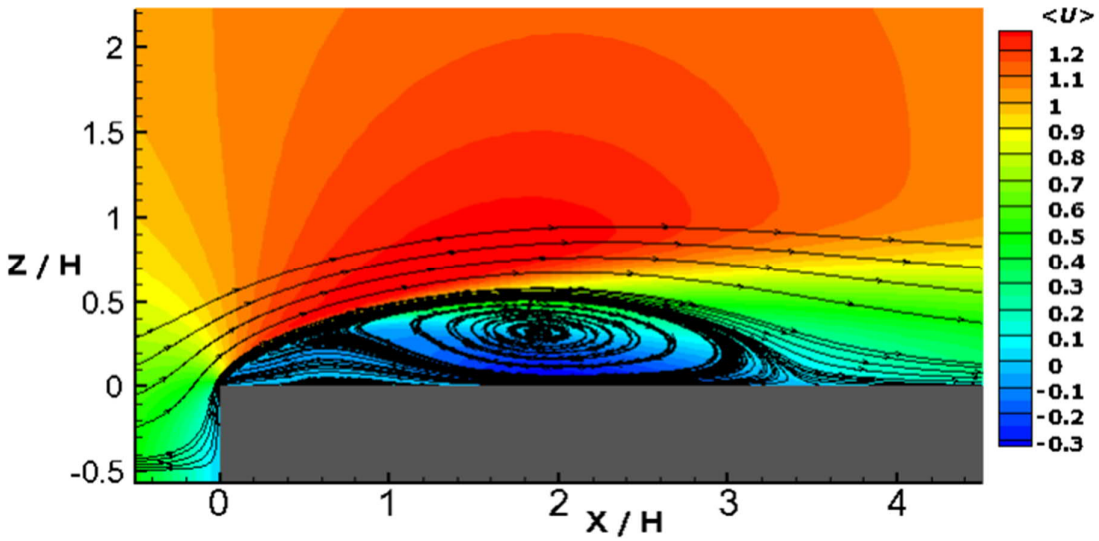

Figure 3.1: Instantaneous flow field of separation bubble (Tenaud, *et al.*, 2016)

The shear zone between the low velocity, high pressure separation bubble and the high velocity, low pressure main flow is referred to as the vortex sheet or mixing layer. This boundary layer is relatively narrow and initially laminar. The layer starts to break down and transitions to turbulent flow through Kelvin-Helmholtz instabilities. Kelvin-Helmholtz instabilities occur when there is a velocity difference between two zones of flow, in this case between the bubble and main flow (Tenaud, *et al.*, 2016). These instabilities grow in amplitude, start to distort and eventually roll up as vortices as shown in **Figure 3.2**.

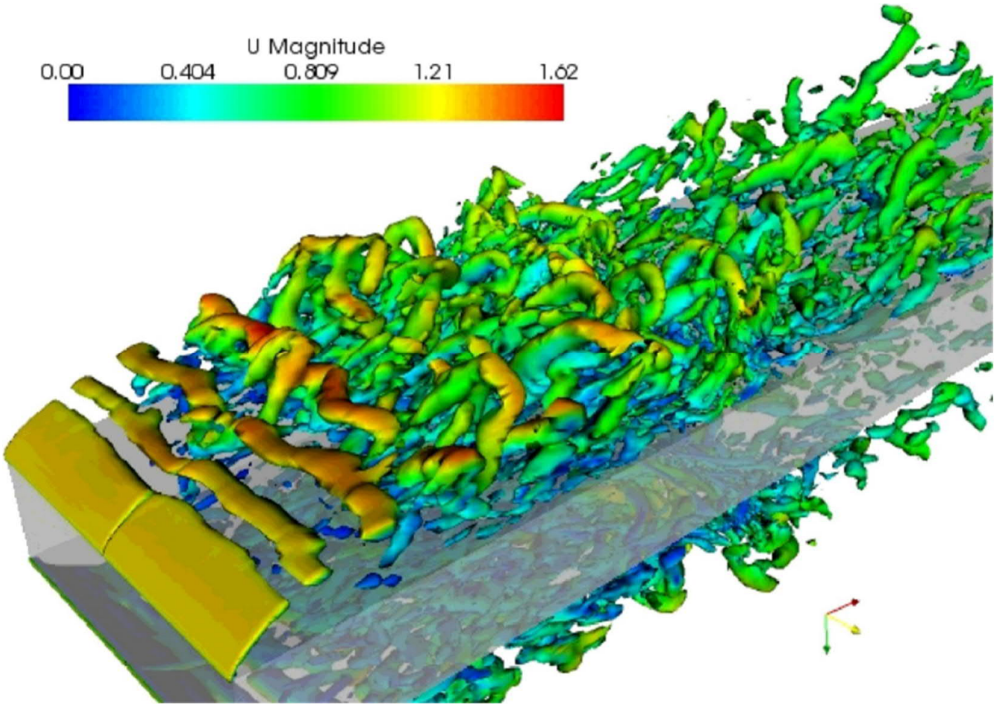

Figure 3.2: Vortex shedding as a result of a collapse of a separation bubble (Tenaud, *et al.*, 2016)

Vortex shedding also occurs due to the sudden collapse in the size of a separation bubble. The bubble gradually grows as mass from the surrounding flow is absorbed into the bubble. When the bubble becomes too large or when there is a short-duration low-flow wave from the upstream turbulent water body, the mass is shed as a large vortex. This is referred to as flapping (Tenaud, *et al.*, 2016) (Denys, 2018).

Vortex shedding and the associated FIV in PKWs were investigated in more detail by Denys (2019) and are not further discussed in this study. However, a short summary of the results is discussed below.

In the case of a PKW, most of the flow (≈ 90%) is discharged via the inlet key. As described in **Section 2.3.1** the near bed flow, as well as the middle depth flow approaching the outlet key diverges around the upstream overhang of the outlet key into the inlet key. As the flow changes direction around the 90° corner of the upstream overhang of the outlet key, a shear boundary forms at the corner. The shear boundary reattaches to the inlet key wall further downstream and forms a separation bubble. Vortices are shed from the separation bubble, transported downstream, merged and then discharged over the sidewall crest of the inlet key as shown in **Figure 3.3** (Denys, 2018). From **Figure 3.4** it can be concluded that the vortices are periodic. It was also concluded by Denys (2018) that the strength of the pressure

fluctuations increases as the discharge increases, although it remains at approximately the same frequency.

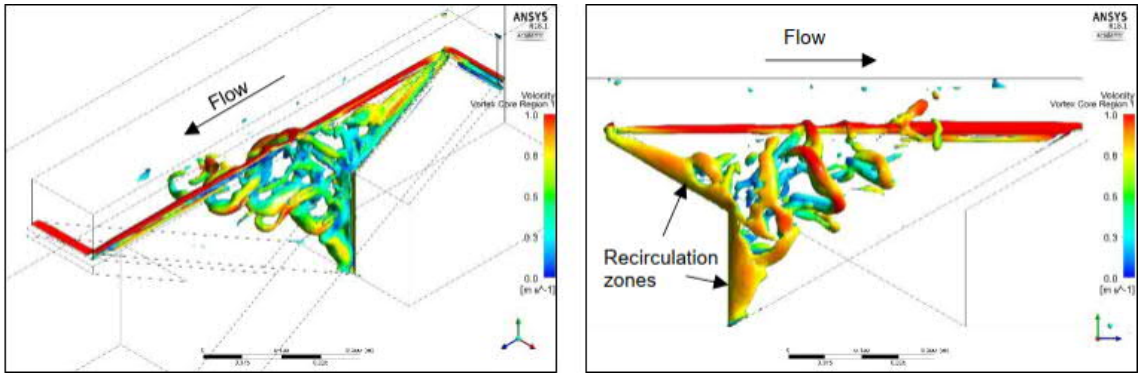

Figure 3.3: Vortex shedding occurring in the inlet key of a PKW, tilted view (right) and side view (left) (Denys, 2018)

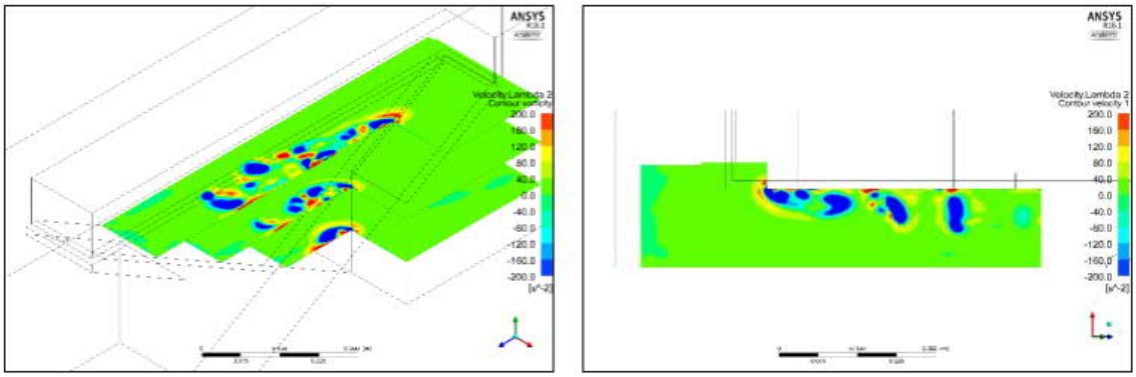

Figure 3.4: Vorticity in the inlet key of a PKW, 3D view (right) and plan view (left) (Denys, 2018)

As shown by **Figure 3.5**, the pressure upstream of the of the PKW is generally hydrostatic and inside the inlet key the pressure is slightly lower than hydrostatic due to the higher velocities. Near the separation bubble, there is a definite pressure drop. As the vortices are shed from the separation bubble pressure fluctuations occur on the sidewall. Large scale vortices within and downstream of the bubble are linked to localised pressure minimums on the sidewall, whereas pressure maximums occur between the discharge of two vortices (Denys, 2019). The highest fluctuations occur were the vorticity is the strongest (upstream of the reattachment point), as well as where the PKW sidewall structure is the weakest – refer to **Figure 3.6** (Denys, 2018).

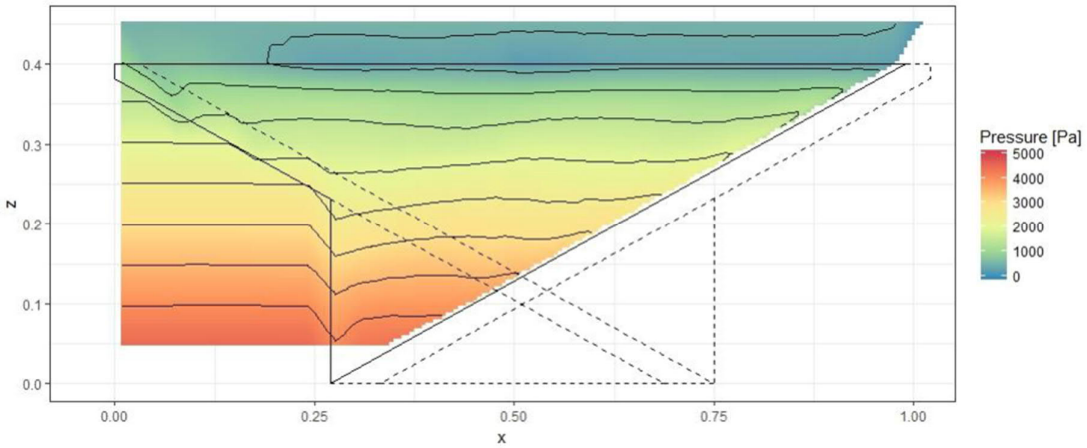

Figure 3.5: Mean pressure on PKW sidewall (Denys, 2018)

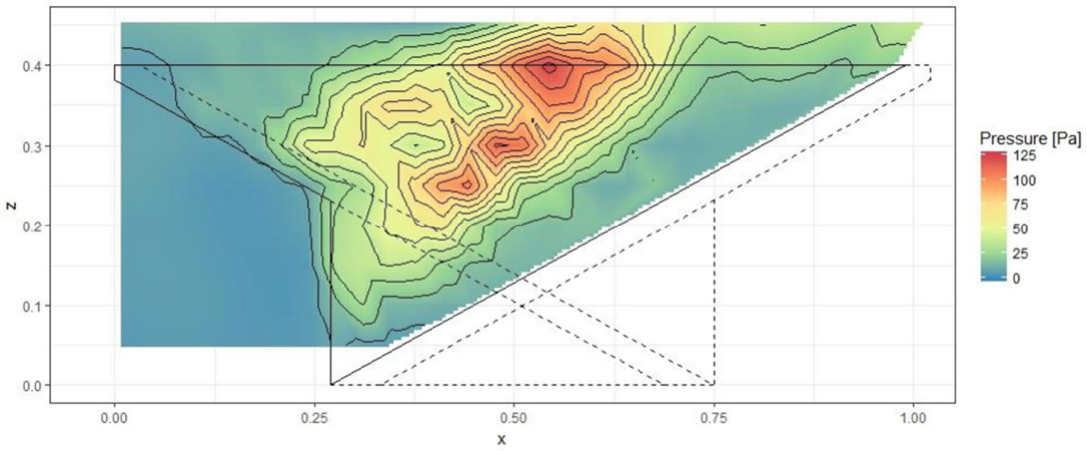

Figure 3.6: Root-mean-square pressure on PKW sidewall (Denys, 2018)

Vortex shedding along the upstream side of the inlet key results in vortex induced vibrations (VIV), i.e. the structure receives energy from a system of vortices caused by the movement of the fluid past the structure (Denys, 2019).

3.2.2 Phase interface instability (Nappe oscillations)

Nappe oscillations occur when pressures in the air cavity behind the nappe become unstable and start to fluctuate, for reasons not yet well understood, and cause the nappe to beat or oscillate (Crookston & Tullis, 2013) (Anderson, 2014). Nappe vibrations can be characterised by intense acoustic pressure waves and noise, as well as horizontal banding and waves or ripples visible on the nappe as shown in **Figure 3.7** (Crookston, *et al.*, 2014) (Lodomez, *et al.*, 2018a).

Nappe oscillations are known to occur at several weir types with large fall distances, such as linear and labyrinth weirs, crest gates and fountains for relatively low headwater ratios (Lodomez, *et al.*, 2018) (Crookston & Tullis, 2013).

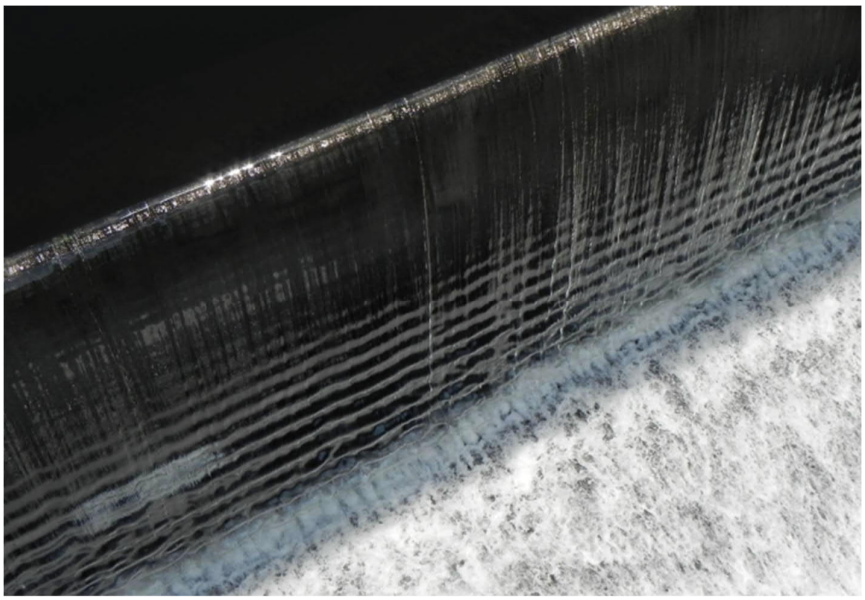

Figure 3.7: Horizontal bands in overflow nappe caused by nappe oscillations (Lodomez, *et al.*, 2018)

In terms of IIE as discussed in **Section 3.2**, the location where the nappe leaves the structures (detachment point) is considered as the sensitive site and where the nappe strikes the downstream pools is considered as the site where new disturbances are generated. These disturbances are fed back to the sensitive site via the air column beneath the nappe (Falvey, 1980).

There are several theories concerning the mechanisms that initiate nappe oscillations. The Kelvin-Helmholtz mechanism attributes nappe vibration to the shear forces that occur on the interface between two fluids that have different velocities – in this case, the nappe and the surrounding air (Crookston, *et al.*, 2014). Studies of a vertical falling water jet in a vacuum chamber reported no nappe oscillations, implying that the presence of air is required to induce nappe vibrations (Binnie, 1971).

Nappe oscillations primarily occur during partially aerated nappe conditions rather than aerated and drowned nappe conditions (refer to **Section 4.1.1** for definitions). Although artificial aeration may have a reducing effect on the nappe instability (Crookston & Tullis, 2013), it does not necessarily prevent vibrations from occurring (Crookston & Tullis, 2011). Nappe instabilities have been observed for fully aerated nappes (Crookston, *et al.*, 2014) (Falvey, 1980) (Lodomez, *et al.*, 2018a). Experimental studies by Lodomez *et al.* (2018a) have showed that the air pocket behind the nappe only serves as an amplification and stabiliser factor and does not affect the occurrence of nappe vibrations.

It has been theorised that nappe oscillations are driven by the stability of the boundary layer and pressure discontinuity on the crest of the weir as water leaves the crest. A pressure discontinuity occurs between the slightly negative air pressure behind the nappe and that of the positive boundary layer pressure. Furthermore, the nappe experiences a sudden pressure drop as it detaches from the crest and the pressure originally induced by the weight of the water reduces to atmospheric or sub-atmospheric pressure (Chanson, 1996). Previous studies have showed that increasing the crest roughness (e.g. by placing stones on the crest) eliminates nappe oscillations completely or at least reduces the discharge range over which nappe oscillations occur. This supports the theory that the point where flow detaches from the downstream end of the crest plays an important role on the occurrence of nappe oscillations (Lodomez, *et al.*, 2018). Kyotoh (2002) concluded that nappe vibrations are affected by the propagation of pressure fluctuations in the air cavity behind the nappe, the shear wave instability induced by the falling water and surface tension effects on the water sheet.

Studies by Lodomez *et al.* (2018a) noted that nappe oscillations are linked to the number of wavelengths existing in the length of the falling nappe – thus implying that nappe oscillations are affected by the fall height of the nappe. Nappe oscillation is therefore not necessarily governed by a single mode and can be initiated, fed back and sustained by more than one mode (Lodomez, *et al.*, 2018a).

Nappe vibrations at the Black Canyon Dam, Idaho USA, resulted in the doors and windows of the nearby power plant and buildings to shake (Glover, *et al.*, 1939). A similar case was experienced due to the nappe vibrations of the Linville Land Harbour Dam labyrinth weir, North Carolina USA, during low overflow heads – the noise affected nearby residents and some homeowners also claimed to feel vibrations in walls and the floors (Crookston, *et al.*, 2014). According to Lodomez *et al.* (2018a) there is a definite link between nappe oscillations and the noise generated by the overflow nappe, however, the sound is generated by the interaction of the nappe with the surrounding air and not the impact of the nappe on the downstream area.

In some cases, nappe instability can cause significant variation in the air cavity size between the nappe and the structure, as well as fluctuations between aerated and drowned nappe behaviour. If the frequency of the nappe instability corresponds to the natural frequencies of the structure, i.e. the resonance phenomenon, damage can be caused to the overflow structure (Crookston & Tullis, 2013). The USA Bureau of Reclamation (Falvey, 1980) recommends that these flow-induced vibrations are investigated in all new hydraulic structures that include an overflow nappe.

According to Falvey (1980), to avoid these vibrations the feedback path (air column beneath the nappe) must be disturbed e.g. by breaking the nappe into smaller sections by incorporating nappe breakers (Falvey, 1980). Nappe oscillations have been successfully reduced in gated spillways by adding splitters to the gate crest. The splitters divide the overflow nappe and aerate the area under the nappe. In the case of uncontrolled free overflow spillways, adding splitters can reduce the hydraulic capacity and cause accumulation of floating debris. Hence, different approaches have been followed to prevent nappe oscillations in free overflow structures. Other solutions include increasing the crest roughness or modifying the crest profile to keep the flow attached to the downstream face of the weir (Lodomez, *et al.*, 2018a) (Lodomez, *et al.*, 2018).

As mentioned, nappe oscillations have been observed in several labyrinth weirs. Considering the similarity between labyrinth and PKWs, there is a possibility of nappe oscillations and potential for structural vibrations to occur in PKWs.

As part of the PKW physical hydraulic model study of St Marc Dam, dynamic pressures were measured on the inside of the inlet key of the PWK and on the downstream face of the inlet key (behind the nappe). These fluctuating pressures caused vibrations in the model structure. These vibrations disappeared when the nappe was aerated artificially as illustrated in **Figure 3.8** (Leite Ribeiro, *et al.*, 2007).

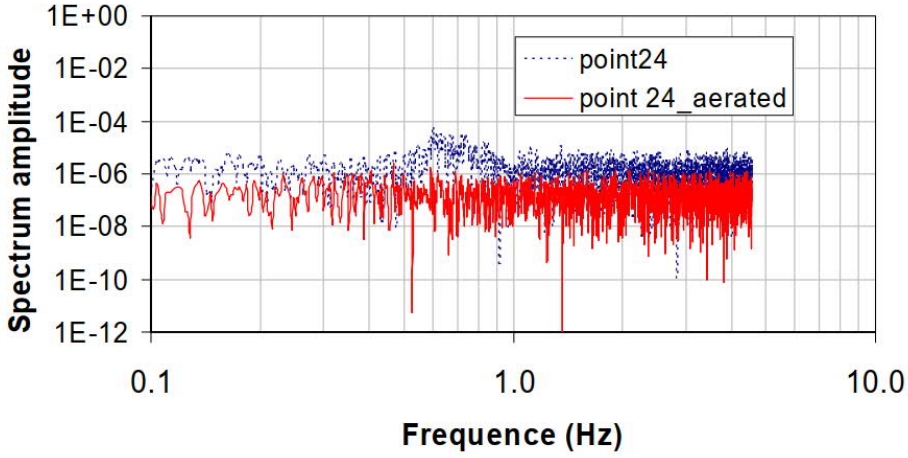

Figure 3.8: St Marc Dam - Energy Spectrum Density inside the upstream alveoli, with and without aeration (Leite Ribeiro, *et al.*, 2007)

Similar observations were made during the physical hydraulic model testing of the Dartmouth Dam, Australia; significant pulsing of the air cavity under the nappe occurred for high flow conditions (H/P > 0.8), however, these pulses disappeared when the nappe was artificially aerated (Phillips & Lesleighter, 2013).

Considering that nappe oscillations are affected by the nappe fall height and that, in the case of the PKW, the fall height varies depending on the position on the PKW, different wavelengths or frequencies may be observed at different positions in PKWs.

One of the objectives of this study is to investigate whether nappe instabilities or pressure fluctuations in the air cavity behind the nappe occur at PKWs, and if so, what are the effects on these instabilities or fluctuations of artificially aerating the nappe.

4. AERATION OF PIANO KEY WEIRS

4.1 OVERVIEW

4.1.1 Natural aeration

Several studies have been conducted regarding the natural nappe aeration conditions for linear weirs as well as labyrinth weirs. In general, four natural nappe aeration conditions occur at labyrinth weirs, which can also be applicable to PWKs. These conditions are referred to as follows (Crookston & Tullis, 2013):

- **Clinging**: The nappe clings to the downstream face of the weir wall for lower headwater ratio (H_T/P) values;
- **Aerated**: An air cavity is formed between the nappe and the weir wall while the nappe trajectory remains relatively constant;
- **Partially aerated**: The size of the air cavity between the nappe and the weir wall becomes non-uniform and unstable for higher H_T/P - distributed, isolated air cavities which fluctuate in size and locations occur rather than one continuous air cavity along the wall with a constant trajectory; and
- **Drowned**: A thick nappe without an air cavity occurs at higher values of H_T/P

The following characteristics influence the aeration condition:

- Weir crest shape;
- Weir height (P);
- Head (H_T);
- Depth and nature of the flow turbulence behind the nappe;
- Momentum and trajectory of the flow passing over the crest; and
- Pressure behind the nappe (sub-atmospheric for non-aerated or atmospheric for aerated nappes)

In general, the flow and aeration conditions of the nappe of a labyrinth weir will transition from clinging to aerated, to partially aerated, and finally to drowned as the head increases (Crookston & Tullis, 2013). Generally, air is entrained into the flow as the falling nappe intersects with the downstream pool of water. The pressure in the air cavity behind the nappe can be sub-atmospheric if the cavity is not vented, and as such can result in nappe oscillations (Chanson, 1994).

4.1.2 Artificial aeration

Artificial aeration of a system refers to the introduction of air to water flow at atmospheric pressure, generally by means of air vents connected to an atmospheric air source. This is

different to the natural air inception through the boundary layer of flow. As discussed under **Section 3.2.2**, if an air pocket under a free-falling nappe becomes isolated or depressed (by sub-atmospheric pressures), the nappe may start to oscillate, reduce the discharge efficiency and may cause a resonance vibration of the structure (Vermeulen, *et al.*, 2017).

Nappe aeration is known to influence the discharge capacity of labyrinth weirs. The discharge efficiency is slightly higher than estimated when the nappe is not aerated, i.e. sub-atmospheric pressures underneath the nappe (Crookston & Tullis, 2013). These small negative pressures develop underneath the nappe for H/P between 0.1 and 0.2 (Tullis, *et al.*, 1995). It was initially expected that the same phenomenon would occur in PKWs, However, according to preliminary tests by Anderson & Tullis (2011) the discharge efficiency of a PKW is independent of nappe conditions (vented and non-vented).

As mentioned in **Section 3.2.2**, artificial aeration of the nappe resulted in dynamic pressures and subsequent structural vibrations disappearing in the physical hydraulic model study of the PKW for St-Marc Dam (Leite Ribeiro, *et al.*, 2007). Other physical hydraulic models constructed by EDF, however, showed that flow over a PKW seems to be naturally aerated, and not subjected to clinging and vibration, even for low heads (ICOLD Technical Committee on Hydraulics for Dams, 2016). On the other hand, at higher flows the cavity under the nappe becomes isolated which may result in negative pressures underneath the nappe, as well as nappe instability (Phillips & Lesleighter, 2013) (Mehboudi, *et al.*, 2017).

According to Vermeulen *et al.* (2017) the air demand underneath the nappe for PKWs is lower than that of other hydraulic structures, such as labyrinth weirs and flap gates. This is attributed to the flow discharged over the outlet keys that does not generate a nappe with an air pocket beneath it, due to the sloped base of the outlet key. The nappe over the outlet key upstream crest transitions directly from clinging to fully aerated (**Section 2.3.2**).

Despite the above, the majority of PKWs installed to date include aeration pipes below the downstream overhang of the inlet key. **Section 4.2** provides a summary of the aeration systems installed in PKWs to date. The aeration pipes are normally connected to atmospheric pressure on both sides of the spillway via a gallery. The aeration systems of Malarce Dam and Goulours Dam, both in France, are shown in **Figure 4.1**. It is believed that artificial aeration of the overflow nappe improves flow characteristics and stability (Laugier, *et al.*, 2013).

Figure 4.1: Aeration network at St Marc (left) and Goulours (right) (Vermeulen, *et al.*, 2017a)

Section 4.3 elaborates on the aeration network designs followed to date for PKWs. However, the added benefits of artificially aerating the nappe, and the influence on the stability of the structure, have not yet been investigated in detail.

Furthermore, very few studies have been conducted to evaluate the air entrainment through PKW aeration pipes. Air entrainment measurement devices have been installed on the Malarce Dam (ICOLD Technical Committee on Hydraulics for Dams, 2016), however, no published data were available at the time of completing this thesis.

One of the objectives of this study is to investigate the effect on the hydraulic characteristics of PKWs of artificially aerating the nappe and whether there are noticeable differences in these characteristics depending on the size of aeration pipes.

4.2 AERATION SYSTEMS IMPLEMENTED FOR EXISTING PIANO KEY WEIRS

A summary of the aeration pipe sizes for several of the PKWs constructed to date are given in **Table 4.1**. The sizing methodologies followed for the aeration networks of the PKWs given in the table are described in **Section 4.3.2**.

Table 4.1: Summary of PKWs with aeration systems

Dam	Country	Date of construction	Q at MWL (m^3/s):	H_{design} (m)	Aeration (type and diameter of the pipe)	P (m)	H/P	W (m)	Nr of inlets	Nr of outlets
Goulours	France	2006	68	0.95	PVC pipe of 150 mm ø	3.05	0.311	14.1	2+0.5	3
Saint-Marc	France	2008	134	1.35	PVC pipe of 500 mm ø	5.15	0.262	15.1	2	3
L'Etroit	France	2009	97	0.95	PVC pipe of 500 mm ø	5.02	0.189	11.67	2	3
Gloriettes	France	2010	90	0.8	HDPE pipe of 160 mm ø	3	0.267	16.5	3	4
Malarce	France	2012	568	1.5	PVC pipes of 250 mm ø + collectors of 400 mm ø	4.4	0.341	42.5	11 +1 closing	11 +1 closing
Campauleil	France	2014	190	0.9	PVC pipe of 150 mm ø + collector of 300 mm ø	5.35	0.168	16.55	4	4
Charmines	France	2015	300	1	PVC pipe of 250 mm ø + collector of 500 mm ø	4.38	0.228	2 x 33	2 x 4	2 x 4
Rassisse (2 PKWs)	France	2015	431		HDPE pipe of 200 mm ø	3.75 2.7		37.75 14	9 6	8 4
Raviege	France	2015	284	1.4	PVC pipes of 200 mm ø + collector of 350 mm ø	4.67	0.300	25.8	4 + 2 closing	5
Record	France	2016	1350		PVC pipe of 200 mm ø + collector of 500 mm ø	3		4 x 12.5	4 x 3	4 x (2 + 2 closing)
Gage	France	2017	398	1.75	PVC pipes of 300 mm ø + collector of 800 mm ø	6	0.292	26.6	7	6 + 2 closing
Hazelmere	South Africa	2017	4288	3.23	HDPE pipe of 300 mm ø	10	0.323	16.5	14	14
Oulet Mellegue	Algeria	In progress	3805		HDPE pipe of 400 mm ø	6.8	0.660	99.8	11	12

4.3 AERATION NETWORK DESIGN

4.3.1 Aeration design for overflow structures

Traditional labyrinth weirs have improved aeration characteristics compared to straight weirs (Wormleaton & Soufiani, 1998). However, by changing the nappe aeration conditions and nappe stability, the discharge capacity and forces experienced by the flank walls are affected (Chanson, 1994).

In the case of linear weirs with a vertical step below the crest, the nappe ventilation requirements can be calculated as follows (Levin, 1968):

For 3 < Fr < 10

$$\frac{{Q_{air}}^{nappe}}{Q_w} = 0.19\left(\frac{h-d_p}{d_b}\right)^{0.95} \quad \textbf{4-1}$$

For 13 < Fr < 15

$$\frac{{Q_{air}}^{nappe}}{Q_w} = 0.21\left(\frac{h-d_p}{d_b}\right)^{1.03} \quad \textbf{4-2}$$

Where:

Q_{air}^{nappe} Nappe aeration (m^3/s)

Q_w Water discharge (m^3/s)

h Step height (m)

d_p Flow depth in the pool beneath the nappe (m)

d_b Flow depth at the brink of a step (m)

Fr $\frac{q_w}{\sqrt{gd^3}}$

q_w = unit flow ($m^3/s/m$)

d = Flow depth (m)

Based on experimental studies on aeration of labyrinth weirs by Crookston & Tullis (2011) artificially aerating the overflow nappe has increased nappe stability and reduced noise. Furthermore, the provision of air vents below the downstream crest, has not had any significant effect on the discharge capacity, however, aeration vents close to the downstream crest result in a less effective discharge capacity (Crookston & Tullis, 2011).

4.3.2 Aeration design for Piano Key Weirs

Initially the aeration systems for the first PKWs were based on the “flap gate rule”, which allows for air flow equal to between 5% to 10% of the water flow and then sizing the pipes to not exceed an air speed of 50 m/s to 100 m/s (Vermeulen, *et al.*, 2017).

However, by following this method the diameter of the aeration pipes for the PKW of Record Dam would have had to be larger than 1200 mm. Not only would these size pipes have caused

construction difficulties, these sizes might also be too conservative. Furthermore, it should be noted that this methodology was developed to reduce the resonance phenomenon that occurs for flap gates, which is not likely to occur for a concrete PKW structure (Vermeulen, *et al.*, 2017).

Therefore Vermeulen *et al.* (2017) developed a new aeration demand estimation method (Equation 4-3) based on the aeration of labyrinth weirs. This resulted in the reduction of the aeration network pipe diameters of the Record Dam to 500 mm. This new method is based on the work of Ervine & Elsawi (1975) which uses an empirical formula to predict the volume of air carried in a rectangular falling water jet. The empirical formula is as follows (Vermeulen, *et al.*, 2017):

$$Q_{air} = 0.26\, q_s \frac{L^2}{p_n}\left(\frac{d}{h_n}\right)^{0.446}\left(1 - \frac{V_m}{V_i}\right) \qquad 4\text{-}3$$

Where:

Q_{air}	Carried air flow (m^3/s)
q_s	Linear water flow overflowing inlet keys and sidewalls (m^3/s)
L	Nappe width (m)
h_n	Nappe thickness (m)
p_n	Nappe perimeter, assumed $p_n = 2\,(h_n+L)$ (m)
d	Falling jet height (m)
V_i	Jet speed at impact (m/s)
V_m	Minimum velocity required to entrain air (assumed as 1.1 m/s)

The parameters for Equation 4-3 can be estimated from numerical or physical modelling. The following should be considered when using Equation 4-3 for the air demand in PKWs (Vermeulen, *et al.*, 2017a):

- Only the air contained in the bottom half of the nappe is applicable, i.e. the actual air entrainment is Q_{air} divided by 2.
- Only the flow discharged over the inlet key and sidewalls should be taken into account as no air cavity is formed under the nappe of the outlet key.
- Air flow is dependent on the fall height of the nappe – which is different along the lateral and downstream crest. Hence, it is recommended that the air requirement is calculated for segments of the nappe with different fall heights.

This new method by Vermeulen *et al.* (2017) also recommends taking into account the pressure losses in the aeration network when sizing the pipes, and not a single air speed criterion. The allowable negative pressure under the nappe to avoid potential resonance is difficult to estimate, however, Levin (1968) attempted to provide acceptable limits for the pressure losses (ΔP):

- Δ P < 1.5 m of water (1200 m of air) for a bottom gate;
- Δ P < 0.3 m of water (240 m of air) for a flap gate (acceptable for a PKW); and
- Δ P < 0.01 m of water (8 m of air) for a measuring weir.

The allowable negative pressure below the nappe needs to be further investigated as it directly relates to the pressure drop in the aeration network.

Figure 4.2 to **Figure 4.4** show the comparison of the estimated air demand, air flow velocity and air head losses, using Equation 4-3, compared to the actual measurements for the Malarce Dam PKW. The PKW comprises twelve 250 mm diameter pipes that connect either directly to the gallery or to a primary 400 mm diameter pipe. Considering these diameters, it can be concluded that the method proposed by Vermeulen *et al.* (2017) is less conservative than the 5 to 10% of flow recommended by previous methods, while still allowing a safety margin. The criteria of maximum head losses equal to 1200 m of air are also adhered to.

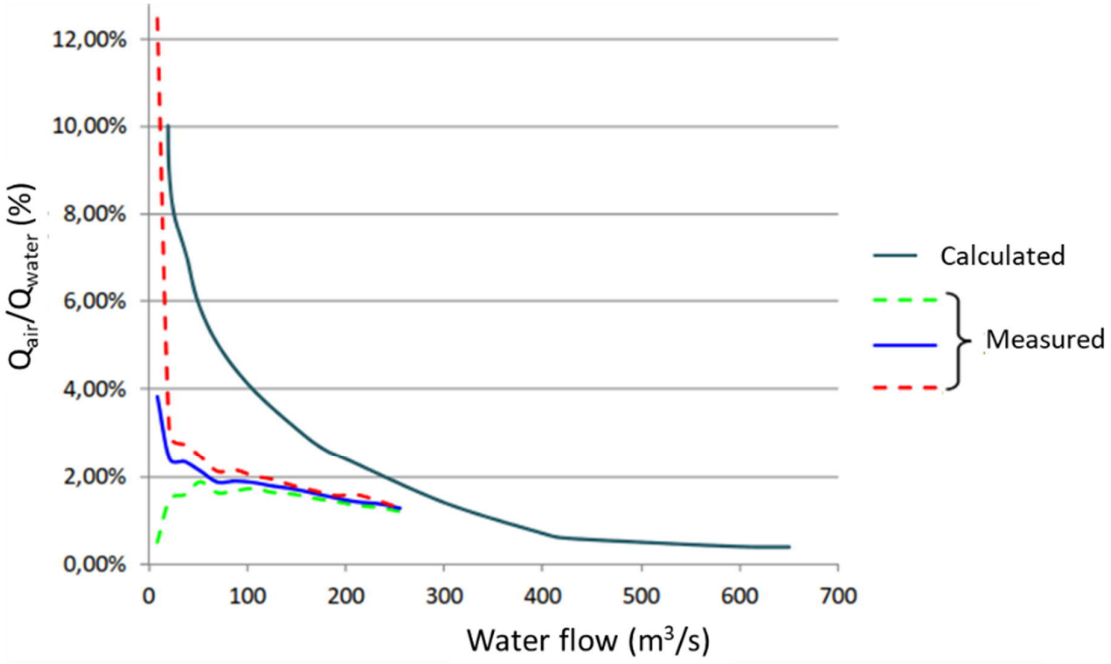

Figure 4.2: Ratio of air flow to water flow at Malarce PKW (Vermeulen, *et al.*, 2017a)

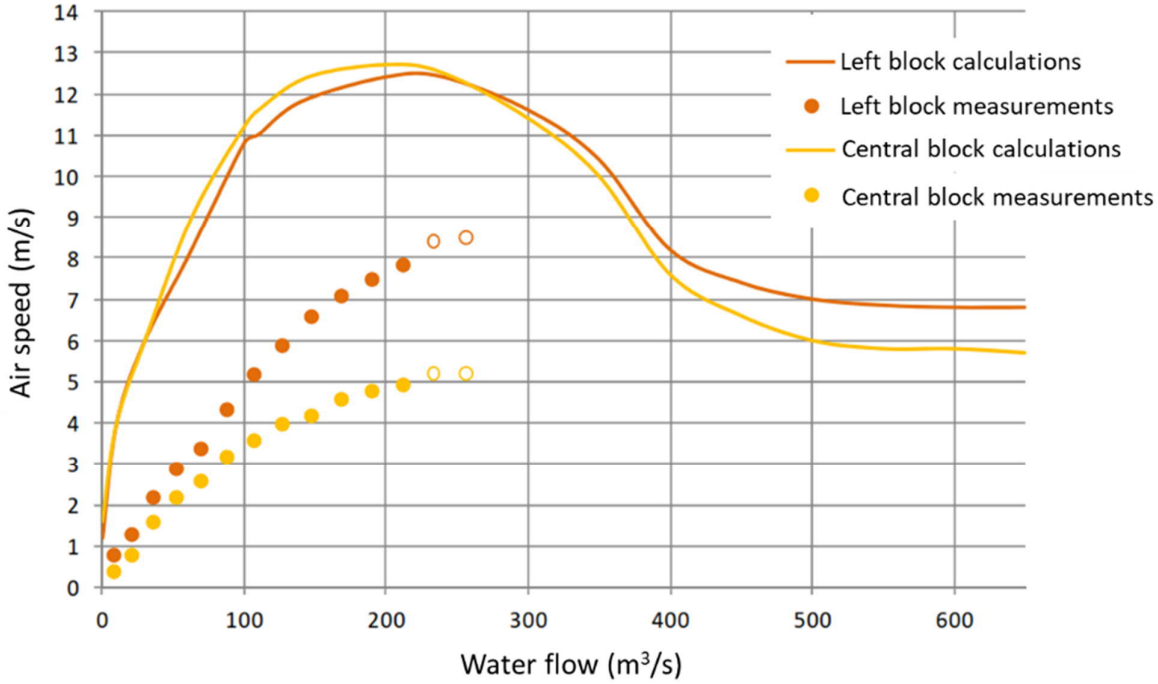

Figure 4.3: Air speed in primary aeration pipes of Malarce PKW (Vermeulen *et al.*, 2017a)

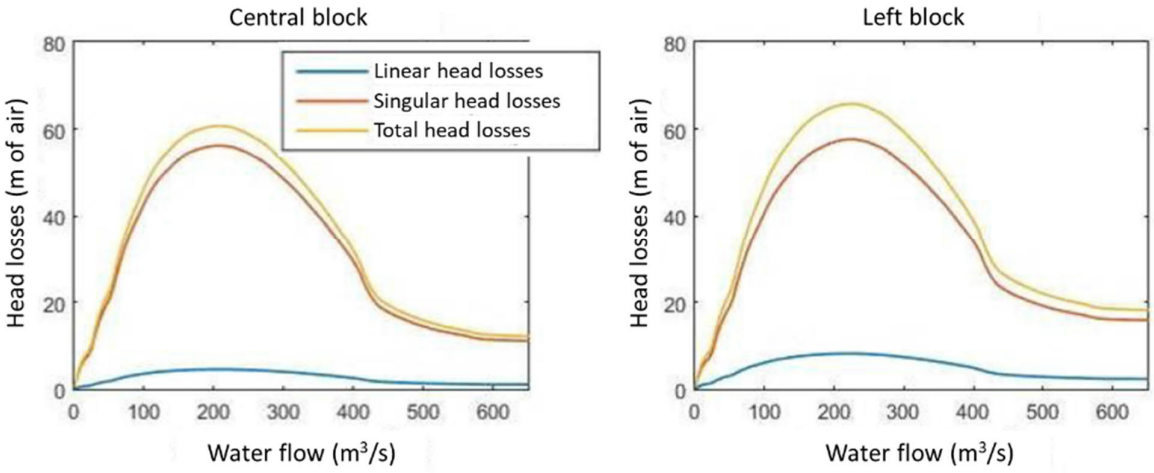

Figure 4.4: Aeration network head losses of Malarce PKW (Vermeulen, *et al.*, 2017a)

5. EXPERIMENTAL SETUP

5.1 INTRODUCTION

This chapter describes the experimental investigation followed, by means of scaled physical hydraulic model studies, to fulfil the objectives of this study.

Hydraulic models are widely used to investigate the design and performance of hydraulic structures, as well as complex flow situations and sediment transport, which cannot necessarily be determined analytically or with computer simulations. A hydraulic model is a scaled representation of the full-scale prototype and is used to evaluate the design performance of complex prototype situations or to simulate specific generic physical processes (ASCE, 2000). Hence, boundary conditions and scales are specified to minimise laboratory and scale effects as discussed later.

All physical hydraulic model experiments were conducted in the Hydraulics Laboratory of the Stellenbosch University. Two physical hydraulic models were constructed to test various parameters - a single half unit large scale steel model and a multi-unit smaller scale wooden model.

The steel model was mainly used to evaluate the possible effect of artificial aeration on FIV (specifically nappe oscillations), if any. The wooden model was used to evaluate the effect of artificial aeration on the discharge capacity, pressure within the air cavities behind the overflow nappe, as well as the overall behaviour of the PKW under different aeration conditions. In both models, three aeration conditions were evaluated – no artificial aeration, and the introduction of artificial aeration via either small diameter or large diameter aeration pipes connected to atmosphere and with an opening under the downstream overhang of the inlet key.

Data collected included flow discharge, flow surface profile, air and water pressure behind the overflow nappe along the sidewalls and downstream overhang of the inlet key, as well as air flow through the aeration pipes, and vibration of the sidewalls.

The following sub-sections describe the general layout of the experimental setup, the various hydraulic models, scaling of the models and scale effects, measuring instrumentation and techniques, experimental procedures and scenarios and data analysis.

5.2 GENERAL LAYOUT OF EXPERIMENTAL SETUP

As mentioned, all hydraulic model tests were conducted at the Hydraulics Laboratory of the Department of Civil Engineering at the Stellenbosch University in South Africa. The laboratory can provide flows of up to 700 l/s through a set of five pumps in a closed system. Both hydraulic models (one at a time) were constructed at the downstream end of a 25 m long by 1.5 m wide

and 1.5 m high flume. The models represented an in-channel application, rather than an application into an existing dam.

The flume was supplied with constant flow through a 600 mm diameter steel pipe that discharged into an upstream stilling basin. The flow was controlled by manually opening and closing a control valve along the pipeline and was measured with an electromagnetic flow meter. Water from the flume was discharged downstream into a sump below the laboratory floor to be returned to the pumps and discharged into the flume via the supply pipe.

The flow into the flume was stabilized by two flow baffle walls located downstream of the supply stilling basin and by the remainder of the flume length before reaching the models. This ensured that the flow lines were undisturbed by the time that they reached the models. The flume was constructed from brick walls, plastered and painted with waterproof bitumen paint, and provided with a concrete floor.

A permanent pitot tube and point gauge was installed midway along the flume for recording upstream headwater levels. A second point gauge was installed on a rail mounted trolley above the PKW models to enable surface flow profile measurements. The remainder of the instrumentation is discussed under **Section 5.4**.

A schematic of the laboratory layouts of the PWK hydraulic model setup is illustrated in **Figure 5.1** and **Figure 5.2**.

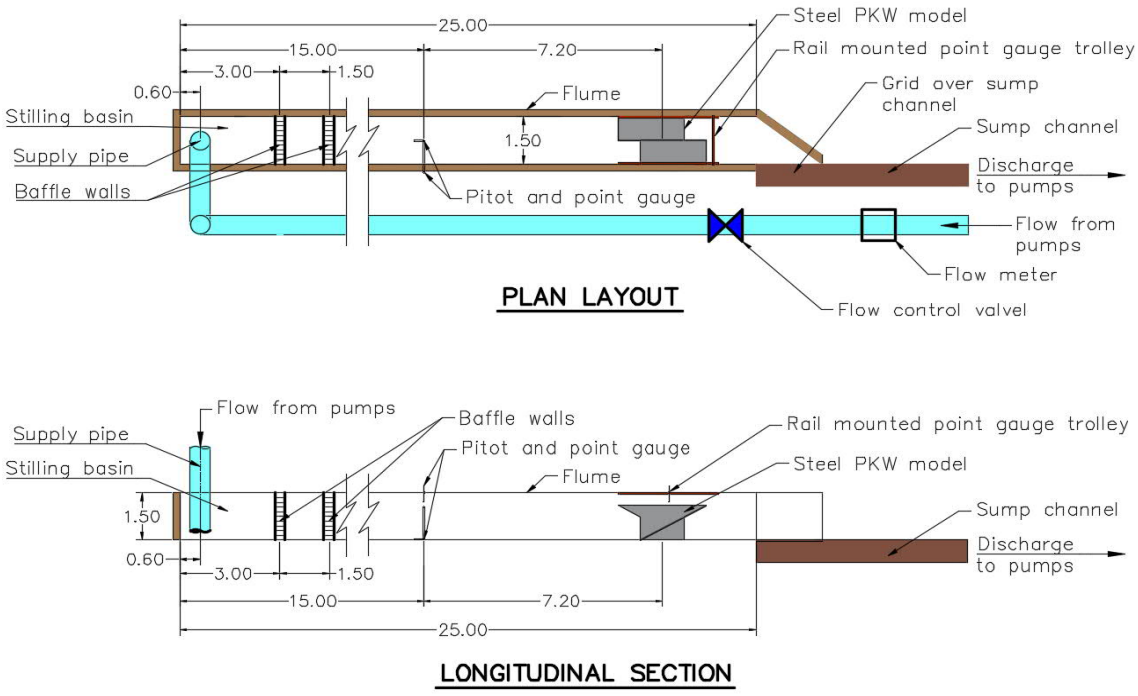

Figure 5.1: Schematic layout of the laboratory setup – Steel model (Model 1)

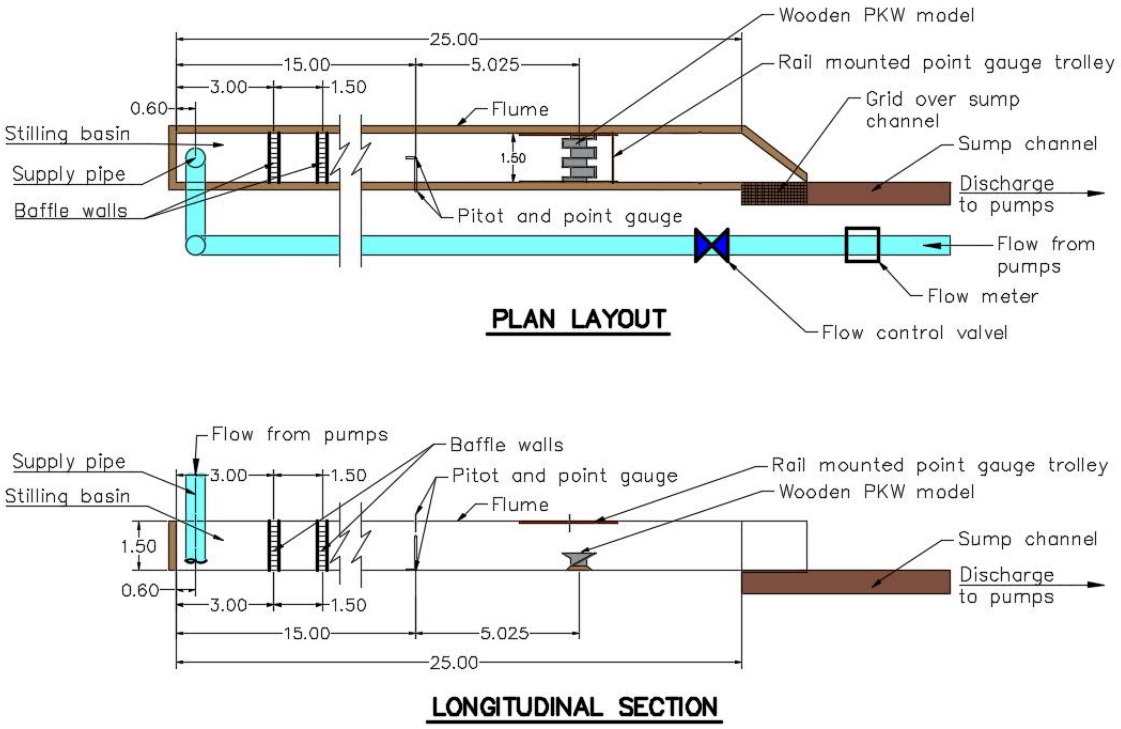

Figure 5.2: Schematic layout of the laboratory setup – Wooden model (Model 2)

5.3 PHYSICAL HYDRAULIC MODELS

In general, PKWs are constructed from reinforced concrete, which provides sufficient stiffness against any structural vibrations induced by flow. However, several projects (e.g. PKW of Oule Dam, France) have considered steel as a possible alternative construction material for PKWs (Erpicum, *et al.*, 2017). The advantage of a steel PKW is the thinner crest width, which has been shown to significantly increase the discharge efficiency (Machiels, *et al.*, 2009) (Laugier, *et al.*, 2013). These thinner steel PKWs may be more susceptible to resonant FIV. FIV, as a result of nappe oscillations, is not only a concern for the structural durability of an overflow structure but can also produce significant noise that can affect communities living or working close by (Crookston, *et al.*, 2014).

As mentioned earlier and with consideration of the above, two physical hydraulic models were designed, constructed and installed separately into the allocated flume – a single half unit large scale steel model and a multi-unit smaller scale wooden model. It should be noted that these models were designed as part of a parallel study on PKWs by Denys (2019). Both models represent a typical Type A PKW with geometric characteristics and ratios within the ranges recommended in several parametric studies. The main parameters of the prototypes on which the models were based are provided in **Table 5.1**. Both models represented overall similar prototypes, however, some parameter were different.

In both models, three different aeration conditions were simulated:

- No artificial aeration, which serves as the control model to which hydraulic conditions of artificially aerated systems were compared to;
- Introduction of artificial aeration by means of small diameter aeration pipes underneath the downstream overhang of the inlet keys, connected to the atmosphere; and
- Introduction of artificial aeration by means of large diameter aeration pipes underneath the downstream overhang of the inlet keys, connected to the atmosphere.

The models were scaled based on the space, discharge capacity and materials available at the Stellenbosch University Hydraulics Laboratory, as well as to limit any potential scale effects. Consideration was also given to the practicality of installing these models in the allocated flume. Both models were scaled according to the Froude similitude. The scaling of the models and considered scale effects are discussed in **Section 5.3.3**.

The main differences between the two models are the scale, construction material and number of PKW units. Details of the models are given in the subsequent sub-sections. The main model dimensions and parameters, as scaled and constructed, are summarised in **Table 5.1**.

Table 5.1: Prototype and model dimensions and parameters

Parameter	Definition	Model 1 (Steel)			Model 2 (Timber)		
		Prototype	Model (as scaled)	Model (as constructed)	Prototype	Model (as scaled)	Model (as constructed)
Q	Discharge (m^3/s)	4.926	0.40	0.40	77.0	0.50	0.50
H_T	Design headwater level (m)	0.464	0.17	0.17	1.313	0.175	0.175
P_i, P_o	Height of the inlet entrance/outlet exit measured from PKW crest (m)	3	1.10	1.10	3	0.40	0.40
B_b	Base length of PKW footing (m)	3.6	1.32	1.32	3.6	0.48	0.48
B_i, B_o	Overhang length of the inlet/outlet key (m)	1.8	0.66	0.66	2.025	0.27	0.27
B	Upstream-downstream length of PKW, $B = B_b + B_i + B_o$ (m)	7.2	2.64	2.64	7.65	1.02	1.02
N_u	Number of PKW units(1)	1	1	0.5(1)	2.5	2.5	2.5
T_s	Sidewall thickness (m)	0.025	0.009	0.006(2)	0.225	0.03	0.03
W_i	Width of the inlet key (wall to wall) (m)	2	0.72	0.72	2.25	0.30	0.30
W_o	Width of the outlet key (wall to wall) (m)	2	0.72	0.72	1.8	0.24	0.24
W_i/W_o	Inlet to outlet key width ratio	1	1	1	1.25	1.25	1.25
D_{air}	Diameter of aeration pipes (mm)	150 and 400	55 and 147	32 and 105(3)	150 and 400	20 and 53	19 and 52

Note: (1) Flow only tested over half an inlet and half an outlet key

(2) For the required similarity a plate thickness of 0.0066 m was required, but not available

(3) Only half the aeration pipe area was provided given that flow over only half an inlet and half an outlet key was simulated.

5.3.1 Model 1 (large scale steel model)

The main purpose of the steel PKW model was to evaluate the vibrations of the structure itself, if FIV (specifically nappe oscillations) occur, and whether these oscillations, if any, can be alleviated by artificially aerating the nappe, i.e. the relationship between the vibrations of the thin sidewalls and aeration condition of the overflow nappe.

To limit scale effects and to sufficiently mimic the hydro-elastic behaviour of a thin walled PKW, this model was designed to have the largest scale possible that will fit into the allocated flume (Denys, 2019). A scale of 2.73 allowed for a weir height, P, of 1.1 m, one full inlet key and one full outlet key to be installed. The main dimensions of the model are shown in **Figure 5.3.** The detailed design drawings, as prepared by Denys (2019), are included in **Appendix C**.

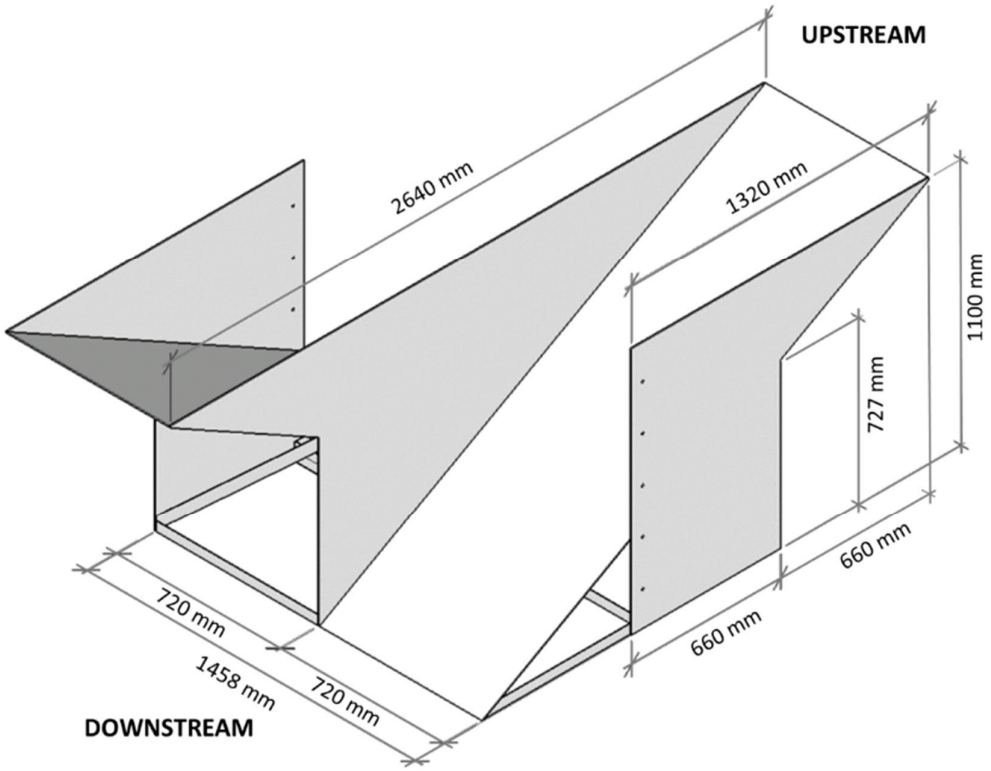

Figure 5.3: Steel model dimensions (adapted from (Denys, 2019))

The model was constructed from 6 mm thick structural steel. The material and material thickness were selected by Denys (2019) to adequately represent the stiffness, inertia, density and damping properties of a similar steel prototype to evaluate the hydro-elastic behaviour. It should be noted that this study only aimed to identify if there is a relationship between structural vibrations, nappe oscillations and aeration and did not focus on the structural or hydro-elastic behaviour of PKWs as such.

By constructing a complete outlet and inlet key, and not only half an inlet key and half an outlet key, the structure was less braced by the flume walls and thus the centre sidewall had a greater degree of freedom in terms of bending and vibration and thus better simulated the prototype behaviour (Denys, 2019). However, considering that the flow of a PKW is symmetrical along the longitudinal axis of the inlet and outlet keys, the flow was limited to the central portion of the PKW, i.e. only over half the inlet key and half the outlet key. Flow guides were installed along the flume and parapet walls were installed on the non-overflow crest portions to guide the flow over only the central area of the model – refer to **Figure 5.4**.

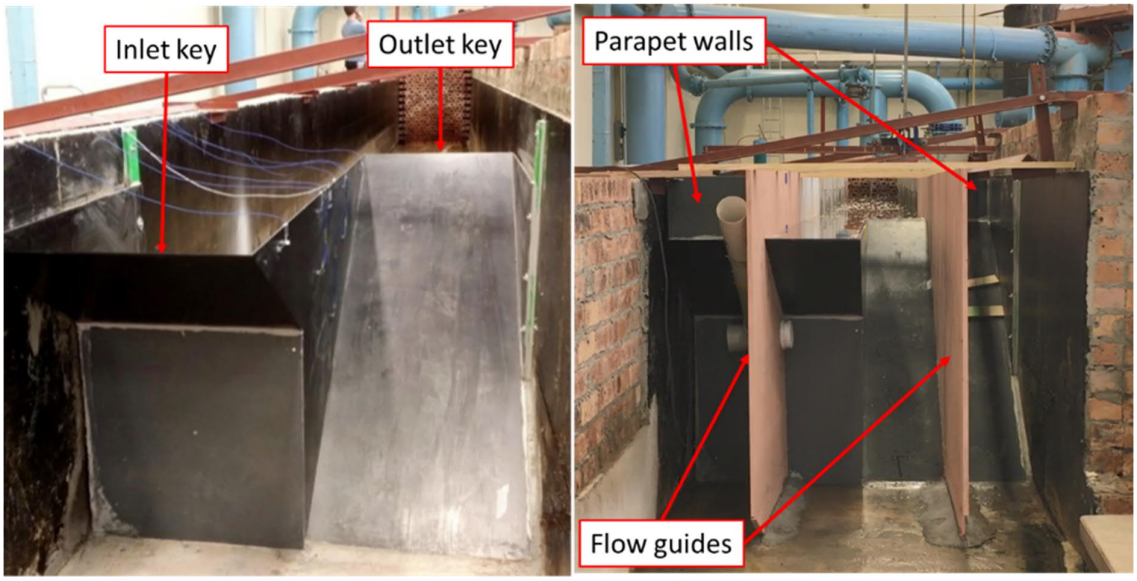

(a) (b)

Figure 5.4: Steel model (a) before installation of flow guides (Denys, 2019) and (b) after installation of flow guides

An aeration pipe was installed below the downstream overhang of the inlet key through the flow guide wall as shown in **Figure 5.5**. The smaller plastic aeration pipe (32 mm inner diameter) was installed into the larger PVC aeration pipe (105 mm inner diameter) and could simply be removed after doing the relevant tests. The aeration pipe opening behind the nappe could be closed to simulate unaerated conditions. Considering that flow was only over a half of the inlet key, pipes with half the opening area were installed. The end cap on the downstream side could be removed to enable the drainage of the aeration pipe should it have become full of water.

A pressure sensor was installed below the aeration pipe and a strain gauge was installed in the middle of the sidewall, near the crest, as shown in **Figure 5.5**. Details of the instrumentation are discussed in **Section 5.4**.

Additional detail and photographs of the model are included in **Appendix C**.

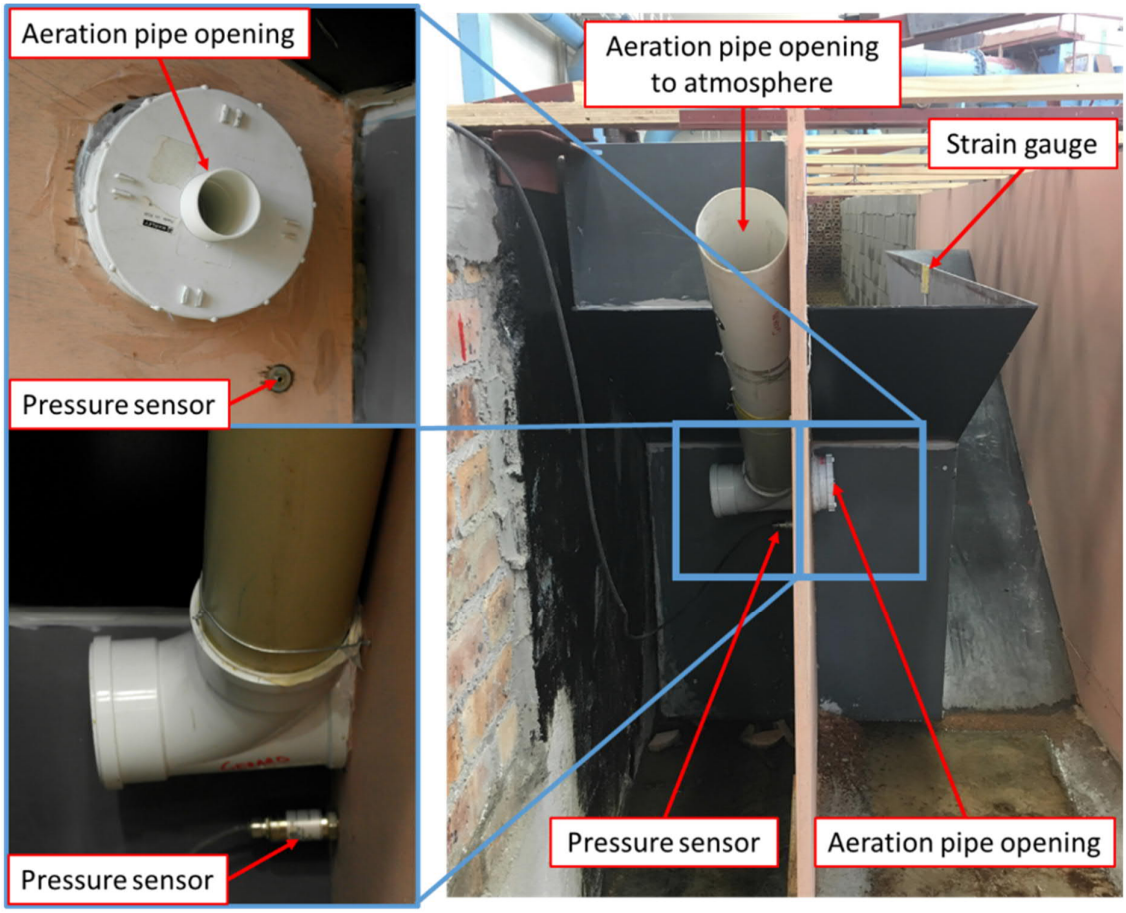

Figure 5.5: Instrumentation and aeration pipe positions on steel model

The data collected from this model included flow surface profile data, time variant vibrations on the sidewalls, time variant air pressures of the air cavity behind the overflow nappe, and air speed in the aeration pipes (where applicable).

5.3.2 Model 2 (smaller scale wooden model)

The smaller scale wooden model was used to evaluate the effect of artificial aeration on the discharge capacity, the pressure in the air cavities behind the overflow nappe downstream of the inlet key overhang, as well as behind the sidewalls, and the overall behaviour of a multi-unit PKW.

A model scale of 7.5 was selected. This allowed for 2.5 PKW units to be installed in the flume and a weir height, P, of 0.4 m. According to Denys (2019), the selected scale was large enough to enable a sufficient band of frequencies to develop, as scaled models are generally not capable of generating high frequency oscillations (Phillips & Lesleighter, 2013), while considering construction practicality and the measurement range of instrumentation, specifically the measurement depth of the acoustic Doppler velocimeter (ADV). The main

dimensions of the model are shown in **Figure 5.6.** The detailed design drawings, as prepared by Denys (2019), are included in **Appendix C**.

The model was constructed from 30 mm thick pine wood which was coated with water proofing, alkali and acid resistant paint. The model was considered to be sufficiently rigid to avoid any structural vibrations affecting the hydrodynamics (Denys, 2019).

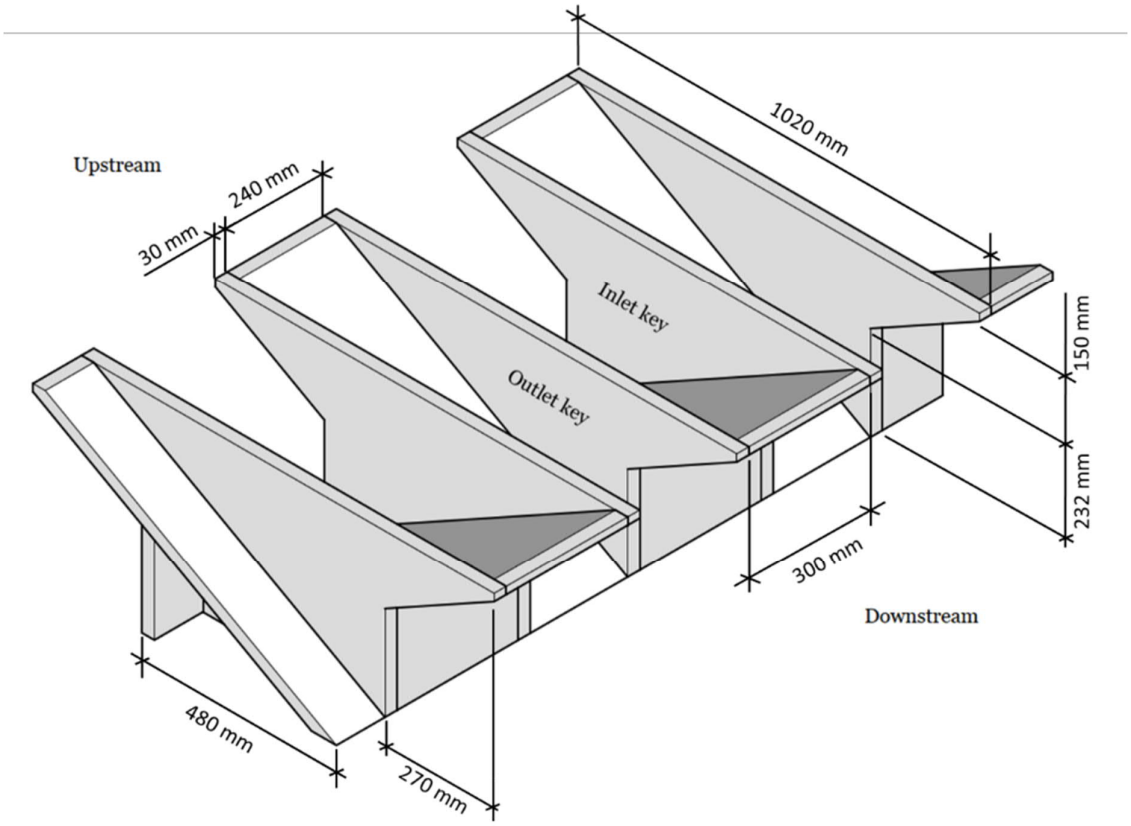

Figure 5.6: Wooden model dimensions (adapted from (Denys, 2019))

Aeration pipes were installed, with openings below the downstream overhang of each complete inlet key, except for the half inlet key – refer to **Figure 5.7**. The aeration pipes were connected to a collector pipe running along the bottom of the PKW. The PKW wooden model was lifted 150 mm from the flume floor to allow for the aeration pipes to pass through underneath, as well as to prevent the aeration pipes from becoming submerged for the tested flow ranges.

Similar to the steel model, the smaller aeration pipes (19 mm inner diameter) were installed into the larger PVC aeration pipe (52 mm inner diameter) and could simply be removed after doing the relevant tests. The collector pipe extended through the flume wall and could either be extended further with a 25 mm diameter plastic pipe or a 52 mm diameter PVC pipe to enable air velocity readings as is shown in **Figure 5.8**. For unaerated conditions the openings

below the inlet key overhangs were closed. All other openings and joints were sealed with silicone to prevent unwanted air entrainment. The 90° bend on the collector pipe outside of the flume could be removed to enable the drainage of the aeration pipe should it become full of water.

Figure 5.7: Wooden model view from downstream

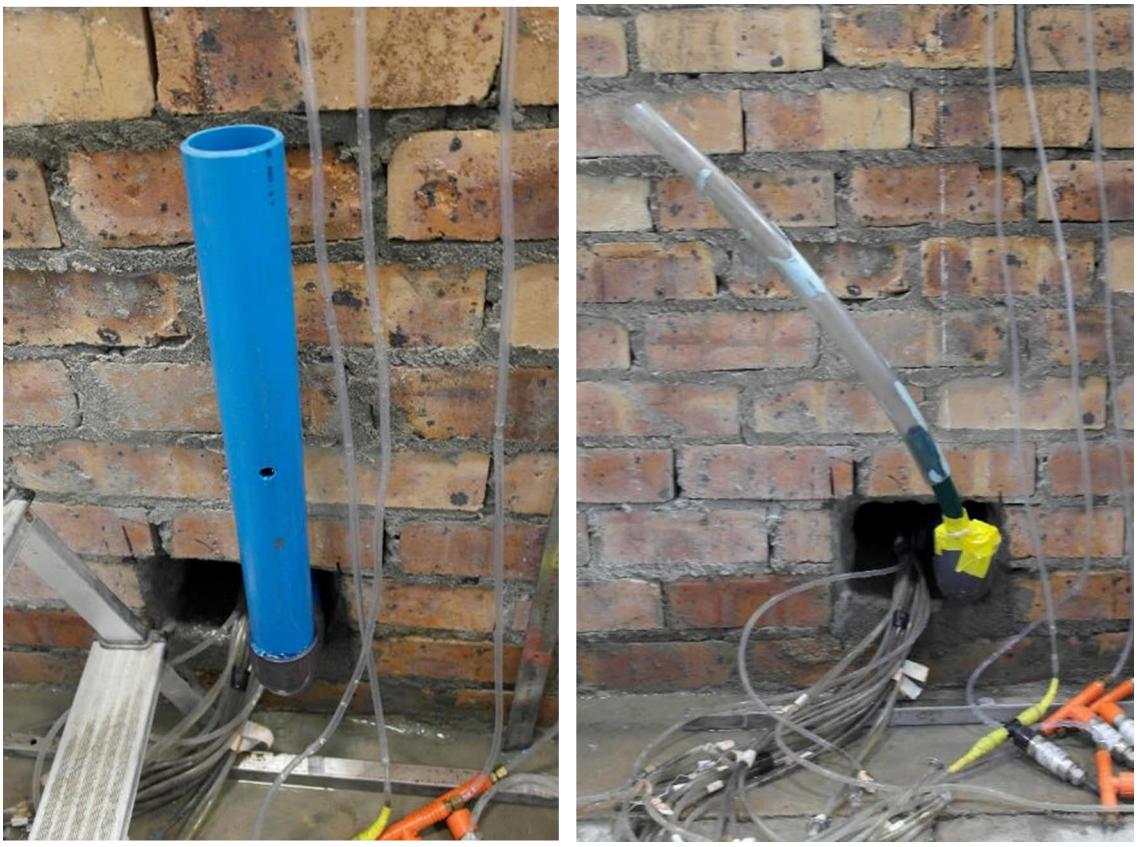

(a) (b)

Figure 5.8: Aeration collector pipe outside of the flume, (a) 52 mm diameter extender and (b) 25 mm diameter extender

A pressure sensor was installed 10 mm above the crown of each of the aeration pipes. Three pressure sensors were installed on the downstream side of one of the sidewalls. Details of the instrumentation are discussed in **Section 5.4**.

The data collected from this model included flow surface profile data, time variant air and water pressures behind the overflow nappe, and air speed in the aeration pipes (where applicable).

Additional details and photographs of the model are included in **Appendix C**.

5.3.3 Model scale and scale effects

A hydraulic model is a scaled representation of the full-scale prototype. It is critical that, as far as possible, the model be correctly scaled to realistically and precisely represent the prototype characteristics being investigated.

The relationship between the hydraulic performance of the scaled hydraulic model and the prototype is governed by laws of hydraulic similitude, which include the geometric, kinematic and dynamic similarity. Hydraulic similitude is based on the interdependency of the variables obtained in a set of dimensionless parameters through dimensional analysis. The contributing variables include the dimensions of the model and prototype, flow velocity, pressure, shear stress, specific weight, mass density, dynamic viscosity etc. The dimensionless parameters are based on the main forces that are present, and include the Froude number, Reynolds number, Weber number and Euler number (University of Pretoria, 2004). Other force ratios that must be included in the dimensional analysis when evaluating compressibility and hydro-elastic vibrations, as the case for this study, include the Cauchy number or Mach number (Cauchy for a structure and Mach for a fluid) and Strouhal number (ASCE, 2000) (Novak, *et al.*, 2010). A summary of the hydraulic similitude laws or main force ratios applicable to this study, as well as the formulations, is provided in **Table 5.2** (Webber, 1979) (ASCE, 2000) (Heller, 2011).

Additional information on the geometric, kinematic and dynamic similarity, as well as on the laws of hydraulic similitude is included in **Appendix B**.

Table 5.2: Summary of hydraulic similitude laws (Heller, 2011)

Similitude law	Importance	Force ratio	Formulation
Froude	Gravity - free surface flows	$Fr = \sqrt{\frac{Inertial\ force}{Gravitational\ force}}$	$Fr = \frac{V}{\sqrt{gL}}$
Reynolds	Fluid viscosity	$Re = \sqrt{\frac{Inertial\ force}{Viscous\ shear\ force}}$	$Re = \frac{LV}{v}$
Weber	Surface tension – shallow free surface flows	$We = \sqrt{\frac{Inertial\ force}{Surface\ tension\ force}}$	$We = \frac{\rho V^2 L}{\sigma}$
Euler	Pressure – free surface flows	$Eu = \frac{Pressure\ force}{Inertial\ force}$	$Eu = \frac{p}{\rho V^2}$
Cauchy (structure) or Mach (fluid)	Elasticity	$Ch = \frac{Inertial\ force}{Elastic\ force}$	$Ch = \frac{\rho V^2}{E}$ $Ma = \frac{V}{c_s} = Ch^{1/2}$
Strouhal	Oscillations	$St = \frac{Inertial\ force\ due\ to\ flow\ unsteadiness}{Inertial\ force\ due\ to\ velocity\ gradient}$	$St = \frac{fL}{V}$

Where:

V	*Velocity (m/s)*
g	*Gravitational acceleration (9.81 m/s^2)*
L	*Length of homologous sections in model and prototype, e.g. headwater depth (m)*
v	*Kinematic viscosity (≈ 1.13 x 10^{-6} m^2/s for water)*
ρ	*Fluid density (kg/m^3)*
σ	*Fluid surface tension (≈ 0.073 N/m for water)*
p	*Pressure (Pa)*
E	*Young's modulus (GPa)*
c_s	*Speed of sound in air (343 m/s)*
f	*Frequency (Hz)*

If the same fluid is used in the model as in the prototype, simultaneous compliance with all the laws of hydraulic similitude, and hence the accurate simulation of all flow processes of the prototype in the model, is impossible and therefore some discrepancies in scaling the results from the model to the prototype are unavoidable. These discrepancies are referred to as scale effects and should be addressed (Chanson, 2009) (Heller, 2011). The severity of scale effects increases as the ratio of the prototype to model size increases and as the number of the physical processes simulated increases (Chanson, 2009).

A specific scale does not determine whether a scale effect can be neglected, but rather the objective of the investigation. In general, models are scaled based on the most relevant and dominant force additional to inertial force, and the effects of the other unsatisfied force ratios

are minimised. Scale effects can be minimised if the discrepancy between the model and prototype can be limited (Heller, 2011). In turbulent open channel flow models gravitational and inertial forces are the dominant forces, meaning that Froude's Law is mostly used (Webber, 1979) (Chanson, 2009). Scaling ratios to adhere to Reynolds similitude are sometimes inconvenient and impractical. No model has been constructed according to Weber similitude to date (Heller, 2011).

As previously mentioned, the hydraulic models used in this study were designed by Denys (2019) to investigate the hydrodynamics, transient flow behaviour and hydro-elastic (structural) behaviour of PKWs. Hence, the scaling of the models was not only focused on the hydraulic similarities, but also on the material similarities, specifically the elastic behaviour (Denys, 2019). This study, however, only focuses on the hydraulic similarities, but a brief overview of the materials scaling is provided.

Both the physical hydraulic models for this study were scaled to meet Froude similitude. Thus, implying that the Reynolds, Weber, and Cauchy similarities are not met between the model and prototype – all of which are important to the investigations of this study.

a) Weber number

Surface tension effects start playing a role in physical hydraulic models when the Weber number is smaller than 100 – when the radius of surface curvature is small relative to the fluid depth (ASCE, 2000). Surface tension is thus a dominant force for air entrainment models and models with very shallow flows. Under Froude similitude, the Weber number is overestimated. Since the physics of bubble generation and size does not change if the same fluid is used in the model as in the prototype, relative air bubble sizes are larger and air detrainment is faster in the scaled model – making modelling of gas-fluid flows very difficult (Heller, 2011). Surface tension scale effects can be overcome if the flow velocity is higher than 6 m/s, which is unlikely in most hydraulic models. However, scale effects can be limited for turbulent flow conditions ($Re > 1 \times 10^5$) (Novak, *et al.*, 2010).

For this study, overestimating the Weber number may have affected the overflow nappe behaviour and air demand of the air cavity behind the nappe. Erpicum *et al.* (2016) investigated the scale effects of surface tension and viscosity on the discharge capacity and nappe behaviour for several scales based on Froude similitude. The more turbulent the flow, the more air is entrained into the nappe and the more aerated the nappe becomes. As air entrainment and bubble size are not affected by scale, the larger the scale, the less turbulent and more stable the air-water interface becomes, resulting in less nappe aeration. The volume of the air cavity behind the overflow nappe is also affected by the scale ratio. For smaller scale

ratios, less air is provided to the air cavity, resulting in reduced air pressures in the cavity and causing the nappe to be sucked in. The effect of scale on the nappe aeration condition and trajectory is illustrated in **Figure 5.9**.

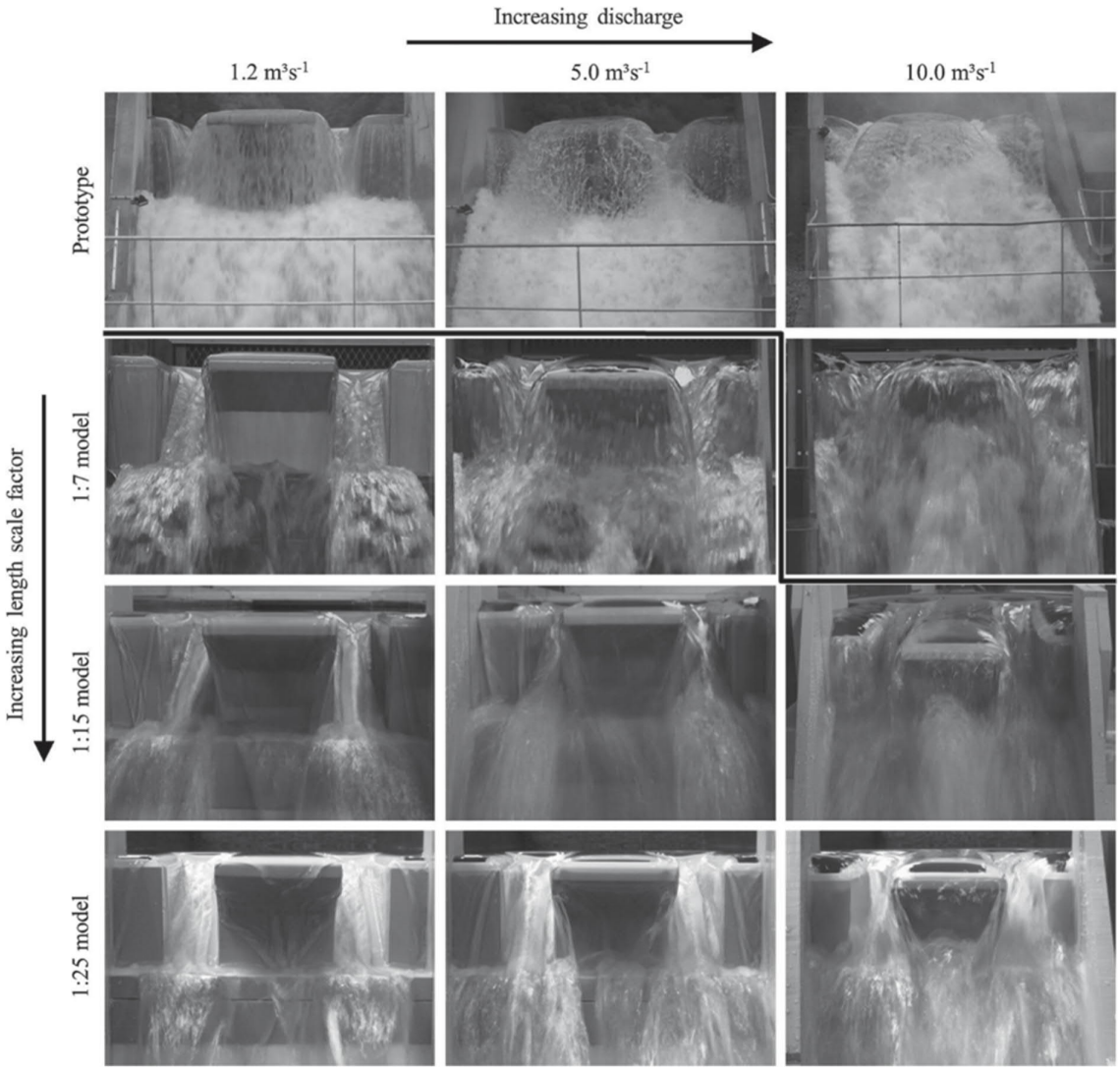

Figure 5.9: Effect of scale on the nappe aeration of PKWs (Erpicum, et al., 2016)

b) Reynolds numbers

Flow turbulence or vorticity is dominated by viscous forces and governed by the Reynolds number. Under Froude similitude, the Reynolds numbers are significantly smaller than for the corresponding prototype flows (Chanson, 2009). The flow can shift from the fully turbulent zone to the transition flow zone, or even to the laminar zone, as depicted in the Moody diagram for pipes, if scaled using Froude similitude (ASCE, 2000).

Weber and Reynolds similitude cannot be simultaneously met as their numbers are co-dependent. Since vortex shedding, which is directly influenced by viscosity, was the main focus point for Denys's study (Denys, 2019), limiting the scale effects caused by discrepancies in the Reynolds number was the main target. However, by keeping the Weber and Reynolds numbers above certain thresholds, the magnitude of the discrepancies can be minimised.

Pfister & Chanson (2012) recommend a Weber number $We^{0.5} > 140$ and a Reynolds number between 2 to 3 x 10^5 to limit scale effects in high-velocity air-water two-phase flows when using Froude similitude. Erpicum *et al.* (2016) recommend a minimum total upstream head, H, of 0.03 m to prevent surface tension effects. If temperature is constant, the Weber number is a function of the overflow head (Equation 5-1). A head of 0.03 m thus equates to a Weber number of 54.

$$We = \frac{4\rho g {H_T}^2}{9\sigma} \qquad \textbf{5-1}$$

Where:

We	Weber number
g	Gravitational acceleration (m^{-2}/s)
ρ	Fluid density (kg/m^3)
σ	Fluid surface tension (≈ 0.073 N/m for water)
H_T	Total upstream head (m)

Furthermore, previous studies recommend that the minimum overflow head in the model should be 0.02 m to accurately replicate the discharge coefficient of the prototype and between 0.04 to 0.06 m to replicate the over flow nappe profile (Kobus, 1980) (Novak, *et al.*, 2010).

Table 5.3 provides the Froude, Reynolds and Weber numbers for the range of flows tested in the smaller scale wooden model as estimated by Denys (2019).

Table 5.3: Force ratios for wooden model flow scenarios (Denys, 2019)

Discharge (m^3/s)	Head (m)	H/P (-)	Velocity (m/s)	Froude (-)	Reynolds (-)	Weber (-)
0.050	0.029	0.073	0.078	0.038	3.3×10^4	50.9
0.100	0.044	0.110	0.150	0.072	6.7×10^4	116.1
0.150	0.059	0.148	0.218	0.103	1.0×10^5	209.8
0.200	0.075	0.186	0.281	0.13	1.3×10^5	333.2
0.300	0.106	0.265	0.395	0.177	2.0×10^5	672.9
0.400	0.138	0.345	0.496	0.216	2.7×10^5	1140.0

The Reynolds number relates to the water body upstream of the weir and the Weber number to the water depth at the overflow crest. For the Reynolds Numbers shown in **Table 5.3**, the flow over the smaller scale wooden PKW model remained fully turbulent for all flow ranges – implying that that the modelled vortex shedding behaviour was representative of the vortex formation in the prototype.

The majority of flow ranges tested in both the wooden and the steel models for the purpose of this study exceed the 0.03 m upstream head or 54 Weber number limit. However, the overflow depth at the point where the flow leaves the downstream inlet key crest was below the limit of 0.03 m for flows up to 50 l/s in the case of the wooden model. The scale effects due to the low Weber number were expected to have been counteracted by the turbulent flow in the outlet key which allowed more air entrainment.

Some scale effects in terms of the air entrainment due to surface tension would have been present. Therefore, results attributable to these factors were limited to visual, qualitative comparisons only.

Due to the large scale of Model 1 (steel model) and large overflow depths (> 0.06 m), the model results for this study can be considered to have been free of any potential scale effects.

c) Euler number

Euler similitude is generally maintained when Reynolds or Froude similitude is applied (ASCE, 2000). This implies that the same scale factor applied to a dimension is applicable to pressure. Euler similitude on its own is applied in the replication of high pressures in pipes or cavitation (Heller, 2011).

d) Cauchy and Mach number

The Cauchy number, or Mach number in the case of a fluid, considers the compressibility in terms of Young's modulus and become applicable when vibrations or oscillations are modelled (Novak, *et al.*, 2010). If the same fluid and gas is used in the model and prototype, it may behave too "hard" in small scale models. However, air compressibility is important when the Mach number is $Ma > 0.3$ in compressible flow or when velocity approaches wave celerity, shockwaves and underwater explosions occur (Heller, 2011) (ASCE, 2000). Therefore, for this model study scale effects in terms of water and air compressibility can be neglected. On the other hand, Novak *et al.* (2010) recommends a scale factor smaller than 20.

The Cauchy number is applicable to the stiffness of the structure, denoted by Young's Modulus (Heller, 2011). To ensure hydro-elastic similitude, consideration must be given to the modulus of elasticity, Poisson's ratio and density of the material. Hydro-elastic similarity can be achieved by scaling the modulus of elasticity, using the same scale factor as for the Froude similitude while keeping the same density and Poisson's ratio, or by using the same material, but with a reduced stiffness to simulate the lower modulus of elasticity (Denys, 2019). The latter was followed for the steel model (Model 1) used as part of this study. The prototype wall thickness (25 mm steel plate) was scaled to 9 mm using the Froude scale factor. However, this still resulted in a too stiff a model. The plate thickness was further reduced to 6.6 mm to ensure that the product of the reduced area moment of inertia and the modulus of elasticity were similar to that of the product for the 9 mm plate. The actual model was constructed from 6 mm plate (Denys, 2019).

The effect of damping also plays a role in hydro-elastic models as it can reduce the vibration amplitudes of resonant vibrations. Resonant conditions can be simulated if the damping value is equal or lower than the value for the prototype. This can be achieved by using the same material in the model as in the prototype, (Denys, 2019).

e) Strouhal number

Although not a hydraulic similitude requirement, the Strouhal number is applicable to oscillating flow scenarios or vibrations, e.g. vortex shedding and interface stability. Strouhal uniformity is maintained if Froude similitude is satisfied (ASCE, 2000). The inability of a structure itself to generate higher frequencies can be considered to be a scale effect. (Phillips & Lesleighter, 2013).

Experiments by Lodomez *et al.* (2019) have shown that nappe oscillation intensity and frequency are functions of the fall height and the crest profile and are independent of the model scale. The fall height and associated aeration rate cannot be accurately replicated in models

scaled according to standard laws of similitude, and therefore neither can the nappe oscillations. Nappe oscillations observed in the models constructed for the purpose of this study can only be used for data comparison under the different scenarios. However, the steel model can be considered as a full-scale prototype for assessing the nappe oscillations and the aeration rate.

f) Summary of scale effects

Physical hydraulic models scaled using Froude similitude can replicate the forces associated with gravity, pressure and frequency. However, complete dynamic similarity cannot be achieved if the same fluid is used in both the model and prototype. Scale effects due to the discrepancies in similarity can be limited or neglected, depending on the objective of the study.

In the case of the two PKW hydraulic models designed and constructed for this study, using Froude similitude, scale effects related to viscosity (Reynolds number) and surface tension (Weber number) were limited by adhering to fully turbulent flow conditions ($Re > 10^5$) and minimum overflow depths of 0.03 m ($We > 54$). However, for some low flow conditions, the Weber number was below the recommended limit and some discrepancies were expected. Furthermore, up-scaling of air entrainment was not practical, and data was limited to visual and qualitative comparisons only. The scale effects were further limited by choosing larger than usual scales - 1:2.73 for Model 1 and 1:7.5 for Model 2 compared to a typical model scale of 1:10. Model 1, however, can be considered a prototype on its own due to its large scale.

Table 5.4 and **Table 5.5** provide the dimensions, forces and scaling ratios for Model 1 and Model 2 respectively.

Table 5.4: Model 1 scaling ratios and dimensions (Denys, 2019)

Dimension / Ratio	Symbol	Scaling ratio	Unit	Prototype	Model (as scaled)	Model (as desired)	Model (as constructed)	Up-scaled from as-built	Comment
Scale	λ	$\frac{Prototype}{model}$	-	1	2.727	2.727	2.727	0.37	-
Depth	H_T	λ	m	0.464	0.170	0.170	0.170	0.464	-
Height	P	λ	m	3.00	1.10	1.10	1.10	3.00	-
Length	B_t	λ	m	7.20	2.64	2.64	2.64	7.20	-
Wall thickness	T_s	λ	m	0.025	0.009	0.0066	0.006	0.016	Thinner
Velocity	V	$\sqrt{\lambda}$	m/s	1.418	0.859	0.859	0.859	1.418	-
Discharge	Q	$\lambda^{5/2}$	m^3/s	3.684	0.300	0.300	0.300	3.684	-
Force	F	λ^3	N	20.3	1.0	1.0	1.0	20.3	-
Moment	M	λ^4	Nm	55.3	1.0	1.0	1.0	55.3	-
Plate mass	W	λ^3	kg	1413	69.7	49.9	45.6	924.8	Lighter
Acceleration	g	1	g	9.81	9.81	9.81	9.81	9.81	-
Pressure	p	λ	Pa	27.3	10.0	10.0	10.0	27.3	-
Water density	ρ	1	kg/m^3	1000	1000	1000	1000	1000	-
Material density	ρ	1	kg/m^3	7850	7850	7850	7850	7850	Steel
Young's Modulus	E	λ	GPa	200	73.3	200	200	545.4	-
Moment of inertia	I	λ^4	$10^6 m^4$	2.604	0.047	0.017	0.013	0.073	$I = \frac{1}{12} P_m T^3$
Flexural rigidity	EI	λ^4	Nm	520833	3454	3454	2640	398174	-
Kinematic viscosity	v	1	m^2/s	1×10^{-6}	1×10^{-6}	1×10^{-6}	1×10^{-6}	1×10^{-6}	
Frequency	ω	$1/\sqrt{\lambda}$	Hz	3.03	5.00	5.00	5.00	3.03	-
Surface tension	σ	1	N/m	0.073	0.073	0.073	0.073	0.073	-
Froude number	Fr	gravity	−	0.243	0.243	0.243	0.243	0.243	Similitude
Reynolds number	Re	viscosity	−	4.9×10^6	1.1×10^6	1.1×10^6	1.1×10^6	4.9×10^6	Mismatch
Weber number	We	surface	−	12 871	1731	1731	1731	12 871	Mismatch
Strouhal number	St	frequency	−	1	1	1	1	1	Similitude
Cauchy number	Ca	elasticity	−	79	79	29	29	29	Mismatch
Euler number	Eu	pressure	−	0.014	0.014	0.014	0.014	0.014	Similitude

Table 5.5: Model 2 scaling ratios and dimensions (Denys, 2019)

Dimension / Ratio	Symbol	Scaling ratio	Unit	Prototype	Model (as scaled)	Model (as constructed)	Comment
Scale	λ	$\frac{Prototype}{model}$	-	1	7.5	7.5	-
Depth	H_T	λ	m	1.313	0.175	0.175	-
Height	P	λ	m	3.0	0.4	0.4	-
Length	B_t	λ	m	7.5	1.0	1.0	-
Wall thickness	Ts	λ	m	0.225	0.03	0.03	-
Velocity	V	$\sqrt{\lambda}$	m/s	1.588	0.58	0.58	-
Discharge	Q	$\lambda^{5/2}$	m^3/s	77	0.5	0.5	-
Force	F	λ^3	N	421.9	1.0	1.0	-
Moment	M	λ^4	Nm	3164	1.0	1.0	-
Plate mass	W	λ^3	kg	4050	9.6	2.2	-
Acceleration	g	1	g	9.81	9.81	9.81	-
Pressure	P	λ	Pa	75	10	10	-
Water density	ρ	1	kg/m^3	1000	1000	1000	-
Material density	ρ	1	kg/m^3	2400	2400	550	Concrete and pine timber
Young's Modulus	E	λ	GPa	20	2.7	11	-
Moment of inertia	I	λ^4	$10^6 m^4$	1898	0.6	0.6	$I = \frac{1}{12} P_m T^3$
Flexural rigidity	EI	λ^4	Nm	37968750	1600	1600	-
Kinematic viscosity	v	1	m^2/s	1 × 10−6	1 × 10−6	1 × 10−6	-
Frequency	ω	$1/\sqrt{\lambda}$	Hz	1.826	5.000	5.000	-
Surface tension	σ	1	N/m	0.073	0.073	0.073	-
Froude number	Fr	gravity	−	0.244	0.244	0.244	Similitude
Reynolds number	Re	viscosity	−	6.8×10^6	3.3×10^5	3.3×10^5	Mismatch
Weber number	We	surface	−	103 170	1834	1834	Mismatch
Strouhal number	St	frequency	−	1.51	1.51	1.51	Similitude
Cauchy number	Ca	elasticity	−	302.5	302.5	16.8	Mismatch
Euler number	Eu	pressure	−	0.03	0.03	0.03	Similitude

5.4 INSTRUMENTATION AND DATA COLLECTION TECHNIQUES

The following instrumentation was used to measure variables in the hydraulic model studies:

- Electromagnetic flow meter – Flow rate through the supply pipe;
- Needle gauges and pitot tube – Headwater level, water surface profile, and velocity head (estimated);
- Pressure transducers – Air and water pressure behind the overflow nappes;
- Lutron hot-wire anemometer – Air velocity through the aeration pipes; and
- Half-bridge strain gauge – Structural vibration of the PKW sidewall.

The instrumentation used, instrumentation position, data sampling and sampling time are described in the following subsections.

5.4.1 Flow measurement

All variables tested are related to the discharge over the PKW. The model discharge was defined as the average discharge for each similar test. The flow into the test flume was regulated by closing and opening the flow control valve on the supply pipeline (refer to **Figure 5.1** and **Figure 5.2**).

The water discharges over the PKW, for both the steel and wooden model, were measured with a Flowmetrix SAFMAG electromagnetic flow meter. The flow meter includes a meter sensor, mounted on the pipeline through which the water flows, and a flow meter signal converter and display unit that can be mounted remotely. The flow meter has an accuracy of ± 0.5% for flow velocity rates higher than 0.5 m/s and a ± 0.1% repeatability rate.

The flow is measured using Faraday's Law of electromagnetic induction – the voltage induced across an electrical conductor is directly proportional to the movement of the flowing liquid. A magnetic field is channelled into the liquid flowing through the pipe and causes a voltage signal to be sensed by electrodes located on the meter sensor. The flow velocity is calculated, based on the induced voltage, and converted to the flow rate. The flow total (in m^3) and flow rate (in l/s) are continuously displayed on the LCD display unit. **Figure 5.10** shows the display unit of the flow meter.

The flow meter is installed on the DN600 mm steel pipe that delivers flow to the test flume as shown in **Figure 5.1** and **Figure 5.2**. The flow meter is installed in accordance with the instrument specifications to avoid any inaccurate measurements or disturbances. The signal converter and display unit are mounted on one of the laboratory walls.

Figure 5.10: Flowmetrix SAFMAG electromagnetic flow meter

The flow meter does not have any data logging capabilities – hence the flow was recorded manually. The flow was recorded approximately two minutes after the flow had been adjusted or after the flow reading had stabilised. In most experiments, the flow rate displayed on the LCD unit, remained constant during the testing procedure. However, in cases when the flow rate varied slightly, the different flow rates were manually recorded over a period of 60 seconds. In these cases, the discharge readings varied between ±0.5% for the low flows and ±1% for the higher flows.

5.4.2 Headwater level and velocity head

The total head (water surface level plus velocity head) was required to determine and compare the discharge rating curves of the different test scenarios.

The water surface level upstream of the PKW was manually measured for each test with a needle gauge installed upstream of the PKW model. The needle gauge was mounted on a rail above the flume (**Figure 5.11**).

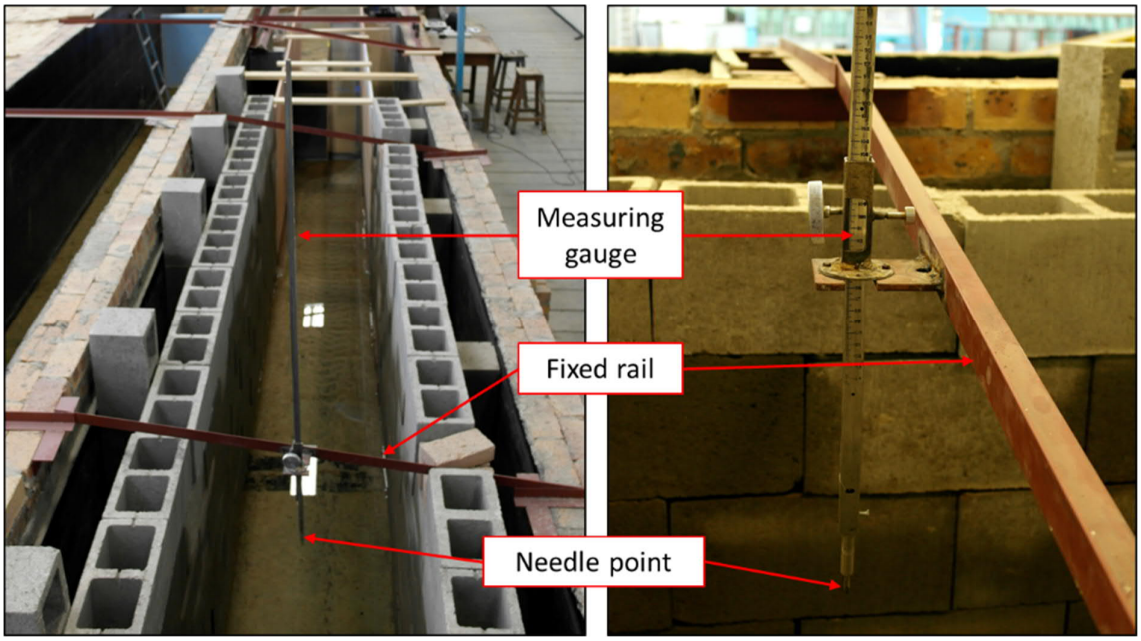

Figure 5.11: Headwater measuring needle

The total head upstream of the PKW was measured using a pitot tube installed the same distance away from the PKW as the needle gauge. The velocity or dynamic head could thus be estimated from the level difference between the needle gauge and pitot readings. However, the velocity or dynamic head was generally small relative to the upstream water surface level and for most cases the upstream water surface level was used with minimal effect on the results.

The pitot tube comprised a 20 mm diameter plastic tube with one open end installed on the floor of the flume facing in the upstream direction, and the other end extending through and along the height of the flume wall. A metal ruler was fixed next to the pitot tube to enable readings to be taken. **Figure 5.12** shows the pitot tube installation.

The accuracies of the needle gauge and the ruler next to the pitot tube were 0.1 mm and 1.0 mm respectively.

5.4.3 Water surface profile measurement over the Piano Key Weir

The water surface profile over the PKW was measured for each test scenario to ascertain whether artificially aerating the nappe had an influence on the nappe profile. The water surface profile was measured at set locations for a number of test scenarios using the needle gauge which was installed on a movable trolley and rail system.

The needle gauge trolley and rail system are shown in **Figure 5.13**. The grid layout of the water surface profile measurements for Model 1 and Model 2 are illustrated in **Figure 5.14** and **Figure 5.15** respectively.

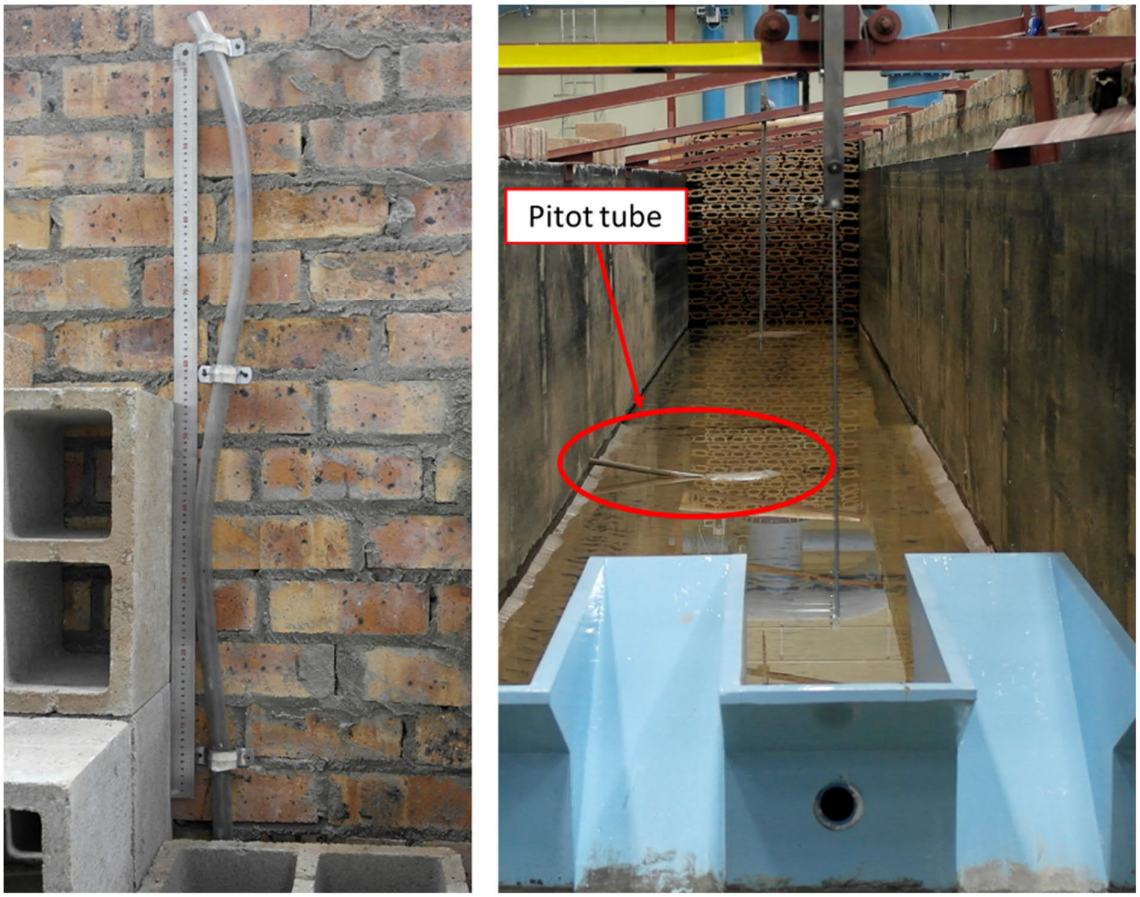

(a) (b)

Figure 5.12: Pitot tube installation: (a) tube on outside of flume with ruler and (b) pitot tube inside the flume

Figure 5.13: Point gauge trolley and rail system

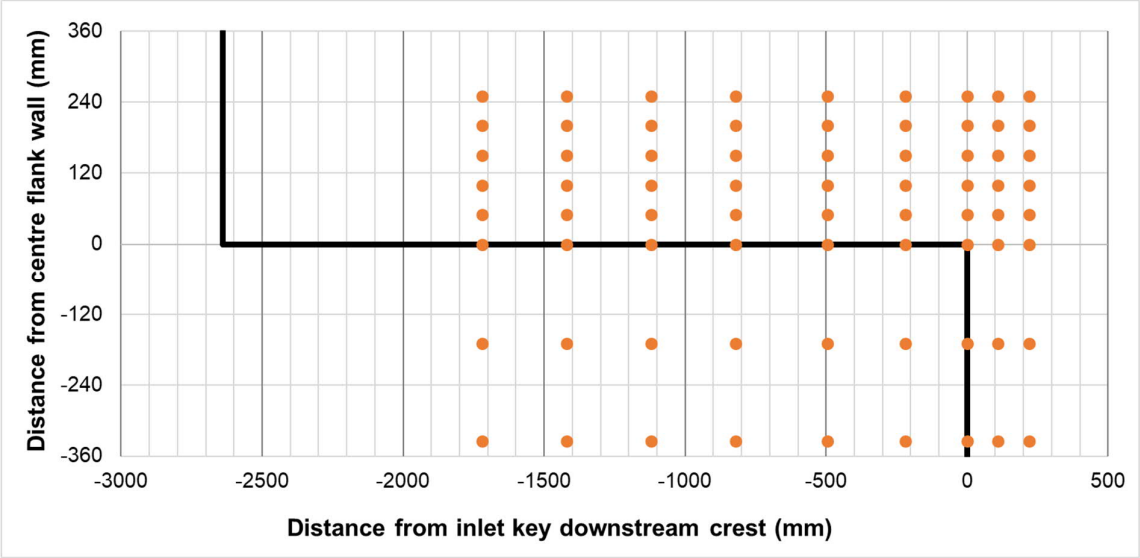

Figure 5.14: Water surface profile measurement grid layout for Model 1

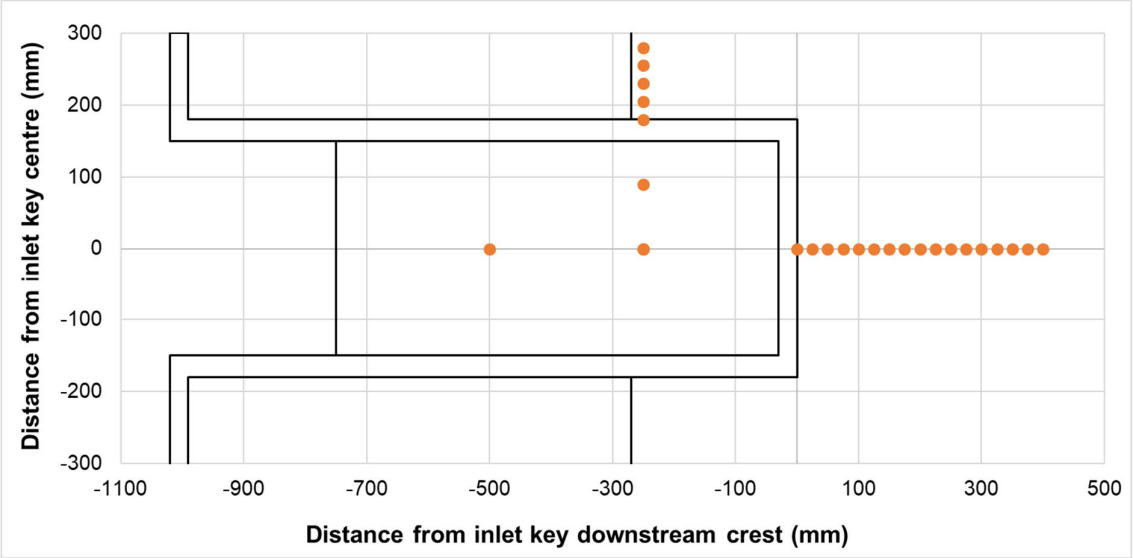

Figure 5.15: Water surface profile measurement grid layout for Model 2

5.4.4 Air velocity measurement in the aeration pipe

The air velocity within the aeration pipe was measured with a Lutron hot-wire anemometer to determine the air discharge and subsequently to determine the estimated volume of air entrained under the nappe for the different modelling scenarios as described later in **Section 5.5**.

The Lutron hot-wire anemometer consists of a thin metal wire element and tiny glass bead thermistor, located in the closed sensing head, that is heated electrically to a temperature above the ambient prior to measurement and once the sensing head is opened, the wire cools down as air flows over it.

The temperature of the wire relates to electrical resistance and consequently to current, which is directly related to the air flow velocity. The air flow velocity can be obtained by measuring the change in the wire temperature under constant current or the current required to maintain a constant wire temperature, i.e. based on the rate of cooling of the wire (TruTechTools, 2016).

The air velocity is displayed as the output on the instrument in m/s, km/h, ft/min, mile/h and knots. The anemometer has a measurement range between 0.2 m/s and 20 m/s, measured at a resolution of 0.1 m/s. It has an accuracy of ± 5 % over its total measurement range, i.e. an accuracy of ± 0.01 m/s at 0.2 m/s and ± 1 m/s at 20 m/s. Furthermore, it has an extremely high frequency response and fine spatial resolution by using a combination of the hot wire and a standard tiny glass bead thermistor to provide rapid and precise response to velocity fluctuations, even at low air velocities (TruTechTools, 2016).

Figure 5.16 shows the hot wire anemometer and detail of the sensing head. Note that the sensor cover can move up and down to cover the wire during heating and to expose it during measuring.

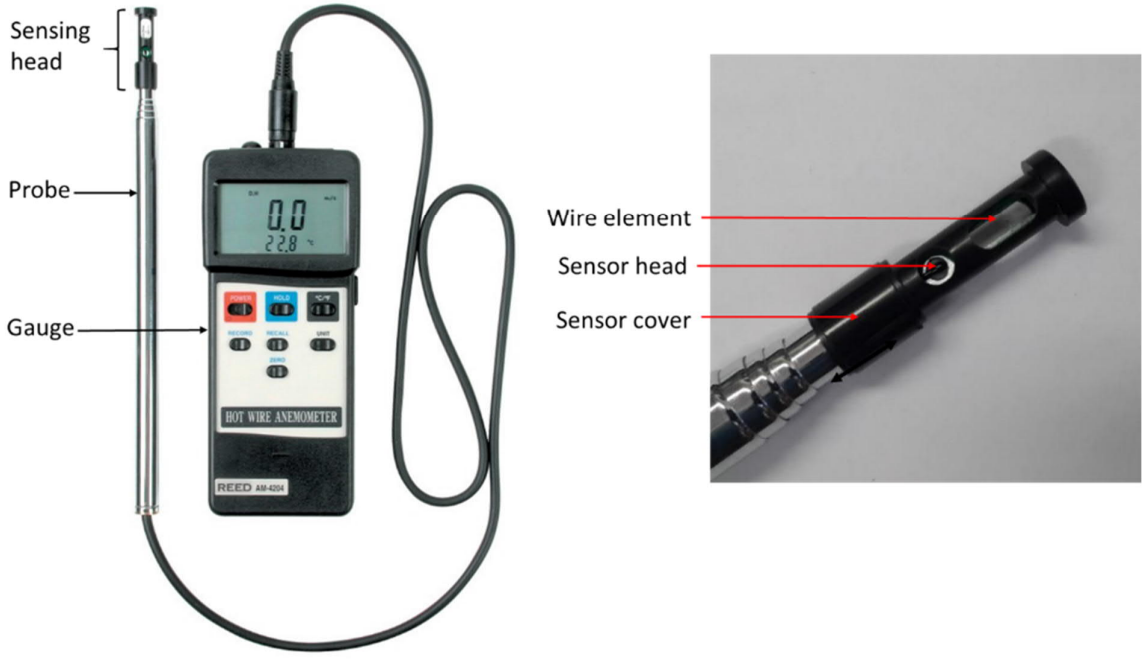

Figure 5.16: Lutron hot wire anemometer

The air velocity in the aeration pipe was measured by placing the sensing head at the centre of the pipe through a hole located at least three times the pipe diameter away from the pipe opening to the atmosphere – refer to **Figure 5.17**. At this position airflow is considered straight and uniform, without significant effect of turbulence generated at the mouth of the pipe (Calitz, 2016).

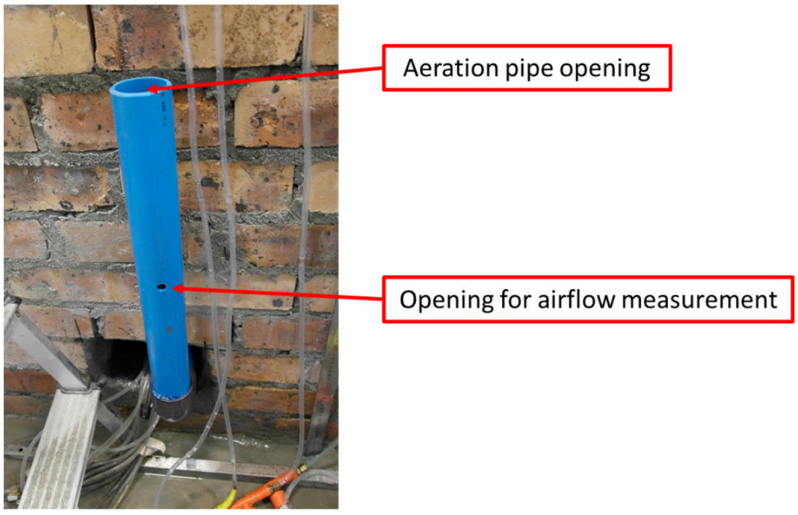

Figure 5.17: Anemometer test opening position

Once heated, the sensor cover was moved downward to expose the wire before inserting the sensing head into the pipe and taking measurements. The sensing head was orientated perpendicular to the direction of airflow. Due to the layout of the model and the operation of the anemometer, the gauge was placed on the sidewall and the probe held inside the pipe by hand during measurement. Caution was taken to not move or rotate the probe while measuring.

The anemometer does not have any data logging capabilities, and hence the measurements were recorded manually. For consistency, measurements were taken every 5 seconds over a period of 60 seconds. This gave approximately 12 readings per modelling scenario that were statistically analysed for further utilisation in the air entrainment estimation. In case of the steel model, m/s was selected for the air velocity output, however, for the wooden model, ft/min was selected and converted to m/s for data analysis purposes. The display resolution for measurements in ft/min (1.0 ft/min) is equivalent to 0.0051 m/s (Calitz, 2016), and thus provided a higher degree of accuracy.

5.4.5 Pressure measurement

Nappe oscillations are characterised by fluctuating unstable air cavities behind the nappe (Crookston & Tullis, 2013). Dynamic pressures behind the nappe were measured at fixed locations on the PKW structure using WIKA S-10 type pressure transducers and PicoLog data logging software for all test scenarios.

For the steel model (Model 1), one pressure transducer was installed directly into the flow guide wall below the inlet key overhang to make direct contact with the air behind the nappe (no tube) – refer to **Figure 5.5**. This pressure sensor picked up the sound generated by the nappe oscillations. No other pressure sensors were installed into this model itself due to the

thin construction material and the likelihood that they would be affected by the movement of the model itself.

In the case of the wooden model (Model 2) five pressure sensors were installed – one just above the aeration pipe opening of the two complete inlet keys, and three along the downstream face of one sidewall. The positions of the pressure sensors are shown in **Figure 5.18**.

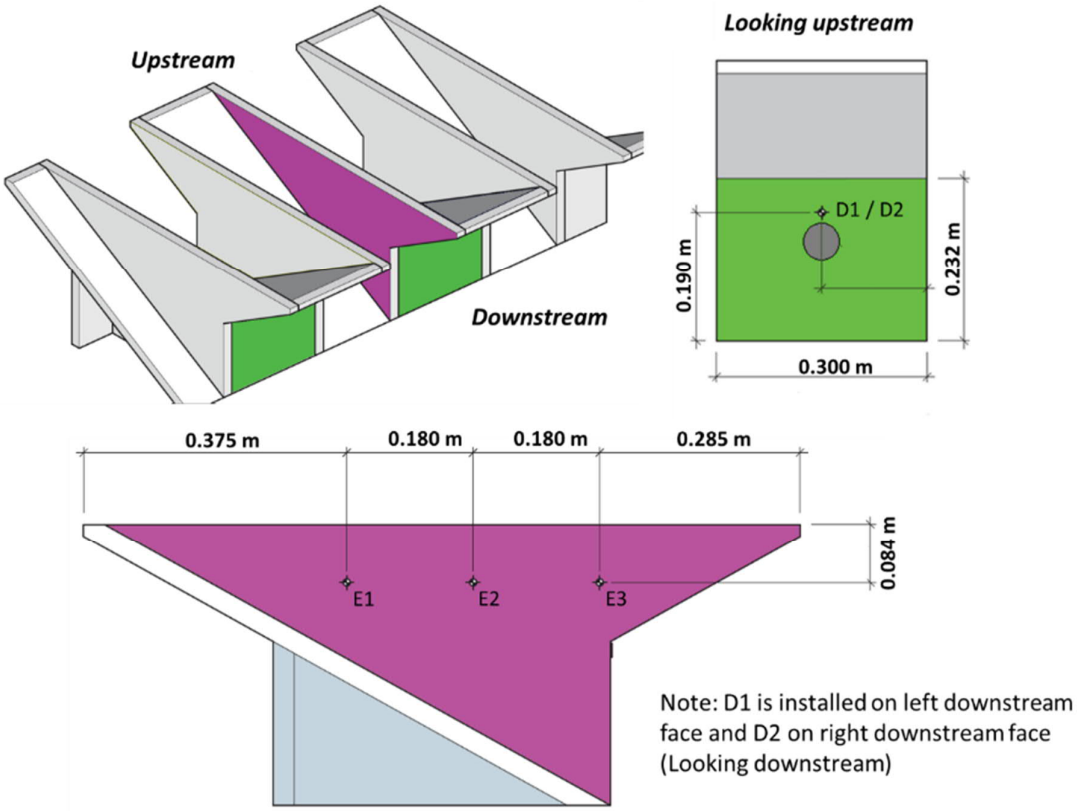

Figure 5.18: Pressure sensor locations for wooden model (Adapted from Denys (2019))

These pressure sensors were installed by drilling small holes into the walls of the PKW model and connecting a 2.5 m long 5 mm diameter plastic tube to the hole from the inside of the model. The other end of the tube was connected to a T-piece on the outside of the flume. The one end of the T-piece was fitted with a WIKA S-10 type pressure transducer, and the third end with an additional piece of plastic tube for priming purposes before each test set. These tubes were primed before logging data by injecting water into the tube with a syringe to remove any air. This end of the tube was then closed off to avoid any transfer of mass in these tubes during pressure logging, and ultimately unwanted disturbances in the pressure signals. However, the measurement methodology was changed from and close pipe system to an open pipe system (i.e. the tubes were not closed off after priming). **Figure 5.19** shows the configuration of the pressure sensors on the outside of the flume.

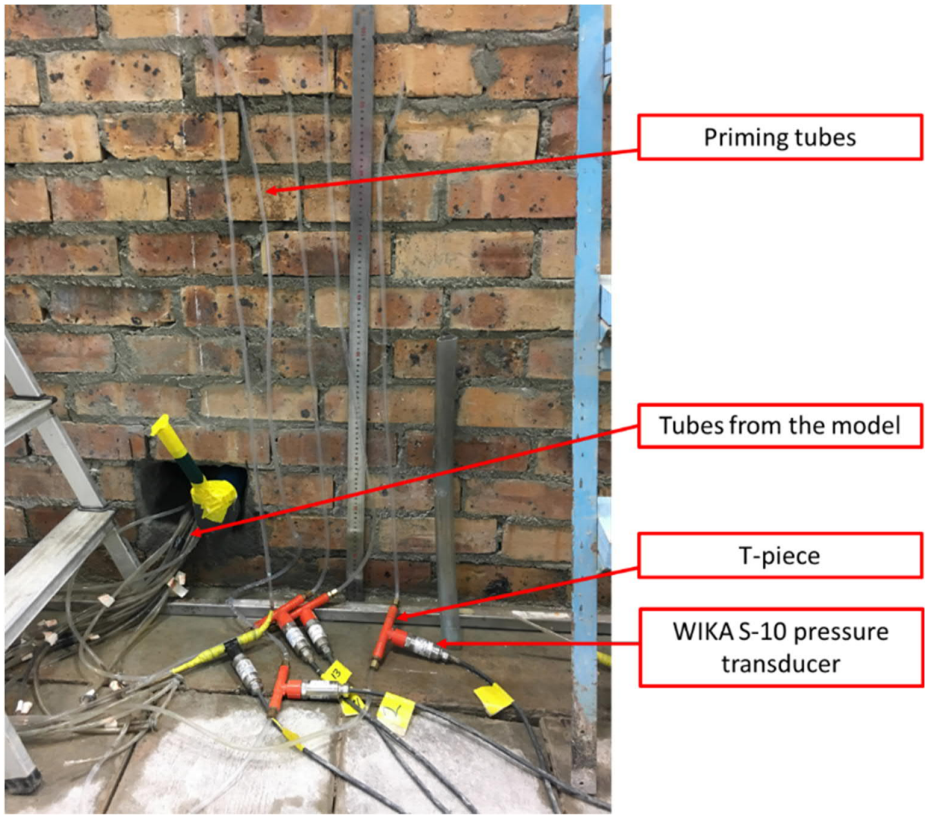

Figure 5.19: Pressure sensor configuration on outside of flume

The pressure transducer type used has a pressure measurement range of +1 m and -1 m range (± 100 mbar) and an accuracy of ±0.5 % of the measurement range (i.e. maximum 10 mm). The pressure transducer has an output range of 4 to 20 mA or DC 10 to 30 V (power supply range).

The pressure transducer measures in milliampere which is then converted to volts by a 120 Ω resistor using Ohm's Law. The voltage output is logged using a 12-channel analogue to digital data logger, which transmits the signal via a USB cable to a computer using PicoLog software. The software collects and can plot the signal over time as it is received – allowing for visual inspection of the data during the measurement. The data can be exported in CSV format for further data processing (refer to **Section 5.7**).

The voltage readings were converted to meters head by using the following equation (Calitz, 2016):

$$H = \frac{H_{max} - H_{min}}{I_{max} - I_{min}} \times \frac{x}{R} - V_{atm} \qquad \textbf{5-2}$$

Where:

H	Measured pressure head (m)
H_{max}	Maximum pressure head limit of transmitter (m), +1 m
H_{min}	Minimum pressure head limit of transmitter (m), -1 m
I_{max}	Maximum current output of transmitter (A), 20 mA
I_{min}	Minimum current output of transmitter (A), 4 mA
x	Measured voltage reading (V)
R	Resistance of transmitter (Ω), 120 Ω
V_{atm}	Voltage reading of atmospheric hydrostatic pressure (V), 1.5 V recommended by manufacturer

The above equation can be rewritten as follows to accurately account for the voltage reading of the hydrostatic pressure (Calitz, 2016):

$$H = \frac{H_{max} - H_{min}}{I_{max} - I_{min}} \times \frac{x - V_{atm,act}}{R} \qquad \textbf{5-3}$$

Where:

$V_{atm,act}$	Actual voltage reading of atmospheric hydrostatic pressure before tests (V)

The pressure head (m) can be easily converted to Pascal (Pa). According to Leite Ribeiro *et al.* (2007) dynamic pressure readings sampled at a frequency of 100 Hz over a time period of 90 seconds is sufficient for classical statistical analysis, including the Power Spectral Density (PSD) and the distribution function curves. Dynamic pressure readings were sampled at a frequency of 1000 Hz for a duration of at least 120 seconds. The sampling frequency was selected to pick up any high frequency pressure fluctuations, that would normally not be picked up at 100 Hz and to permit efficient Fast Fourier Transform (FFT) and PSD post processing (**Section 5.7**). The duration allowed for a sufficient number of cyclical pressure fluctuations to be recorded. In the case of the wooden model, pressure readings were logged simultaneously from all pressure transducers to allow for cross-correlation.

5.4.6 Vibration measurement

The structural vibration of the sidewall of the steel model (Model 1) was measured for various test scenarios to determine:

- If there is any correlation between the structural vibration and the pressure (or sound) fluctuations of the air cavity behind the nappe (keeping in mind that the pressure readings might be influenced by the vibration of the flow guide and PKW structure); and
- The effect, if any, of artificial aeration of the air cavity behind the nappe.

A strain gauge operates by measuring strain of a material, caused by an external force, as a change in electrical resistance. Resistance changes are measured in a bridge circuit to allow precise measurement in small resistance changes, as well as to eliminate any temperature effect. The term half-bridge refers to when two strain gauges are placed on either side of a material in such a manner that they experience the strain caused by the opposing force fields. This also enables the strain gauges to be more sensitive to change in resistance (Hoffman, 2011).

The vibrations of the PKW sidewall, deflection (µm/m) over time, were measured by a single half-bridge strain gauge (350 Ω) installed in the middle of the PKW sidewall near the crest (**Figure 5.20**). It was expected that this would be the location where the deflections would be largest. Furthermore, this location allowed the strain gauge to be placed in half-bridge formation – one on each side of the crest.

Figure 5.20: Strain gauge position on Model 1

The signal data from the strain gauge was collected by an HBM Spider 8 signal processor and recorded using HBM CatmanEasy (v4.1) computer software. The software collects and displays the signal (deflection as µm/m) over time as it is received. Real time signal data and FFT graphs could be displayed by the software during data logging to enable visual checks for stationary nature of the signal and any significant background noise or discrepancies.

Vibration readings were sampled at a frequency of 2400 Hz for a duration of at least 180 seconds. The sampling frequency was selected to pick up high, as well as low frequencies and to permit FFT and PSD post processing (**Section 5.7**).

5.5 EXPERIMENTAL SCENARIOS AND PROCEDURES

Various discharge rate and aeration condition scenarios were tested in the models. A summary of the experimental scenarios for both models is given in the subsequent sub-sections. **Table C.1** and **Table C.2** in **Appendix C** provide the different test scenarios and relevant data collected for each scenario. Several tests were repeated independently to validate the data. Tests that were repeated are indicated by a "*" in **Table C.1** and **Table C.2. I**n some cases, data capturing, was repeated up to five times for the given test scenario to compare and verify data, as well as to identify any errors.

5.5.1 Model 1 (large scale steel model)

The flow or discharge in the steel model ranged from 50 l/s to 400 l/s in 50 l/s increments. For each flow scenario three aeration conditions were tested – no aeration of the air cavity behind the overflow nappe, aeration through a small diameter pipe and aeration through a large diameter pipe. For all scenarios the upstream headwater level, time variant pressure and time variant vibrations were recorded. Air velocity readings were recorded for both aerated conditions (small and large diameter pipe) for the aforementioned range of discharges. The water surface profiles over the PKW were measured and recorded for no aeration and for the large diameter aeration pipe for flows of 50, 100, 200, 300 and 400 l/s.

5.5.2 Model 2 (smaller scale wooden model)

The flow or discharge to the wooden model ranged from 50 l/s to 500 l/s in 100 l/s increments above 50 l/s (i.e. 50, 100, 200…). For each flow scenario three aeration conditions were tested – no aeration of the air cavity behind the overflow nappe, aeration through a small diameter pipe and aeration through a large diameter pipe. For all scenarios the upstream headwater levels and time variant pressures were recorded. Air velocity readings were recorded for both aerated conditions (small and large diameter pipes) for the aforementioned range of discharges. The water surface profiles over the PKW were measured and recorded for no aeration and for the large diameter aeration pipes for flows of 50, 100, 200, 300 and 400 l/s.

Additional scenarios whereby the tail water level was raised in 100 mm increments for different aeration conditions and flows were also tested. Tests were also conducted whereby the nappe was completely broken by placing a brick on one of the lateral crests.

5.6 LIMITATIONS AND POTENTIAL ERRORS

Scale can be one of the main limiting factors for physical hydraulic models. Both the steel and wooden models were constructed at relatively large scale of 1:2.73 and 1:7.5 respectively, compared to general hydraulic model scales of 1:20 to 1:50 (University of Pretoria, 2004) (Heller, 2011). The scale of the steel model had to be large enough to ensure that expected

vibrations do occur and are strong enough that these can the measured and recorded by the selected instrumentation. Potential scale effects caused by surface tension and viscosity were eliminated by these large scales.

Nappe oscillation intensity and frequency cannot be accurately scaled using laws of similitude as it is a function of the fall height (Lodomez, *et al.*, 2019). The fluctuating pressures behind the nappe were only analysed in a comparative manner and should not be upscaled to represent the expected pressure fluctuations for the prototype. The same applies to scaling of air entrainment since the physics of bubble generation and size does not change if the same fluid is used in the model as in the prototype. However, the steel model can be considered as a full-scale prototype to enable the nappe oscillations and the aeration rate to be assessed.

Secondly, caution should be taken to ensure that the instruments used have the required degree of accuracy and sensitivity to record the required data or occurrences. The instrumentation used all had an acceptable degree of accuracy, measurement range and resolution as summarised in **Table 5.6**. The sampling frequency for all time variant data (pressure and vibration) was equal to or higher than 1 000 Hz and the sampling duration at least 120 seconds. This allowed for capturing of high frequencies to a high degree of accuracy. Furthermore, some of the tests and data capturing was repeated and compared to verify data and to identify any errors.

Table 5.6: Instrumentation accuracies, ranges and resolution

Instrument	Accuracy	Measurement range	Resolution
SAFMAG flow meter	±0.5 %		5 numbers
Water level needle gauge	0.1 mm	0 - 2 000 mm	0.1 mm
Pitot tube	1.0 mm	250 – 1 250 mm	1.0 mm
Anemometer	5% over measurement range	0.2 – 20 m/s 40 – 3 940 ft/min	0.1 m/s 1.0 ft/min
Pressure transmitter	±0.5 %	±100 mbar	0.000 V
Strain gauge	-	-	-

The rail mounted trolley had a slight misalignment of 4 mm in both the longitudinal (upstream to downstream) and transverse (left to right) direction (Denys, 2019). The effect of this misalignment on the water surface profile readings was negligible. All readings were taken at the same location for the range of tests, so as to determine the difference in the water surface profiles at a specific position for any pair of test scenarios.

In the case of the wooden model (Model 2), it was expected that there would be a time lag between the pressure fluctuations experienced in the model and the pressure (or pressure transducer signal reading in volt) captured by the pressure transducer. The reason for this was the length of the plastic tube between the model and pressure transducer and the speed of

sound in water (Denys, 2019). Care was taken to ensure the lengths of the tubes of all pressure sensors were the same.

Ideally pressure transducers should be installed to directly measure the water or air pressures. Due to the size of the available pressure transducers and the fact that these should not get wet, the plastic tube configuration was opted for Model 2. Furthermore, the fluctuations in the air-water contact at the pressure sensors caused air bubbles to enter the pressure tube and affect the pressure readings. This prevented the identification of true negative pressures (Denys, 2019). Therefore, the pressures recorded in Model 2 were relative pressures and not absolute pressures. This was particularly the case with pressure sensors E1, E2 and E3 installed on the downstream side of the inlet key sidewall to measure the fluctuations in pressures behind the lateral crest nappe. The pressure sensors installed under the inlet key overhang were not expected to be affected for low tail water levels.

In the case of the steel model, the pressures readings in the air cavity behind the overflow nappe were susceptible to the vibrations of the pressure sensor which was itself installed into the downstream flow guide wall. The wall was braced to prevent vibrations, but cognisance must be taken that the true hydrodynamic pressures might not have been recorded. Furthermore, this pressure sensor picked up the sound generated by the nappe oscillations. The pressure data behind the nappe of the steel model were evaluated in a comparative qualitative manner only and not necessarily to reflect the true behaviour of a prototype PKW.

The air velocity measurements in the 19 mm aeration pipe were not successful, possibly because of the large relative size of the anemometer sensing head compared to the inner area of the pipe itself. Therefore, this data was discarded.

5.7 DATA PROCESSING

5.7.1 Single point measurements

No additional data processing was required for single point measurements, such as the flow measurements and the water surface profile and headwater readings. These readings were repeated and compared in order to identify any inaccurate readings.

5.7.2 Air demand

Measured air velocity data collected in ft/min were converted to m/s using Equation 5-4. The average air velocity for a test scenario was calculated and converted to an average air demand in m^3/s using Equation 5-5. The air velocity data was inspected for any potential outliers that might affect the average and if any, this data was discarded. These readings were also repeated and compared to identify discrepancies.

$$V_{converted} = \frac{V_{measured}}{196.85} \quad \textbf{5-4}$$

Where:

$v_{converted}$ Converted air velocity (m/s)

$v_{measured}$ Measured air velocity (ft/min)

$$Q = AV \quad \textbf{5-5}$$

Where:

Q Air demand (m^3/s)

A Cross-sectional area of collector aeration pipe (m^2)

V Air velocity (m/s)

5.7.3 Pressure and vibration

Vibration frequencies or any time variant force fluctuations are better analysed in the frequency domain than in the time domain. A PSD allows one to view a time variant data signal in the frequency domain by presenting the energy, or power content, associated with a frequency. The peak frequencies will have higher energies, which makes them easier to identify (Hanley, 2016).

A time signal can be converted to the frequency domain through FFT. FFT is an algorithm that calculates the Discrete Fourier Transform (DFT) of a sequence with a reduced execution time. A DFT works by multiplying the raw signal waveform by sine waves of discrete frequencies groups them according to selected frequency values and determines the corresponding amplitude (Hanley, 2016).

The FFT algorithm is most efficient when the number of samples is equal to some power of 2. For example, if 2 000 samples are captured, only 1024 (2^{10}) of the samples will be used to create the FFT (Hanley, 2016).

According to the Nyquist theorem, the sampling rate must be at least twice that of the highest frequency to accurately measure the frequency of the signal. The pressure data sampling rate (1000 Hz) and the vibration data sampling rate (2400 Hz) allowed for frequencies up to 500 Hz and 2400 Hz respectively to be measured. The frequency resolution in an FFT directly depends on the signal length or time period and the number of samples (Equation 5-6) (National Instruments, 2018):

$$df = \frac{1}{T} = \frac{f_s}{N} \quad \textbf{5-6}$$

Where:

df	Frequency resolution (Hz)
T	Period of the signal (sec)
f_s	Sampling frequency (Hz)
N	Number of samples

A PSD is computed by multiplying each FFT frequency bin by its complex conjugate[1] (amplitude in g^2) and normalizes the amplitude value to the frequency bin width to get rid of the dependency on bin width (amplitude in g^2/Hz) (Hanley, 2016).

The conversion from a normal signal to a FFT and ultimately to a PSD plot is shown in **Figure 5.21**.

The time variant pressure and vibration data were checked for stationarity and other discrepancies, such as background noise, obviously incorrect variability and spikes. The pressure and vibration recording software, PicoLog and HBM CatmanEasy (v4.1) respectively, can both display the time variant signal data during capture and thereafter. Data affected by background noise or data that was obviously incorrect were excluded from the time variant data signal record.

The pressure data, as recorded, was converted from Volts to pressures (in meters of water) using Equations 5-2 and 5-3. The pressure and vibration data were further processed to obtain the PSD of the data signals. The PSD for each data signal was obtained by first removing the mean from the data signal and then converting the time signal into the frequency domain using FFT. FFT analysis was done using the SciPy fftpack (scipy.fftpack) module. The PSD data points where then plotted on a log-log scale to manually identify the peak frequencies as shown in **Figure 5.21**.

[1] *"The complex conjugate of a complex number is a number with an equal real part and an imaginary part equal in magnitude but opposite in sign."*

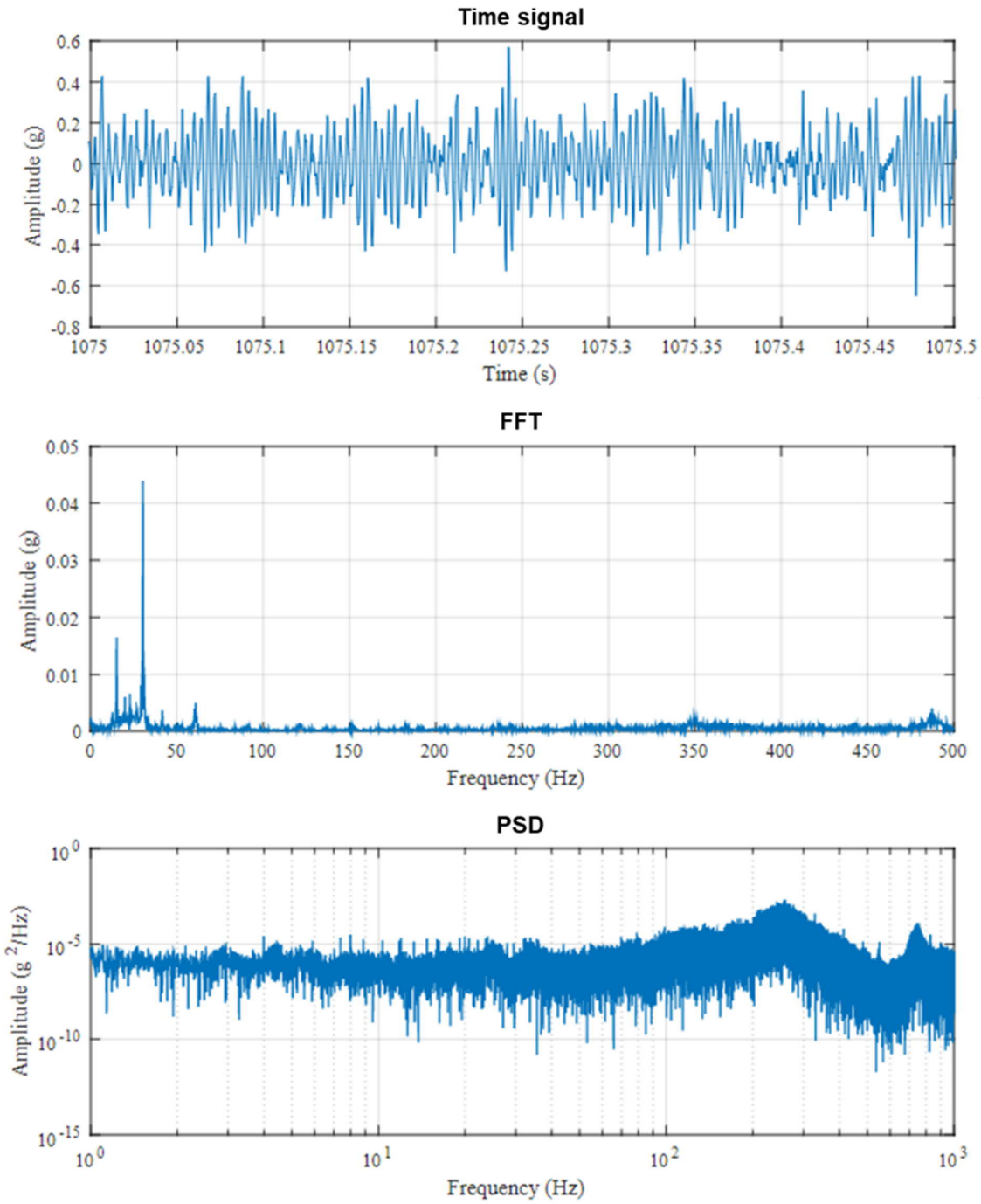

Figure 5.21: Example of time signal, FFT and PSD graphs

6. EXPERIMENTAL RESULTS AND ANALYSIS

The results and observations from the physical hydraulic model are analysed, summarised and discussed in this chapter. The main objective of this study was to investigate the potential effect of artificial aeration on the hydraulic behaviour of PKWs, specifically discharge capacity and nappe behaviour, and vibration of the thin PKW wall elements as a result of nappe oscillations, or FIV, if any.

6.1 DISCHARGE CAPACITY

One of the objectives of this study was to evaluate whether artificially aerating the air cavity behind the overflow nappe of a PKW has any effect on the discharge capacity. Previous studies have noted the discharge efficiency for labyrinth weirs is slightly higher than the theoretical value when the nappe is not aerated due to the slight sub-atmospheric pressures developing underneath the nappe (Crookston & Tullis, 2013). It was expected that the same would be true for PKWs.

The discharge coefficient obtained from the two physical hydraulic models can be considered an adequate representation of the prototype as all overflow heads were more than the 0.02 m limit recommended by Kobus (1980).

The head-discharge relationship for Model 1 (steel model) is shown in **Figure 6.1** and the discharge coefficient[2] vs. H/P is shown in **Figure 6.2**.

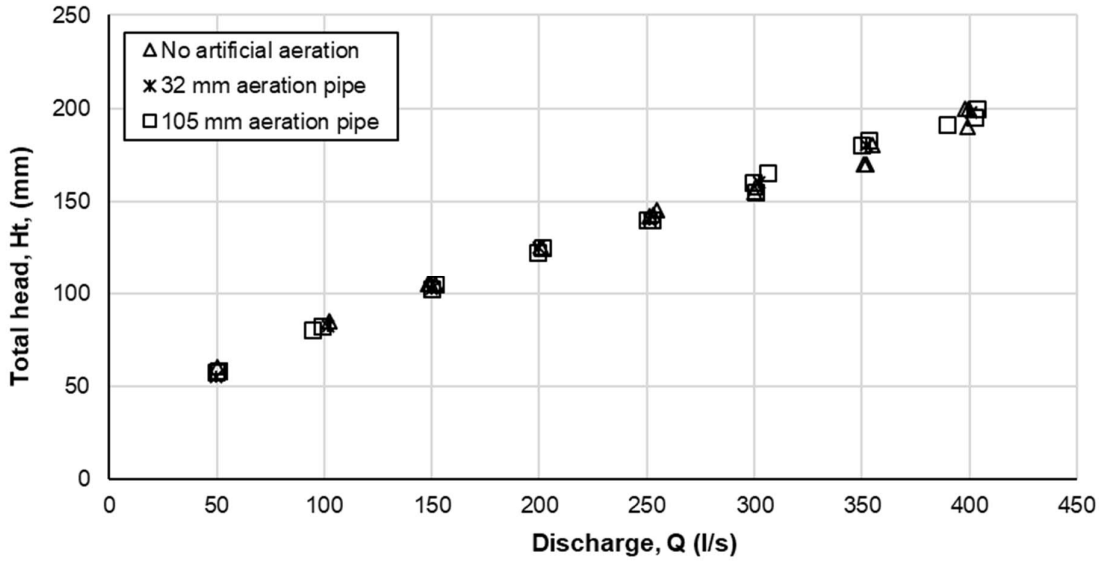

Figure 6.1: Model 1 – Measured head discharge relationship

[2] Discharge coefficient calculated using Equation 2-7.

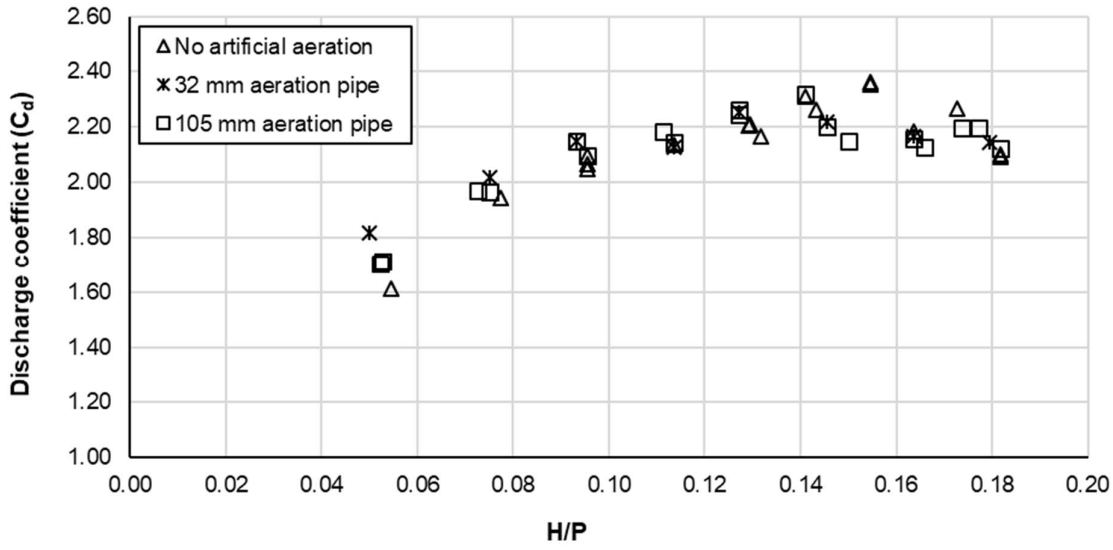

Figure 6.2: Model 1 - Measured discharge coefficient

With reference to **Figure 6.1**, there is no noticeable difference between the headwater depths for the different artificial aeration conditions, particularly for low discharges. The difference between the headwater levels for different artificial aeration conditions becomes more distinct for discharges higher than 300 l/s. At higher flows it appears that the headwater level is lower for unaerated conditions.

From **Figure 6.2** it seems that the discharge efficiency for unaerated conditions is slightly lower compared to artificially aerated conditions for low discharges, but higher for larger discharges. The graph also shows that the discharge coefficient increases as the discharge increase up to approximately H/P < 0.14 and then start to decrease with increase in discharge. One should note that high discharges were not simulated. The findings that the discharge coefficient increases and then decreases as the discharge increases are consistent with those of Anderson & Tullis (2011) and Machiels *et al.* (2011), and are related to the nappe transitioning from clinging to leaping to springing (**Section 2.3.2**).

To better evaluate the effect of artificially aerating the nappe on the discharge efficiency, **Figure 6.3** depicts the percentage difference in the discharge coefficient for different artificial aeration scenarios compared to no artificial aeration for Model 1 (steel model).

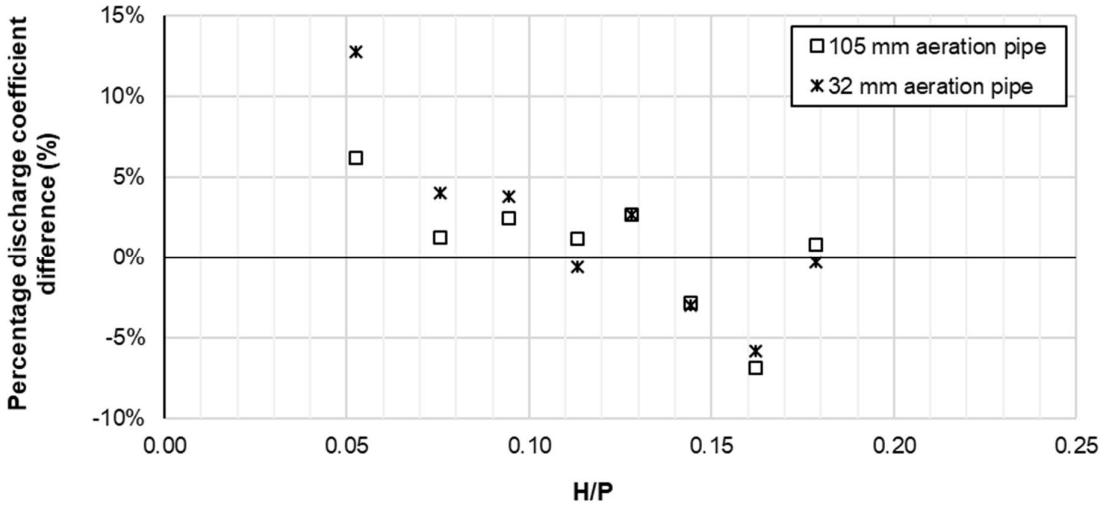

Figure 6.3: Model 1 - Measured percentage difference in the discharge coefficient compared to no artificial aeration

For lower discharges with H/P < 0.13, the discharge capacity of Model 1 is approximately 5% more efficient under artificially aerated conditions compared to unaerated conditions. However, for higher flows (H/P > 0.13) the unaerated scenarios performed up to 7% better in terms of discharge efficiency. For low flows with H/P < 0.10 the scenarios with the smaller aeration pipe performed better than the scenarios with the large aeration pipe. The two pipe sizes preformed almost equally for higher discharges (H/P > 0.10).

The head-discharge relationship and the discharge coefficients for Model 2 (wooden model) are shown in **Figure 6.4** and **Figure 6.5** respectively. The theoretical head-discharge relationships and discharge coefficients according to the three design methodologies discussed in **Section 2.4.4** are also shown on both graphs for comparison purposes.

The head-discharge curve and discharge coefficient – H/P relationship for Model 2 (wooden model) fall between the two theoretically predicted relationships using the Leite Ribeiro (2012a) and Machiels *et al.* (2012) methodologies. The parameters of the physical hydraulic model fall within the parametric limits of these two methodologies, but not within that of Kabiri-Samani & Javaheri. The head-discharge curve trends towards that predicted using Leite Ribeiro for higher discharges.

Similar to what was observed by Machiels *et al.* (2011), the discharge coefficient increases with an increase in H/P until the nappe behaviour transitions from leaping to springing along the lateral crest - in the case of this study H/P < 0.1. For higher discharges the nappe becomes springing and results in the discharge coefficient to gradually decrease with an increase in head or discharge.

The differences in the physical model discharge coefficient and that predicted by Leite Ribeiro (2012a) for H/P can be attributed to the fact that the theoretical discharge coefficient considers half rounded crests, which are more efficient compared to flat topped crest, as the case with this physical hydraulic model (Denys, 2019).

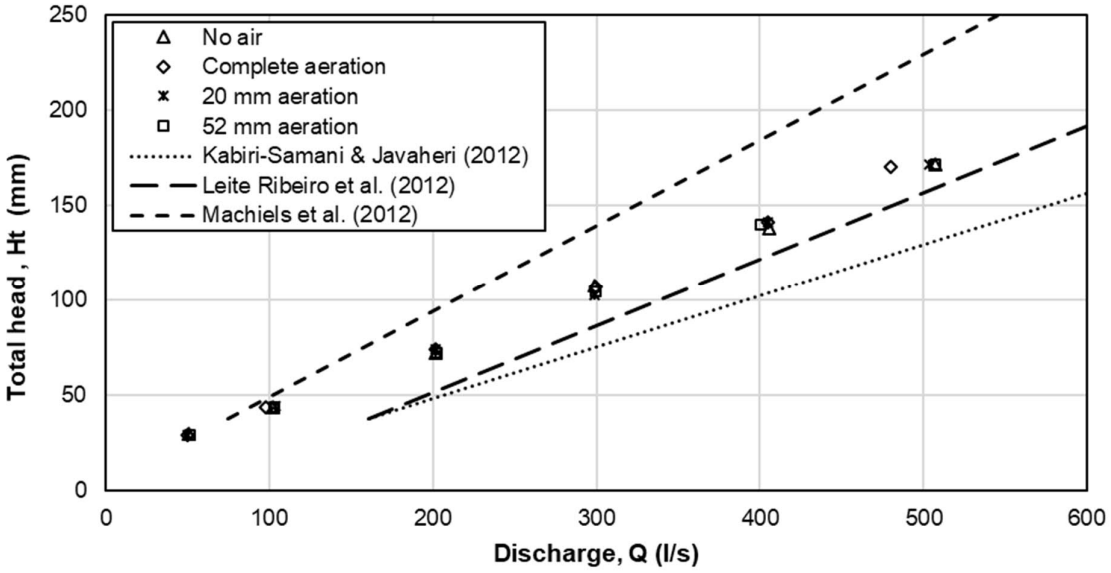

Figure 6.4: Model 2 - Measured head discharge relationship

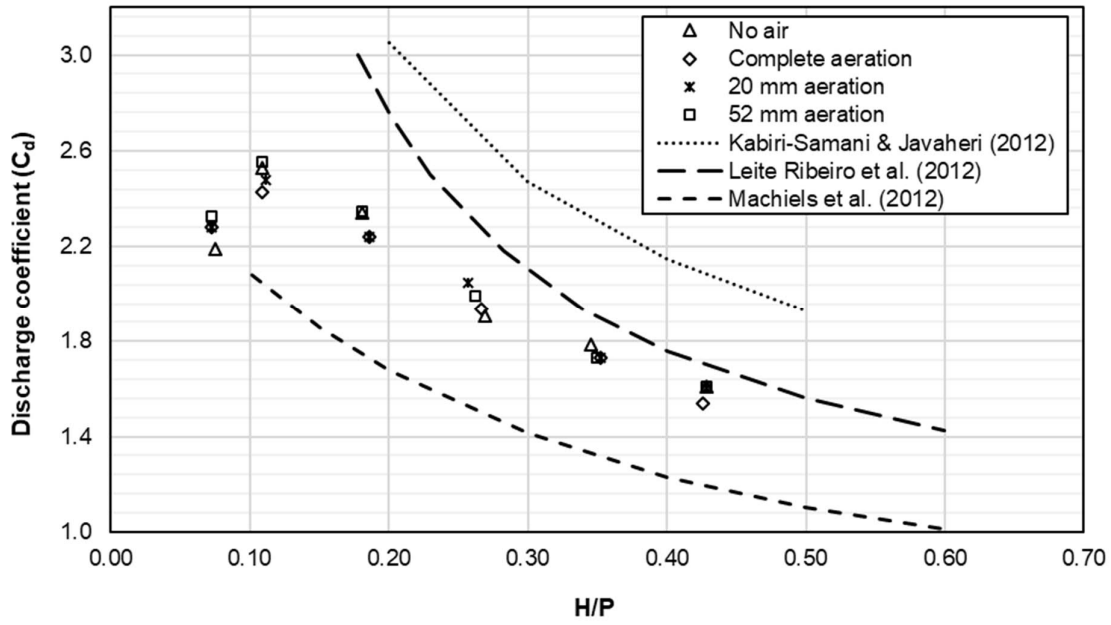

Figure 6.5: Model 2 - Measured discharge coefficient

Figure 6.6 depicts the percentage difference in the discharge coefficient for different artificial aeration scenarios compared to no artificial aeration for Model 2 (wooden model). Similar to the findings of Model 1, the aerated scenarios are more efficient at low discharges compared

to unaerated scenarios, however, as the discharge increase (H/P > 0.10), the aerated scenarios performed less efficiently.

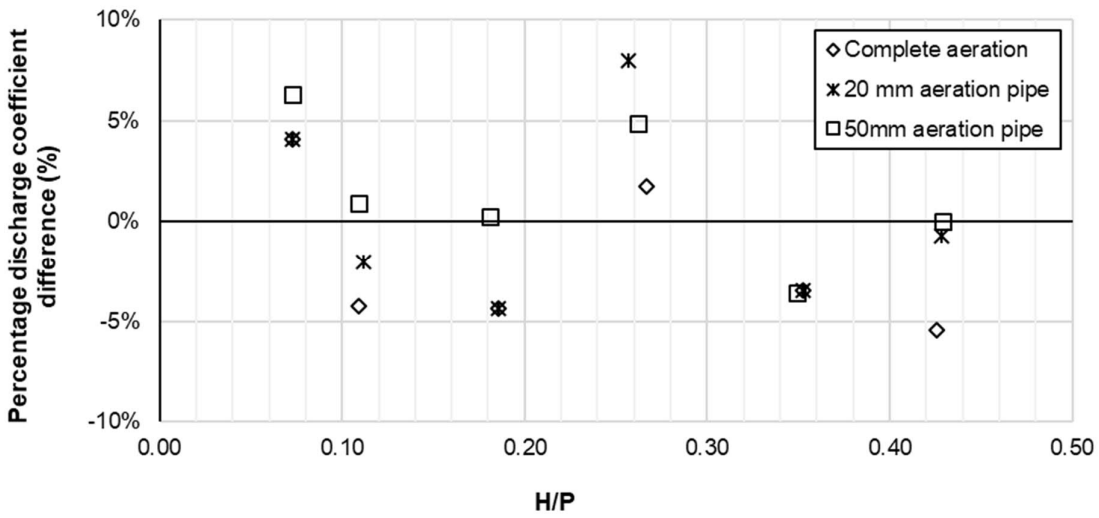

Figure 6.6: Model 2 - Measured percentage difference in the discharge coefficient compared to no artificial aeration

For most discharges the larger aeration pipe seemed to result in a better discharge efficiency compared to the other aeration scenarios. One would expect that the complete aeration scenario would have a higher efficiency compared to the larger aeration pipe. However, the reduced efficiency could be explained by the brick placed on one of the lateral crests to open the nappe and which resulted in a reduced effective overflow crest length.

The discharge efficiency data for both Model 1 (steel model) and Model 2 (wooden model) are attached in **Appendix D**. A summary of the H/P ratios for the various discharges for Model 1 and Model 2 are given in **Table 6.1** for ease of reference for the remainder of this chapter.

Introducing air to the air cavity behind the overflow nappe seemed to have a positive effect on the discharge capacity of the models tested for H/P < 0.10, however for higher discharge capacities the efficiency reduced. Therefore, the impact of artificially aerating the nappe on the discharge capacity can be considered negligible based on the results of this study.

Table 6.1: Summary of H/P values for Model 1 and Model 2 (measured data)

Discharge (l/s)	Model 1 (Scale 1:2.73)		Model 2 (Scale 1:7.5)	
	No air	Large aeration pipe	No air	Large aeration pipe
50	0.055	0.053	0.075	0.073
100	0.077	0.074	0.110	0.110
150	0.095	0.094	-	-
200	0.114	0.113	0.180	0.180
250	0.130	0.127	-	-
300	0.142	0.145	0.270	0.260
350	0.158	0.165	-	-
400	0.179	0.178	0.345	0.350
500	-	-	0.430	0.430

6.2 NAPPE PROFILE AND BEHAVIOUR

The nappe profile and characteristics can aid in evaluating the effect of aeration to the overall behaviour of a PKW. The introduction of atmospheric air pressure to the air cavity behind the nappe had noticeable effects on the nappe trajectory and profile. The nappe flow profile characteristics observed under different aeration conditions and discharges are discussed in this section.

With exception of the 50 l/s discharge scenarios in Model 2, the minimum overflow depth was more than 0.04 m – the limit recommended by Novak *et al.* (2010) to adequately replicate the nappe profile of a prototype in a scaled model.

6.2.1 Overview

For all discharges and aeration conditions evaluated as part of this study, the nappe formed a continuous water curtain over the lateral and downstream inlet key crests. The flow surface was generally smooth and stable for lower discharge rates, which allowed for observation and measurement of the nappe trajectory and characteristics. For larger flows however, the flow became more turbulent, making surface profile measurements and observations more difficult.

Figure 6.7 shows the view from downstream of Model 2 for the different discharges tested. Higher discharge rates resulted in noticeably more aerated tail water conditions. The nappe water curtain itself contained no air at lower discharge rates. At higher discharge rates and increased tail water levels, air entrainment into the nappe curtain itself was visible, although limited.

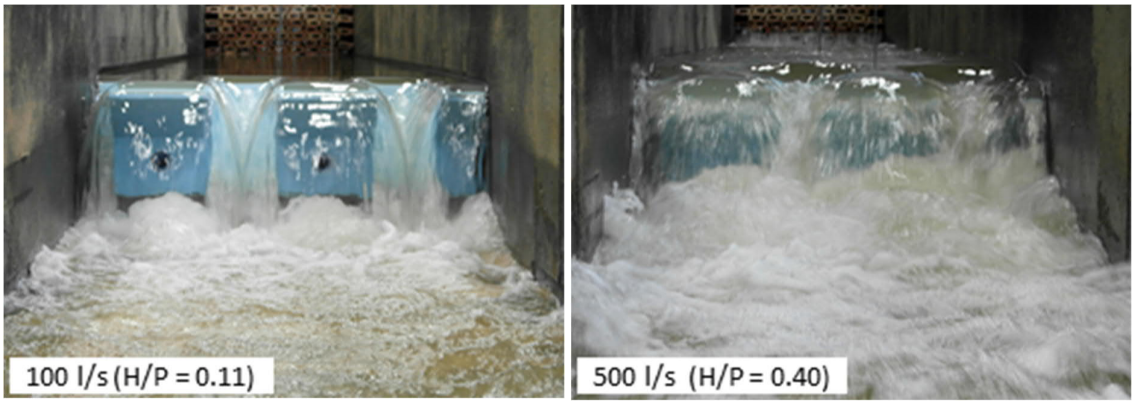

Figure 6.7: View from downstream for the different discharge rates (Model 2)

6.2.2 Inlet key

The nappe profiles over the downstream crest and sidewalls of the inlet key, especially for low discharges, are noticeably affected by artificially aerating the nappe air cavity. The nappe expands when air is introduced behind the nappe, either via the aeration pipes or by breaking the nappe itself, especially for lower flows. This is best illustrated in the nappe surface profile measurements of the no aeration and completely aerated conditions (breaking the nappe) tested in Model 2 (wooden model) – refer to **Figure 6.8** and **Figure 6.9**. "Q300" for example refers to a discharge of 300 l/s. This expansion reaction indicates that sub-atmospheric pressures exist behind the nappe when it is not artificially aerated. The profile also expands if the downstream water level is increased, implying that the volume of the air cavity behind the nappe stays constant for a certain discharge. The profiles of other scenarios and of Model 1 are included in **Appendix D.**

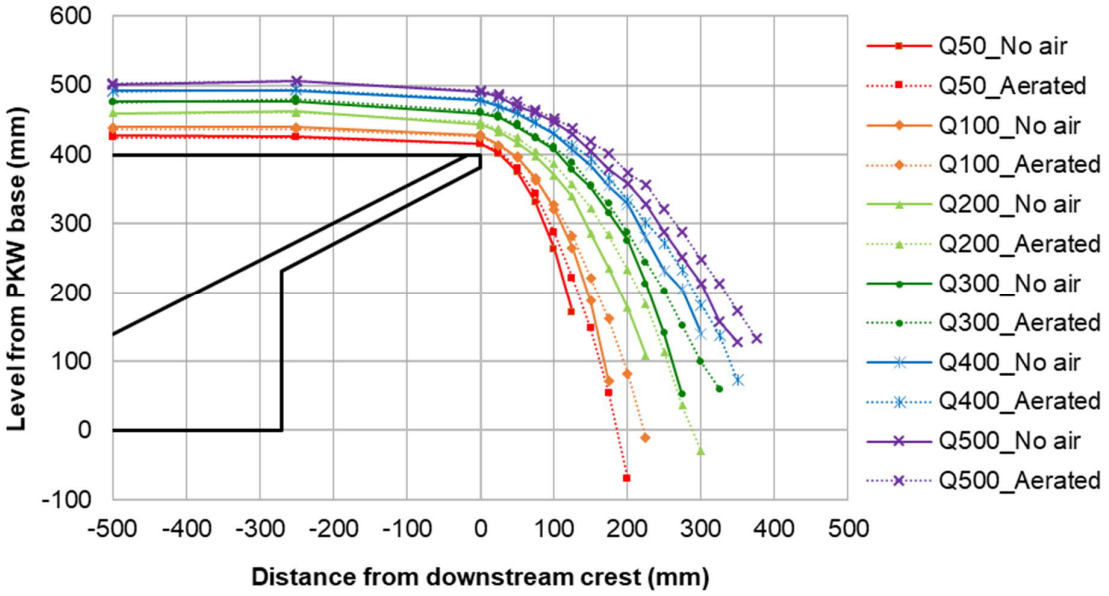

Figure 6.8: Measured nappe profile – Longitudinal view (Model 2)

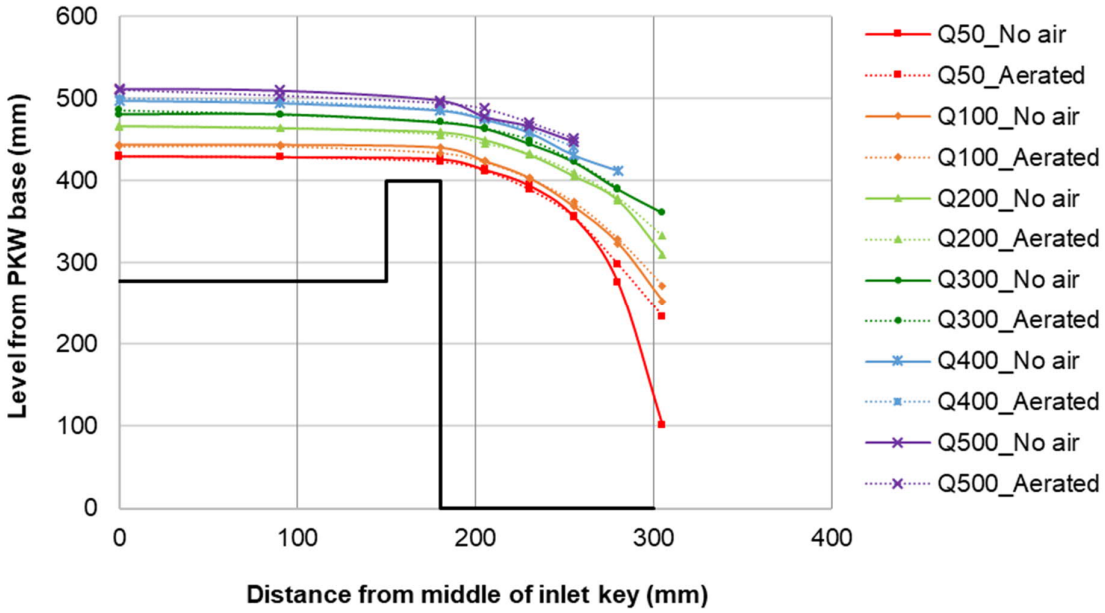

Figure 6.9: Measured nappe profile – Transverse view (Model 2)

For flows up to 150 l/s (H/P = 0.094) for Model 1 and up to 100 l/s for Model 2 (H/P = 0.11), the nappe at the corner edges of the downstream crest is drawn in into a concave shape. The flow over the corner edge is very limited compared to the rest of the crest and therefore the nappe is at its thinnest there. Compared to the rest of the nappe, the low momentum in this thinner jet of water is more susceptible to being overcome by the sub-atmospheric pressures behind the nappe, and results in the nappe being drawn in (Denys, 2019).

Denys (2019) reported that at low discharges between 8 l/s to 12 l/s in Model 1, these concave nappe indentations develop instabilities and start to oscillate causing the entire nappe to continuously expand and contract. The results of his, and this study, regarding nappe oscillations are discussed in **Section 6.4.3**.

As shown in **Figure 6.10** (encircled), these nappe indents were slightly less severe with the introduction of artificial aeration behind the nappe and disappeared completely when the nappe was broken. This implies that although the aeration pipes do reduce the sub-atmospheric pressures behind the nappe, these did not produce enough air to completely alleviate sub-atmospheric conditions behind the nappe.

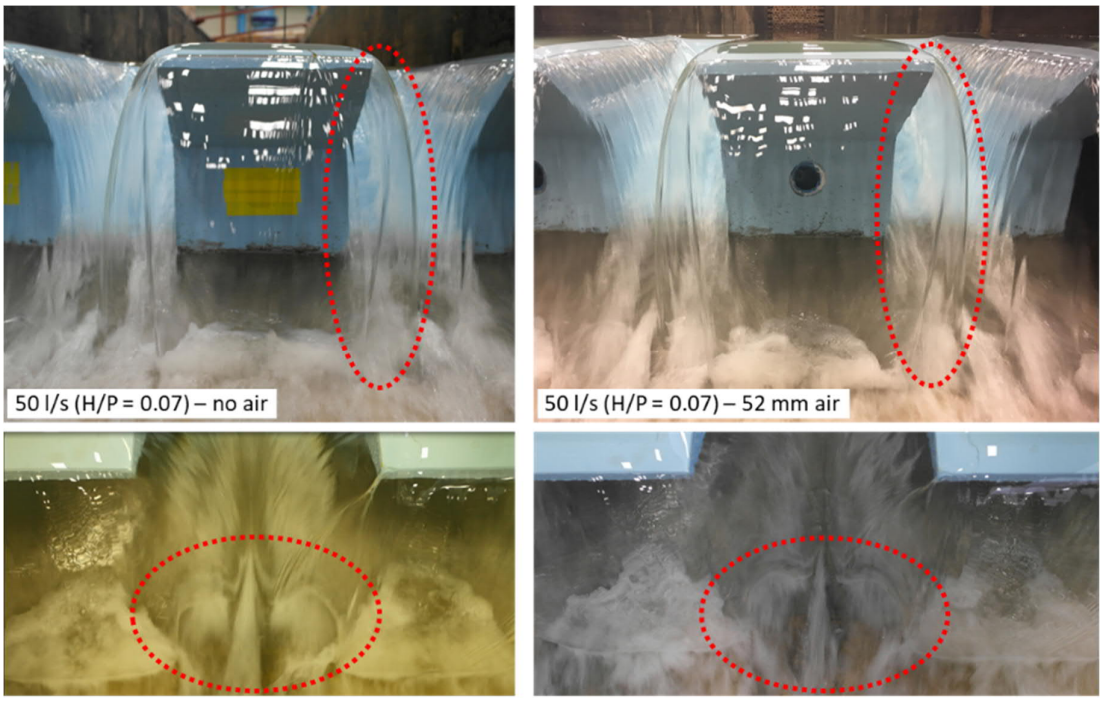

Figure 6.10: Concave nappe indentations at crest edge of inlet key (Model 2)

6.2.3 Outlet key

Figure 6.11 illustrates the discharge development in the outlet key as the discharge increases. Discharge over the upstream crest of the outlet key (red arrows) collides with the flow from the lateral crest (yellow arrows) and forms a diagonal thicker stream from the corner of the outlet key towards the centre of the outlet key (orange arrows) where it collides with the thicker stream from the opposite corner. As the discharge increases this collision point moves further upstream. A standing wave forms where these two thicker streams meet in the centre of the outlet key. The nappe from the lateral crest splits direction as it connects with the sloped base of the outlet key. Half the discharge from the nappe is directed to the lateral wall (blue arrows), forming a pronounced and aerated stream in the corner of the outlet key base and lateral wall. It is presumed that air is entrained into the stream from the air cavity behind the nappe. The other half is directed towards the centre of the outlet key (green arrows), further contributing to the thicker stream and standing wave.

At higher flows the nappes of the adjacent lateral crests will collide, increasing the standing wave size and instability (**Figure 6.12**). The turbulent colliding nappes also entrain sufficient air to replace the air lost from the air cavity behind the nappe. In the case of Model 2, nappe curtains of adjacent sidewalls start to collide at discharges equal to 100 l/s (H/P = 0.11), although the collision only occurs near the base of the PKW. As the discharge increase, the higher the collision point relative to the base of the PKW, the more turbulent and aerated the flow in the outlet key become.

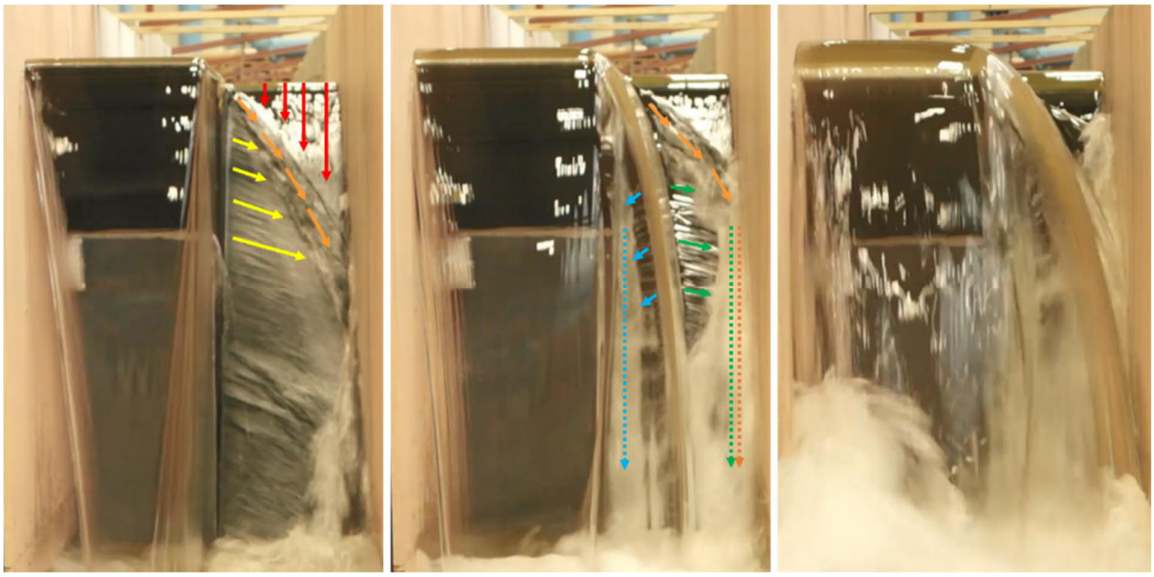

Figure 6.11: Flow development in the outlet key (Model 1)

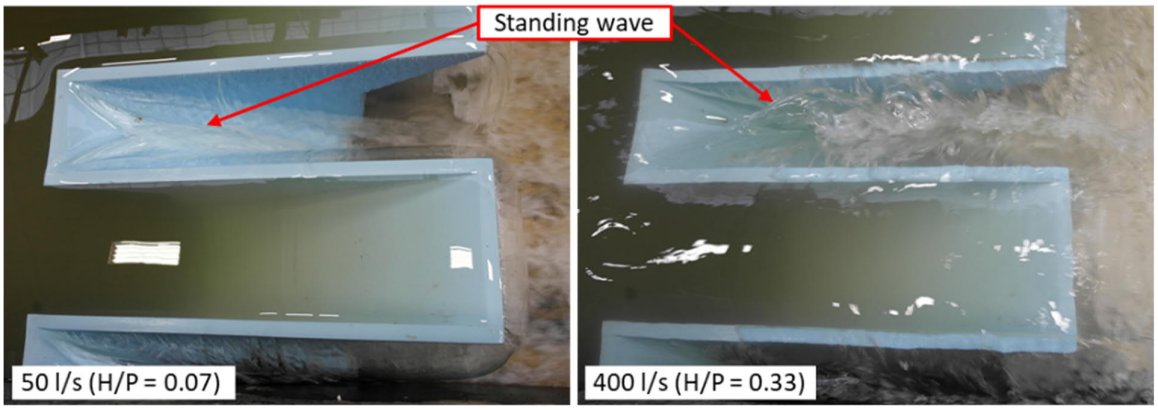

Figure 6.12: Standing wave in outlet key (Model 2)

6.2.4 Lateral sidewall

With reference to **Section 2.3.2**, three typical nappe behaviours are observed for PKWs (clinging, leaping and springing) and can all occur simultaneously at different locations along the lateral crests for a specific flow (Machiels, Erpicum, Dewals, Archambeau, & Pirotton, 2011) (Machiels, Erpicum, Archambeau, Dewals, & Pirotton, 2009). The nappe behaviours along the lateral crest, as well as the air cavity characteristics observed along the lateral crests, are discussed in this sub-section.

A leaping nappe forms along the entire lateral sidewall and downstream crest for discharges equal to 50 l/s (H/P = 0.7) and 100 l/s (H/P = 0.11) in Model 2. The nappe detaches and transitions from leaping to springing along approximately the half of the downstream section of the lateral crest for discharges higher than 100 l/s (H/P > 0.11). This is in line with the findings of Machiels *et al.* (2009) (2011) and Karbiri-Samani & Javaheri (2012). The position

where the transition takes place continuously moves up and down over a short distance along the length of the sidewall. The higher the discharge, the further upstream along the length of the sidewall the transition takes place and the more the transition position fluctuates. It was noted that the transition between leaping and springing took place further upstream along the sidewall of the outlet key closest to the flume wall compared to others. The difference in the nappe behaviour between the keys or sidewalls is likely due to a small misalignment and orientation of the model relative to the flume. However, the effect on the overall behaviour of the PKW can be considered negligible. Based on visual inspection from the top, it appeared that the nappe springs free from the downstream crest for discharges higher than 300 l/s (H/P = 0.25). The nappe transition from leaping to springing is shown in **Figure 6.13**.

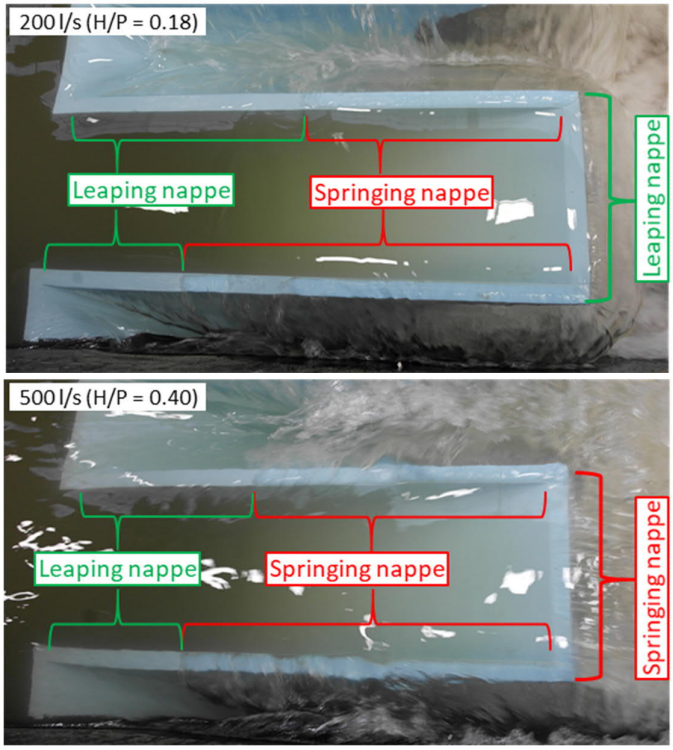

Figure 6.13: Nappe transitions from leaping to springing (Model 2)

Visually, artificially aerating the nappe cavity had no effect on the range of flows during which the transition from a leaping to a springing takes place, the position that the transition takes place or the fluctuation of the transition position.

The air cavity behind the nappe along the sidewalls forms a tapered or conical shape due to the increase in fall height in the downstream direction (**Figure 6.14**). The tip of this conical shape originates from the upstream corner edge of the outlet key and remains stable for most of the discharges tested in both models. However, for discharges equal to or larger than 500 l/s (H/P ≥ 0.4) in Model 2, the tip detaches from the corner edge and fluctuates further downstream along the outlet key sidewall. Although not tested in this study, Denys (2019)

observed that the cavity tip moves downstream and then rapidly upstream for discharges equal to 600 l/s and higher (H/P = 0.5). This occurred randomly at no set time intervals.

In some scenarios, the tip of the air cavity at the sidewall of the half outlet key attached to the flume wall detaches and moves downstream at lower discharges compared to the other sidewall cavities (**Figure 6.15**). For discharges 200 l/s (H/P = 0.18) and up with tail water levels increased to 200 mm and higher, the tip of the conical shape also moves slightly downstream, more so for the nappe over the sidewall closest to the flume wall compared to others. For discharges 200 l/s (H/P = 0.18) and higher, with tail water levels increased to 400 mm, and no air cavity formed along the sidewall due to the submergence of the outlet key.

Figure 6.14: Conical air cavity behind the nappe along the sidewall

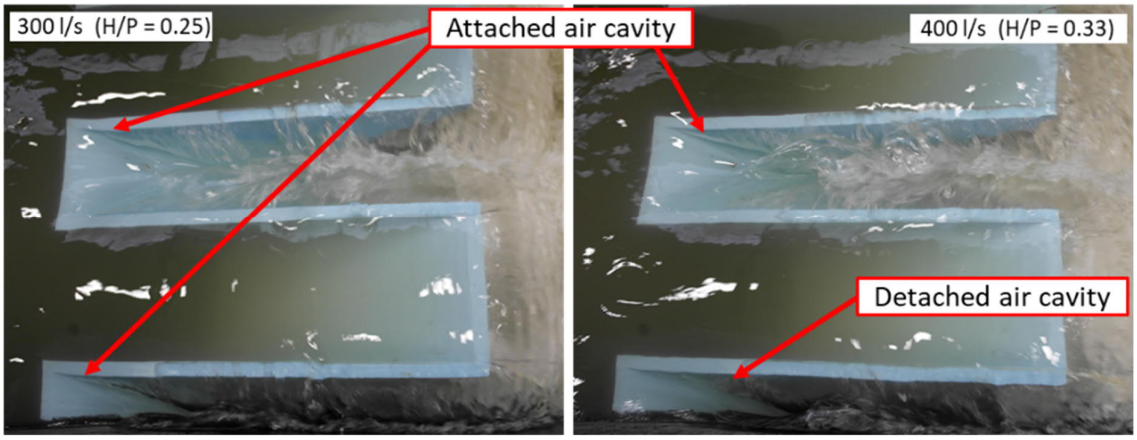

Figure 6.15: Conical air cavity tip at different positions (Model 2)

In the case of Model 2, the nappe remains completely attached to the upstream crest of the outlet key for all discharges and aeration conditions evaluated. For Model 1, however, the nappe transitioned from clinging to springing for discharges larger than 100 l/s (H/P > 0.075) – refer to **Figure 6.16**. The air cavity was also conical in shape along the width of the outlet key and extends further to the centre of the key for higher discharges. The tip remained attached to the corner edge of the outlet key for all flows observed, whereas the position of

the wider end fluctuated. Artificial aeration had no visible effect on the occurrence or vorticity of the springing nappe. It is assumed that air was entrained from the standing wave colliding with the flow guide wall.

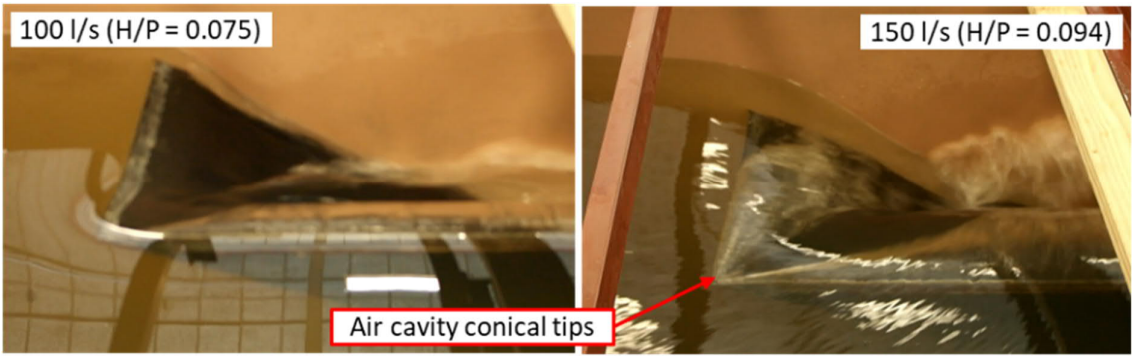

Figure 6.16: Upstream outlet key crest nappe (Model 1)

Periodic swirls of flow over the lateral crests were also observed in both models and are discussed in more detail in **Section 6.6.1**.

The pressure fluctuations experienced in the conical air cavity along the sidewalls are discussed in more detail in **Section 6.4.2.**

6.2.5 Downstream

A highly aerated hydraulic jump forms directly below the inlet key overhang where the nappe from the downstream crest impacts the downstream apron (refer to **Figure 6.7**). As the nappe over the inlet key crest impacts the downstream apron, some flow is directed to the centre of the air cavity behind the nappe (**Figure 6.17 a**). The two outlet key flow streams on either side of the inlet key drew toward the centre below the inlet key overhang and collided with the flow underneath the nappe (**Figure 6.17 b**), causing swirls of flow before being carried downstream. The aeration and the wave increased with discharge.

It is assumed that the hydraulic jump entrains air from the air cavity behind the nappe and causes a reduction in the volume of the air cavity, and as such the air pressure (Chanson, 1994). The air taken from the air cavity and discharged downstream is thought to be replaced by the air entrained from the atmosphere through the colliding nappes in the outlet key (Machiels, 2012). For low flows (H/P ≤ 0.11), the adjacent nappes do not collide and can thus explain why the nappes in these cases appear to be drawn in and the air pressures behind the nappe is much lower (**Section 6.4**).

(a) (b)

Figure 6.17: Hydraulic jump downstream of inlet key overhang

6.3 AIR DEMAND

The majority of the PKWs installed to date have aeration pipes underneath the downstream overhang that connect the air cavity behind the nappe to atmospheric pressure. It is believed that artificial aeration of the overflow nappe improves flow characteristics and stability (Laugier, Vermeulen, & Lefebvre, 2013). However, the sizing of the aeration pipes and the actual influence of artificially aerating the nappe have not received much attention. As part of this study, three aeration conditions were tested; no artificial aeration, aeration through a small diameter pipe and aeration through a larger diameter pipe below the inlet key downstream overhang. The measured air velocity and evaluated air demand through the different sizes of aeration pipes are discussed in this section.

Figure 6.18 shows the air velocity through the different sizes of aeration pipes and models. The air velocity through the aeration pipes is similar for corresponding H/P values, irrespective of the model and pipe size. In the case of the 19 mm diameter aeration pipe of Model 2, the air velocity readings were significantly affected by the relatively large size of the anemometer sensing probe compared to the area of the aeration pipe. This caused inaccurate readings and the related airflow data were therefore discarded.

Figure 6.19 to **Figure 6.21** display the air demand underneath the nappe as a percentage of the discharge for different discharges and aeration pipe sizes.

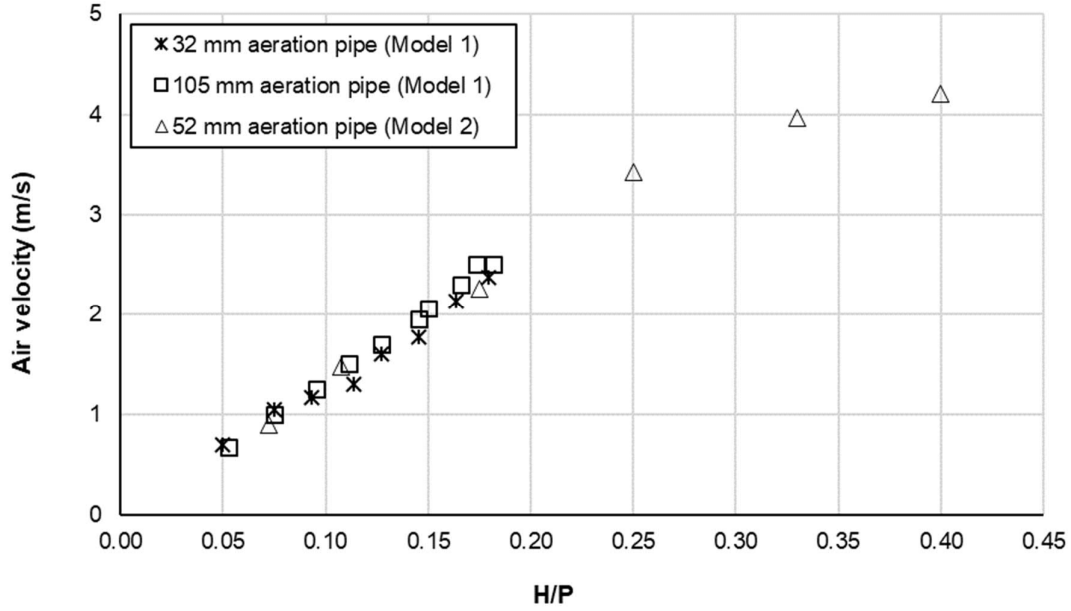

Figure 6.18: Measured air velocity through aeration pipes

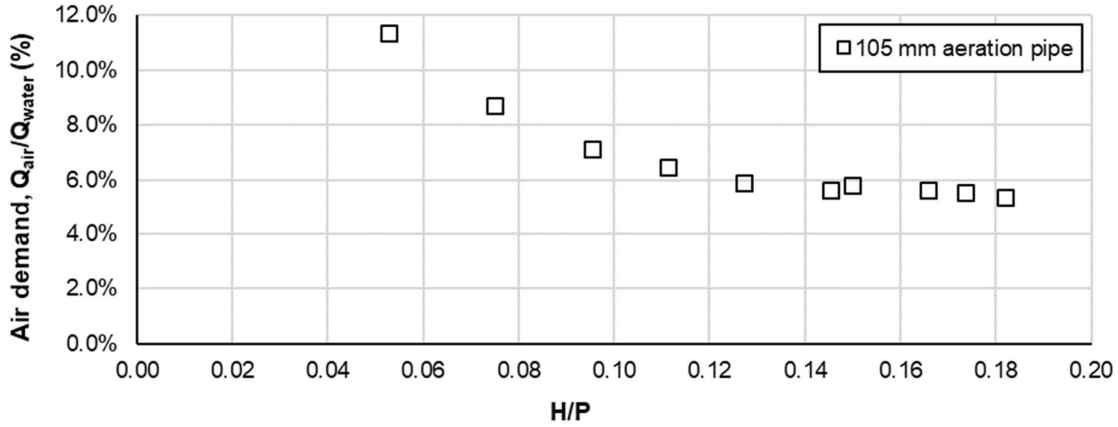

Figure 6.19: Measured air demand as a percentage of discharge (105 mm diameter aeration pipe – Model 1)

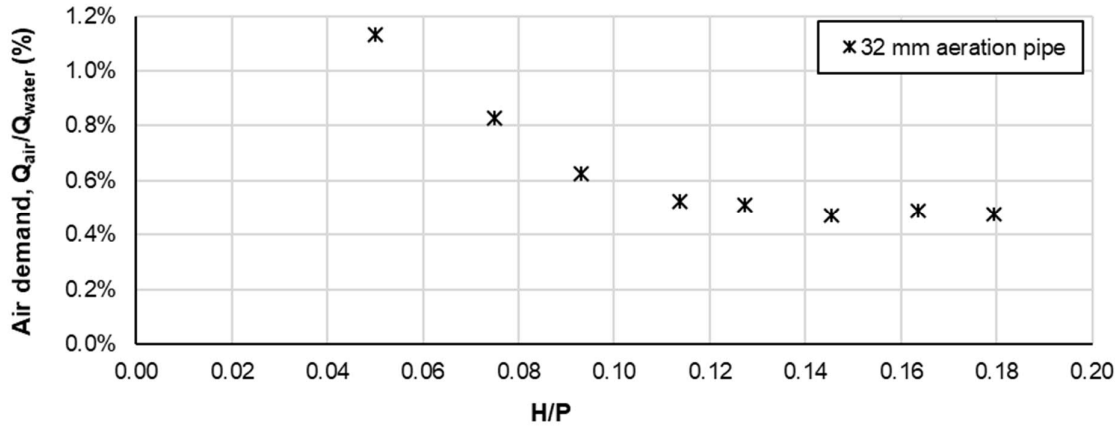

Figure 6.20: Measured air demand as a percentage of discharge (32 mm diameter aeration pipe – Model 1)

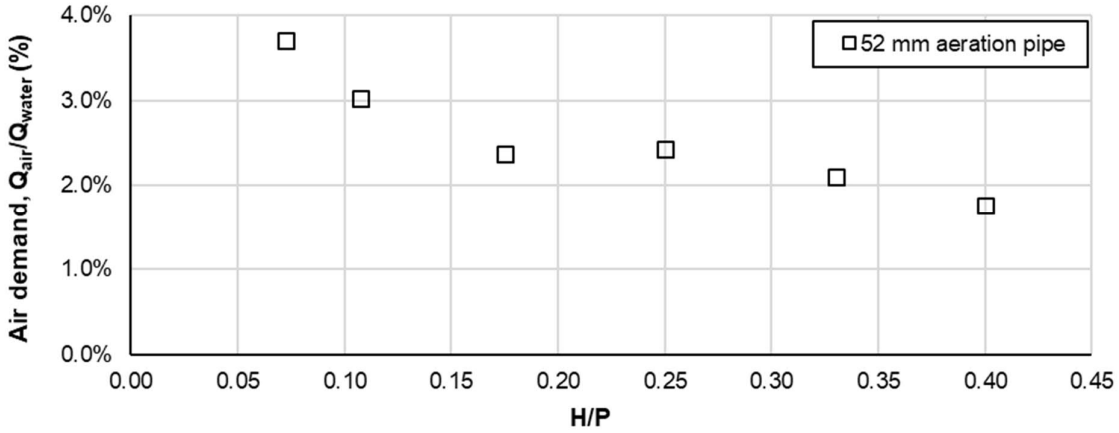

Figure 6.21: Measured air demand as a percentage of discharge (52 mm diameter aeration pipe – Model 2)

In all cases, the air demand decreases with an increase in discharge but appears to stabilise at a constant demand for H/P > 0.10. The decrease in air demand from the aeration pipes as the flow increases can be attributed to the natural aeration that occurs as a result of the air entrainment via the turbulent colliding nappes from adjacent lateral crests. It is presumed that most of the air lost from the air cavity to sustain the hydraulic jump downstream of the PKW is replaced by the air entrained through the colliding nappes and not the aeration pipes – hence the stabilisation in the air demand. This trend of the air demand decreasing and then stabilising at larger discharges is similar to that observed in the actual measured data of Malarce Dam PKW (Vermeulen, *et al.*, 2017a).

Of note is that the amount of air entrained through the aeration pipes, as a percentage of the total discharge, is directly related to the size of the aeration pipe, irrespective of the model or scale. The air demand for any given H/P value between any two aeration pipe sizes is almost directly proportional to the ratio of the cross-sectional area of the aeration pipes, i.e. for an H/P value of 0.08, the air demand through the 105 mm diameter pipe is 9.5% more than through the 32 mm diameter pipe and the area of the 105 mm diameter pipe is 9.3% more than for the 32 mm diameter. This occurrence can be attributed to the fact that air entrainment and bubble generation cannot be scaled. Generally, the air-water interface is more stable for large scale factors, resulting in less air demand and reduced air pressures.

6.4 NAPPE AIR CAVITY PRESSURES AND NAPPE OSCILLATIONS

Nappe oscillations are a type of FIV that can potentially result in resonant vibration of thin walled hydraulic elements, such as the sidewall of a PKW. Nappe oscillations occur when pressures in the air cavity behind the nappe become unstable and start to fluctuate, causing the nappe beat or oscillate (Crookston & Tullis, 2013) (Anderson, 2014). Experimental studies

have shown that although the air cavity behind the nappe only serves as an amplification and stabiliser factor, air is required to induce nappe vibrations (Binnie, 1971) (Lodomez, *et al.*, 2018a).

Previous PKW model studies observed that dynamic pressures behind the nappe resulted in vibrations in the model structure. These vibrations disappeared when the nappe was aerated artificially (Leite Ribeiro, *et al.*, 2007). On the other hand studies by Crookston & Tullis (2011) (2013) concluded that although artificial aeration may have a reducing effect on the nappe instability, it does not necessarily prevent vibrations from occurring.

The objectives of this study were to determine if nappe oscillations occur for the discharge rates considered, if they have any significant effect on the vibration of the PKW itself and what the effect of artificially aerating the air cavity behind the nappe has on the said oscillations or vibrations. This section presents the findings of the dynamic air pressure analysis for the different discharges and aeration scenarios considered.

The pressures behind the nappe were recorded using pressure sensors below the inlet key downstream overhangs in both models and in the case of Model 2 along the downstream face of the sidewall at three positions (refer to **Section 5.4.5**). Pressures were recorded at a frequency of 1000 Hz for a duration of at least 120 seconds in both models. In the case of Model 2, pressures were recorded simultaneously at all five sensors for cross-correlation purposes.

Note that the pressures presented in this chapter are relative pressures and not absolute pressures due to the pressure sensor installation and limitations as discussed in Section **5.4.5 and 5.6**. Therefore, it is possible that some negative pressures were recorded, however, the measurement methodology did not allow for accurate representation of negative pressures. The pressure fluctuations and fluctuation magnitudes are valid.

6.4.1 Inlet key overhang pressures

A continuous nappe curtain forms over the downstream inlet key and sidewall crests for all discharges and models considered. For both Model 1 and Model 2 pressure sensors were installed below the downstream inlet key overhang close to the aeration pipe opening. In the case of Model 1, the pressure transducer was installed directly into the downstream flow guide wall (**Figure 5.5**). In the case of Model 2, two pressure transducers were each connected to a plastic tube with its other opening installed below the downstream overhang – refer to **Figure 5.18**.

In both models, the pressure sensors mostly picked up the air pressure fluctuations in the air pocket behind the nappe, as well as sound waves generated by the falling nappe. The

pressure sensors came into contact with water only during limited scenarios in this study, e.g. during increased tail water level scenarios.

a) Model 1

Figure 6.22 shows the air pressure (in Pascal) recorded for a five second interval behind the overflow nappe in Model 1 for different discharges ranging from 50 l/s (H/P = 0.05) to 400 l/s (H/P = 0.18). “Q300”, for example, refers to a discharge of 300 l/s in the model. The figure also shows the difference in air pressures with and without the introduction of air behind the nappe via the 105 mm diameter aeration pipe installed below the inlet key downstream overhang.

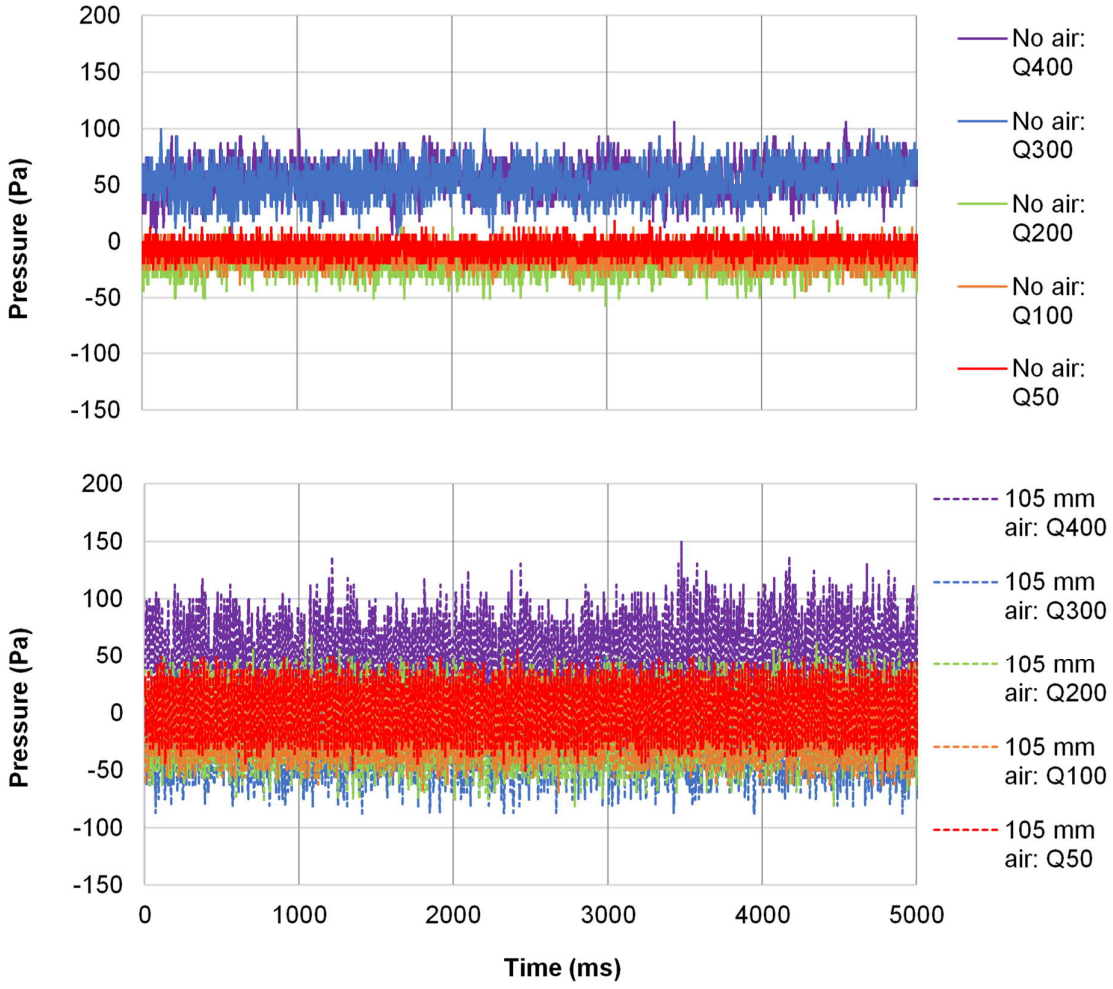

Figure 6.22: Measured time variant air cavity pressure below inlet key overhang with and without artificial aeration (Model 1)

For unaerated conditions and for discharges lower than 300 l/s (H/P = 0.144) the relative pressure behind the nappe seems to be lower, and even slightly sub-atmospheric, compared to higher discharges. For higher discharges (300 l/s and 400 l/s) the air pressure is also more

variable, although only very slightly. It appears that the air pressure varies around 0 Pa, or the atmospheric air pressure, for most discharges with the introduction of air via the aeration pipe behind the nappe.

The range over which the pressures fluctuate increase with the introduction of air into the nappe air cavity for all discharge ranges as illustrated in in more detail in **Figure 6.23** for discharges equal to 50 l/s and 400 l/s. The coloured time series lines show the scenarios without artificial aeration and the black dotted lines show the scenario with artificial aeration. The figure also highlights that the pressure increases with an increase in discharge, although only very slightly.

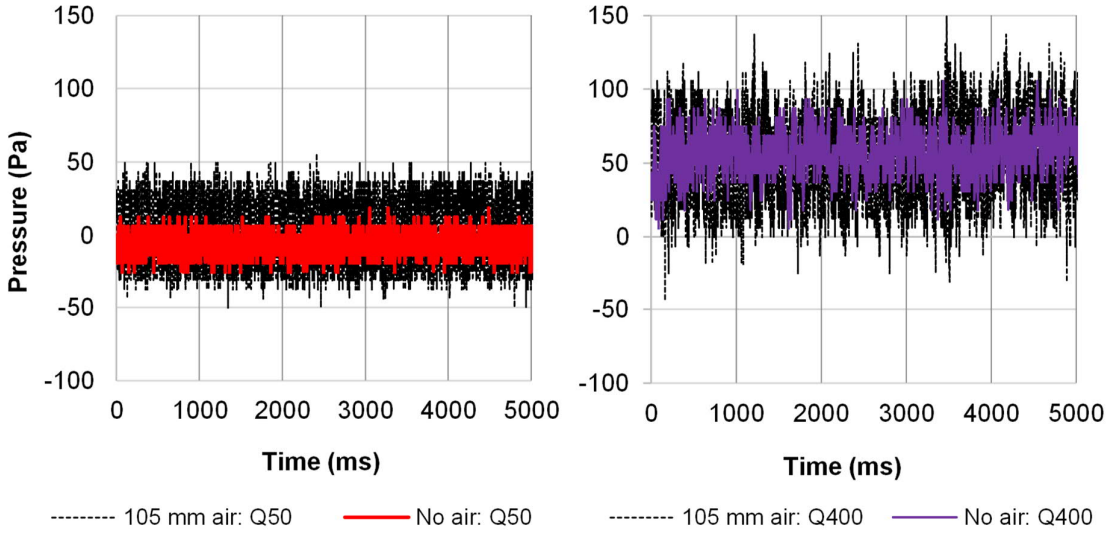

Figure 6.23: Measured time sequence effect of aeration on air cavity pressure below inlet key overhang with and without artificial aeration (Model 1)

The lack of noticeable large sub-atmospheric pressures in **Figure 6.22** and **Figure 6.23** supports the findings of previous studies claiming that PKWs are naturally self-aerating (ICOLD Technical Committee on Hydraulics for Dams, 2016).

The fluctuation in the air pressure over the discharge range is too low (only a few Pascals) to consider it as being caused by FIVs or nappe oscillations as such. There are no horizontal bands, waves or ripples visible in the nappe curtain, or intense acoustic pressure waves, which are both characteristics of nappe oscillations. The variation in air pressure behind the nappe could be a result of the increased turbulence present in the water body as it passed over the PKW and due to the continuous exchange of air through the colliding nappes from the sidewalls and impact with the downstream apron (refer to **Section 6.2**). The pressure fluctuations could also be a result of the vortices from the inlet key upstream overhang that are shed over the sidewall as later discussed in **Section 6.4.2**.

Nonetheless, the pressure analysis revealed that the air pressures behind the nappe do vary and can potentially contribute the excitation and ultimately the vibration of the PKW structure itself. The time variant pressure data for a given scenario was converted from the time domain to the frequency domain by using FFT and plotting the spectral density. This allowed the frequencies at which the pressure fluctuation occurred to be identified.

Figure 6.24 and **Figure 6.25** provide the PSD graphs for the air pressure fluctuation behind the overflow nappe of Model 1 for unaerated and aerated conditions respectively. The highest or most identifiable frequency peak, as well as other highest peaks visible in the PSD, are summarised in **Table 6.2** for each of the discharge and aeration scenarios. Note that not all peak frequencies are evident in all discharge and aeration scenarios. Peak frequencies are identified by wider peak frequency signals and not by a single sharp signal point.

The sharp high peak at 50 Hz and at other intervals of 50 Hz can be attributed to interference from the electrical grid. Other noticeable peaks at higher frequencies (> 45 Hz) are either harmonics of the initial peak frequencies tabulated in **Table 6.2** or from other unrelated interferences from the surrounding during the data capturing. These unrelated frequencies were identified by producing the PSD for the scenario where there was no water in the flume.

The peak frequency at which the nappe, or rather the air pressure behind the nappe, fluctuates remains in the same range for all flows tested, although the air pressure fluctuates at slightly lower frequencies as the discharge increases. The strength of the fluctuations can be characterised by the area under the PSD graphs. The strength of the fluctuations increases as the discharge increases, with the highest incremental increase occurring between lower discharges. It should be noted that these strength increases are small.

Through comparing **Figure 6.24** and **Figure 6.25** it is evident that the introduction of air behind the nappe has a negligible effect on the frequency, as well as intensity, at which the air pressure varies. This is further illustrated in more detail in **Figure 6.26**. The direct comparison of the PSD of the aerated scenario with that of the unaerated scenario for the same discharge reveals that the peak frequencies are similar in both aeration scenarios. This is true for both low and higher discharges simulated in Model 1. With reference to the 50 l/s discharge scenario shown in **Figure 6.26**, as well as **Figure 6.23** earlier, the strength of the pressure fluctuations for aerated conditions seems to be slightly higher than that for unaerated conditions.

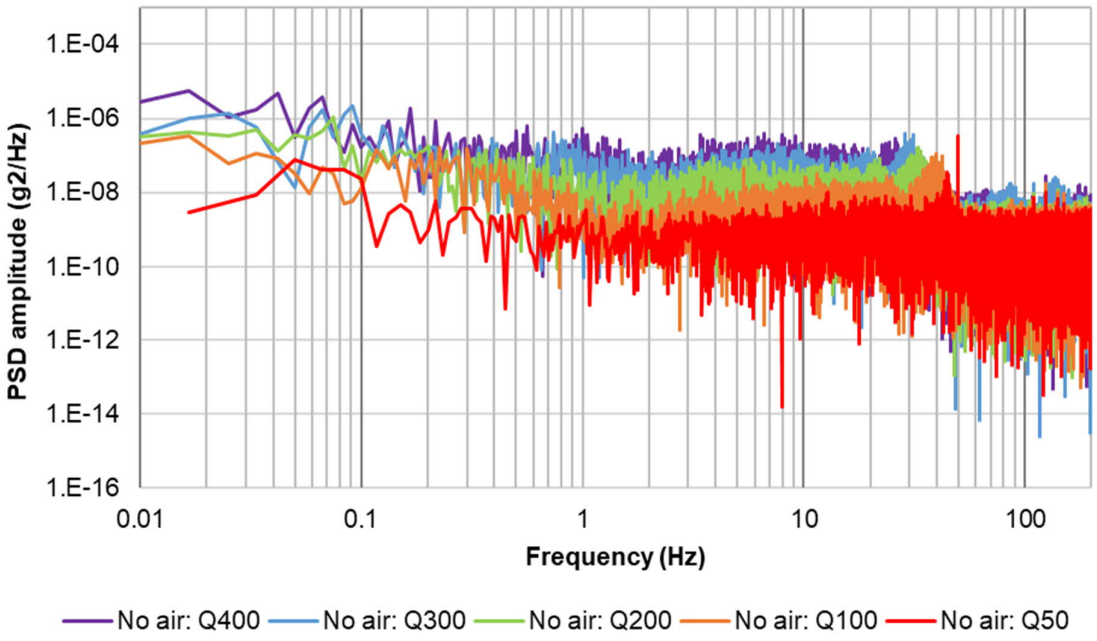

Figure 6.24: Measured air pressure PSD for unaerated conditions (Model 1)

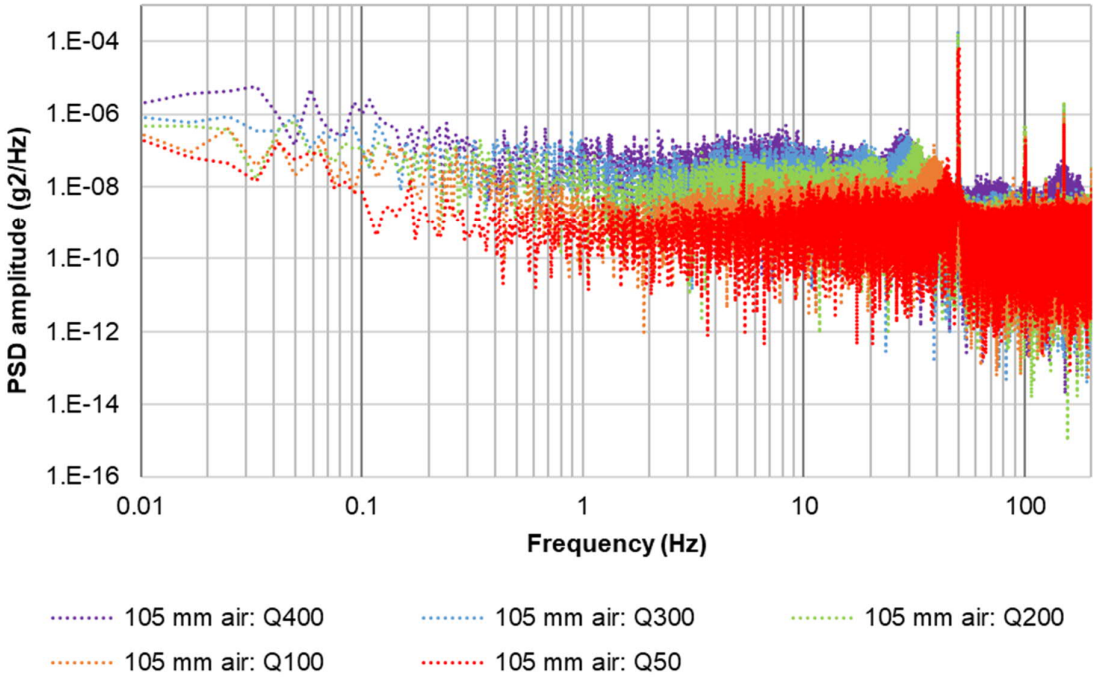

Figure 6.25: Measured air pressure PSD for aerated conditions (Model 1)

Table 6.2: Measured air pressure frequency peaks behind the nappe for Model 1

Discharge (l/s)	Aeration	Peak (Hz)	Other peaks (Hz)				
50	No air	44.7	1.0	5.6	12.8	17.0	-
	105 mm aeration pipe	44.6	1.3	5.3	10.6	16.9	-
100	No air	39.3	1.6	5.2	11.3	-	88
	105 mm aeration pipe	39.1	1.3	5.3	11.7	-	87
150	No air	30	1.4	3.8	-	-	38
	105 mm aeration pipe	35.7	1.1	4.8	-	22.6	-
200	No air	33.0	-	4.2	-	21.9	84.0
	105 mm aeration pipe	32.9	1.2	5.4	-	20.3	83.9
250	No air	27.0	1.2	2.3	-	17.3	84.0
	105 mm aeration pipe	30.9	1.2	4.52	-	19.3	83.3
300	No air	31.0	0.75	5.6	12.0	18.2	85
	105 mm aeration pipe	29.1	0.9	4.3	12.3	18.5	84
350	No air	25.6	0.9	4.0	9.5	18.6	-
	105 mm aeration pipe	28.2	1.1	4.5	9.6	18.5	-
400	No air	27.2	1.0	6.6		17.2	-
	105 mm aeration pipe	27.7	1.1	5.7	9.3	18.2	-

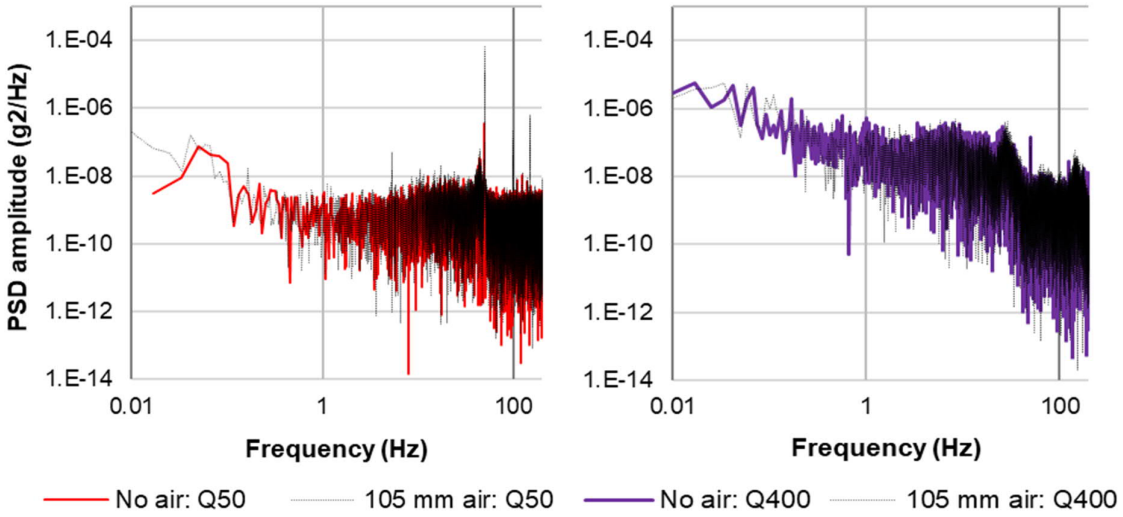

Figure 6.26: Comparison of measured air pressure PSD with and without aeration (Model 1)

b) Model 2

The air pressure signals (in Pascal) below the inlet key overhang of Model 2 for different discharges are shown in **Figure 6.27** over a ten second interval. The pressure fluctuations in

Model 2 appear to be more variable compared to those measured in Model 1. However, it should be noted that the H/P value for a specific discharge differs for the two models. For example, 400 l/s in Model 1 has an H/P value of 0.18, corresponding to a discharge of 200 l/s in Model 2. Similar to the observations in Model 1, the pressures become increasingly more variable with an increase in discharge, especially for discharges higher than 200 l/s (H/P > 0.18).

The pressure spike in 200 l/s unaerated scenario visible in **Figure 6.27** can be attributed to a water drop that has potentially splashed onto the pressure sensor tube opening. The effect of the presumed water drop on the spectral density analysis of the under nappe pressures are negligible. Data sequences with and without the pressure spike included had similar peak frequencies.

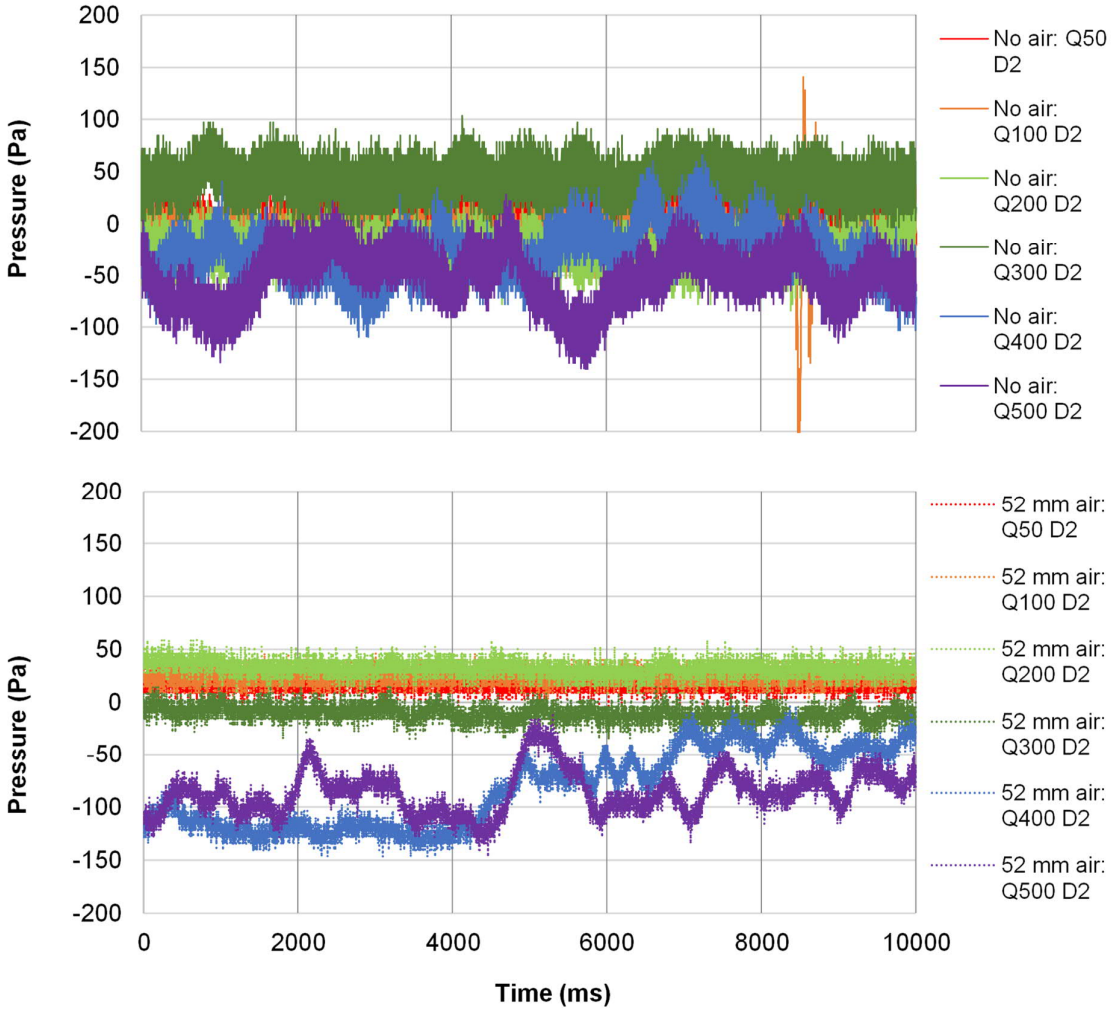

Figure 6.27: Measured time variant air cavity pressure at D2 with and without artificial aeration (Model 2)

Lower and potentially sub-atmospheric pressures develop for higher flows as the air cavity behind the nappe becomes isolated. This is in line with the findings of Phillips & Lesleighter (2013) and Mehboudi, Attari, & Hosseini (2017). The pressure fluctuations observed for discharges higher than 400 l/s (H/P = 0.33) can be attributed to the higher turbulence in the water body itself, the fluctuation of the conical air cavity tip along the sidewall, or alternatively nappe disturbances caused by the shed vortices from upstream (discussed in **Section 6.2.4** and **6.4.2**).

Contrary to what was observed in Model 1 (**Figure 6.23**), the instantaneous range of the pressure fluctuations reduce with the introduction of air in Model 2 - note that the "band width" of the pressure fluctuations is thinner under aerated conditions in **Figure 6.27**. However, aeration seems to have no damping effect on the occurrence of the fluctuations itself for discharges equal or higher than 400 l/s.

As can be observed in **Figure 6.27**, the mean air pressure slightly reduces with the introduction of air via the 52 mm aeration pipes installed under the inlet key overhangs for the two complete inlet keys. If the presented figures and pressure measurements can be considered as referenced pressures, the air pressure reduces to atmospheric with the introduction of air into the air cavity. This is typically what is expected by artificially aerating the air pocket behind a nappe.

Figure 6.28 provides the air pressure PSD of the unaerated conditions for the different discharges simulated in Model 2. For unaerated conditions, the pressure directly below the inlet key overhang fluctuates at two main frequency ranges – the first between 1.3 and 1.6 Hz, and the second between 6.5 and 10.0 Hz. There is no clear trend between the frequencies within these ranges and the different discharge capacities, except for, as observed in the Model 1 pressure fluctuation results, the increase in the strength or intensity of the frequency as the discharge increase. However, this is only valid for the first frequency range (1.3 to 1.6 Hz). The increase in the frequency strength can be attributed to the increased turbulence at higher discharges and does not appear to be a result of nappe FIV oscillations.

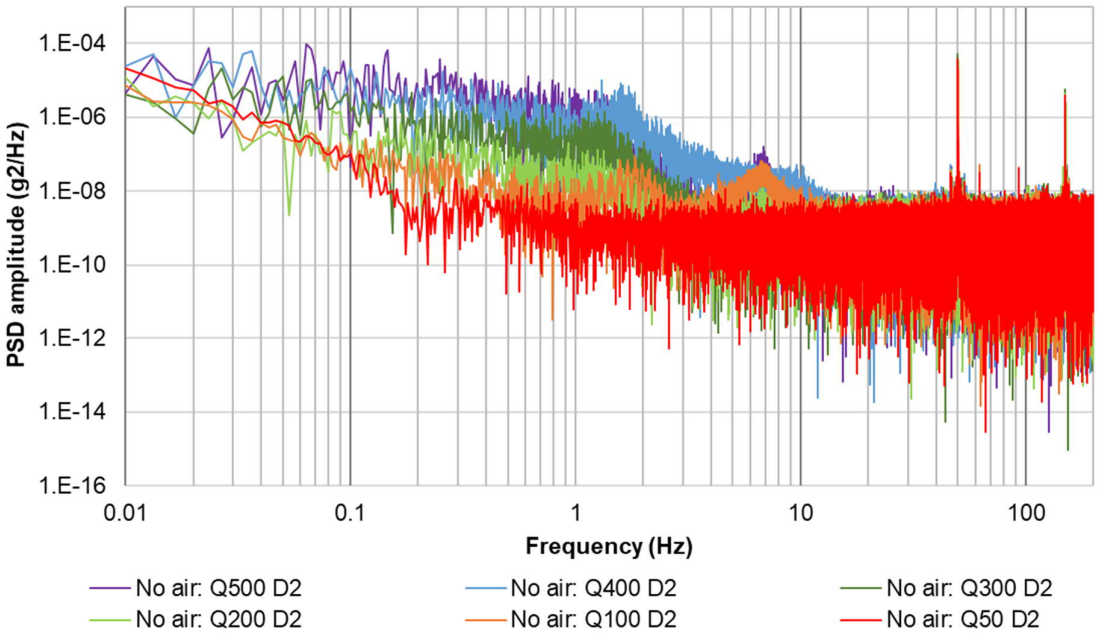

Figure 6.28: Measured air pressure PSD directly under the inlet key overhang for unaerated conditions (Model 2)

Again, as with the Model 1 pressure PSD results, the peaks at 50 Hz or intervals thereof are due to interference from the electrical grid. Also, of note from **Figure 6.28** is that the lower the discharge, the less distinct the frequency peaks are above the noise bed, especially in the case of the 50 l/s scenario. This corresponds to the time domain graph of the scenario (**Figure 6.27**) where almost no variation in the pressure data is visible.

In **Figure 6.28**, the high peak at 7.0 Hz observed for the 100 l/s discharge (H/P = 0.11) can either be a result of a water drop that fell on the pressure sensor opening during the data capture or relate to the fact that the nappe transforms from leaping to springing within this discharge range.

Figure 6.29 provides the pressure PSD of the aerated condition with the large diameter aeration pipe (52 mm diameter) open, directly below the inlet key overhang and for the different discharges simulated in Model 2. The main peak pressure frequencies for both aerated and unaerated conditions are provided in **Table 6.3**. The higher frequency peaks (> 50 Hz) are either harmonics of the lower frequencies listed in the table or ambient frequencies that were identified from the “no water” scenario.

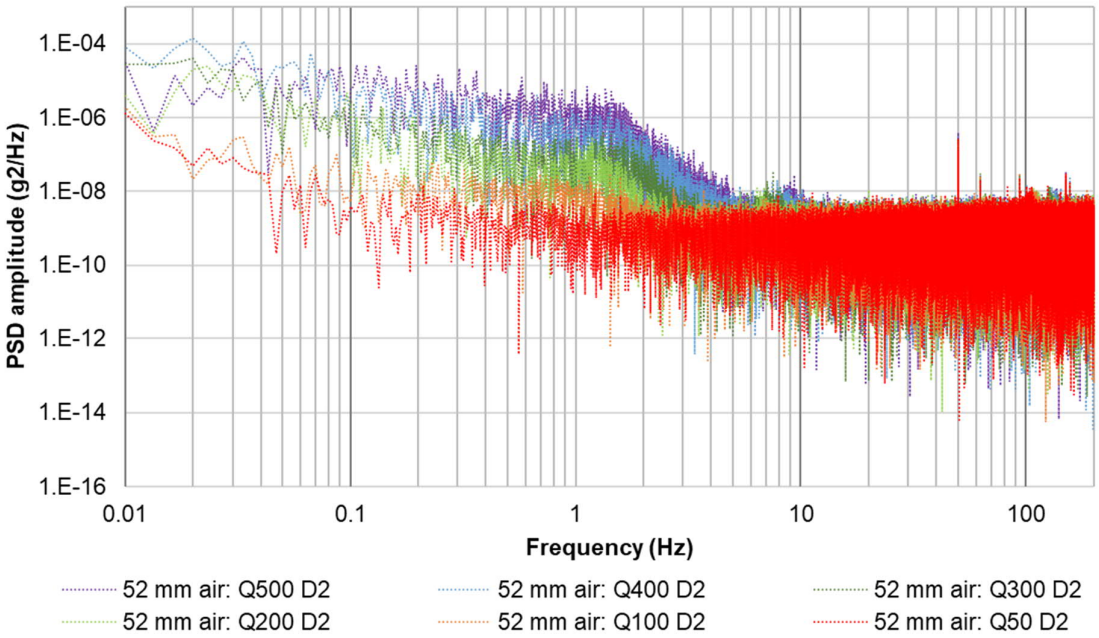

Figure 6.29: Measured air pressure PSD directly under the inlet key overhang for aerated conditions (Model 2)

Table 6.3: Measured air pressure frequency peaks behind the nappe (D2) for Model 2

Discharge (l/s)	Aeration	Peaks (Hz)				
50	No air	0.29	0.60	1.60	4.6	7.12
	52 mm aeration pipe	0.29	0.54	1.57	-	7.90
100	No air	-	0.82	1.85	4.33	6.75
	52 mm aeration pipe	0.25	0.70	1.42	-	6.90
200	No air	-	0.90	1.33	4.33	6.70
	52 mm aeration pipe	0.13	-	1.20	-	6.70
300	No air	0.24	0.70	1.33	-	7.30
	52 mm aeration pipe	-	0.46	1.32	-	7.52
400	No air	0.25	0.45	1.31	-	10.3
	52 mm aeration pipe	0.23	0.67	1.41	-	7.83
500	No air	0.25	0.61	1.22	-	6.80
	52 mm aeration pipe	-	0.57	1.35	-	9.3

As expected, the introduction of air behind the nappe had no significant effect on the air pressure fluctuations. The peak frequencies observed during the unaerated conditions are similar to the peak frequencies observed during aerated conditions. The frequencies at which the air pressure fluctuates appear to be much more stable and within a narrower frequency range compared to those of the unaerated conditions. The increase in the frequency strength

with the increase in discharge is also more distinct for the lower peak frequency range (1.2 to 1.6 Hz). The strength of the higher frequency range peaks (6.0 to 9.0 Hz) is much lower than the first frequency peak range for aerated conditions. At lower discharges (up to 300 l/s or H/P =0.25), the frequency peaks at 7 to 8 Hz and for higher discharges at 9 Hz.

c) Comparison between models

There is some correspondence between the air pressure fluctuation peak frequencies occurring in the two physical hydraulic models when upscaled to prototype frequencies, although it should be kept in mind that the two models do not have exactly the same prototype geometrical dimensions. Discharges of 100 l/s, 200 l/s and 400 l/s in Model 1 correspond to discharges of 50 l/s, 100 l/s and 200 l/s in Model 2 respectively in terms of H/P ratio. **Table 6.4** provides a comparison of the peak frequencies when scaled from the one model to the other.

Table 6.4: Comparison of Model 1 and Model 2 measured frequencies below the inlet key overhang

H/P ratio	Discharge		Peaks (Hz)					
	Model 1	Model 2	Measured in Model 1	Scaled to Model 2	Measured in Model 2	Scaled to Model 1	Measured in Model 2	Scaled to Model 1
0.075	100	50	39	65	1.6	1.0	7.1	4.3
0.11	200	100	33	55	1.85	1.1	6.8	4.2
0.18	400	200	27	46	1.3	0.8	6.7	4.0

The high peak frequencies between 46 and 65 Hz that should occur in Model 2 from the scaled peak frequencies of Model 1 are visible in the PSD graphs but are not very distinct. The two peak frequency ranges of Model 2 correspond to some of the lower peak frequencies observed in Model 1. Although it seems that there is some comparison, it should be noted that air entrainment and subsequent air pressure data cannot be adequately scaled using normal similitude laws, as they are not driven by gravity and inertia only (**Section 5.3.3**).

The air pressure fluctuations under the inlet key overhang only range over a few Pascals and are unlikely to amplify other FIV and cause vibrations in the PKW structure itself. Nonetheless, cognisance of these pressure fluctuations should be taken if they oscillate at the same frequency as the natural frequency of the PKW structure. This phenomenon in discussed in more detail in **Section 6.5**.

6.4.2 Sidewall pressures

A fully established conical shaped air cavity exists along the lateral sidewall behind the overflow nappe. Pressure sensors E1, E2 and E3 were installed along the downstream face of the sidewall in Model 2 to measure the air pressure present under the nappe. The positions of these pressure sensors are shown in **Figure 5.18**. Unfortunately, the model construction material and available pressure transducers did not allow the pressures along the sidewall to be monitored in Model 1.

The pressure sensors (transducer and plastic tube) are most efficient when completely submerged in water. However, for the discharge range tested as part of this study, the pressure sensor plastic tube openings along the downstream face of the sidewall were mainly exposed to air pressure. Only at the highest discharge (500 l/s or H/P = 0.4) were the sensors exposed to some fluctuation between water and air as the tip of the conical air cavity behind the nappe start to fluctuate (refer to **Section 6.2.4**). Nonetheless, valid pressure data, although not referenced and absolute pressures, could be obtained and evaluated.

Figure 6.30 to **Figure 6.32** show the air pressures (in Pascal) recorded along the downstream face of the sidewall for discharges ranging from 50 l/s to 500 l/s over a five second time interval for both aerated and unaerated conditions.

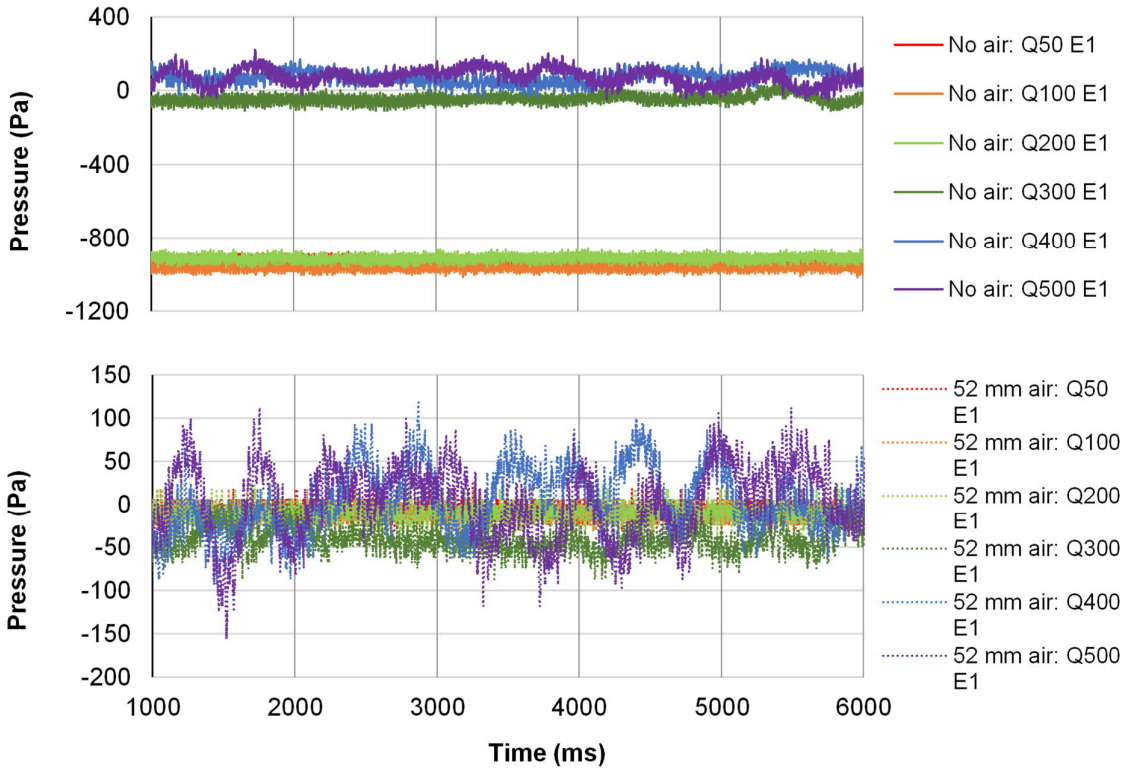

Figure 6.30: Measured time variant air cavity pressure at E1 with and without artificial aeration (Model 2)

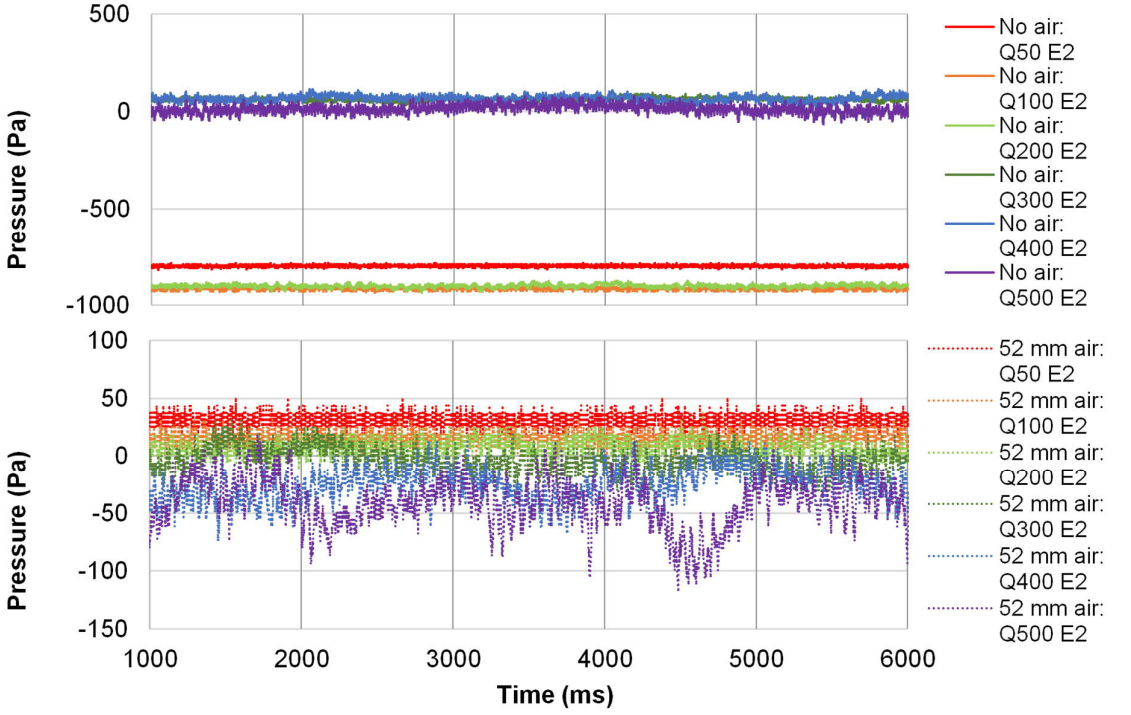

Figure 6.31: Measured time variant air cavity pressure at E2 with and without artificial aeration (Model 2)

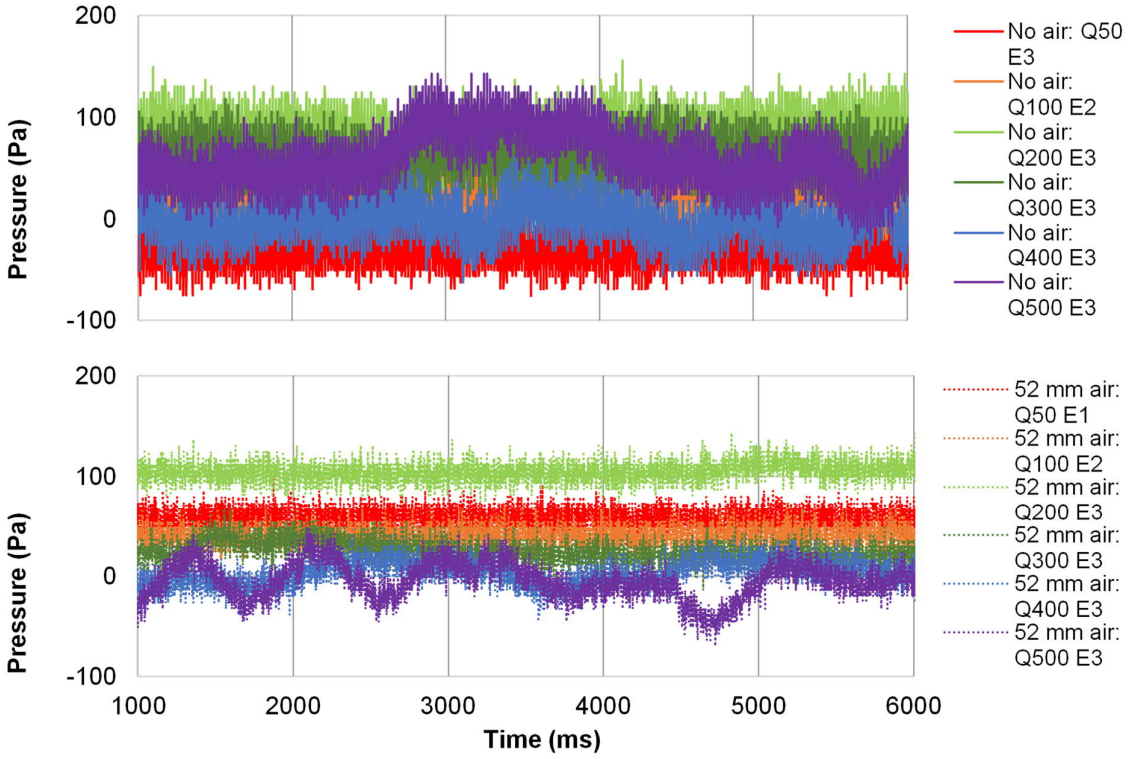

Figure 6.32: Measured time variant air cavity pressure at E3 with and without artificial aeration (Model 2)

With reference to **Figure 6.30** to **Figure 6.32**, it appears that sub-atmospheric conditions develop in the air cavity behind the nappe along the upstream portion of the sidewall for discharges lower than 300 l/s (H/P < 0.25) under unaerated conditions. These presumed sub-atmospheric pressures at sensor E1 and E2 seem to be alleviated with the introduction of air via a 52 mm aeration pipe underneath the inlet key downstream overhang. According Denys (2019) the presumed negative pressures are a result of the interplay between the transverse flow momentum and rotation away from the sidewall crest, and the strong longitudinal flow momentum from the upstream crest of the outlet key. The negative pressures can also be due to the air that is entrained from the cavity to aerate the downstream flow.

The pressure fluctuations for discharges higher than 200 l/s (H/P > 0.18) are illustrated in more detail in **Figure 6.33**. The figure shows the air pressure readings at sensor E1 for unaerated (left) and aerated (right) conditions by means of a 52 mm diameter aeration pipe. Compared to lower discharges, the cavity air pressures for discharges 400 l/s and 500 l/s are higher and seem to be less affected by artificial aeration. The higher pressures for discharges 400 l/s and 500 l/s slightly reduce to atmospheric pressure with the introduction of air but still experience a similar amount of pressure variation. It is also at these discharges where the air demand through the aeration pipes starts to stabilise in the case of Model 2 – refer to **Section 6.3**. It is presumed that at these discharges, the air previously entrained from the air cavity to aerate the downstream flow at lower discharges is replaced by the more turbulent flow from the now colliding nappes from opposite sidewalls and hence the reason for the higher pressures and lesser effect of artificial aeration.

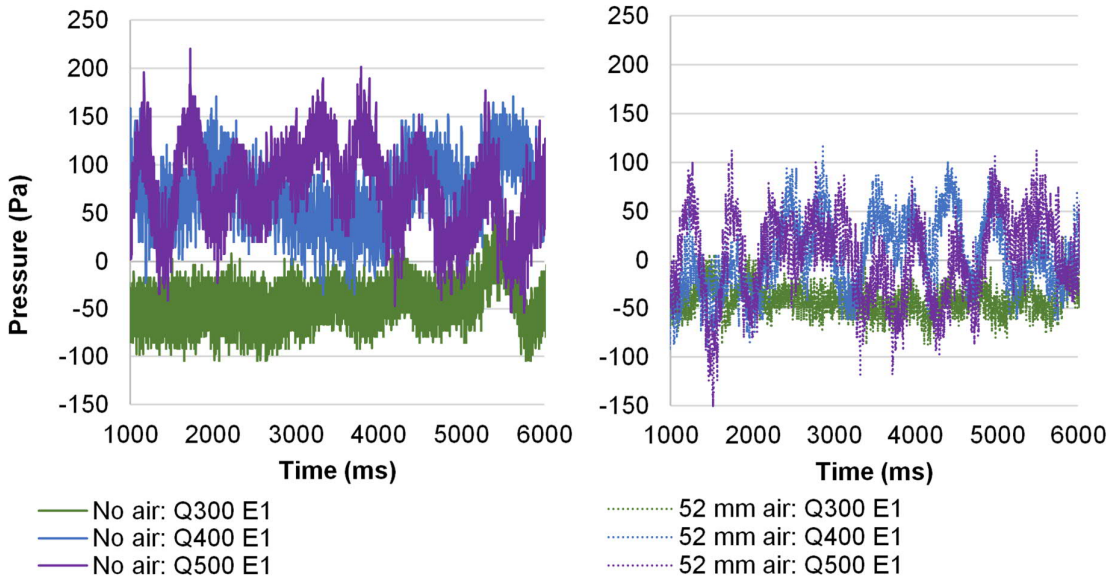

Figure 6.33: Measured time variant air cavity pressure at E1 with and without aeration for high flows

The air pressures measured at sensors E1 and E2 noticeably fluctuate significantly more for discharges 400 l/s (H/P = 0.33) and 500 l/s (H/P = 0.40) compared to other lower discharges. These are also the discharges at which the tip of the conical air cavity along the sidewall visibly starts to detach from the outlet key corner edge, moves slightly downstream and at even higher discharges (500 l/s and up) fluctuates – refer to **Section 6.2.4**. Note that, at the furthest downstream sensor, E3, air pressures are slightly higher compared to E1 and E2 and remain within the same pressure range irrespective of discharge (**Figure 6.32**). Furthermore, the air pressure at E3 does not seem to be significantly affected by the introduction of air behind the nappe, except for the fact the pressure fluctuation amplitude is reduced.

The fluctuations of the conical air cavity tip at high discharges are a result of the continuous air movement in the cavity behind the nappe due to the interplay of forces explained earlier. At higher discharges (500 l/s and up) the longitudinal flow momentum dominates the transverse momentum and push the tip of the cavity downstream. The rotational transverse flow still causes a negative pressure zone along the downstream face of the wall approximately in the same position as the original cavity at lower flows. At random intervals air travels rapidly in an upstream direction to relieve this negative pressure, causing significant infrequent pressure fluctuations (Denys, 2019). These high pressure fluctuations were most notable in the 600 l/s discharge scenario evaluated by Denys (2019).

Although not part of this study, another source of the pressure fluctuations observed at pressure sensors E1 and E2 could be, according to Denys (2019), the vortices that are shed from the separation bubble that form along the edges of the upstream outlet key overhang as flow is directed to the inlet key. As discussed in **Section 6.2.4** and later in **Section 6.6.1** these shed vortices cause noticeable undulations to travel periodically along the sidewall. The nappe curtain thickness extending from the undulation is noticeably different compared to the rest of the nappe curtain. It is explained by Denys (2019) that the rotational energy of these undulations can cause sufficient disturbances to the underside of the nappe so that pressure fluctuations occur. This effect is discussed later in this section.

The E1 sensor is the furthest upstream sensor and experiences the highest pressure variation along the sidewall. The time domain pressure signal data recorded at pressure sensor E1 was converted to the frequency domain by plotting the spectral density of the pressure variation as shown in **Figure 6.34** and **Figure 6.35** for unaerated and aerated conditions respectively for discharges 200 l/s (H/P = 0.18) and higher only. The frequency peaks for 50 l/s and 100 l/s are not very distinct and very little variation in the time sequence pressure data was observed. The peak frequencies for all discharges and both aeration conditions are summarised in **Table 6.5**. The 50 Hz peak frequency or intervals thereof, as well as frequencies larger than 40 Hz, ambient interferences, e.g. the electrical grid.

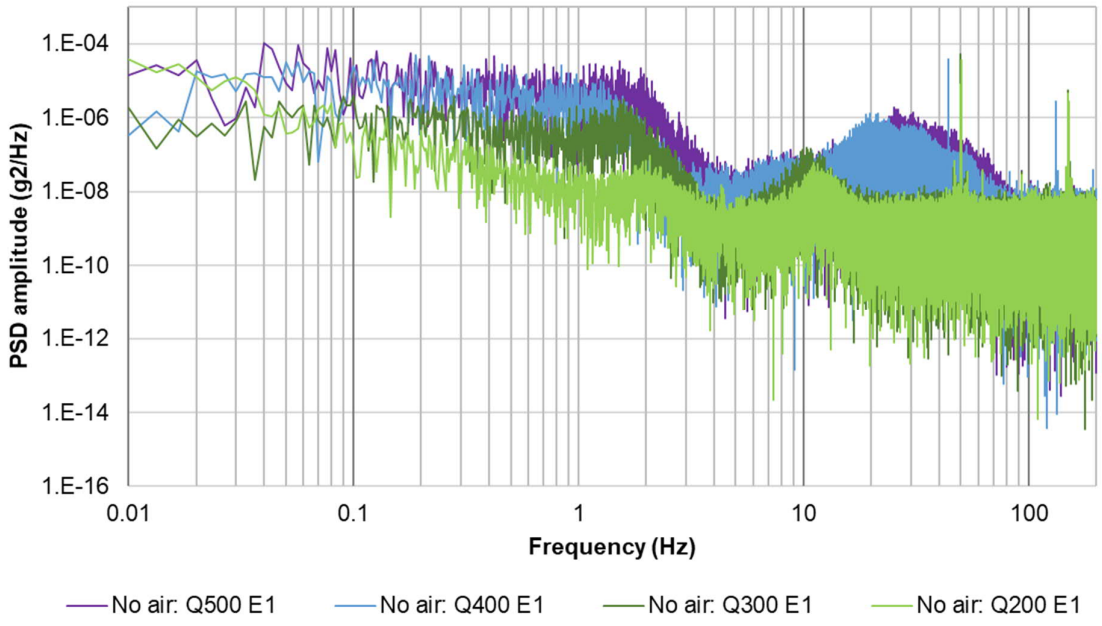

Figure 6.34: Measured air pressure PSD at sensor E1 for unaerated conditions (Model 2)

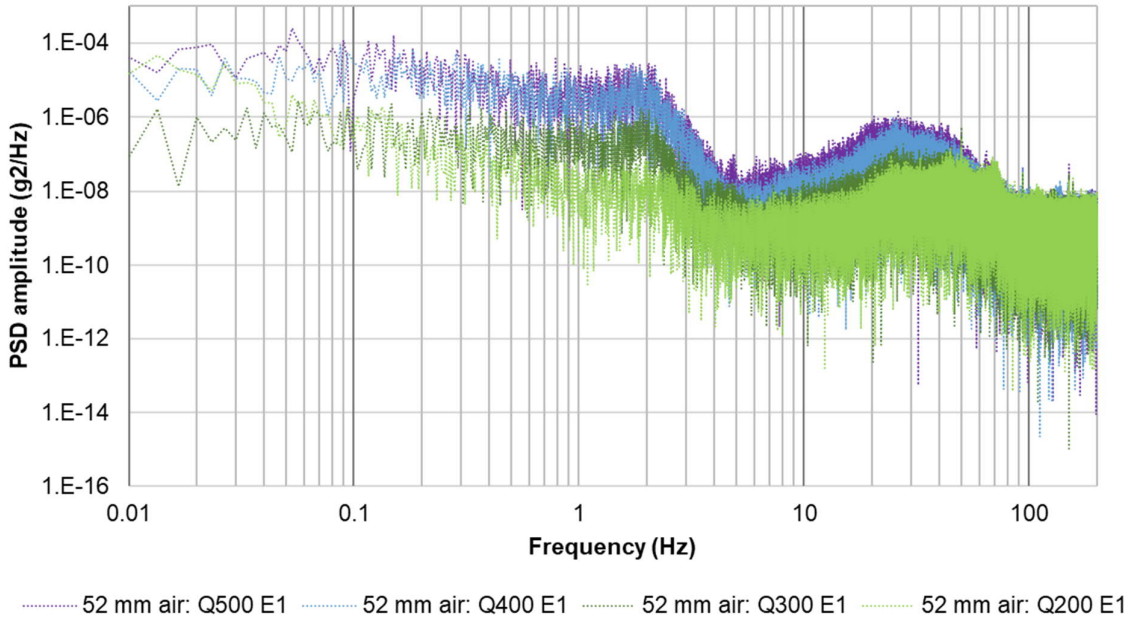

Figure 6.35: Measured air pressure PSD at sensor E1 for aerated conditions (Model 2)

Table 6.5: Measured air pressure frequency peaks behind the nappe (E1) for Model 2

Discharge (l/s)	Aeration	Peaks (Hz)				
50	No air	0.45	**1.98**	-	-	-
	52 mm aeration pipe	-	**1.56**	4.35	12.12	24.46
100	No air	0.69	**2.60**	-	**10.7**	-
	52 mm aeration pipe	0.53	**2.66**	4.54	-	24.55
200	No air	-	**2.08**	4.27	**11.25**	-
	52 mm aeration pipe	0.55	**1.97**	-	9.7	24.5
300	No air	0.62	**1.60**	4.3	**10.3**	-
	52 mm aeration pipe	0.47	**1.87**	4.2	-	**27.8**
400	No air	0.51	**0.94**	4.3	-	**21.5**
	52 mm aeration pipe	0.44	**1.73**	-	9.05	**24.5**
500	No air	-	**1.50**	-	-	**25.7**
	52 mm aeration pipe	0.61	**1.78**	4.88	10.33	**26.22**

The air pressure at pressure sensor E1 fluctuates at two main frequencies. For all discharges without artificial aeration, the first frequency at which the pressure oscillates is in the range of 1.5 Hz to 2.0 Hz. As with the pressures under the downstream overhang, the strength of the first peak frequency increases with an increase in discharge. The second peak oscillation frequency range differs for the discharges simulated without a distinct trend. For discharges 200 l/s and 300 l/s a second peak frequency at approximately 10.0 Hz occurred, whereas at 400 l/s and 500 l/s a second peak frequency in the range of 20.0 to 25.0 Hz occurred.

Artificially aerating the air cavity behind the nappe has a noticeable influence on the second peak frequency for the 200 l/s and 300 l/s discharge scenarios. The peak frequencies of these two discharges change to similar frequencies of the 400 l/s and 500 l/s discharge scenarios in the range of 25 Hz. The second peak frequency of the higher discharges (400 l/s and 500 l/s) remained in the same frequency range and intensity. Similar to what has been observed in the PSD graphs for the pressure fluctuation under the inlet key downstream overhang (**Figure 6.29**), the introduction of air appears to have a stabilising effect on the air pressure fluctuation frequencies. However, the data does did not allow for this finding to be confirmed.

Denys (2019) noted that the fluctuations in the air pressure along the sidewall have an identical peak frequency to the water pressures observed on the upstream side of the sidewall. The PSD graphs of these sensors' recorded pressure data in Denys's study showed peak frequencies between 3 to 6 Hz – higher than those recorded on the downstream sidewall for this study (approximately 2 Hz). The change in frequencies later in the model was also observed by Denys (2019). The lower frequencies recorded can be potentially contributed to the switch from a closed pipe pressure system to an open pipe system – i.e. the plastic tubes

connected to the other end of the pressure transducer were not closed but open to atmosphere. This could have resulted in air or mass entering the pressure system and damping the frequency data (Denys, 2019).

Nonetheless, according to Denys (2019), the fluctuations observed in the pressure data and PSD graphs can be attributed to the vortices that are shed from upstream. As these vortices are discharged over the sidewall crest, they induce enough disturbance to the underside of the nappe to cause fluctuation in the air cavity pressure. His numerical analysis confirmed that although the vortices and associated swirls of flow along the lateral crest (**Section 6.6.1**) seem to disappear at higher discharges in the physical model, these swirls still exist but are masked by the high turbulence present in the flow. As the discharge increases, the rotational energy of these swirls increases, causing an increase in the strength of the pressure fluctuations but not the frequency – exactly what is seen in the PSD plots in **Figure 6.34** and **Figure 6.35**. Denys (2019) also noted that the pressure fluctuations in even higher flows (> 500 l/s) can be attributed to localised drowning of the air cavity near the upstream crest, subsequent development of negative pressures and the periodic rush of air in the upstream direction to alleviate the negative pressure.

As noted under **Section 6.4.1**, the air pressure fluctuations observed under the sidewall overflow nappe are of low intensity (only a few Pascals) for discharges up to 500 l/s (H/P = 0.40) and are therefore unlikely to amplify other FIV and cause resonance vibrations in the PKW structure itself. The more significant pressure fluctuations caused by the detachment and movement of the conical air cavity tip for discharges of 600 l/s (H/P = 0.5) observed by Denys (2019) are more likely to cause structural vibrations. However, it should be noted that most PKWs operate at maximum H/P values of 0.3 (Leite Ribeiro, *et al.*, 2013).

6.4.3 Nappe oscillations

Experimental studies by Lodomez *et al.* (2019) indicated that nappe oscillations are a function of water fall height, as well as crest profile, and thus independent of scale. More specifically the crest profile affected the oscillation frequencies and the fall height both the frequencies and sound intensity. Hence, nappe oscillations will most likely occur in the larger Model 1. The scale and fall height of the model itself is such that it can be considered as a prototype.

Nappe oscillations as a dominant FIV and characterised by intense acoustic pressure waves and noise, as well as horizontal banding and waves or ripples visible on the nappe, were not observed for the range of discharges (50 l/s to 400 l/s) tested as part of this study.

However, it is worth noting that Denys (2019) investigated nappe oscillations for very low discharge conditions ranging from 5 l/s to 30 l/s. Audible and visible nappe oscillations occurred for discharges between 8 l/s and 12 l/s. For discharges between 12 l/s and 16 l/s

nappe oscillations were still visible but not audible and disappeared completely for discharges larger than 16 l/s. Distinct horizontal bands occurred along the nappe profile and the nappe contracted and expanded as a whole. The nappe oscillated at peak frequencies of 14.1 Hz, 16.6 Hz or 19.0 Hz, depending on the discharge. With reference to studies by Lodomez *et al.* (2018a) these frequencies are believed to be linked to the number of wavelengths existing in the length of the falling nappe. Similar to the findings of Lodomez *et al.* (2019), hysteresis played a role – affecting the frequency which occurred at a specific discharge. The introduction of air by breaking the nappe did not affect the occurrence of the nappe oscillations but did alter the strength of the frequencies. This supports the findings from other studies that the air pocket behind the nappe and associated air pressure fluctuations only amplify the oscillations and are not responsible for the onset of oscillations itself.

Although the three frequencies given above are within the same range as the damped natural frequencies of the sidewall (discussed in **Section 6.5**), the oscillation energy is transported through the low strength sound waves and is unlikely to cause a resonance effect and compromise the safety of the PKW (Denys, 2019).

6.5 SIDEWALL VIBRATIONS

The vibration analysis results to determine whether artificially aerating the nappe has any effect on the vibrations experienced by the lateral sidewall, one of the objectives of the study, are discussed in this section.

The larger steel model (Model 1) was used for the vibration analysis. The model was constructed from steel and at the largest scale possible to limit scale effects and to sufficiently mimic the hydro-elastic behaviour of a thin walled PKW. Vibrations were measured with a single half-bridge strain gauge installed in the middle of the sidewall near the crest where the highest deflections are expected - refer to **Section 5.4.6**. The discharges tested were ranged between 50 l/s and 400 l/s in 50 l/s intervals. Three aeration conditions were evaluated for all discharge scenarios – no artificial aeration of the air cavity behind the nappe, artificial aeration by means of a small diameter aeration pipe and a larger aeration pipe. The vibrations, in terms of deflection over a time period, were sampled at a frequency of 2400 Hz for a minimum of 180 seconds for all considered scenarios tested in Model 1. The captured data were converted to PSD plots to evaluate the spectral content and to identify the peak frequencies that occur for the different discharge and aeration scenarios.

The PSD graphs for both unaerated and aerated (larger diameter air pipe) and the range of discharges are illustrated in **Figure 6.36** and **Figure 6.37**. Note that these graphs do not include the PSDs for discharges 150 l/s, 250 l/s and 350 l/s – the PSD graphs are included in

Appendix D. The main frequency peaks for each discharge and aeration scenario identified from the respective PSD plots are summarised in **Table 6.6**.

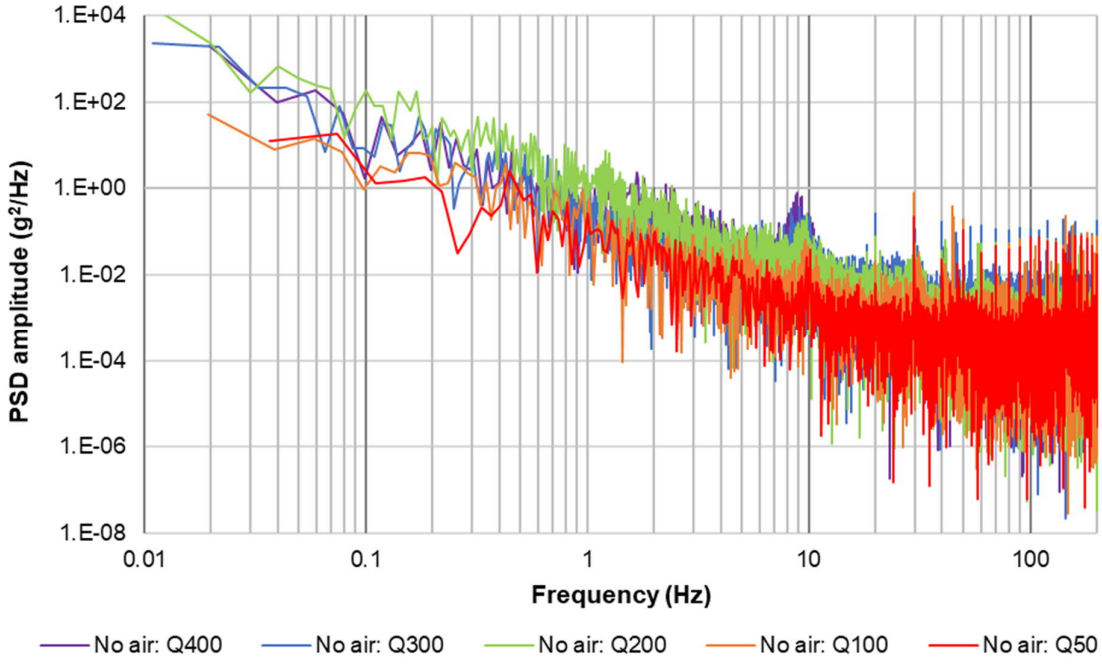

Figure 6.36: Measured vibration PSD for unaerated conditions (Model 1)

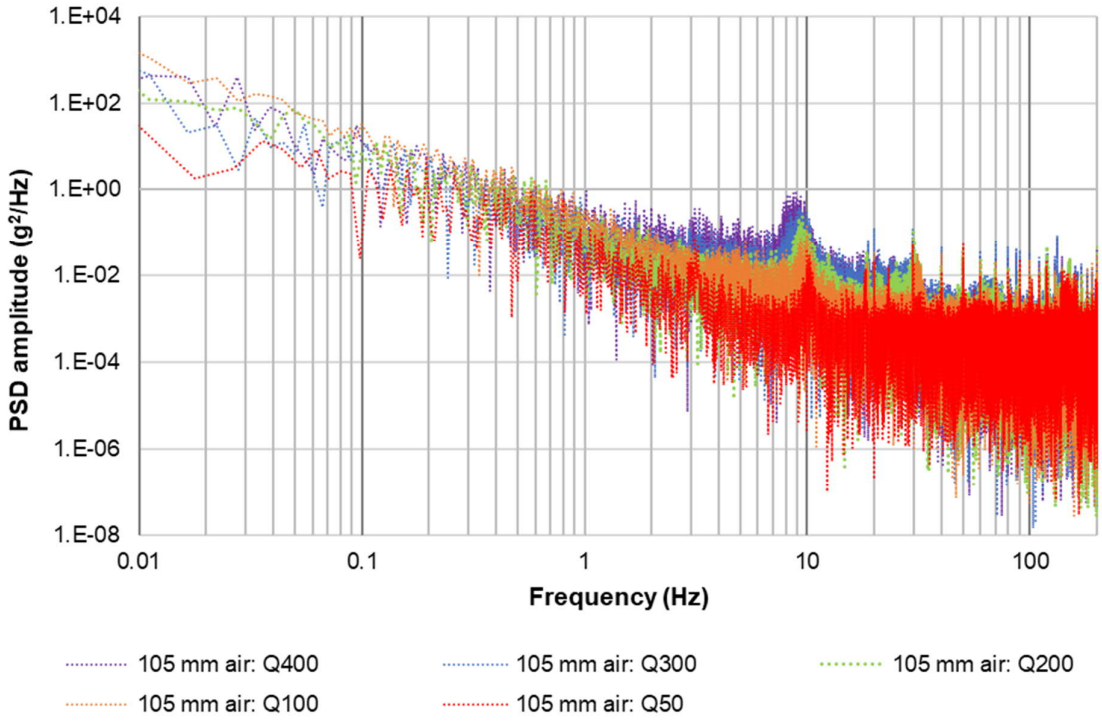

Figure 6.37: Measured vibration PSD for aerated conditions (Model 1)

Table 6.6: Measured sidewall vibration frequency peaks (Model 1)

Discharge (l/s)	Aeration	Peak frequencies (Hz)					
50	No air	1.30	2.60	**10.0**	16.50	24.1	29.8
	105 mm aeration pipe	1.43	3.13	**9.98**	18.35	23.3	29.8
100	No air	1.24	3.00	**9.80**	19.80	-	29.8
	105 mm aeration pipe	1.30	5.29	**10.06**	18.60	-	29.9
150	No air	1.26	3.14	**10.60**	18.48	25.3	29.8
	105 mm aeration pipe	1.20	3.60	**9.60**	14.90	19.9	31.3
200	No air	1.26	2.40	**9.57**	18.20	-	30.0
	105 mm aeration pipe	1.27	2.70	**9.53**	18.50	24.8	29.8
250	No air	1.54	2.90	**9.35**	17.90	25.3	29.8
	105 mm aeration pipe	1.21	2.30	**9.60**	-	23.3	29.8
300	No air	-	3.90	**9.18**	18.20	25.7	30.0
	105 mm aeration pipe	1.70	3.20	**9.20**	18.80	-	29.9
350	No air	1.21	2.65	**9.28**	17.90	25.9	29.8
	105 mm aeration pipe	1.36	3.60	**9.23**	18.79	24.5	30.2
400	No air	1.80	2.46	**8.89**	-	23.2	29.8
	105 mm aeration pipe	1.85	3.30	**8.90**	18.70	23.9	30.0

From **Figure 6.36** and **Figure 6.37** and as summarised in **Table 6.6**, it can be concluded that the sidewall vibrates at two distinct main frequencies – around 9 to 10 Hz, which is the stronger of the two peaks, and is around 30 Hz. Other peak frequencies around 1.3 to 3.6 Hz, 18 Hz and 24 Hz are also visible, although to a lesser extent. The peaks around 3.6 Hz are likely harmonics of the peaks around 1.3 Hz. Again, the peaks at 50 Hz or intervals thereof are due to the interference from the electrical grid. The sharp peaks visible at intervals of 10 Hz, excluding the peak at 30 Hz, are presumed to be harmonics of the first main peak around 10 Hz or alternatively other ambient interferences.

As with the pressure fluctuation frequencies, the vibration peak frequencies remain within the same range for all discharges evaluated. However, there is a slight decrease in the frequency as the discharge increases. Furthermore, the strength of the frequency (dictated by the area under the PSD graph) or alternatively the strain in the sidewall increases with the increase in discharge – more so between lower discharges compared to higher discharges.

The peak frequencies for all discharge scenarios are almost identical for both aerated and unaerated conditions. By way of direct comparison as illustrated in **Figure 6.38**, it seems that there is also no difference in the strength of the peak frequency signals between aerated and

unaerated conditions. However, it appears that the frequency strength is slightly higher for unaerated conditions for frequencies lower than 10 Hz.

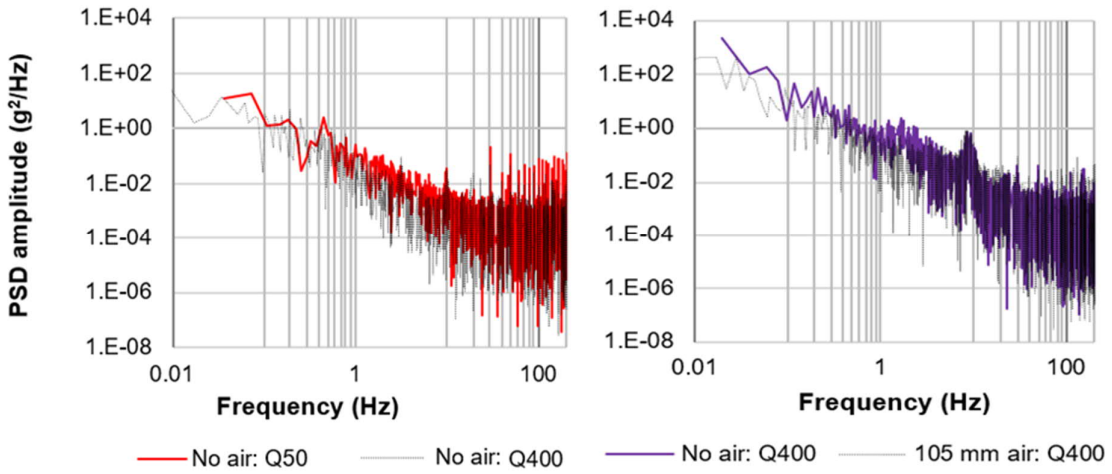

Figure 6.38: Comparison of measured sidewall vibration PSD with and without aeration (Model 1)

Based on the findings, it can be concluded that introducing air to the air cavity behind the nappe has no effect on the vibrations experienced by the sidewall. Artificial aeration does have some reducing effect on the intensity of lower frequencies, however, these are not the dominating frequencies.

With reference to the study of Denys (2019), several deflection mode shapes were identified for the PKW sidewall. The first mode shape applicable to this study is where the expected deflection is the highest at the middle top centre of the sidewall. The second mode shape relates to a s-shaped deflection of the sidewall. The mode shapes characterised by Denys (2019) and considered in this study are shown in **Figure 6.39**. The water mass upstream of the PKW has a damping effect on the natural frequencies of the sidewall. The natural frequencies for the mode shapes, as well as the effect of different water levels in terms of the weir crest height (P), as determined by Denys (2019), are summarised in **Table 6.7**. These mode shape and natural frequencies, although not part of the focus of this study, give insight to whether the vibrations of the sidewall are excited by the fluctuation of the air pressure behind the nappe or something else.

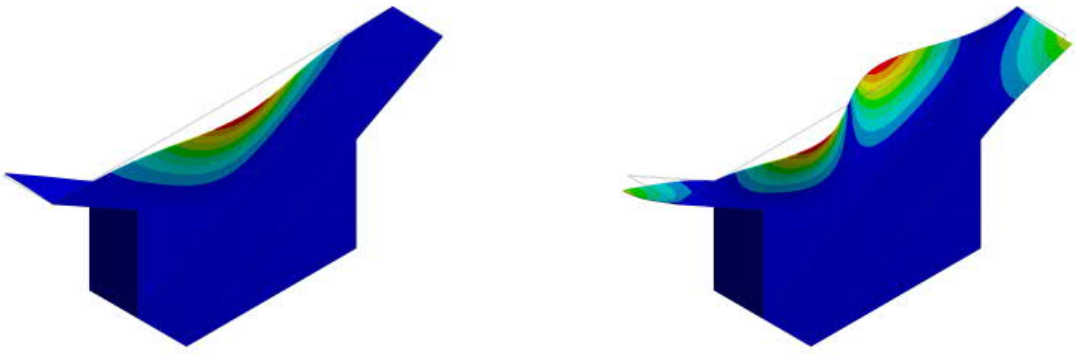

(a) Mode shape 1 (b) Mode shape 2

Figure 6.39: Mode shapes of PKW sidewall (Denys, 2019)

Table 6.7: Natural frequencies for different mode shapes and water level (Denys, 2019)

	Peak frequencies (Hz)			
Water level	**0.0P**	**0.5P**	**1.0P**	**1.2P**
Mode 1	20.3	20.3	12.4	7.1
Mode 2	41.5	41.6	39.5	32.0

The maximum water depth recorded over the Model 1 PKW for the highest discharge in this study (400 l/s) is 200 mm - less than 1.2 P. The main peak frequency at which the PKW sidewall vibrates (9 to 10 Hz) falls within the range of the damped natural frequency of the first mode shape for the corresponding water level as given in **Table 6.7**. The second vibration peak frequency, 30 Hz, is close to the range of the natural frequencies for the second mode shape. It can therefore be concluded that the PKW sidewall vibrates at its first modes and potentially at its second mode as well.

Only the air pressure below the inlet key downstream overhang could be measured in Model 1 due to the instrument limitations and model construction (refer to discussed in Section **5.4.5 and 5.6**). The air pressure behind the nappe at the measuring point fluctuates at peak frequencies between 27.7 to 44.7 Hz, depending of the discharge – the higher frequencies occurring at the lower discharges (**Table 6.2**). These are well within the range of the natural frequencies of the PKW sidewall of the second mode shape and it could be said that the sidewall vibrations are excited by the pressure fluctuations of the air cavity. However, cognisance should also be given to the fact that the pressure transducer might have picked up the vibration of the flow guide wall into which it was installed.

Furthermore, it should also be noted that the air pressure fluctuations in the cavity behind the sidewall nappe are said to be induced by the vortices that are shed along the upstream face

of the sidewall (refer to **Section 6.4.2**). According to Denys (2019), the PKW sidewall responds to the pressure fluctuations on the upstream face of the sidewall by continuously deflecting. Thus, the vibrations are excited by the vortices and not the air cavity as such. Only at very high discharges with H/P values equal to or larger than 0.50 could the outlet key flow dynamics start playing a major role in the air cavity fluctuations and wall vibrations. However, it should be noted that most PKWs constructed to date operate below this headwater level.

If the peak frequencies measured along the sidewall downstream face of Model 2 are upscaled to be representative of Model 1, the first and most distinct peak frequency would range between 0.9 Hz and 1.6 Hz. The lowest peak frequency at which the sidewall vibrates (**Table 6.6**) corresponds to this frequency range. The second peak frequency observed in Model 2, ranging from 21.5 Hz to 28.0 Hz, would range between 6.6 Hz and 14.8 Hz if upscaled. The upscaled second peak pressure fluctuation frequency thus corresponds to the natural vibration frequency range of the first mode shape of the wall.

Based the correspondence between the pressure fluctuation frequencies, sidewall vibration frequencies and the natural frequencies of the two modes described in this study, it can be said that the sidewall vibrations are excited by the shedding of vortices around the upstream outlet key overhang. The frequency analysis results imply that the wall is experiencing vibration at both mode shapes described in this study. The vibration amplitudes, however, are relatively low and none of the modes where favoured to such an extent that it would activate resonant behaviour of the PKW sidewall. Lastly, the small negative pressures that seem to exist behind the nappe are not considered to have any noticeable effect on the vibration behaviour of the sidewall. The air pocket behind the nappe merely appears to function as an amplifier of the vibrations and does not onset the vibrations as such.

6.6 OTHER OBSERVATIONS

6.6.1 Vortex swirls along lateral crest

As mentioned in **Section 6.2.4**, periodic swirls were observed in the discharge passing over the lateral crests. There swirls, characterised by an indent in the flow profile and followed directly by a bulge or wave, appeared along the centre of the sidewall crest, travelled for a short distance along the crest in the downstream direction and then disappeared. These small swirling waves are best illustrated in by eight snapshots taken from a video of Model 1 (**Figure 6.40**). As illustrated in **Figure 6.41**, the nappe curtain extending from the bulge of the swirl is noticeably thicker compared to the nappe portion that extends from the indent of the swirl, which was noticeably thinner. However, these swirls were never so severe that the nappe curtain would break.

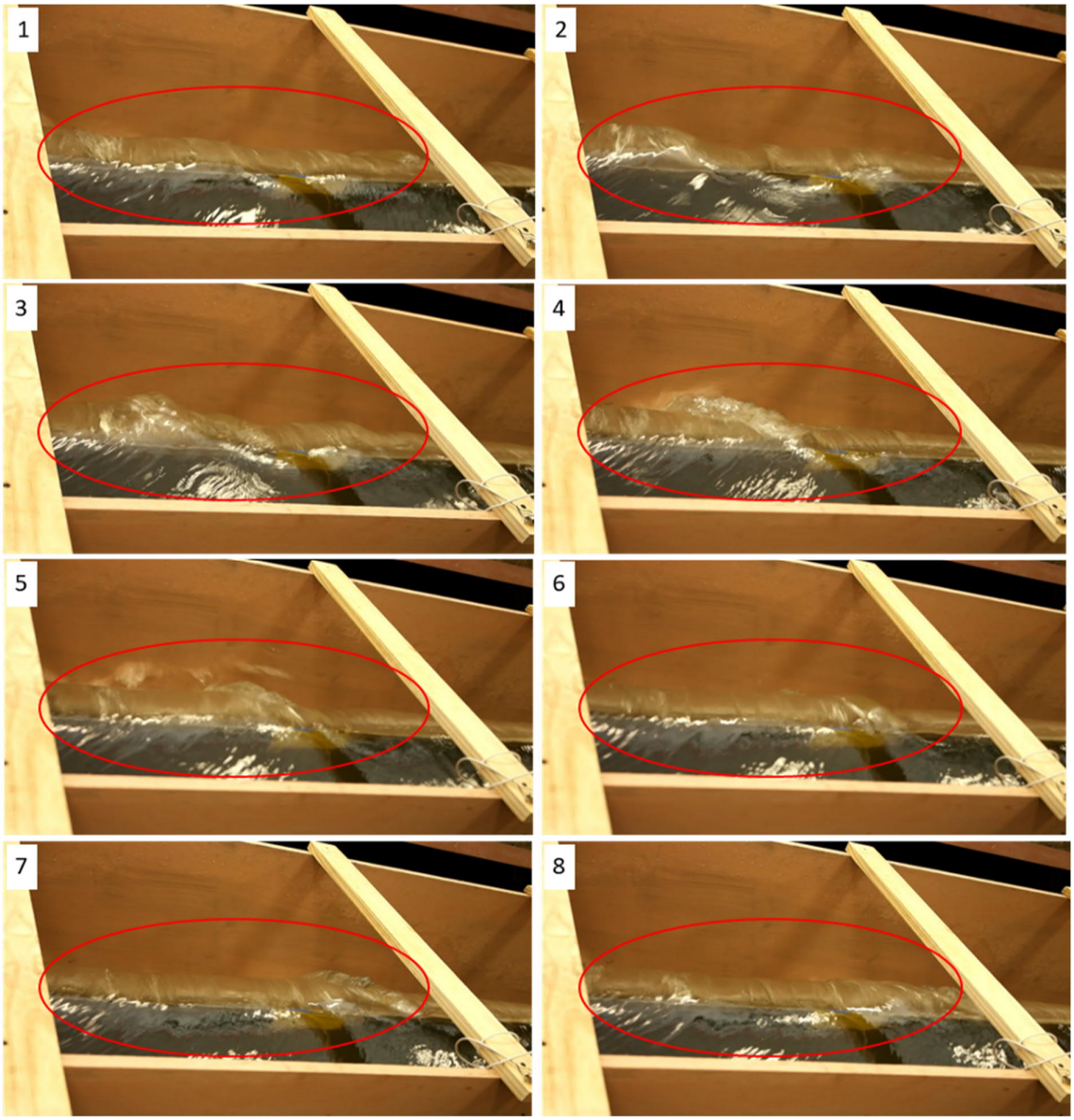

* *Note: Water flow from left to right*

Figure 6.40: Traveling of vortex swirls along the lateral crest (Model 1)

Figure 6.41: Traveling of vortex swirls along the lateral crest (Model 1)

The waves or swirls appeared on all sidewall crests at irregular intervals in both models. The regularity of these swirls increased with the increase in discharge but became less obvious as the overflow depth increased. These swirls either disappeared or were not visible anymore due to the high turbulence and water surface level fluctuations that occurred for discharges 400 l/s and higher (H/P ≥ 0.33). Furthermore, in the case of Model 2, there appeared to be no synchronisation between the swirls along adjacent lateral crests.

According to Denys (2019), these swirls relate to the vortices that are shed from the separation bubble that occurs as a result of flow changing direction and diverging around the 90° corner of the outlet key upstream overhang. As discussed earlier, these swirls had a noticeable effect on the pressure fluctuations experienced by the air cavity under the nappe

6.6.2 Effect of tail water level

Additional scenarios with an increase in the tail water level were also evaluated. The tail water levels were increased by slotting in a wooden plank some distance downstream from the PKW model in the flume (**Figure 6.42**).

Figure 6.42: Increasing the tail water level for Model 2

The tail water level was raised from 0 mm to 400 mm in 100 mm increments for unaerated scenarios. The tail water was raised by placing wooden planks downstream of the PKW Model 2. The tail water level for 300 l/s was only increased up to 100 mm and not increased at all for 400 l/s and 500 l/s due to the amount and power of the flow. For aerated scenarios the tail water level was only raised by 100 mm and for discharges up to 200 l/s. Higher tail water levels or discharges caused the aeration pipes to be filled with water.

Increasing the tail water level had no effect on the discharge efficiency for the discharge ranges tested and remained within the same range. As illustrated by **Figure 6.43**, increasing the tail water level had a very limited effect on the overflow profile, except for the tail water level.

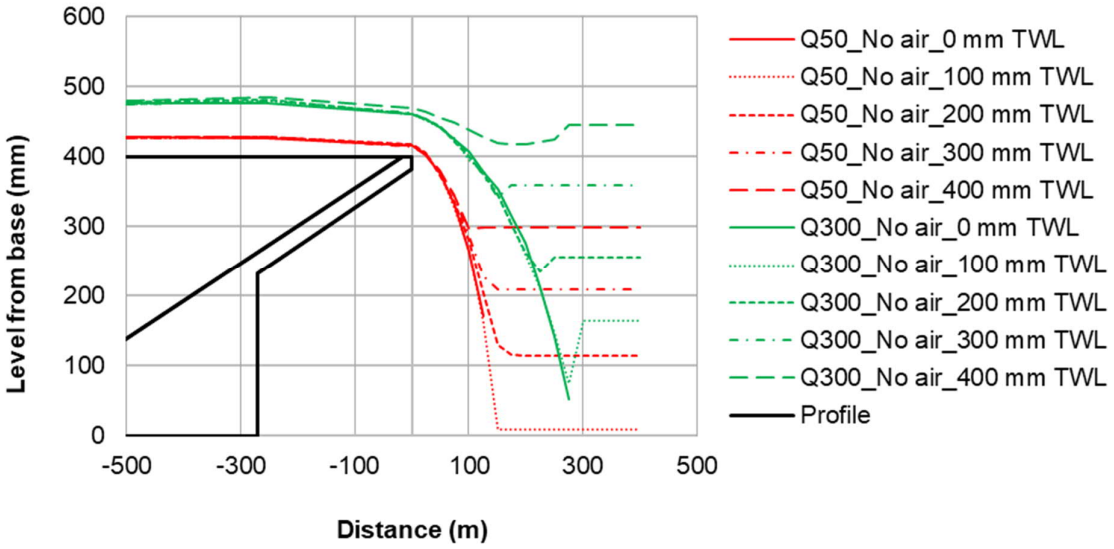

Figure 6.43: Model 2 measured longitudinal water surface profile along centre of inlet key (Effect of tail water level)

At higher discharges and increased tail water levels, air entrainment into the nappe curtain itself was visible, although limited. For discharges 200 l/s (H/P = 0.18) and up with tail water levels increased to 200 mm and higher, the tip of the conical shape also moved slightly downstream, more so for the nappe over the sidewall closest to the flume wall compared to others. For discharges 200 l/s (H/P = 0.18) and higher, with tail water levels increased to 400 mm, no air cavity formed along the sidewall due to the submergence of the outlet key.

7. MAIN FINDINGS AND CONCLUSIONS

PKWs are becoming increasingly popular for increasing the discharge capacity of existing dams due to their high discharge efficiency compared to linear and traditional labyrinth weirs, as well as their small structural footprint.

Previous PKW hydraulic model studies have indicated that vibrations that occur in the PKW structure disappear by artificially aerating the air cavity behind the overflow nappe. The vibrations were assumed to be a result of negative pressures that develop in the air pocket, become unstable and cause oscillations. It was assumed that these negative pressures and oscillations were alleviated by the introduction of air at atmospheric pressure. However, some studies have observed nappe oscillations for fully aerated nappes. Although PKWs have proved to be self-aerating, most of the PKWs installed to date are equipped with aeration pipes. The benefits of these aeration pipes, as well as the pipe sizes required, have not yet been studied in detail.

The main objectives of this study were to investigate, by means of physical hydraulic model studies, the effect of artificially aerating the air cavity behind the overflow nappe of a PKW on the discharge capacity, the overall hydraulic behaviour and FIVs, specifically nappe oscillations. The effect of different aeration pipe sizes installed under the overflow nappe on the aforementioned was also investigated.

Two physical hydraulic models were constructed in the Hydraulics Laboratory of the Stellenbosch University, South Africa. Model 1 was a large-scale model (1:2.73) constructed from structural steel to sufficiently mimic the hydro-elastic behaviour of a thin walled PKW. The purpose of this model was to evaluate the vibration of the sidewall itself, whether nappe oscillations occur and whether artificially aerating the air cavity behind the nappe had any effect of the vibrations and pressure fluctuations. Model 2, a smaller scale (1:7.5) multi-key model, constructed from pine timber, was mainly used to evaluate the effect of artificial aeration on the overall hydraulic behaviour and the pressure fluctuations along the downstream face of sidewall and downstream of the inlet key overhang. Both models were equipped with an aeration pipe under each downstream overhang of the inlet key that are open to the atmosphere. The pipe sizes could be changed between a small diameter and large diameter, as well as be entirely closed off for unaerated simulations.

The main findings and conclusions of this study are discussed in the following sub-sections.

7.1 DISCHARGE CAPACITY AND OVERALL BEHAVIOUR

The discharge capacity and efficiency of both of the hydraulic models corresponded well with that of other models with similar geometrical characteristics. Details of the discharge capacity of the two physical hydraulic models are discussed under **Section 6.1**. It was noted that the discharge efficiency increases with the increase in discharge for H/P values up to 0.1 (Model 2) and 0.14 (Model 1). For higher discharges the discharge coefficient gradually decreases with an increase in headwater or discharge. The initial increase in the discharge coefficient followed by a gradual decrease as more flow is passed over the PKW, is related to the nappe transitioning from clinging to leaping and finally springing. The relationships between the discharge coefficient and the headwater level (as H/P) are shown in **Figure 7.1** for both Model 1 and Model 2.

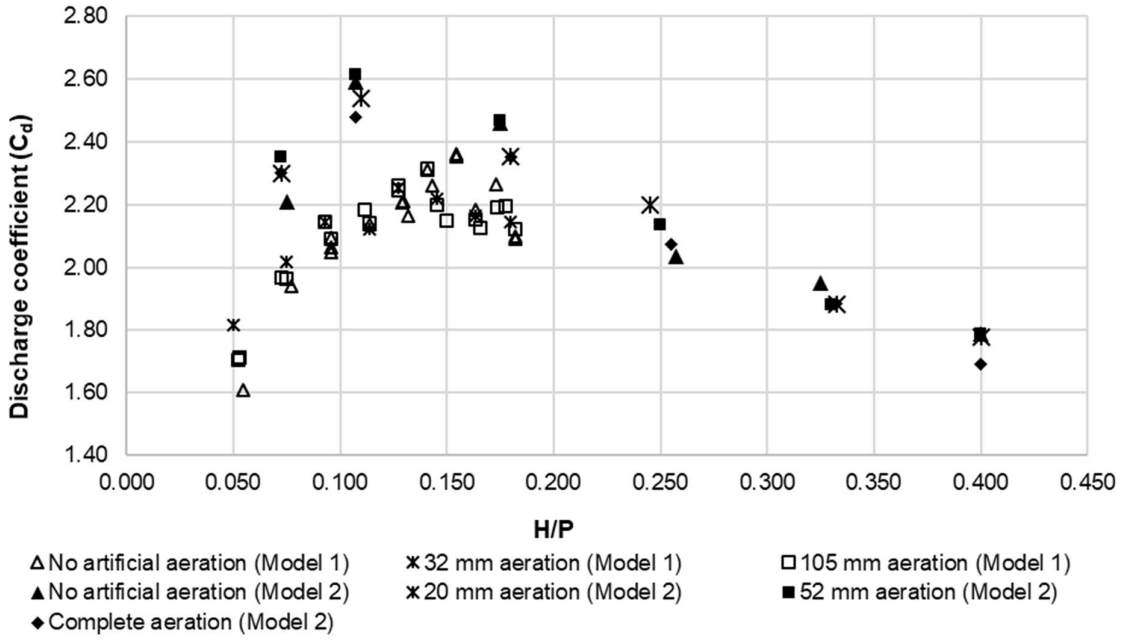

Figure 7.1: Measured discharge efficiency for Model 1 and Model 2

The PKW performed up to 5% better in terms of discharge coefficient under aerated conditions for low headwater levels (H/P < 0.13 for Model 1 and H/P < 0.10 for Model 2). At these discharges or headwater levels the smaller of the two aeration pipe sizes resulted in a slightly higher efficiency in the case of Model 1. However, in the case of Model 2, the larger aeration pipe performed better. At higher headwater levels, both PKW models performed better without artificially aerating the nappe.

The headwater level at which artificial aeration appears to have a declining effect on the discharge efficiency corresponds to the headwater level for which the nappe transitions from leaping to springing and for which the nappes of the opposite sidewalls start to collide

(H/P > 0.10). It can be said that the modelled PKWs become self-aerating for headwater levels higher than H/P = 0.10. It is presumed that sufficient air is entrained through the turbulent colliding nappes from the opposite sidewalls. This finding is supported by the observation that the air demand through the aeration pipes decreases with the increase in discharge but stabilises at a constant demand for discharges higher than H/P > 0.10. Based on the above it can be concluded that artificial aeration has a limited effect on the discharge efficiency of a PKW and is most beneficial only for low headwater levels or discharges (H/P ≤ 0.10).

In all scenarios in both models, the nappe forms a continuous water curtain over the lateral and downstream inlet key crests (**Figure 7.2 a**). The flow surface of the nappe was generally smooth and stable for lower discharges but become more turbulent for higher discharges. The nappe profile over the downstream crest and sidewalls of the inlet key noticeably expands with the introduction of air into the air cavity behind the nappe, especially for low discharges. Furthermore, the nappe curtain at the corner edges of the downstream crest is drawn in into a concave shape for H/P values lower and equal to approximately 0.10, irrespective of the model. These nappe indents were slightly less severe with the introduction of artificial aeration behind the nappe and disappeared completely when the nappe was broken. These observations imply that sub-atmospheric pressures do develop behind the nappe for low discharges and are alleviated, although not completely, by means of artificial aeration. The pressure analysis also confirmed that pressures behind the nappe are sub-atmospheric for these lower discharges.

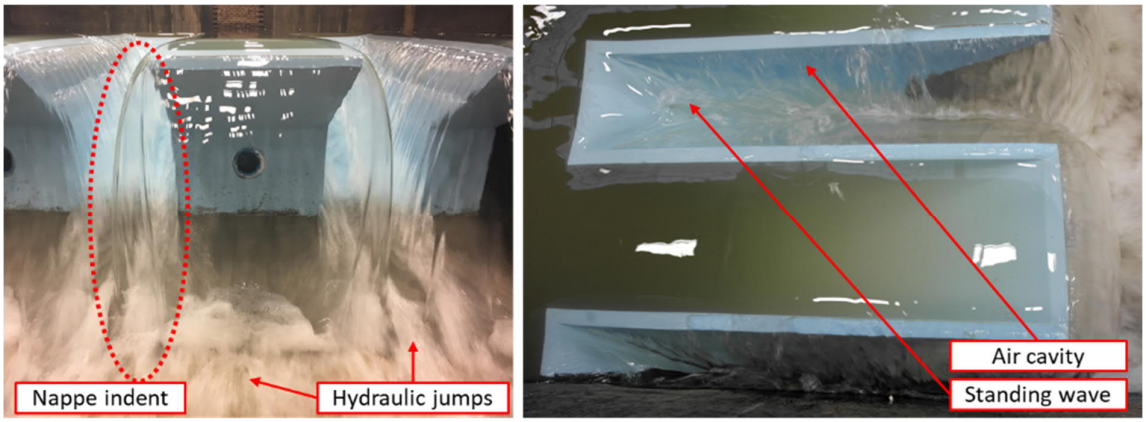

(a) (b)

Figure 7.2: Flow profile characteristics

A conical air cavity forms behind the nappe along the downstream face of the sidewall due to the increase in the water curtain fall height in the downstream direction (**Figure 7.2 b**). Under low headwater levels the tip of the cavity remains attached to the upstream corner edge of the outlet key. Due to an interplay between the transverse flow momentum, rotation away from the sidewall crest, and the strong longitudinal flow momentum from the upstream crest of the

outlet key, the tip detaches from the corner edge, moves downstream and starts to fluctuate. However, this only occurs for very high headwater levels (H/P > 0.4). Hydraulic jumps form downstream where the nappe curtain over the downstream crest collides with the apron, and also where several flow streams meet.

Periodic swirls of flow were observed over the lateral sidewall crests in both models. These swirls appear at approximately the centre of the sidewall crest, travel a short distance along the crest and then disappear. The thickness of the nappe curtain extending from the swirl is noticeably altered, but never to such an extent that the nappe curtain opens. These swirls are believed to be related to the vortices that are shed from the separation bubble that develops as flow travels around the upstream overhang of the outlet key into the inlet key. The swirls also had a noticeable effect on the air pressure fluctuations in the air cavity along the sidewall.

Visually, artificial aeration had no effect on the onset of the several characteristics mentioned above, except for the expansion of the nappe profile under low flow conditions.

7.2 AIR DEMAND

Previously, the air demand for a PKW was estimated as 5 to 10 % of the water flow and the pipes were sized not to exceed an air speed of 50 m/s to 100 m/s. This method however, resulted in very large diameter aeration pipes for some PKWs. Only very recently has an aeration demand method been developed for PKWs by Vermeulen *et al.* (2017). This method proved to accurately estimate the air demand for the existing Malarce Dam and was verified by actual measured data.

In the hydraulic model study, the air velocity through the aeration pipes installed in both models was measured using a Lutron hot-wire anemometer and then converted to air demand (in m^3/s) for the relevant pipe sizes. The air velocity increased almost linearly with the increase in discharge. Furthermore, air velocities through the aeration pipes are similar for corresponding H/P values, irrespective of the model and pipe size. The air demand decreases with an increase in discharge and then seems to stabilise for H/P > 0.1 – similar to that of the air demand measured at Malarce Dam. As mentioned earlier, it is presumed that the PKWs become self-aerating at higher headwater levels due to air entrained through the turbulent flow of the colliding water nappes from the opposite sidewalls. Details of the air demand and relevant graphs are discussed under **Section 6.3**.

The amount of air entrained through the aeration pipes, as a percentage of the discharge, was found to be directly related to the size of the aeration pipe, irrespective of model or scale. Generally, the air-water interface is more stable for large scale factors, resulting in less air demand and reduced air pressures. This occurrence can be attributed to the fact that air

entrainment and bubble generation cannot be scaled and explains the reason for the direct link between air and pipe size irrespective of scale.

7.3 NAPPE OSCILLATIONS

Time variant pressure data was captured in both models by means of pressure transducers or sensors installed below the inlet key overhangs. Three additional pressure sensors were installed along the downstream face of the sidewall in the case of the smaller multi-key model (Model 2). Pressure data were evaluated in both the time domain and the frequency domain to get a better understanding of the behaviour.

7.3.1 Nappe oscillations as flow induced vibrations

No nappe oscillations, as a dominant FIV and characterised by intense acoustic pressure waves and noise, and horizontal banding and waves or ripples visible on the nappe, were observed for the range of discharges (H/P = 0.05 to 0.18) tested as part of this study. Nappe oscillations, however, were observed in the parallel study conducted on the same physical hydraulic models by Denys (2019). Audible and visible oscillations, where the nappe curtain contracted and expanded as a whole, were observed for flows ranging from 8 l/s to 12 l/s. Oscillations still occurred for higher flows up to 16 l/s but were not audible. The nappe oscillations disappeared completely for discharges higher than 16 l/s. It is also worth noting that artificial aeration had no effect on the occurrence of the nappe oscillations. However, introducing air to the nappe cavity or breaking the nappe did reduce the intensity of the oscillations. These findings support the fact that the air pocket behind the nappe only amplifies the oscillations and is not responsible for the onset of oscillations itself.

7.3.2 Nappe oscillations as pressure fluctuations

The pressure analysis, as presented in **Figure 7.3** (pressure along the sidewall of Model 2), revealed that sub-atmospheric pressures do occur in the air cavity behind the nappe, especially for low discharges and headwater levels. The occurrence of sub-atmospheric pressures was also confirmed by the indents that occurred at the downstream corners of the nappe for low headwater levels as earlier illustrated in **Figure 7.2 a**. In most cases, these sub-atmospheric pressures are alleviated with the artificial introduction of air behind the nappe. The lack of sub-atmospheric pressures at higher headwater levels further confirms that PKWs are self-aerating for higher discharges. Aerating the air cavity for these higher headwater levels also had no significant effect on the already atmospheric or positive pressures.

The analysis also revealed that there is a considerable amount of air pressure fluctuation behind the nappe for high headwater levels (H/P ≥ 0.25) – also illustrated in **Figure 7.3**. The pressure fluctuations are more distinct along the sidewall compared to the area under the inlet

key overhang. These fluctuations, if strong enough, can potentially contribute to the excitation and ultimately the vibration of the PKW structure itself. However, the fluctuations ranged over only a few Pascals and are unlikely to induce vibrations.

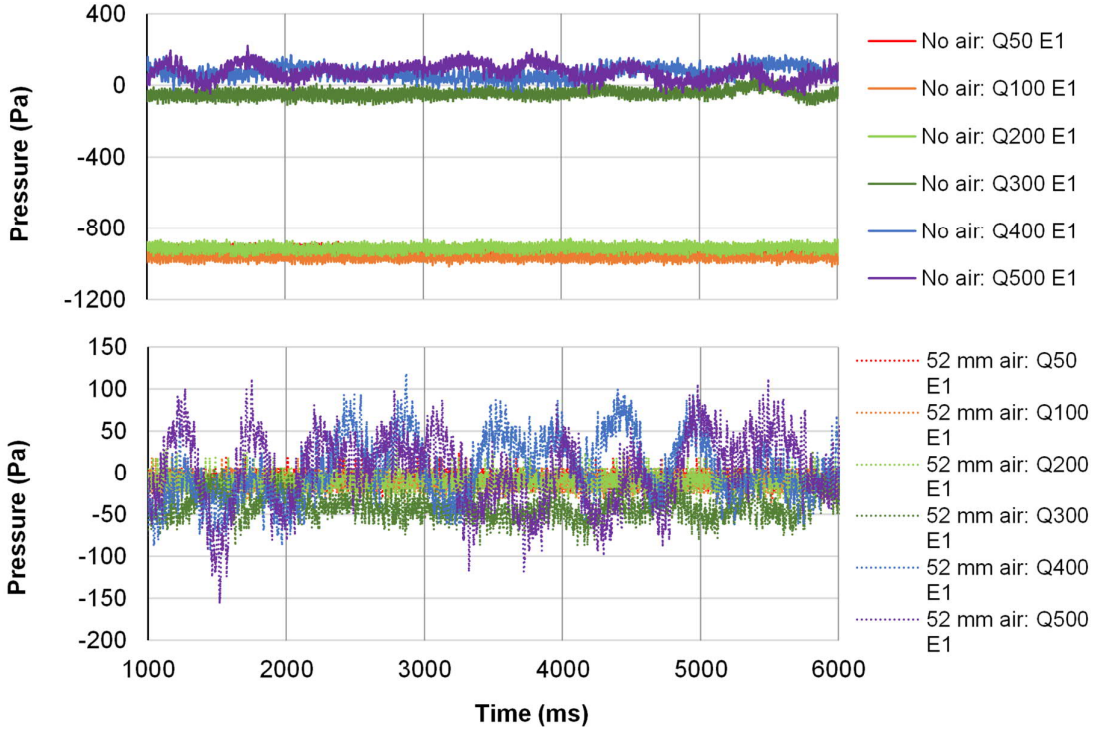

Figure 7.3: Measured time variant air cavity pressure along the sidewall with and without artificial aeration (Model 2)

The time domain pressure fluctuations were converted to the frequency domain in the form of a PSD plot as shown in **Figure 7.4**. Frequency analysis showed that the air pressure behind the nappe fluctuated at main peak frequencies ranging from 27.7 Hz to 44.7 Hz in the case of the larger steel model (**Figure 7.4**). Other noticeable peak frequencies ranged from 0.9 to 1.6 Hz, 4.0 to 6.6 Hz and 17.0 to 22.0 Hz, although at a much lower strength (dictated by the area under the PSD graph). These are from the pressure readings of the pressure transducer directly installed below the inlet key downstream overhang.

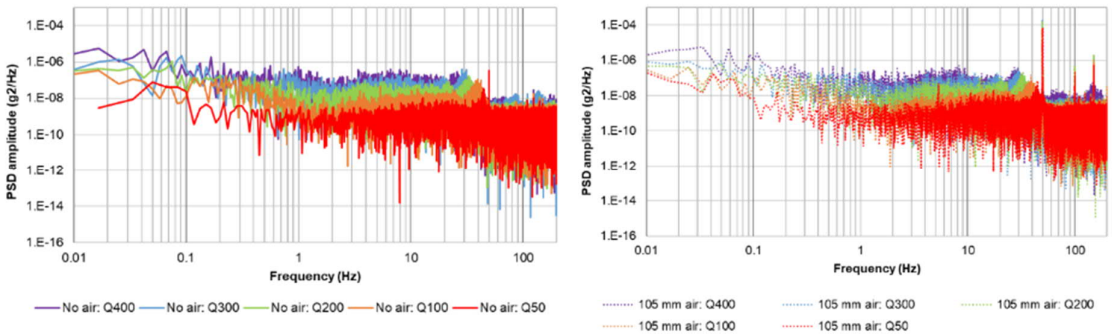

Figure 7.4: Measured air pressure PSD for unaerated (left) and aerated (right) conditions (Model 1)

In the case of the smaller multi-key model, the pressures were measured with remote pressure sensors located below the inlet key overhang and downstream face of the sidewall. Pressures under the inlet key overhang fluctuated at main peak frequencies ranging from 1.2 to 1.6 Hz, as well as lower strength frequencies from 6.0 to 9.0 Hz (**Figure 7.5**). The fluctuation frequencies along the sidewall were slightly higher than those at the inlet key overhang, ranging from 1.5 to 2.0 Hz for the main peak frequency, and from 20.0 to 25.0 Hz, as well as around 10 Hz, for the second main peak (**Figure 7.6**). The strength of the second peak frequencies along the sidewall was higher compared to that below the inlet key overhang. This implies that the air pressure fluctuations behind the nappe were mostly governed by the flow characteristics over the sidewall crest. It should also be noted that peak frequencies for lower discharges or headwater level were not very distinct.

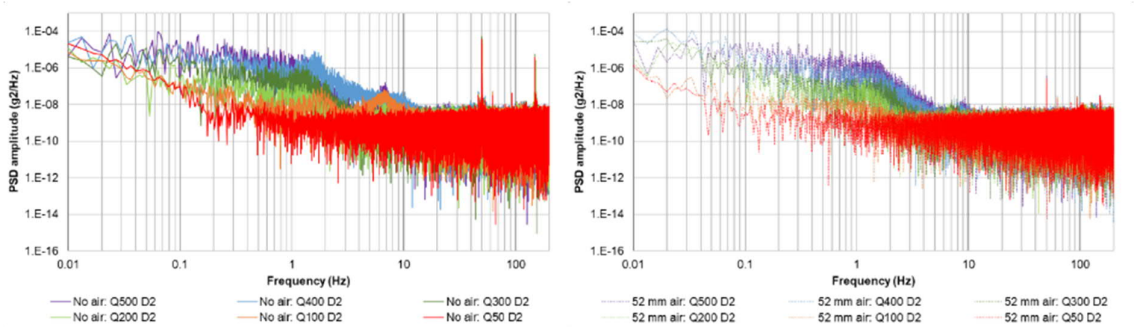

Figure 7.5: Measured air pressure PSD below the inlet key overhang for unaerated (left) and aerated (right) conditions (Model 2)

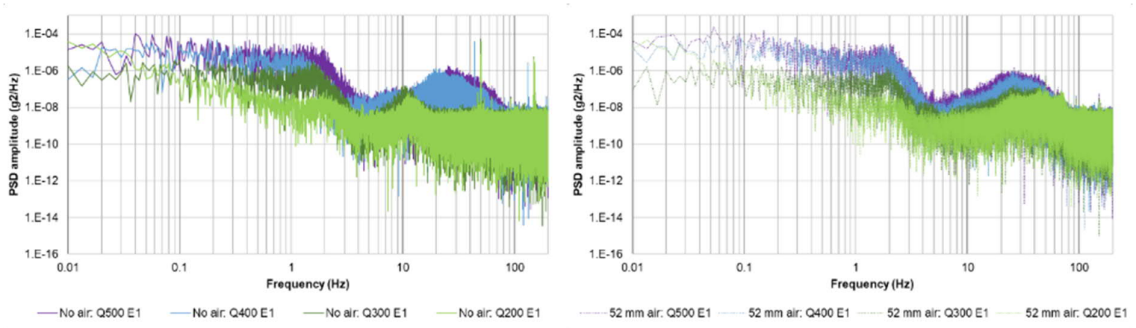

Figure 7.6: Measured air pressure PSD along the sidewall for unaerated (left) and aerated (right) conditions (Model 2)

Although it should be kept in mind that the two physical hydraulic models did not have the exact same prototype geometrical characteristics, there was some correspondence between the peak frequencies of the two models if upscaled to prototype frequencies. It should, however, be noted that air entrainment and subsequent air pressure data cannot be adequately scaled using normal similitude laws due to the physics of bubble generation and size.

In both model cases, the peak frequencies remained within the same range with the increase in discharge and only the strength of the frequencies increased. In the case of the larger steel model, however, the frequencies slightly reduced at a trend as the discharges increased. For both models and for all discharges, the artificial introduction of air had no effect on the frequencies or frequency strength. The introduction of air did have some stabilising effect on the frequencies identified along the sidewall in the case of the smaller model (Model 2) as shown in **Figure 7.6**.

The pressure fluctuations in the nappe air cavity are believed to have been related to the vortices that were shed from upstream of the outlet key overhang and passed over the sidewall crest as swirls of flow. As mentioned earlier, the nappe thickness that extended from these swirls was noticeably altered. This sudden change in nappe thickness induces enough disturbance to the underside of the nappe to cause fluctuation in the air cavity pressure. This finding contributes to the conclusion that the air cavity behind the nappe only functions as an amplifier.

A parallel study by Denys (2019) on the same physical hydraulic models confirmed that the air pressure fluctuations along the downstream face of the sidewall have an identical peak frequency to the water pressures fluctuations on the upstream side of the sidewall induced by the vortex shedding. His numerical analysis of the PKW flow dynamics showed that the rotational energy of these vortex swirls would increase as the discharge increases, causing

an increase in the strength of the pressure fluctuations but not the frequency – exactly what is evident from the PSD plots for the sidewall pressure fluctuations on the downstream face.

At headwater levels higher than H/P = 0.4, tested by Denys (2019), the pressure fluctuations increased even more along the sidewall. These fluctuations were due to the localised drowning of the air cavity near the upstream crest of the outlet key, which forced the tip of the conical air cavity to detach from the upstream outlet key corner edge and move downstream. The negative pressures that developed due to a rotational zone of flow along the downstream face of the sidewall were relieved by a sudden infrequent rush of air in the upstream direction, which caused a large pressure fluctuation.

7.4 SIDEWALL VIBRATIONS

The larger steel model (Model 1) was used for the vibration analysis. The deflection of the sidewall was measured using a single half-bridge strain gauge installed in the middle of the sidewall near the crest where the highest deflections were expected.

The frequency analysis revealed that the sidewall vibrates at two main peak frequencies – around 9 to 10 Hz, which is the stronger of the two peaks, and around 30 Hz, as shown in **Figure 7.7**. Other peak frequencies around 1.3 to 3.6 Hz, 18 Hz and 24 Hz are also visible, although to a lesser extent. Similar to the findings of the dynamic pressure analysis, the peak frequencies remained within the same range for all discharges and increased in intensity as the discharge increased. The first peak frequency slightly reduced as the discharge increased – also similar to what was observed in the dynamic pressure analysis of the larger steel model. The second peak frequency remained stable over the discharge range. There was also almost no difference in the peak frequencies, or their strength, between unaerated and aerated conditions.

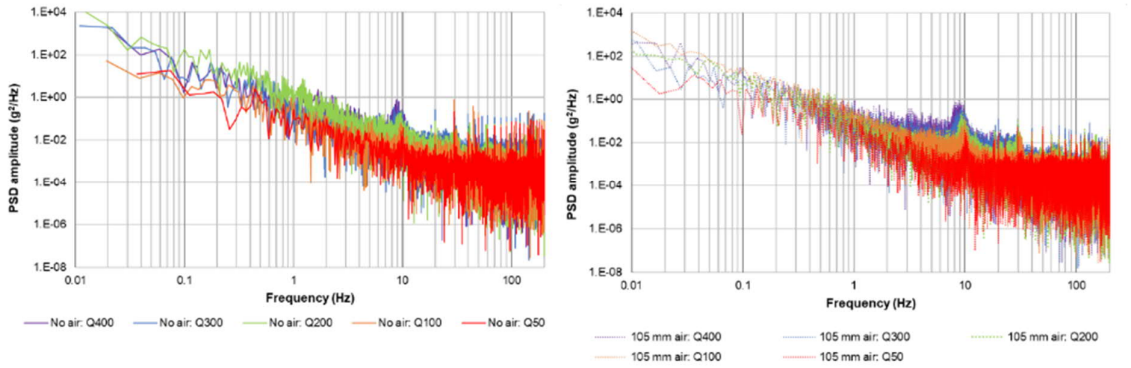

Figure 7.7: Measured vibration PSD for unaerated and aerated conditions (Model 1)

Although not a focal point of this study, the deflection mode shapes most likely to occur in the PKW sidewall and the associated natural frequencies, as determined by Denys (2019), was

used to identify if there was any correspondence with the pressure fluctuation peak frequencies likelihood of these pressure fluctuations activating any of the modes. The natural frequencies of the first mode shape (most deflection at middle top centre of the sidewall) ranged from 12.4 Hz to 7.1 Hz for water levels equal to P and 1.2P respectively. The natural frequencies of the second mode shape (s-shaped deflection of the sidewall) ranged from 39.5 Hz to 32.0 Hz for water levels equal to P and 1.2P respectively. The water level had a damping effect on the natural frequencies.

The main peak frequency of the PKW vibration corresponded to the damped natural frequency of the first mode shape and the second peak frequency was close to that of the second mode shape. It can thus be said that the sidewall vibrateed at its first mode shape and likely the second shape. The main peak pressure fluctuations measured in the same model (Model 1) corresponded to the natural frequencies of the second mode shape. If the peak frequencies of the air cavity fluctuations along the downstream face of the sidewall of the smaller model (Model 2) are upscaled to the larger model (Model 1), these correspond to the lowest peak frequency of the wall vibrations, as well as the natural frequencies of the first mode shape. It could thus be said that the sidewall vibrations were likely to be excited by the pressure fluctuations of the air cavity. However, keeping in mind that the air cavity pressure fluctuations are said to be related to vortex shedding from upstream, the sidewall vibrations were excited by the vortices and the air pocket behind the nappe merely functions as an amplifier of the vibrations.

Lastly, although the wall vibrations were said to be excited by vortex shedding and experience vibration at the first two mode shapes, the vibration amplitudes were relatively low and none of the mode shapes were favoured to such an extent that these would have activated resonant behaviour of the PKW sidewall.

7.5 CONCLUDING REMARKS

The following main conclusions can be drawn based on the findings of this hydraulic model study:

- The PKW physical hydraulic models performed comparable to those in other PKW model studies with similar geometric characteristics.
- Introducing air to the air cavity behind the overflow nappe seemed to have a positive effect on the discharge capacity of the models tested for H/P ≤ 0.10, however for higher discharge capacities the efficiency reduced.
- PKWs can be considered self-aerating for higher headwater levels - in the case of this study for H/P values larger than 0.10 to 0.14. This can be confirmed by the similar

discharge coefficients for both unaerated and aerated conditions, the stabilisation of the air demand and the lack of sub-atmospheric pressures behind the nappe at higher headwater levels.

- Larger aeration pipes automatically entrained more air into the nappe air cavity. The amount of air entrained, as a percentage of flow, was directly related to the size of the aeration pipe, irrespective of model or scale. Other than the amount of air entrained, there was no significant difference between the two aeration pipe sizes. The aeration pipe sizes need to be further investigated.
- Nappe oscillations, characterised as FIV, did not occur for the discharge ranges tested as part of this study (H/P = 0.05 to 0.40). Findings from a parallel study by Denys (2019) on the same larger steel physical hydraulic model, noted that nappe oscillations occur at very low discharges (H/P = 0.006 to 0.01). Introducing air to the cavity behind the nappe, or breaking the nappe, did not alleviate the occurrence of the oscillations but did reduce the intensity of the oscillations. This further confirmed that the air pressure behind the nappe only serves as an amplifier and is not responsible for the onset of vibrations.
- The dynamic pressure analysis revealed that there is some pressure variation in the air cavity behind the nappe. These pressure fluctuations were likely due to the vortices that were shed from upstream of the sidewall and caused enough disturbance to the underside of the nappe to cause a pressure variation. Hence, the artificial introduction of air into the cavity did not have any effect on the frequencies at which the air pressure fluctuated. Only at very high discharges (H > 0.5) did the flow dynamics of the outlet key start to dominate the pressure fluctuations.
- The introduction of air behind the nappe did seem to have a somewhat stabilising effect on the air pressure fluctuations near the tip of the sidewall cavity, however, the data did not produce enough evidence to confirm this finding.
- Artificial aeration had no effect on the vibration frequencies or their intensity of the PKW sidewall for the flow ranges tested. It is considered that the sidewall vibrations were excited by vortex shedding and that the air pocket behind the nappe merely functioned as an amplifier of the vibrations. Furthermore, the first two vibration modes of the sidewall were excited, however, the vibration amplitudes were relatively low and none of the mode shapes was favoured to such an extent that resonant behaviour of the PKW sidewall would have been activated.

8. RECOMMENDATIONS

The following recommendations can be made based on the findings of this hydraulic model study:

- Artificial aeration is most beneficial under low flow conditions with H/P ≤ 0.10 and therefore recommended when the expected discharge over a PKW over its lifecycle will mostly be within this range.
- In terms of operation and hydraulic characteristics, no significant differences were found between the different aeration pipe sizes for this study. It is therefore recommended that the proposed methodology for aeration pipe sizing, as well as the effect of different pipe sizes, be further expanded on.
- If nappe oscillations are expected for low flow conditions artificial aeration can be considered as a mitigation measure to reduce the intensity of the fluctuations. However, it is preferable to either break the nappe entirely or to alter the crest roughness as recommended by previous nappe oscillation studies.

The following are recommended for future hydraulic model studies and research:

- Better observation of the overflow nappe is required to evaluate the suitability of the air demand estimation methodology proposed by Vermeulen *et al.* (2017). This includes *inter alia* measuring of the nappe thickness, nappe width and nappe fall height.
- Measurement of the air pressure along the downstream face of the sidewall in the vibration model, as well as the effect of higher headwater levels (H/P > 0.4) on the air cavity pressure fluctuations.
- Considering that water mass has a damping effect on the natural frequency of the structure, the influence of increased downstream water levels on the vibrations can be evaluated.

9. REFERENCES

Ackers, J. C., Bennet, F. C., Scott, T. A., & Karunaratne, G. (2013). Raising the bellmouth spillway at Black Esk reservoir using Piano Key Weirs. *Proceedings of the 2nd International Workshopon Labyrinth and Piano Key Weirs II - PKW 2013* (pp. 235-242). CRC Press, Taylor & Francis Group.

Anderson, A. A. (2014). *Causes and countermeasures for nappe oscillation: An experimental approach.* Master's thesis, Utah State University.

Anderson, R. M. (2011). *Piano Key Weir Head Discharge Relationships.* Utah State University.

Anderson, R. M., & Tullis, B. P. (2011). Influence of Piano Key Weir geometry on discharge. *Proceedings of the International Conference on Labyrinth and Piano Key Weirs – PKW 2011* (pp. 75-80). CMC Press, Taylor & Francis Group.

Anderson, R. M., & Tullis, B. P. (2011). Piano Key Weir hydraulics. *Proceedings of the 31st Annual USSD Conference* (pp. 1697 - 1707). USSD.

ASCE. (2000). *ASCE Manuals and Reports on Engineering Practice No. 97: Hydraulic Modelling Concepts and Practice.* Virginia: American Society of Civil Engineers (ASCE).

Ausoni, P. (2009). *Turbulent Vortex Shedding from a Blunt Trailing Edge Hydrofoil.* Ph.D. Thesis. École Polytechnique Fédérale de Lausanne.

Binnie, A. M. (1971). The stability of a falling sheet of water. *Proceedings of the Royal Society of London. Series A, Mathematical and Physical*, (pp. 149-163).

Blancher, B., Montarros, F., & Laugier, F. (2011). Hydraulic Comparison Between Piano Key Weirs and Labyrinth Spillways. *Proceedings of the International Conference on Labyrinth and Piano Key Weirs - PKW 2011* (pp. 141–150). CRC Press, Taylor & Francis Group.

Bruno, L., Fransos, D., Coste, N., & Bosco, A. (2010). 3D flow around a rectangular cylinder: A computational study. *Journal of Wind Engineering and Industrial Aerodynamics, 25*(6-7), 263-276.

Calitz, G. (2016). *Aeration of Robertson Splitters through an Internal Gallery of a Dam.* M.Sc Thesis, University of Stellenbosch.

Chadwick, A., Morfett, J., & Borthwick, M. (2013). *Hydraulics in Civil and Environmental Engineering* (5th edition ed.). Florida: Taylor & Francis Group.

Chanson, H. (1994). Hydraulics of Nappe Flow Regime above Stepped Chutes and Spillways. *Australian Civil Engineering Transactions, 36*(1), 69 - 76.

Chanson, H. (1996). *Some hydraulic aspects during overflow above inflatable flexible membrane dam.* University of Queensland.

Chanson, H. (2009). Turbulent air–water flows in hydraulic structures: Dynamic similarity and scale effects. *Environmental Fluid Mechanics, 9*, 125-142.

Chemaly, A. G. (2017). Lessons learned from the planning, design, construction, operation and maintenance (O&M), monitoring and safety evaluation of dams. *Proceedings of the Annual SANCOLD Conference 2017* (pp. 271 - 295). SANCOLD.

Circero, G. M., Delisle, J. R., Lefebvre, V., & Vermeulen, J. (2013). Experimental and numerical study of hydraulic performance of trapezoidal PKW. *Proceedings of the 3rd International Workshop on Labyrinth and Piano Key Weirs II - PKW 2013.* CRC Press, Tayor and Francis Group.

Circero, G. M., Vermeulen, J., & Laugier, F. (2016). Influence of Some Geometrical Parameters on Piano Key Weir Discharge Efficiency. *Proceedings of the 6th International Symposium on Hydraulic Structures* (pp. 350-360). Utah State University.

Crookston, B. M., & Tullis, B. P. (2011). Hydraulic characteristics of labyrinth weirs. *Labyrinth and Piano Key Weirs – PKW 2011* (pp. 25-32). CRC, Taylor & Francis Group.

Crookston, B. M., & Tullis, B. P. (2013). Hydraulic Design and Analysis of Labyrinth Weirs. II: Nappe Aeration, Instability, and Vibration. *Journal of Irrigation and Drainage Engineering, 139*, 371 - 377.

Crookston, B. M., Anderson, A., Shearin-Feimster, L., & Tullis, B. P. (2014). Mitigation Investigation of Flow-induced Vibrations at a Rehabilitated Spillway. *5th International Symposium on Hydraulic Structures 25 - 27 June.* Brisbane: Hydraulic Structures and Society: Engineering Challenges and Extremes.

Denys, F. M. (2019). *Investigation into Flow-induced Vibrations of Piano Key Weirs.* Stellenbosch University.

Denys, F. M. (2015). *Piano Key Weir Spillway Standard Design Principles.* Proceedings of the SANCOLD Conference 2015, pp. 231-239. South African National Committee on Large Dams (SANCOLD).

Denys, F. M. (2018). Transient Hydromechanics of Piano Key Weirs. *Proceedings of the 7th International Symposium on Hydraulic Structures.* IAHR.

Denys, F. M., Basson, G., & Strasheim, J. (2017). Fluid Structure Interaction of Piano Key Weirs. *Proceedings of the 3rd International Workshop on Labyrinth and Piano Key Weirs III - PKW 2017*, (pp. 119-126).

Erpicum, S., Archambeau, P., Dewals, B., Pirotton, M., Tralli, H. '., & Alende, J. (2017). A Piano Key Weir to improve the discharge capacity of the Oule Dam spillway (France). *Procedings of the 3rd International Workshop on Labyrinth and Piano key weirs III - PKW 2017* (pp. 195-204). CRC, Taylor and Francis Group.

Erpicum, S., Archambeau, P., Pirotton, M., & Dewals, B. J. (2014). Geometric parameters influence on Piano Key Weir hydraulic performances. *Proceedings of the 5th International Symposium on Hydraulic Structures.* University of Queensland.

Erpicum, S., Laugier, F., Pfister, M., Pirotton, M., Cicero, G. M., & Schleiss, A. J. (2013a). Labyrinth and Piano Key Weirs II - PKW 2013. *Proceedings of the 2nd International*

Workshop on Labyrinth and Piano Key Weirs II - PKW 2013 (p. 291). CRC Press, Taylor & Francis Group.

Erpicum, S., Machiels, O., Dewals, B. J., Pirotton, M., & Archambeau, P. (2012). Numerical and physical hydraulic modelling of Piano Key Weirs.

Erpicum, S., Machiels, O., Dewals, B., Archambeau, P., & Pirotton, M. (2013). Considerations about the optimum design of PKW. *Proceedings of the International Conference on Water Storage and Hydropower Development for Africa.*

Erpicum, S., Tullis, B. P., Lodomez, M., Archambeau, P., Dewals, B. J., & Pirotton, M. (2016). Scale effects in physical piano key weir models. *Journal of Hydraulic Research, 54*(6), 692-698.

Ervine, D. A., & Elsawy, E. M. (1975). Effect of a Falling Nappe on River Aeration. *16th Congress of the International Associations for Hydraulic Research*, (pp. 390-397). Brazil.

Falvey, H. (1980). *Bureau of Reclamation experience with flow-induced vibrations.* Denver, Colorado: United States Department of the Interior, Bureau of Reclamation.

Glover, R. E., Thomas, C. W., & Hammet, T. F. (1939). *Report on Vibration Studies made at Black Canyon Dam Boise Project.* Colorado: United States Bureau of Reclamation.

Hager, W. H., & Schleiss, A. J. (2009). Constructions hydrauliques, Ecoulements stationnaires [Hydraulic structures, steady flow].

Hanley, S. (2016, June 2016). *MIDE Engineering Solutions*. Retrieved from Vibration Analysis: FFT, PSD, and Spectrogram Basics: https://blog.mide.com/vibration-analysis-fft-psd-and-spectrogram

Hanly, S. (2016, June 16). *MIDE Engineering Solutions*. Retrieved from Vibration Analysis: FFT, PSD, and Spectrogram Basics: http://blog.mide.com/vibration-analysis-fft-psd-and-spectrogram

Heller, V. (2011). Scale effects in physical hydraulic engineering models. *Journal of Hydraulic Research, 49*(3), 293–306.

Hoffman, K. (2011). *Applying the Wheatstone Bridge Circuit.* HBM.

ICOLD Technical Committee on Hydraulics for Dams. (2016). *Bulletin 172 - Technical advancements in spillway design: Progress and innovations from 1985 to 2015.* International Committee on Large Dams .

Johnson, M. C. (2000). Discharge coefficient analysis for flattopped and sharp-crested weirs. *Irrigation Science, 19*(3), 133-137.

Kabiri-Samani, A., & Javaheri, A. (2012). Discharge coefficients for free and submerged flow over Piano Key Weirs. *Journal of Hydraulic Research, 50*, 114-120.

Kiya, M., & Sasaki, K. (1983). Structure of a turbulent separation bubble. *Journal of Fluid Mechanics*, 83-113.

Kobus, H. E. (1980). *Hydraulic modelling.* Hamburg: Paul Parey.

Kyotoh, H. (2002). Incipient oscillations of a sheet of falling water and the instability mechanisms. *Journal of Hydroscience and Hydraulic Engineering, 20*(1), 77-93.

Laugier, F. (2007). Design and construction of the first piano key weir spillway at Goulours Dam. *Hydropower and Dams (5)*, 94 - 100.

Laugier, F., Vermeulen, J., & Lefebvre, V. (2013). Overview of Piano Key Weirs: Experience developed at EDF during the past few years. *Labyrinth and Piano Key Weirs II – PKW 2013 – Erpicum et al. (eds)* (pp. 213 - 226). London: Taylor & Francis Group.

Le Doucen, O., Ribeiro, M. L., Boillat, J. L., Schleiss, A. J., & Laugier, F. (2009). *Etude paramétrique dela capacité des PK-Weirs.* Modèles physiques hydrauliques – outils indispensables du XXIe siècle, SHF, Lyon.

Lefebvre, V., Vermeulen, J., & Blancher, B. (2013). Influence of geometrical parameters on PK-weirs discharge with 3D numerical analysis. *Proceedings of the 2nd International Workshop on Labyrinth and Piano Key Weirs II - PKW 2013* (pp. 49–56). CRC Press, Taylor & Francis Group.

Leite Ribeiro, M., Biere, M., Boillat, J. L., Schleiss, A. J., Signhal, G., & Sharma, N. (2012). Discharge capacity of Piano Key Weirs. *Journal of Hydraulic Engineering, 138*, 199-203.

Leite Ribeiro, M., Bieri, M., Boillat, J., Schleiss, A. J., Delorme, F., & Laugier, F. (2009). Hydraulic Capacity Improvements of Existing Spillways - Design of Piano Key Weirs. *Proceedings of the ICOLD Conference 2009.* ICOLD.

Leite Ribeiro, M., Boillat, J. L., Schleiss, A., Laugier, F., & Albalat, C. (2007). Rehabilitation of St-Marc Dam - Experimental Optimization of a Piano Key Weir. *Proceedings of the 32nd Congress of IAHR.* International Symposium on Hydraulic Structures.

Leite Ribeiro, M., Pfister, M., & Schleiss, A. J. (2013). Overview of Piano Key weir prototypes and scientific model investigations. *Proceedings of the 2nd International Workshop on Labyrinth and Piano Key Weirs II - PKW 2013* (pp. 273-281). CRC Press, Taylor & Francis Group.

Leite Ribeiro, M., Pfister, M., Boillat, J. L., Schleiss, A. J., & Laugier , F. (2012b). Piano Key Weirs as efficient spillway structure. *Proceedings of the 24th Congress on Large Dams Q94 R2*, (pp. 176-186). Kyoto, Japan.

Leite Ribeiro, M., Pfister, M., Schleiss, A. J., & Boillat, J. (2012a). Hydraulic design of A-type Piano Key Weirs. *Journal of Hydraulic Research, 50*, 400–408.

Lempérière, F. (2009). *New Labyrinth weirs triple the spillways discharge*. Retrieved from Hydrocoop: Dams, Piano Keys Weirs, Tidal Energy & Energy Storage: http://www.hydrocoop.org/new-labyrinth-weirs-triple-the-spillways-discharge

Lempérière, F., & Ouamane, A. (2003). The Piano Keys Weir: A New Cost-effective Solution for Spillways. T*he International Journal on Hydropower and Dams*, Vol. 10, no. 5, pp. 144-149.

Lempérière, F., & Ouamane, A. (2006). Design of a new economic shape of weir. *Proceedings of the International Symposium on Dams in the Societies of the 21st Century*, (pp. 463-470). Barcelona.

Lempérière, F., Ouamane, A., & Vigny, J. P. (2013). Piano Key Weirs (PK weirs) could be used for most African Spillways. Retrieved from http://www.hydrocoop.org/piano-keys-weirs-could-be-used-for-most-african-spillways

Lempérière, F., Vigny, J. P., & Ouamane, A. (2011). General comments on Labyrinths and Piano Key Weirs: the past and present. *Proceedings of the International Conference on Labyrinth and Piano Key Weirs - PKW 2011* (pp. 17 - 24). CRC Press, Taylor & Francis Group.

Levin, L. (1968). *Formulaire des Conduites Forcées, Oléoducs at Conduits d'Aération (Handbook of Pipes, Pipelines and Ventilation).* Paris, France: Dunod.

Lodomez, M., Crookston, B. M., Tullis, B. P., & Erpicum, S. (2018). Mitigation Techniques for Nappe Oscillations on Free-Overfall Structures. *Journal of Hydraulic Engineering, 145*(2).

Lodomez, M., Pirotton, M., Dewals, B., Archambeau, P., & Erpicum, S. (2018a). Nappe oscillations on free-overfall structures: Experimental analysis. *Journal of Hydraulic Engineering, 144*(3).

Lodomez, M., Tullis, B. P., Dewals, B., Archambeau, P., Pirotton, M., & Erpicum, S. (2019). Nappe Oscillations on Free-Overfall Structures: Size Scale Effects. *Journal of Hydraulic Engineering, 145*(6).

Lux, F., & Hinchliff, D. (1985). Design and construction of labyrinth spillways. *15th Congress ICOLD Vol. IV, Q59-R15*, (pp. 249-274). Lausanne, Switzerland,.

Mabela, M. J. (2017). The raising of Hazelmere Dam using a Piano Key Weir. *Procedings of the Annual SANCOLD Conference 2017* (pp. 181 - 193). SANCOLD.

Machiels, O. (2012). *Experimental study of the hydraulic behaviour of Piano Key Weirs. PhD thesis.* HECE Research Unit, University of Liège, Belgium.

Machiels, O., Dewals, B., Archambeau, P., Pirotton, M., & Erpicum, S. (2013). An analytical approach for Piano Key weir hydraulic design. *Proceedings of the 2nd International Workshop on Labyrinth and Piano Key Weirs II – PKW 2013* (pp. 131 - 138). CRC Press, Taylor & Francis Group.

Machiels, O., Erpicum, S., Archambeau, P., Dewals, B. J., & Pirotton, M. (2009). Large scale experimental study of piano key weirs. *Proceedings of the 33rd Congress of IAHR.* International Symposium on Hydraulic Structures.

Machiels, O., Erpicum, S., Archambeau, P., Dewals, B., & Pirotton, M. (2013a). Parapet Wall Effect on Piano Key Weir Efficiency. *Journal of Irrigation and Drainage Engineering*, 506-511.

Machiels, O., Erpicum, S., Dewals, B. J., Archambeau, P., & Pirotton, M. (2011). Experimental observations of flow characteristics over a Piano Key Weir. *Journal of Hydraulic Research, 49*(3), 359-366.

Machiels, O., Pirotten, M., Archambeau, P., Dewals, B., & Erpicum, S. (2014). Experimental parametric study and design of Piano Key Weirs. *Journal of Hydraulic Research, 52*, 326-335.

Mehboudi, A., Attari, J., & Hosseini, S. A. (2017). Flow regimes over trapezoidal piano key weirs. *Proceedings of the 3rd International Workshop on Labyrinth and Piano Key Weirs II - PKW 2017* (pp. 65-73). CRC Press.

Myburg, M. (2016). *Design Guidelines for Multi-Stage Outlet Structures situated in Stormwater Attenuation Facilities of Residential Developments in South Africa: Physical Model Investigation.* Department of Civil Engineering. Stellenbosch: Stellenbosch University.

National Instruments. (2018, January 08). Retrieved from Determining Size and Sample Frequency for Analyzing Analog Signals: https://knowledge.ni.com/KnowledgeArticleDetails?id=kA00Z0000019MIYSA2

Naudasher, F., & Rockwell, D. (2012). *Flow Induced Vibrations: An Engineering Guide.* Courier Corporation.

Novak, P., Guinot, V., Jeffrey, A., & Reeve, D. E. (2010). Hydraulic Modelling: An Introduction: Principles, methods and applications.

Paxson, G., Campbell, D., & Monroe, J. (2011). *Evolving Design Approaches and Considerations For Labyrinth Spillways.* U.S. Society on Dams, San Diego.

Paxson, G., Tullis, B. P., & Campbell, D. (2012). Potential Applications for Piano Key Weirs at Dams in the United States.

Paxson, G., Tullis, B. P., & Hertel, D. J. (2013). Comparison of Piano Key Weirs with labyrinth and gated spillways: Hydraulics, cost, constructability and operations. *Proceedings of the 2nd International Workshop on Labyrinth and Piano Key Weirs II - PKW 2013* (pp. 123-130). CRC Press, Taylor and Francis Group.

Pfister, M., & Chanson, H. (2012). Scale effects in physical hydraulic engineering models By VALENTIN HELLER. *Journal of Hydraulic Research, 49*(3), 293-306.

Pfister, M., & Schleiss, A. J. (2013). Comparison of hydraulic design equations for A-type Piano Key weirs . *Proceedings of the Conference on Water Storage and Hydropower Development for Africa .* Addis Ababa, Ethiopia.

Pfister, M., Erpicum, S., Machiels, O., Schleiss, A., & Pirotton, M. (2012). Discharge coefficient for free and submerged flow over Piano Key weirs. *Journal of Hydraulic Research, 50*, 642-645.

Pfister, M., Schleiss, A. J., & Tullis, B. P. (2013). Effect of driftwood on hydraulic head on Piano Key Weirs. *Proceedings of the 2nd International Workshop on Labyrinth and Piano Key Weirs II - PKW 2013* (pp. 255-264). CRC Press, Taylor & Francis Group.

Phillips, M. A., & Lesleighter, E. J. (2013). Piano Key Weir spillway: Upgrade option for a major dam. *Proceedings of the 2nd International Workshop on Labyrinth and Piano Key Weirs II – PKW 2013* (pp. 159-168). CRC, Taylor & Francis Group.

Pinchard, T., Farges, J. L., Boutet, J. M., Lochu, A., & Laugier, F. (2013). Spillway capacity upgrade at Malarce dam: Construction of an additional piano key weir spillway. *Labyrinth and Piano Key Weirs II – PKW 2013 – Erpicum et al. (eds)* (pp. 243 - 252). London: Taylor & Francis Group.

PKW 2017. *3rd International Workshop on Labyrinth and Piano Key Weirs - PKW 2017*. Retrieved from http://www.pk-weirs.ulg.ac.be/?q=content/world-register-pkw

Pralong, J., Montarros, F., Blancher, B., & Laugier, F. (2011). A sensitivity analysis of Piano Key Weirs geometrical parameters based on 3D numerical modelling. *Proceedings of the International Conference on Labyrinth and Piano Key Weirs - PKW 2011* (pp. 133–139). CRC Press, Taylor & Francis Group.

Pralong, J., Vermeulen, J., Blancher, B., Laugier, F., Erpicum, S., Machiels, O., . . . Schleiss, A. J. (2011a). A naming convention for the Piano Key Weirs geometrical parameters. *Proceedings of the International Conference on Labyrinth and Piano Key Weirs – PKW 2011* (pp. 271-278). CMC Press, Taylor & Francis Group.

Safarzadeh, A., & Noroozi, B. (2017). 3D Hydrodynamics of Trapezoidal Piano Key Spillways. *International Journal of Civil Engineering, 15*(1), 89-101.

Schleiss, A. J. (2011). From Labyrinth to Piano Key Weirs – A historical review. *Proceedings of the International Conference on Labyrinth and Piano Key Weirs - PKW 2011*, pp. 3-15. CRC Press, Taylor & Francis Group.

Tenaud, C., Podvin, B., Fraigneau, Y., & Daru, V. (2016). On wall pressure fluctuations and their coupling with vortex dynamics in a separated-reattached turbulent flow over a blunt plate. *International Journal of Heat and Fluid Flow*.

TruTechTools. (2016, 11 8). Retrieved from Measuring airflow with a hot-wire anemometer: https://www.trutechtools.com/Measuring-Airlfow-with-a-Hot-Wire-Anemometer_c_1001.html

Tullis, J. P., Amanian, N., & Waldron, D. (1995). Design of Labyrinth Spillways. *Journal of Hydraulic Engineering*, Vol. 121, no. 3, pp. 247-255.

University of Pretoria. (2004). *SHC 320: Physical Models.* Pretoria: Department of Civil & Biosystems Engineering .

USBR. (1987). *Design of Small Dams - 3rd Edition.* United States Bureau of Reclamation.

van Deventer, N. J., Matlala, J., Mulder, E., & Hoosen, S. (2015). Tzaneen Dam Raising: Hydraulic Model Study. *Proceedings of the SANCOLD Conference 2015*, pp. 223-230. South African National Committee on Large Dams (SANCOLD).

Vermeulen, J., Lassus, C., & Pinchard, T. (2017). Design of a Piano Key Weir Aeration Network. *Proceedings of the 3rd International Workshop on Labyrinth and Piano Key*

Weirs III - PKW 2017, Qui Nhon, Vietnam, 22-24 February 2017 (pp. 127-134). London: Taylor & Francis Group.

Vermeulen, J., Laugier, F., Faramond, L., & Gille, C. (2011). Lessons learnt from design and construction of EDF first Piano Key Weirs*. Proceedings International Workshop on Labyrinth and Piano Key Weirs - PKW 2011*. CRC Press, Taylor & Francis Group.

Vermeulen, J., Pinchard, T., Lassus, C., & Laugier, F. (2017a). Développement d'une nouvelle méthode de dimensionnement des. *Hydraulique des barrages et des digues* (pp. 550-558). Comité Francais des barrages et reservoirs.

Webber, N. (1979). *Fluid mechanics for civil engineers.* London: Chapman and Hall.

Wormleaton, P. R., & Soufiani, E. (1998). Aeration performance of triangular platform labyrinth weirs. *Journal of Environmental Engineering, 124*(8), 709-719.

Appendix A

Piano Key Weir Hydraulics and Design

A.1 FACTORS AFFECTING THE DISCHARGE EFFICIENCY

Several studies have been undertaken to determine the effect of the various geometrical parameters on the discharge capacity of PKWs.

The dominant geometrical parameters affecting the discharge efficiency are:

- The developed crest length, L;
- The total weir width, W;
- The upstream head, H_T; and
- The upstream weir height, P_i.

These parameters can be summarised dimensionless ratios L/W and H_T/P_i and can be used to empirically determine the discharge capacity of PKW with an 83% accuracy (Leite Ribeiro, Pfister, & Schleiss, 2013). Although other parameters also play a role on the discharge efficiency, their individual effect is generally less than 5% (Denys, 2019). These other parameters include the key height P, the inlet to outlet key ratios W_i/W_o and the overhang ratios B_i/B_o (Erpicum, Archambeau, Pirotton, & Dewals, 2014). A single optimal value for the parameters, however, do not exist and depend on the combination of other parameters.

The discharge per PKW unit, given that the units and approach conditions are identical, is not sensitive to number of PKW units (Leite Ribeiro, Pfister, Boillat, Schleiss, & Laugier , 2012b).

A.1.1 CREST LENGTH MAGNIFICATION RATIO L/W

The crest length magnification ratio L/W ranges from 4 to 8 in existing PKWs (Pfister, Erpicum, Machiels, Schleiss, & Pirotton, 2012), however, a ratio of 5 seems to be the most cost effective and have been implemented in most existing PKWs (Lempérière, Vigny, & Ouamane, 2011) (Leite Ribeiro, Pfister, & Schleiss, 2013). **Figure A.1** shows the effect of magnification ratio L/W on the discharge enhancement ratio r.

A.1.2 HEAD TO WEIR HEIGHT RATIO, H_T/P_I

As mentioned, PKWs operate most effective for lower heads. PKW have been tested for H_T/P_i ratios ranging from 0 to 3, however, to date no PKW have been constructed to operate at H_T/P_i ratios higher than 0.8. Most PKWs implemented to date have a H_T/P_i ratio of 0.3 at the maximum design flow rate (Leite Ribeiro, Pfister, & Schleiss, 2013). With reference to **Figure 2.18** and **Figure 2.19** in the main text, the decrease in discharge efficiency (in terms of the discharge coefficient) is evident for higher heads.

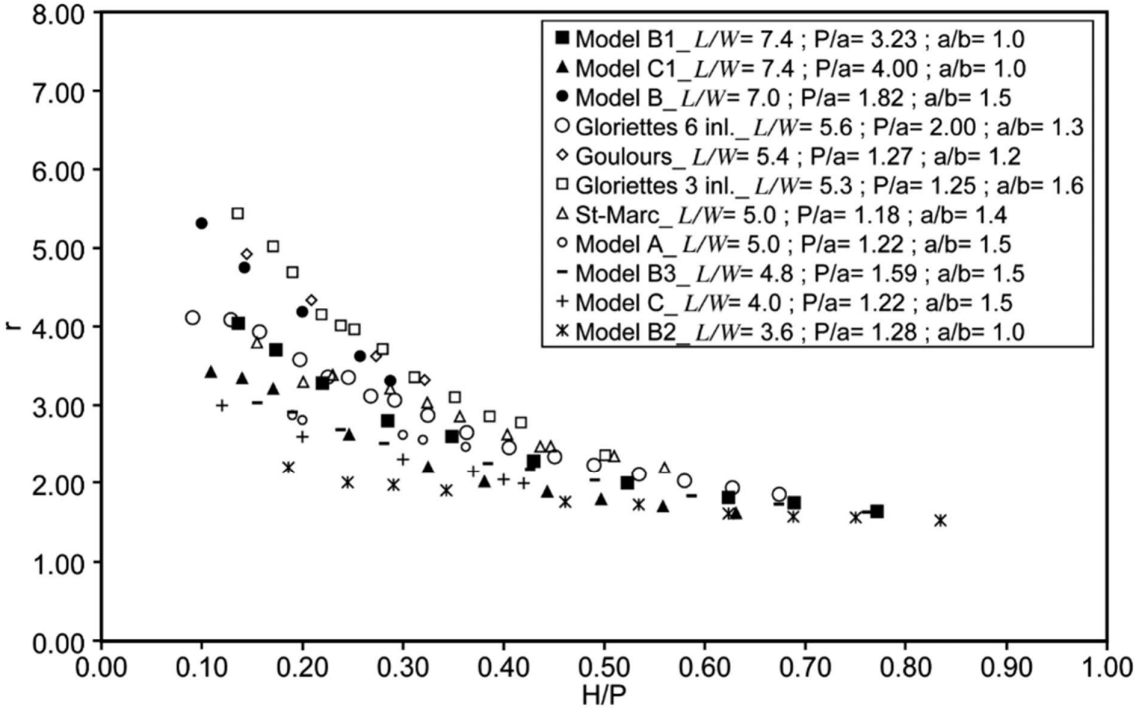

Figure A.1: Effect of magnification ratio L/W on the discharge enhancement ratio (Leite Ribeiro, et al., 2012)

A.1.3 KEY HEIGHT TO UNIT WIDTH RATIO P/W_U

Based on extensive research done by Machiels *et al.* (2014) for standard L/W ratios equal to 5, the optimum key height to unit width ratio, P/W_u, is approximately 1.33. For "low" PKW heights, where $P/W_u < 1$, the discharge capacity increases as the head increases. For "high" PKWs (P/W_u), the discharge capacity becomes virtually independent of the PKW height.

In the case of high PKWs, the outlet key can accommodate the flow from the adjacent inlet keys for a large range of heads. For PKWs with P/W_u ratios smaller than 0.5, the slope of the outlet key is insufficient to allow supercritical conditions and thus results in a reduced efficiency. However, a PKW with a P/W_u ratio of 1.3 might not comply with other design requirements and be practical to construct. A P/W_u ratio of 0.5 is considered a more economical design, especially for dam rehabilitation projects (Machiels, 2012).

Figure A.2 shows that low PKWs are more efficient for a given dimensionless head, whereas for a given head, the overall efficiency increases with increasing keys height for P/W_u ratios lower or equal to 1.33 (refer to **Figure A.3**).

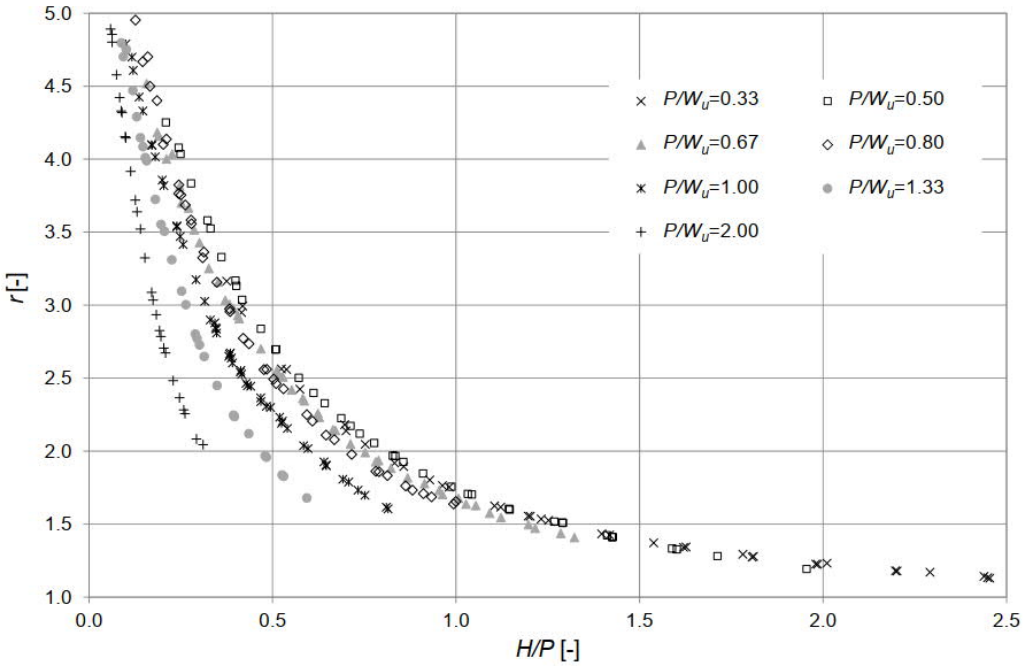

Figure A.2: Enhancement ratio vs. non-dimensional upstream head for different P/W_u ratios (Erpicum, Archambeau, Pirotton, & Dewals, 2014)

Above a P/W_u ratio of 1.33, there is no difference in the discharge efficiency. These comparisons also imply that high PKWs require lower heads to discharge the same flow per unit length compared to low PKWs (Erpicum, Archambeau, Pirotton, & Dewals, 2014).

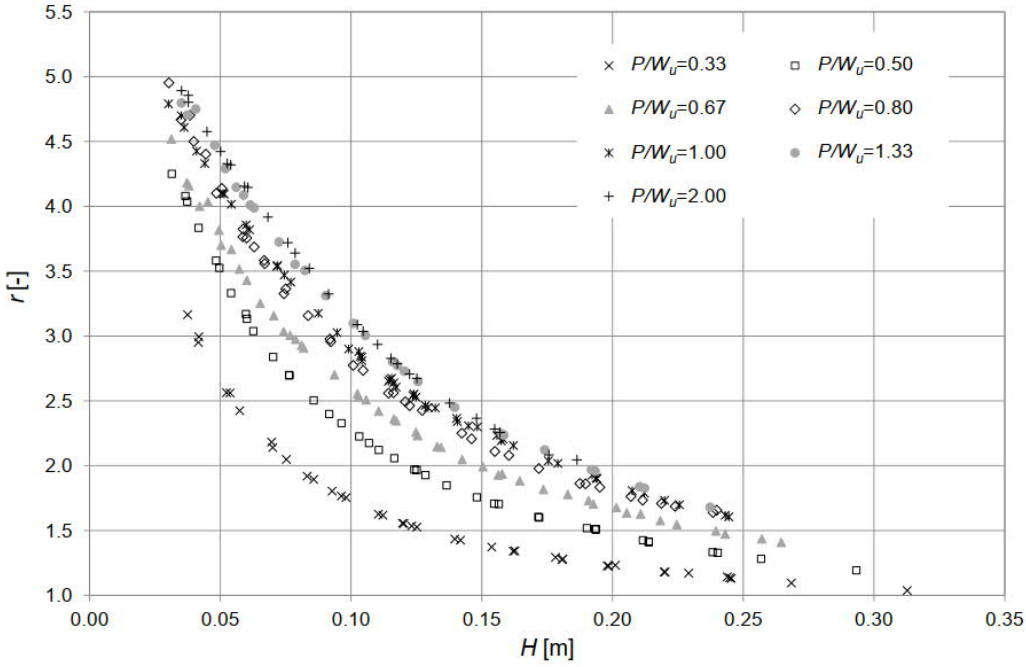

Figure A.3: Enhancement ratio vs. head for different P/W_u ratios (Erpicum, Archambeau, Pirotton, & Dewals, 2014)

A.1.4 INLET AND OUTLET KEY WIDTHS

A higher inlet to outlet key ratio W_i/W_o results in higher discharge efficiency (Le Doucen, Ribeiro, Boillat, Schleiss, & Laugier, 2009). According to Machiels *et al.* (2014), the inlet key cross-section serves as the "engine" of the PKW and the outlet key as the" brake". An increase in the inlet key area reduces the flow velocity and overall effect of flow contraction, and thus reduces the energy loss and increases the efficiency. A too small outlet key and too flat outlet slope loses its ability to collect the additional flow from the adjacent inlet keys causing local submergence and ultimately results in a reduced efficiency.

Several studies have been conducted to determine the optimum W_i/W_o ratio. Although the optimum ratio is between 1.25 and 1.6 (Machiels, Pirotten, Archambeau, Dewals, & Erpicum, 2014), ratios of between 1.0 to 1.5 have been generally used in PKW prototypes (Leite Ribeiro, Pfister, & Schleiss, 2013).

For high PKWs ($P/W_u > 1$), W_i/W_o ratios between 1.29 and 1.57 give the highest discharge efficiency, whereas for low PKWs ($P/W_u < 1$) a W_i/W_o ratio of 1 results in the same discharge efficiency as for a high weir with W_i/W_o ratios between 1.29 and 1.57 as shown in **Figure A.4** (Erpicum, Archambeau, Pirotton, & Dewals, 2014). These results are for a L/W ratio equal to 5.

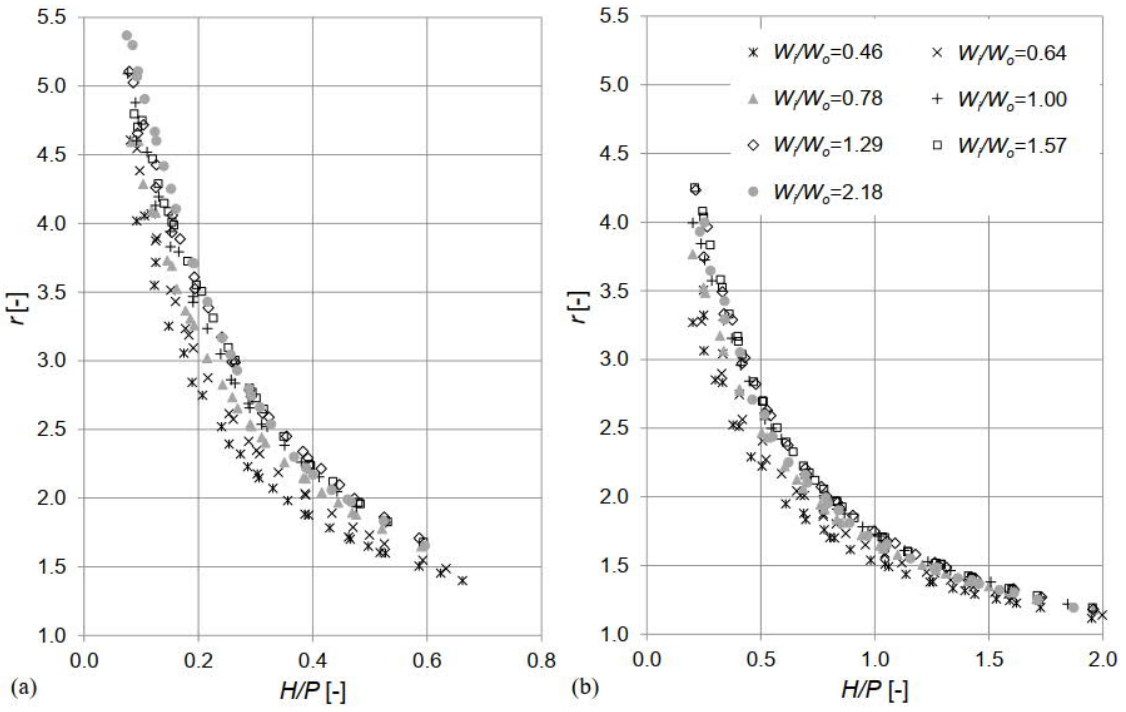

Figure A.4: Effect of the key width ratio on the discharge increase ratio. P/W_u=1.33 (a) and P/W_u=0.50 (b) (Erpicum, Archambeau, Pirotton, & Dewals, 2014)

A.1.5 OVERHANG LENGTHS RATIO, B_O/B_I AND SIDEWALL ANGLES

The main increase in PKW hydraulic capacity compared to labyrinth weirs is attributed to the overhangs – more so, the upstream overhang than the downstream overhang (Kabiri-Samani & Javaheri, 2012). Hydraulic model studies showed that the discharge efficiency of PKW models with only an upstream overhang (Type B) is 12% more than models with symmetrical overhangs. However, models with asymmetrical overhangs is 7% less efficient than models with symmetrical overhangs (Lempérière & Ouamane, 2006). The upstream overhang increases the inlet flow area and wetted perimeter and thus results in reduced inlet velocities, flow contraction and energy loss. This partially explains why a Type B PKW has a higher discharge efficiency compared to a Type A PKW (Anderson & Tullis, 2011).

According to Erpicum *et al.* (2014) and Machiels (2014) a B_o/B_i ratio of 3 yields the highest discharge efficiency for high PKWs with an L/W ratio equal to 5, except for very low heads. For low PKWs, the discharge efficiency is the same for B_o/B_i ratios of 1 and 3. Refer to **Figure A.5**.

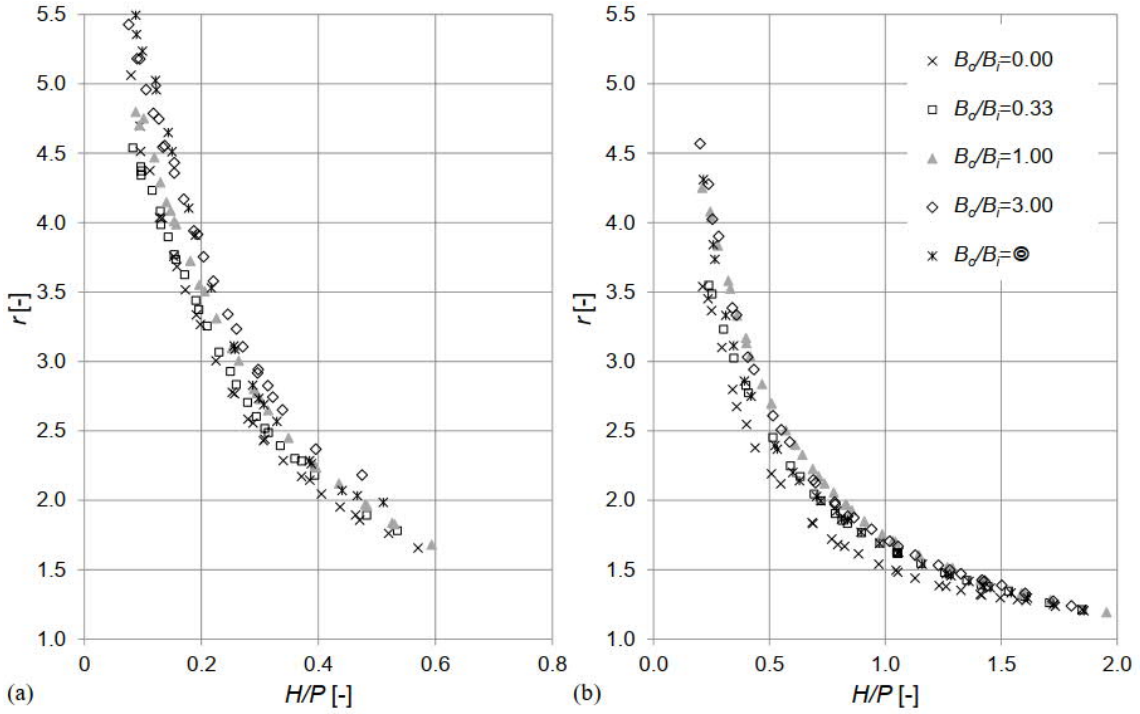

Figure A.5: Effect of overhang lengths ratio on the discharge increase ratio. P/W_u=1.33 (a) and P/W_u=0.50 (b) (Erpicum, Archambeau, Pirotton, & Dewals, 2014)

Schleiss (2011) stated that narrowing the inlet key and widening the outlet key with sidewall angles, the discharge efficiency of a PKW can potentially be increased. The physical hydraulic model study conducted for the raising of Tzaneen Dam comprised of a combination of a labyrinth weir and a PKW (**Figure A.6**). The hydraulic model results showed that PKW-

Labyrinth combination, with sidewall angles of 12°, had a 10% lower head for the same unit discharge compared to a traditional PKW (van Deventer, Matlala, Mulder, & Hoosen, 2015).

Hydraulic model studies by Electricité de France (EDF) indicated that the discharge efficiency of a PKW with a sidewall angle of 5° and wider inlet key compared to outlet key (W_i>W_o), is 5 to 20% more efficient than a Type A PKW with the same L/W ratio at lower heads (Circero, Delisle, Lefebvre, & Vermeulen, 2013).

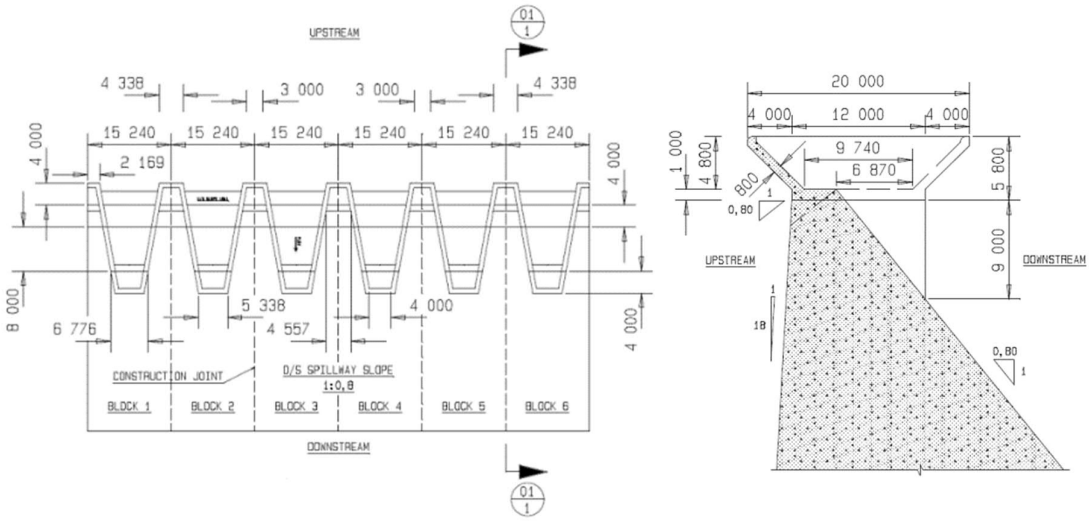

(a) (b)

Figure A.6: Plan view (a) and section view (b) of Tzaneen Dam modified PKW geometry (van Deventer, Matlala, Mulder, & Hoosen, 2015)

A.1.6 WALL THICKNESS AND CREST SHAPE

Like any spillway, the crest thickness and shape affect the discharge efficiency of PKW, especially for low heads. Experimental studies by Machiels *et al.* (2009) showed a decrease in the discharge coefficient compared to the initial experimental study results by Lempérière & Oumane (2006) for H/P < 0.15. The reason being that the models used by Lempérière & Oumane (2006) was constructed with steel plates (negligible wall thickness) whereas the models used by Machiels *et al.* (2009) was constructed from Polyvinyl Chloride (PVC) plates which better represented the concrete wall thicknesses of existing PKWs. According to Blancher *et al.* (2011), as well as Laugier *et al.* (2013), thicker walls can reduce the discharge efficiency by 10 to 15% for a specific discharge. However, one should consider the practicality of constructing thin walled elements.

Leite Ribeiro *et al.* (2007) investigated the effect of the crest shape as part of the hydraulic model studies for St Marc Dam, France. Three crest shapes were investigated – flat, upstream quarter rounded, and downstream quarter rounded. The flat and upstream quarter rounded

crests had higher discharge efficiencies compared to the downstream quarter rounded crest at low flows. The nappe starts separating from the sidewalls of the inlet key for H/P > 0.11 in the case of a flat crest and for H/P > 0.07 for an upstream quarter rounded crest (**Figure A.7**). For higher heads the crest shape is negligible.

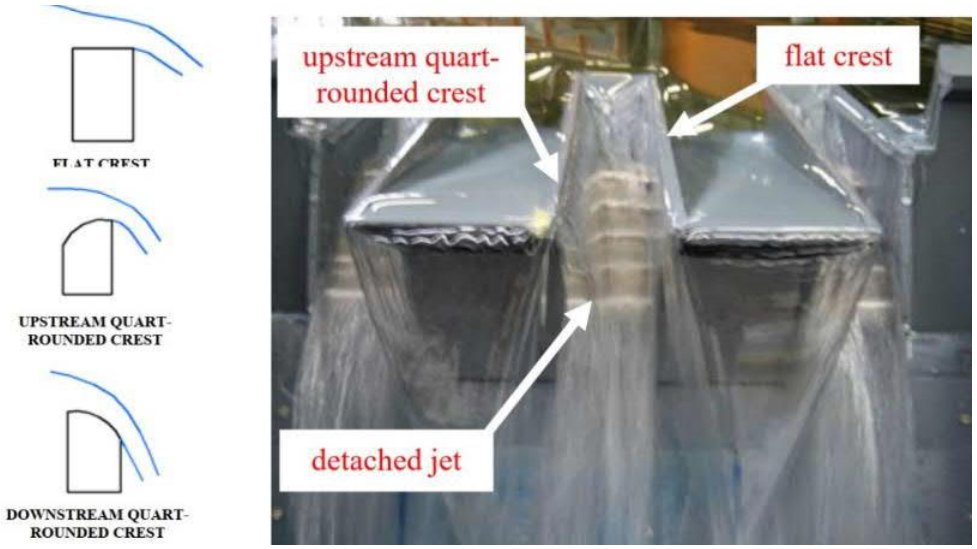

Figure A.7: Effect of crest shape on nappe behaviour (Leite Ribeiro M. L., Boillat, Schleiss, Laugier, & Albalat, 2007)

Half-round or quarter-round upstream crests on the lateral walls, compared to flat crests, can increase the discharge efficiency of PKW at low heads by up to 20%, however, the gain in efficiency reduces as the head increases above H/P > 0.3 (Circero, Vermeulen, & Laugier, 2016). For optimum discharge efficiency it is recommended that the crests be rounded on the upstream side (radii of curvature range from 0.5 to 1 x the wall thickness) and sharp crested on the downstream side (Denys, 2019).

A.1.7 PARAPET WALLS

Based on research by Machiels *et al.* (2014) it revealed that the PKW efficiency is mainly attributed by its height and not by the key slope. Several studies have shown that placing a parapet wall on the upstream crest of the outlet key increases the discharge efficiency of PKWs. The parapet wall streamlines the approach flow into the outlet key, increases the outlet key volume and ultimately the discharge efficiency due to key being able to operate under drowned conditions for longer (Vermeulen, Laugier, Faramond, & Gille, 2011) (Machiels, Erpicum, Archambeau, Dewals, & Pirotton, 2013a). Parapet walls on the downstream crest of the inlet key has a marginal effect on the discharge efficiency.

However, the effect of a parapet wall is negligible for PKWs with an optimal wall height. The discharge efficiency is also similar for a PKW, without a parapet wall, compared to a PKW with

parapet wall and the same total height (Machiels, Erpicum, Archambeau, Dewals, & Pirotton, 2013a).

A.1.8 NOSE UNDER UPSTREAM OVERHANG OF OUTLET KEY

A “nose” under the upstream overhang of the outlet key (**Figure A.8**) have shown to streamline the approach flow into the inlet key, reduce energy losses and vortex shedding, and ultimately increases the PKW discharge efficiency (Denys, 2015). Although no guidelines have been developed for the design of these noses, the shape of the nose should be such that it guides flow into the inlet keys without generating a wake or separation bubble (Lefebvre, Vermeulen, & Blancher, 2013). The general nose shapes that have been implemented to date are triangular, circular, tapered triangular and triangular extruded (Laugier, Vermeulen, & Lefebvre, 2013).

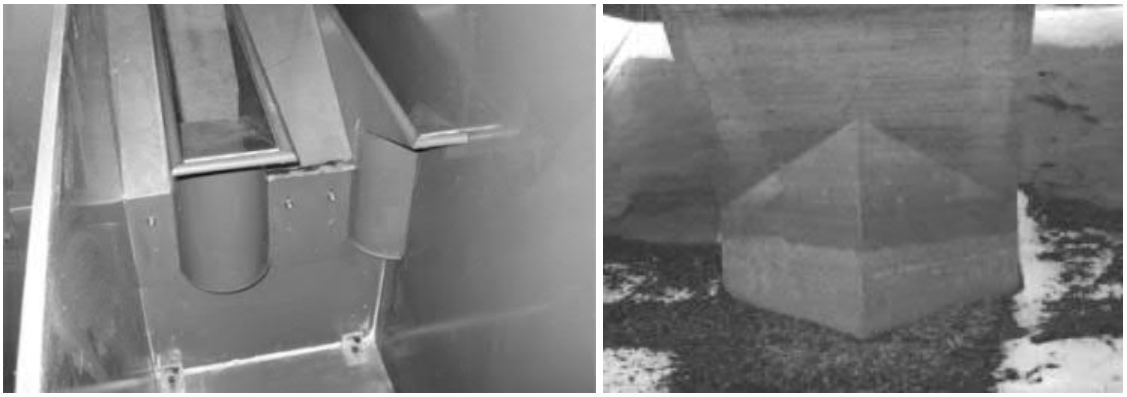

(a) (b)

Figure A.8: Circular nose in hydraulic model study (a) (Leite Ribeiro, Pfister, Schleiss, & Boillat, 2012a) and Triangular nose at Goulours Dam (b) (Laugier, Vermeulen, & Lefebvre, 2013)

A.1.9 SUBMERGENCE AND TAIL WATER LEVEL

Submergence occurs when the downstream water level is at the same level or higher than the crest level and increases the upstream headwater level. PKWs are generally installed on top of dams and therefore not affected by submergence (ICOLD Technical Committee on Hydraulics for Dams, 2016). If indeed submerged, in the case of in-channel or in-river PKWs, they are not significantly influenced and can operate under higher efficiency for submerged conditions compared to other weir types due to their unique flow patterns (Schleiss, 2011).

Submergence only directly affects the most downstream portion of the crest of the weir (outlet key slope). The upper lateral and upstream crests are less affected due to the higher upstream head creating enough momentum to push the downstream water level further downstream and allowing the upper crest positions to operate under more ideal conditions (Denys, 2019).

PKW behaviour under submerged conditions are sensitive to geometry and type. According to hydraulic model studies by Kabiri-Samani & Javaheri (2012), the discharge efficiency is affected by submergence for downstream head[3] to upstream head ratios, H_d/H larger than 0.6 – refer to **Figure A.9**[4].

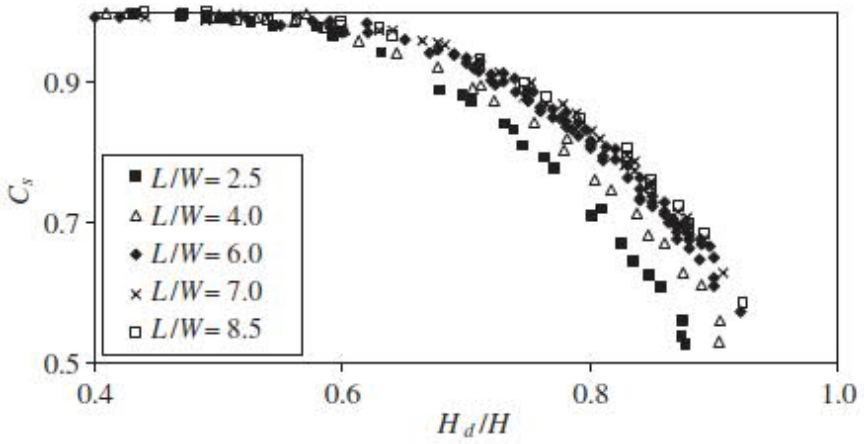

Figure A.9: Effect of submergence on the PKW discharge efficiency (Kabiri-Samani & Javaheri, 2012)

A.1.10 DEBRIS AND DRIFT WOOD

PKWs have been found to be relatively insensitive to floating debris – washing most debris downstream during larger flows and if not, still retains 75 to 80% of its discharge capacity (Pfister, Schleiss, & Tullis, 2013). This make PKW generally safe in afforested catchments (Denys F. M., Piano Key Weir Spillway Standard Design Principles, 2015).

[3] Downstream water level above weir crest
[4] C_s = Discharge reduction factor
$C_s = Q_s/Q$, where Q_s = submerged flow discharge

Appendix B

Physical hydraulic modelling and scaling

B HYDRAULIC MODELLING AND SCALING

Hydraulic models are widely used to investigate the design and performance of hydraulic structures, as well as complex flow situations and sediment transport, which cannot necessarily be determined analytically or with computer simulations. A hydraulic model is a scaled representation of the full-scale prototype and can be categorised as either a design model or a process model. Design models are used to evaluate the design performance of complex prototype situations. Process models are used to simulate specific generic physical processes, and hence the boundary conditions and scales are specified to minimise laboratory and scale effects, discussed later (ASCE, 2000).

The relationship between the performance of the scaled hydraulic model and the prototype is governed by laws of hydraulic similitude, which includes the geometric, kinematic and dynamic similarity, discussed in more detail in **Section B.2**. Hydraulic similitude is based on the interdependency of the variables obtained in a set of dimensionless parameters through dimensional analysis. The contributing variables include the dimensions of the model and prototype, flow velocity, pressure, shear stress, specific weight, mass density, dynamic viscosity etc. The dimensionless parameters include, *inter alia*, the Froude number, Reynolds number, Euler number and the Weber number (University of Pretoria, 2004).

Webber (1979) and the ASCE (2000) describes four laws of hydraulic uniformity that exist based on four main forces presented in the dimensionless parameters:

- Froude's Law: Gravity;
- Reynolds's Law: Fluid viscosity;
- Weber's Law: Surface tension; and
- Euler's Law: Elasticity.

These laws are described in **Section B.1.1**. However, it should be noted that in most physical model cases, the gravitational and inertial forces are the dominant forces, implying that Froude's Law is mostly used to scale the physical models (Webber, 1979) (Chanson, 2009).

Simultaneous compliance with all the laws of hydraulic similitude, and hence to accurately simulate all flow processes of the prototype in the model, is impossible and some discrepancies in scaling the results from the model to the prototype are unavoidable. These discrepancies are referred to as scale effects. The severity of scale effects increases as the ratio of the prototype to model size increases and as the number of the physical processes simulated increases (Chanson, 2009).

Additionally, laboratory effects should also be considered. These effects refer to limitations in space, model constructability, instrumentation and incorrect simulation of boundary conditions (Chanson, 2009).

It is therefore recommended to select the scale of the hydraulic model based on the available laboratory floor space and the dominant forces that will be present and applicable similitude laws. The similarity requirements for the PKW physical hydraulic model are described in **Section B.1.2**.

B.1 HYDRAULIC SIMILARITY

B.1.1 Geometric similarity

The geometric similarity refers to the similarity in geometry between the model and prototype. The ratio between all corresponding length dimensions in the model and prototype are equal as per the following relationship (ASCE, 2000):

$$L_r = \frac{L_p}{L_m} \qquad \text{B-1}$$

Where:

L	Linear dimension (m)
r	Ratio
m	Model
p	Prototype

This length ratio is referred to as the “scale factor (λ)”. Consequently, the area ratio and the volume ratio are as per Equation B-2 and B-3:

$$A_r = {L_r}^2 \qquad \text{B-2}$$

$$V_r = {L_r}^3 \qquad \text{B-3}$$

Where:

A	Area (m^2)
V	Volume (m^3)

B.1.2 Kinematic similarity

The kinematic similitude, or the similarity of fluid motion, implies that the velocity and the acceleration ratios are constant at all equivalent geometric points of the model and prototype and at equivalent times (ASCE, 2000). Refer to the following relationships:

$$v_r = \frac{v_p}{v_m} = \frac{L_r}{T_r} \qquad \text{B-4}$$

$$a_r = \frac{a_p}{a_m} = \frac{v_r}{T_r} = \frac{L_r}{{T_r}^2} \qquad \text{B-5}$$

$$T_r = \frac{T_p}{T_m} \quad \text{B-6}$$

Where:

v	Velocity (m/s)
a	Acceleration (m^2/s)
T	Time (s)

If the kinematic similarity is fulfilled, the flow patterns are geometrically similar at corresponding times.

B.1.3 Dynamic similarity

Dynamic similarity refers to the similarity of the forces within the model and prototype that influence fluid motion. Forces include pressure, gravity, viscosity, surface tension and elasticity, as well as friction in some cases. These forces must have the same ratio at all equivalent geometric points of the model and prototype and must act in the same direction for dynamic similarity to apply. The force ratio can be expressed as (ASCE, 2000):

$$F_r = M_r a_r \quad \text{B-7}$$

$$F_r = \rho_r {L_r}^2 {v_r}^2 \quad \text{B-8}$$

Where:

ρ	Fluid density (kg/m^3)

If the dynamic similarity is satisfied, the kinematic similarity will automatically also be satisfied. Although impossible to achieve complete dynamic similarity, if the gravitational and inertial forces are dominant forces and if the Reynolds number of the flow in the model and prototype can be kept similar by means of turbulent flows, good dynamic similarity can be achieved (Chanson, Turbulent air–water flows in hydraulic structures: Dynamic similarity and scale effects, 2009).

The scale ratios provided in Equations B-1 to B-8 enable the similitude principles to provide scaling laws with which the data obtained from the hydraulic model can be relatively accurately extrapolated (ASCE, 2000).

B.2 HYDRAULIC SIMILITUDE LAWS

B.2.1 Froude's Law

Froude uniformity are mostly used for physical hydraulic model studies, especially for turbulent free surface flow, as gravitational and inertial forces are dominant (Chanson, 2009) (University of Pretoria, 2004), i.e. if the liquid is open to atmosphere somewhere in the model. The law is based on the principle that the Froude number, Equation B-9 (Chadwick, Morfett, & Borthwick, 2013), in the model and prototype is similar.

$$Fr = \frac{v}{\sqrt{gL}} \quad \text{B-9}$$

The corresponding velocities in the model and prototype can be related according to Froude's Law as follows (Webber, 1979):

$$\frac{v_p}{v_m} = \frac{(gL_p)^{\frac{1}{2}}}{(gL_m)^{\frac{1}{2}}} = \lambda^{\frac{1}{2}} \quad \text{B-10}$$

Where:

v	Velocity (m/s)
g	Gravitational acceleration (9.81 m/s^2)
L	Linear dimension (m)
λ	Scale factor

One of the benefits of applying Froude's Law is that the velocity of the model is less than the velocity of the prototype and as such improved measuring instruments, with higher accuracy can be used (Webber, 1979).

If Froude's Law is satisfied, other factors including the frictional losses, surface tension and elasticity are not necessarily scaled down correctly and the dimensionless parameters such as the Reynolds, Webber and Euler numbers are not similar for the prototype and the model. However, for high Reynolds numbers the flow resistance (as a function of the Reynolds number, does not vary as much). Reynolds numbers between 250 and 1000 are recommended for free surface flow models (University of Pretoria, 2004), however, where air entrainment is an important factor to the study, the Reynolds number should at least 1 x 10^5 (Kobus, 1980).

B.2.2 Reynolds' Law

The Reynolds' Law is generally used where laminar friction forces, or viscous shear drag, are important, e.g. in vortices and tidal energy converters. Under Froude similitude, the Reynolds numbers are drastically smaller than in the corresponding prototype flows (Chanson, 2009). The flow can shift from fully turbulent zone to the transition flow zone, or even the laminar zone, as depicted in the Moody diagram for pipes, if scaled using Froude similitude (ASCE, 2000).

The Reynolds number is defined as (Chadwick, Morfett, & Borthwick, 2013):

$$Re = \frac{vL}{\nu} \quad \text{B-11}$$

Where:

Re	Reynolds number
v	Velocity (m/s)
L	Length of homologous sections in model and prototype (m)
v	Kinematic viscosity (≈ 1.13 x 10^{-6} m^2/s for water)

The corresponding velocities in the model and prototype can be related according to Reynolds' Law as follows (Webber, 1979):

$$\frac{v_p}{v_m} = \frac{v_p L_m}{v_m L_p} = \frac{v_p}{v_m}\frac{1}{\lambda} \qquad \text{B-12}$$

Where:

v	Velocity (m/s)
L	Length of homologous sections in model and prototype (m)
v	Kinematic viscosity (≈ 1.13 x 10^{-6} m^2/s for water)
λ	Scale factor

From Equation B-12 the prototype velocity is "x" times greater than that of the model, if the fluid in both is the same.

As mentioned, the Froude and Reynolds laws cannot be satisfied simultaneously. However, it should be bared in mind that viscous forces will only be the dominant force in cases of very low Reynolds numbers.

B.2.3 Weber's Law

Weber's Law is applied in cases when surface tension is important. The influence of surface tension only becomes significant when an air-water boundary exists in structures with small linear dimensions, e.g. physical models with very low heads (weirs), air entrainment, splash or spray (University of Pretoria, 2004) (Webber, 1979).

The Weber number is defined as follows (Chadwick, Morfett, & Borthwick, 2013):

$$We = \frac{\rho v^2 L}{\sigma} \; or \; \frac{v}{\sqrt{\sigma L \rho}} \qquad \text{B-13}$$

Where:

ρ	Fluid density (kg/m^3)
v	Velocity (m/s)
L	Length of homologous sections in model and prototype (m)
σ	Fluid surface tension (≈ 0.073 N/m for water)

Weber's Law depicts the relationship between velocity and surface tension and the corresponding velocities in the model and prototype can be related as follows (Webber, 1979):

$$\frac{v_p}{v_m} = \frac{\sigma_p^{\frac{1}{2}} \rho_m^{\frac{1}{2}} L_m^{\frac{1}{2}}}{\sigma_m^{\frac{1}{2}} \rho_p^{\frac{1}{2}} L_p^{\frac{1}{2}}} = \frac{\sigma_p^{\frac{1}{2}} \rho_m^{\frac{1}{2}}}{\sigma_m^{\frac{1}{2}} \rho_p^{\frac{1}{2}}} \frac{1}{\lambda^{\frac{1}{2}}} \quad \text{B-14}$$

Where:

v	Velocity (m/s)
L	Length of homologous sections in model and prototype (m)
v	Kinematic viscosity (≈ 1.13 x 10^{-6} m^2/s for water)
λ	Scale factor

From Equation B-14 the prototype velocity is $x^{1/2}$ times smaller than that of the model, if the fluid in both is the same.

With reference to the scaled velocities (Equation B-10, B-12 and B-14), the Froude, Reynolds and Weber numbers cannot be simultaneously satisfied. However, as mentioned, viscous forces will only be the dominant force in cases of very low Reynolds numbers and surface tension forces are generally negligible compared to gravitational and inertial forces.

B.2.4 Euler's Law

Euler's law is generally applied when the relationship between velocity and pressure is important, e.g. in the replication of high pressures in pipes or cavitation (Heller, 2011). The Euler number is defined as follows:

$$Eu = \frac{p}{\rho V^2} \; or \; \frac{V}{\sqrt{\frac{2\Delta p}{\rho}}} \quad \text{B-15}$$

Where:

ρ	Fluid density (kg/m^3)
v	Velocity (m/s)
Δp	Change in pressure (kN/m^2)
p	Pressure (kN/m^2)

The corresponding velocities in the model and prototype can be related according to Euler's Law as follows (Webber, 1979):

$$\frac{v_p}{v_m} = \frac{{\Delta p_p}^{1/2}}{{\Delta p_m}^{1/2}} \times \frac{\rho_m^{\frac{1}{2}}}{\rho_p^{\frac{1}{2}}} \quad \text{B-16}$$

Where:

ρ	Fluid density (kg/m^3)
v	Velocity (m/s)
Δp	Change in pressure (kN/m^2)

Appendix C

Experiment details

C.1 MODEL 1

C.1.1 MODEL 1 SCHEMATICS

The design drawings of Model 1, as prepared by Denys (2019), follows:

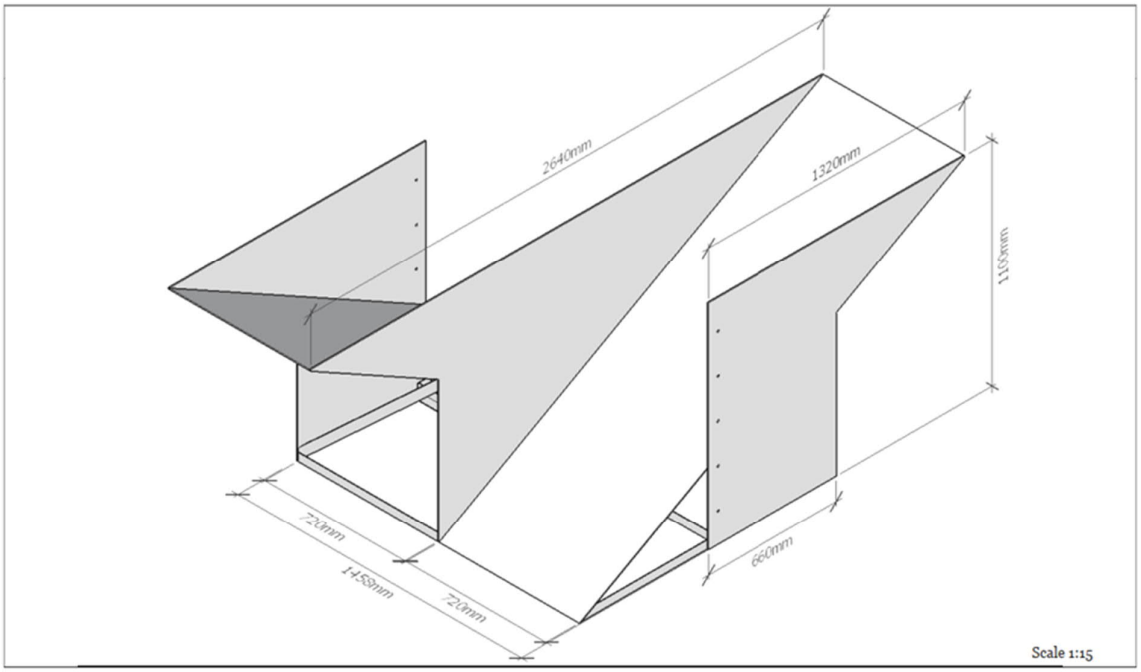

Piank Key Weir: Flow induced vibrations	**Model 1** Isometric view	REVISIONS 1 29/06/2016 Final Draft 2 01/07/2016 Final	01 B

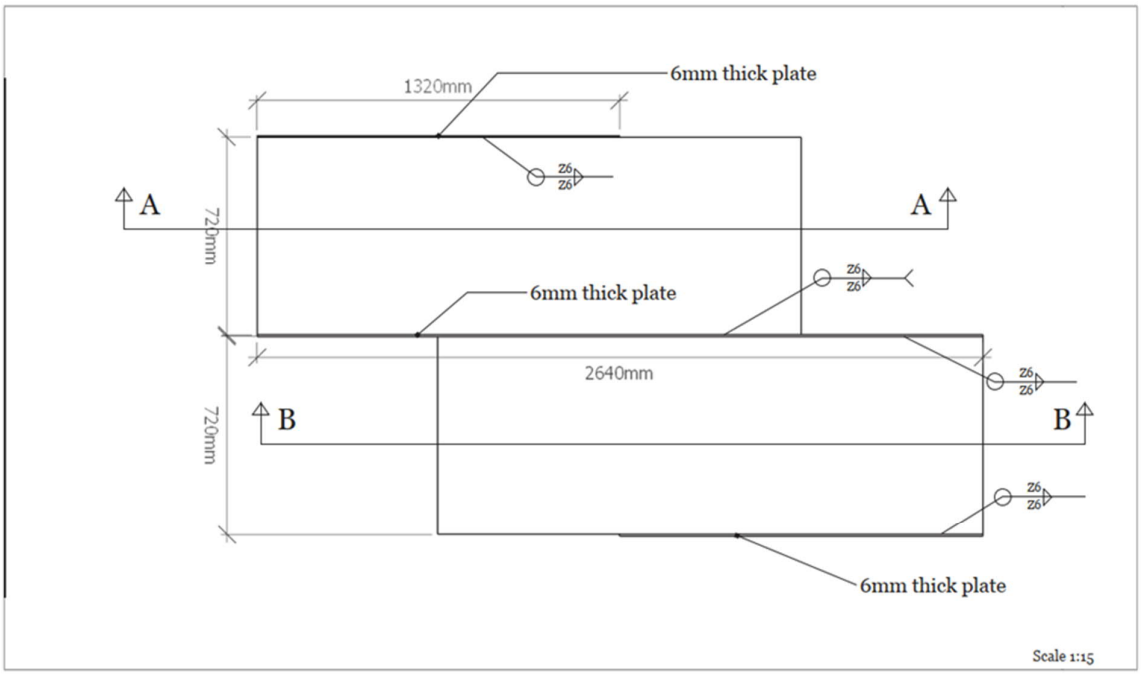

Piank Key Weir: Flow induced vibrations	**Model 1** Top (PLAN) view	REVISIONS 1 29/06/2016 Final Draft 2 01/07/2016 Final	02 B

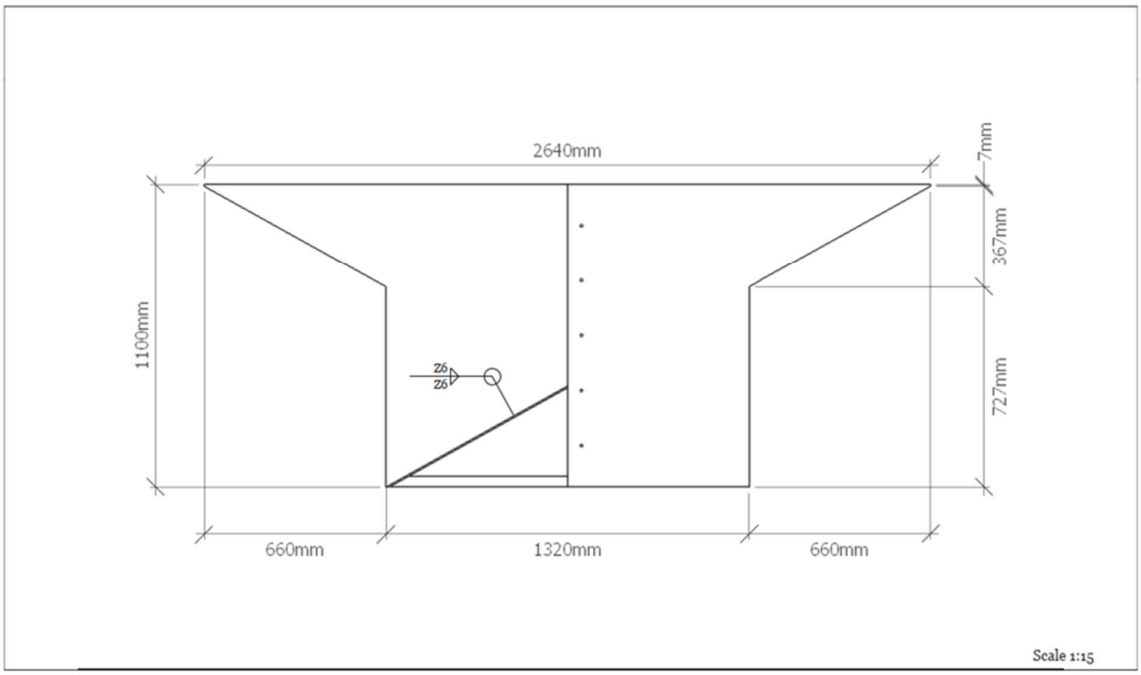

Piank Key Weir: Flow induced vibrations	Model 1	REVISIONS		03
	Side view	MM/DD/YY	REMARKS	B
		29/06/2016	Final Draft	
		01/07/2016	Final	

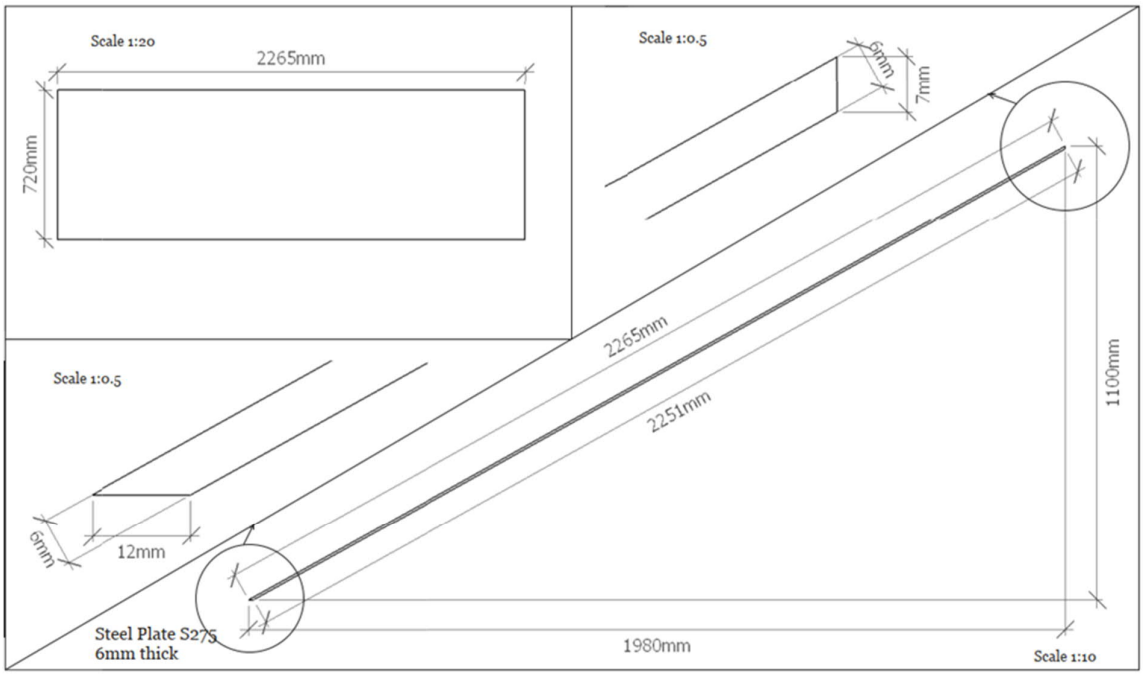

Piank Key Weir: Flow induced vibrations	Model 1	REVISIONS		07
	Part B3 (x2)	MM/DD/YY	REMARKS	B
		29/06/2016	Final Draft	
		01/07/2016	Final	

C.1.2 MODEL 1 TEST SCENARIOS

Table C.1 provides the different test scenarios and relevant data collected for each scenario. Several tests were repeated independently to validate the data. Tests that were repeated are indicated by an "*".

Table C.1: Model 1 test scenarios

Aeration	Flow (l/s)	Measurements					
		Discharge	Upstream water level	Nappe profile	Air flow	Pressure	Vibration
No	50	X*	X*	X		X	X*
	100	X*	X*	X		X	X*
	150	X*	X*			X*	X*
	200	X*	X*	X		X	X*
	250	X*	X*			X*	X*
	300	X*	X*	X		X*	X*
	350	X*	X*			X*	X*
	400	X*	X*	X		X*	X*
32 mm diameter aeration pipe	50	X	X		X	X	X*
	100	X	X		X	X	X*
	150	X	X		X	X	X*
	200	X	X		X	X	X*
	250	X	X		X	X	X*
	300	X	X		X	X	X*
	350	X	X		X	X	X*
	400	X	X		X	X	X*
105 mm diameter aeration pipe	50	X*	X*	X	X*	X	X*
	100	X*	X*	X	X*	X*	X*
	150	X*	X*		X	X	X*
	200	X*	X*	X	X	X*	X*
	250	X*	X*		X	X	X*
	300	X*	X*	X	X*	X*	X*
	350	X*	X*		X	X	X*
	400	X*	X*	X	X*	X*	X*

C.1.3 MODEL 1 TEST PROCEDURES

For every set of daily tests conducted the following preparatory steps were done for Model 1:

1. Confirm the reference readings of the needle gauge relative to the crest level of the PKW.
2. Record air pressure and vibrations without any water in the flume to obtain the “zero readings”.
3. Fill the flume to FSL and take the pitot and upstream needle gauge readings of the FSL.
4. Confirm that the correct aeration condition is applicable and that there are no potential air leaks.
5. Ensure that the strain gauge is sealed.

Following the daily preparatory steps, the test procedure for Model 1 involved the following for every test scenario:

1. Open the water supply valve to the required flow rate (by checking the flow meter installed on the supply pipe).
2. Allow the flow to reach a stable equilibrium and check the model for any abnormalities in terms of flow.
3. Once the flow has stabilised, take the discharge reading and the upstream water surface reading of the needle gauge and the pitot tube installed halfway in the flume. Also take the reading of the water surface upstream of the inlet key.
4. If required for the test scenario, take the water surface profile readings at set positions using the rail mounted moveable needle gauge.
5. Visually observe and record the flow characteristics, taking photographs and videos as required.
6. Record the time-variant pressure readings of the installed pressure transducer.
7. Record the time-variant strain readings of the installed strain gauge.

C.1.4 MODEL 1 PHOTOGRAPHS

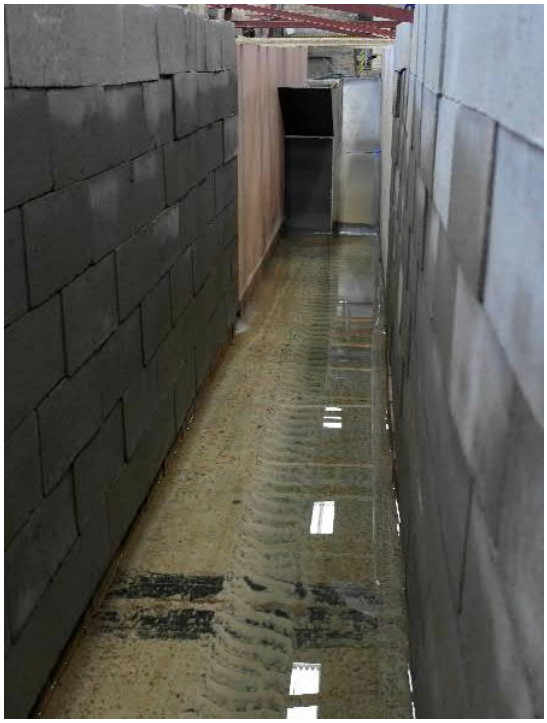

Figure C1.1: Model 1 view from upstream as installed in the flume

Figure C1.2: Model 1 view from above as installed in the flume

Figure C1.3: Model 1 view from downstream as installed in the flume

Figure C1.4: View of flume supply pipes and baffle wall

Figure C1.5: View of aeration pipe and pressure transducer from downstream

Figure C1.6: View of aeration pipe and pressure transducer from upstream

Figure C1.7: Large aeration pipe

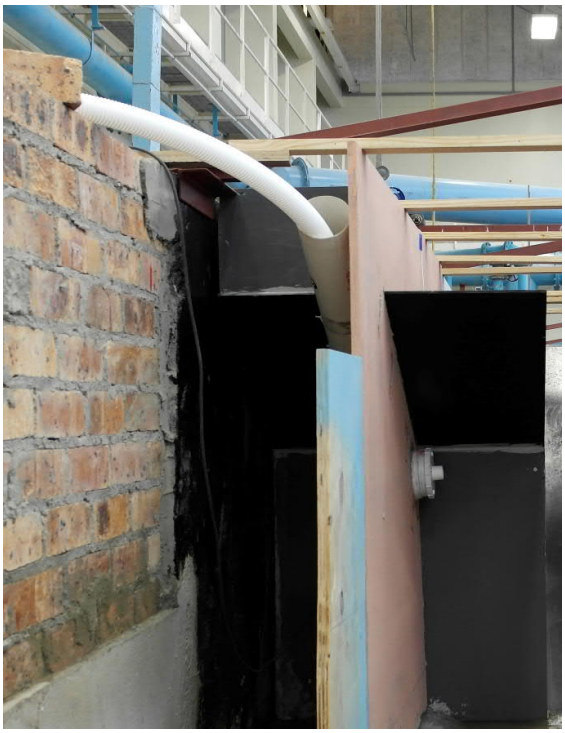

Figure C1.8: Small aeration pipe installed into large aeration pipe

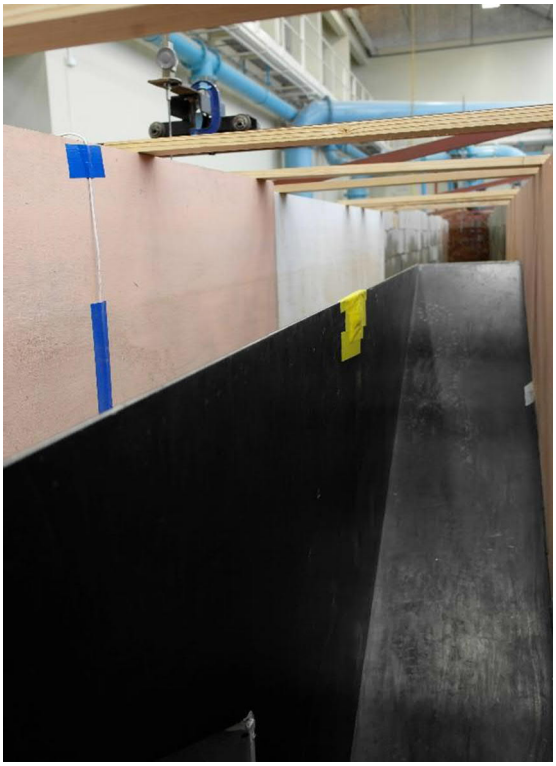

Figure C1.9: Strain gauge detail (protected with yellow tape)

Figure C1.10: Crest detail

Figure C1.11: Model setup from downstream

C.2 MODEL 2

C.2.1 MODEL 2 DESIGN

The design drawings of Model 2, as prepared by Denys (2019), follows:

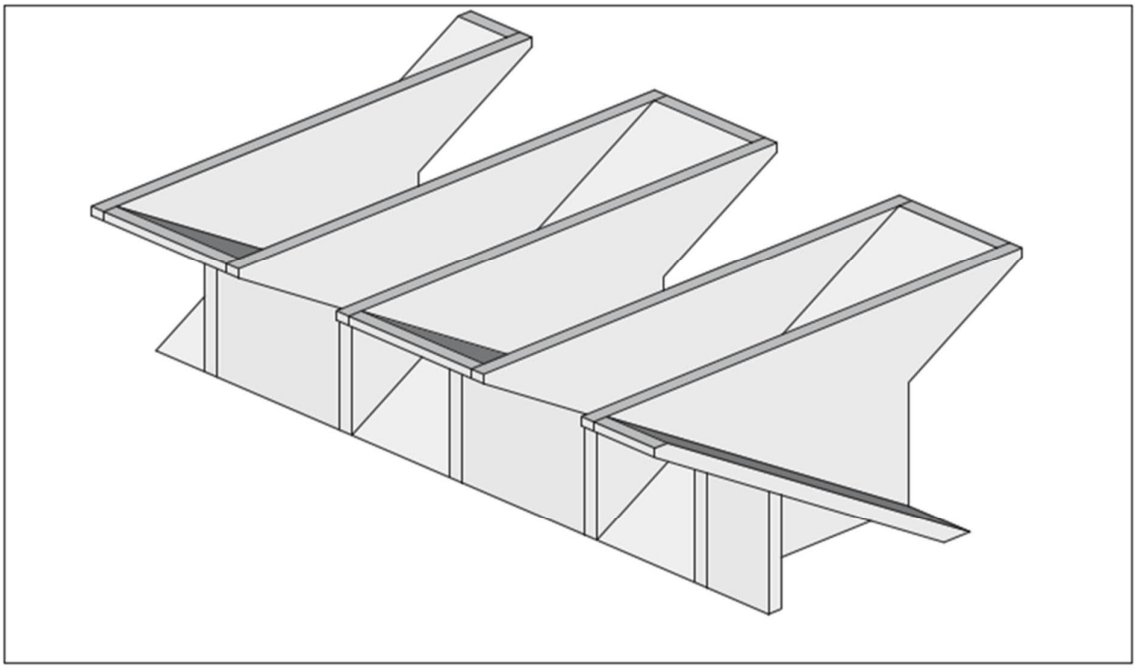

Piano Key Weir: Flow-induced vibrations	Model 2
	July 6, 2015

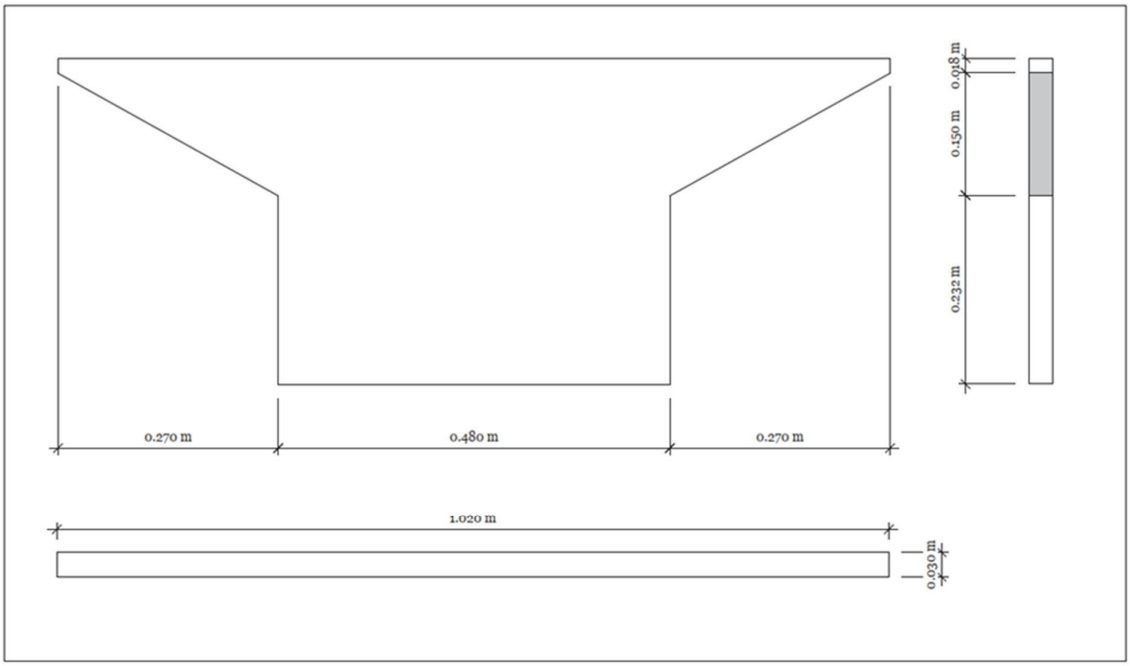

Piano Key Weir: Flow-induced vibrations	Model 2	REVISIONS		01
		DD/MM/YY	REMARKS	
		11 /05 /2015	For discussion	
	Component: Transverse walls			1A

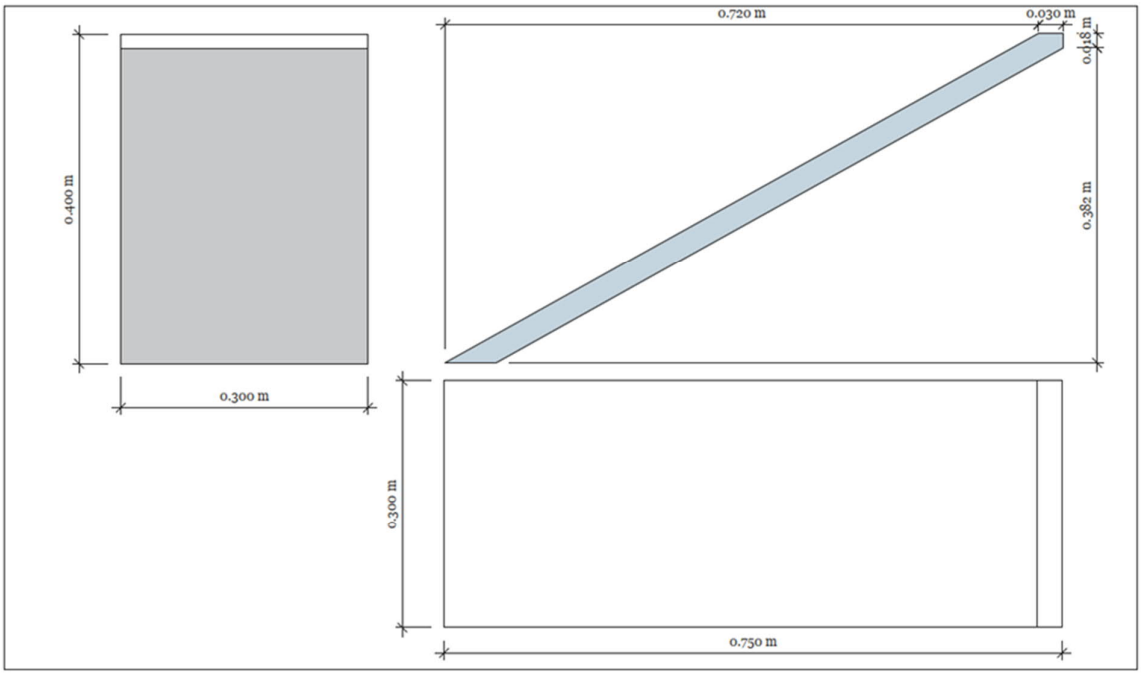

Piano Key Weir: Flow-induced vibrations	**Model 2**	REVISIONS: DD/MM/YY 11/05/2015 — REMARKS: For discussion	02
	Component: Inlet key slope		1A

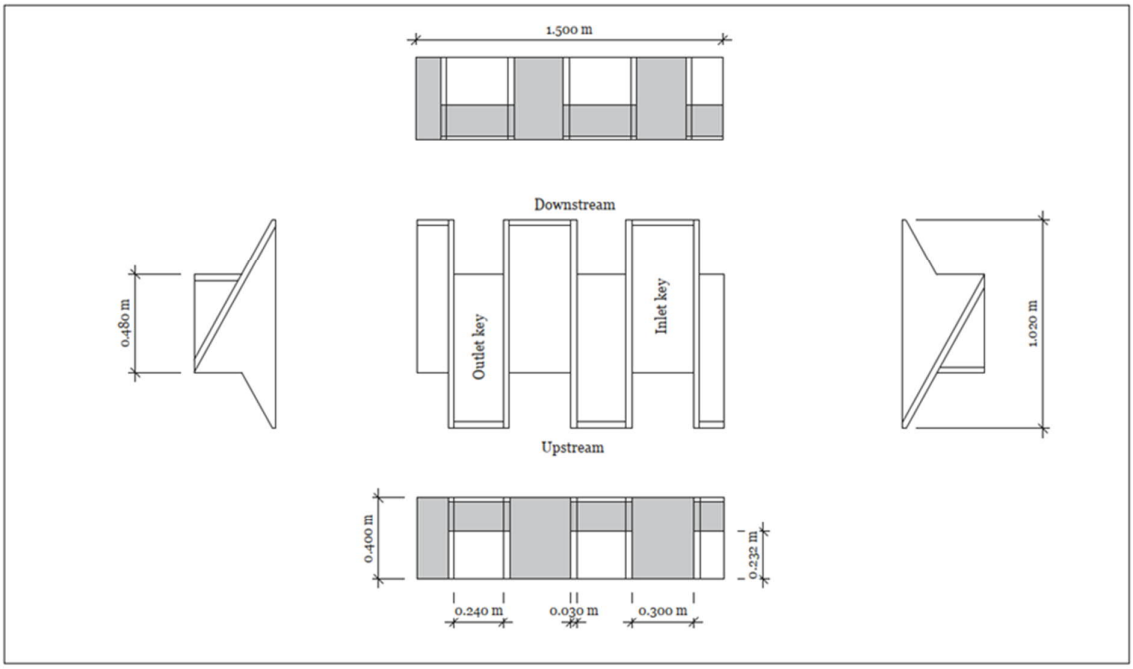

Piano Key Weir: Flow-induced vibrations	**Model 2**	REVISIONS: DD/MM/YY 11/05/2015 — REMARKS: For discussion	05
	Completed model		1A

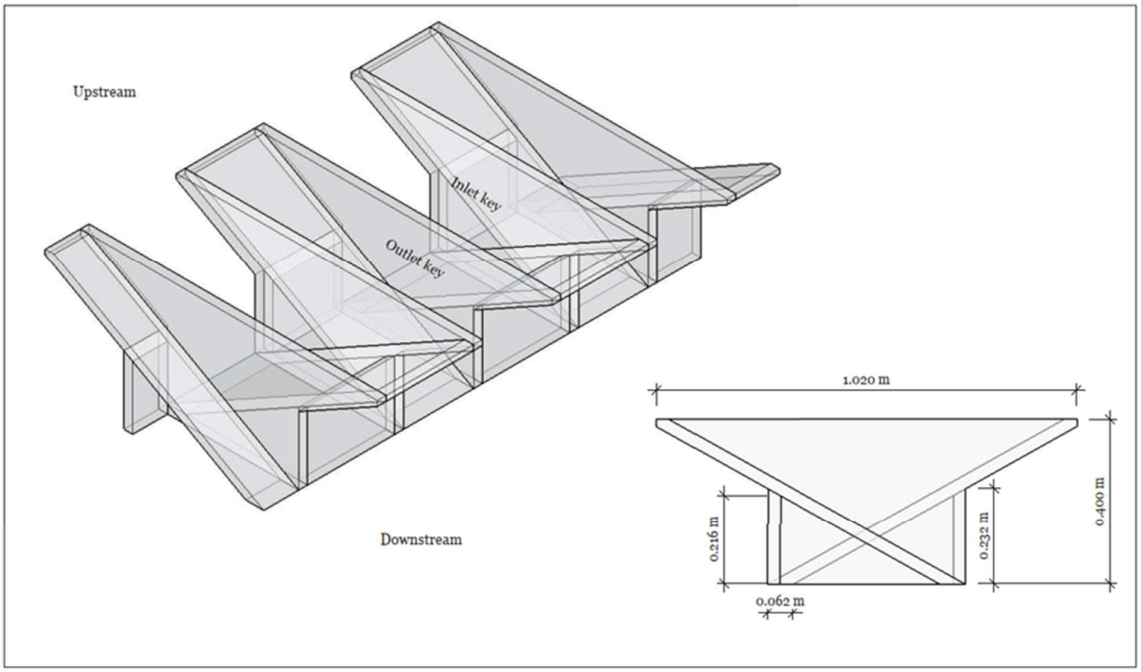

Piano Key Weir: Flow-induced vibrations	**Model 2**	REVISIONS		07
		DD/MM/YY	REMARKS	
		11 /05 /2015	For discussion	
	Completed model: components			1A

C.2.2 MODEL 2 TEST SCENARIOS

Table C.2 provides the different test scenarios and relevant data collected for each scenario. Several tests were repeated independently to validate the data. Tests that were repeated are indicated by an "*".

Table C.2: Model 2 test scenarios

Aeration	Flow (l/s)	Tail water level (mm)	Measurements				
			Discharge	Upstream water level	Nappe profile	Air flow	Pressure
No	50	0 - 400	X*	X*	X*		X*
	100	0 - 400	X*	X*	X*		X*
	200	0 - 400	X*	X*	X*		X*
	300	0 - 400	X*	X*	X*		X*
	400	0 - 400	X*	X*	X*		X*
	500	0 - 400	X*	X*	X*		X*
20 mm diameter aeration pipe	50	0	X	X	X	X	X
	100	0	X	X	X	X*	X
	200	0	X	X	X	X	X
	300	0	X	X	X	X*	X*
	300	0	X	X	X	X	X
	500	0	X	X	X	X	X
52 mm diameter aeration pipe	50	0 - 100	X*	X*	X	X*	X*
	100	0 - 100	X*	X*	X*	X*	X*
	200	0	X	X	X	X	X
	300	0	X	X	X	X	X
	400	0	X*	X*	X	X*	X*
	500	0	X	X	X	X	X
Completely aerated	50	0	X	X	X		
	100	0	X	X	X		
	200	0	X	X	X		
	300	0	X	X	X		
	400	0	X	X	X		
	500	0	X	X	X		

C.2.3 MODEL 2 TEST PROCEDURES

For every set of daily tests conducted the following preparatory steps were done for Model 2:

1. Confirm the reference readings of the needle gauge relative to the crest level of the PKW.
2. Record air pressure without any water in the flume to obtain the “zero readings”.
3. Fill the flume to FSL and take the pitot and upstream needle gauge readings of the FSL.
4. Confirm that the correct aeration condition is applicable and that there are no potential air leaks.

Following the daily preparatory steps, the test procedure for Model 2 involved the following for every test scenario:

1. Open the water supply valve to the required flow rate (by checking the flow meter installed on the supply pipe).
2. Allow the flow to reach a stable equilibrium and check the model for any abnormalities in terms of flow.
3. Once the flow has stabilised, take the discharge reading and the upstream water surface reading of the needle gauge and the pitot tube installed halfway in the flume. Also take the reading of the water surface upstream of the inlet key.
4. If required for the test scenario, take the water surface profile readings at set positions using the rail mounted moveable needle gauge.
5. Visually observe and record the flow characteristics, taking photographs and videos as required.
6. Record the time-variant pressure readings of the installed pressure transducer.

C.2.4 MODEL 2 PHOTOGRAPHS

Figure C2.1: Model 2 construction (Denys, 2019)

Figure C2.2: Model 2 construction (Denys, 2019)

Figure C2.3: Model 2 construction (Denys, 2019)

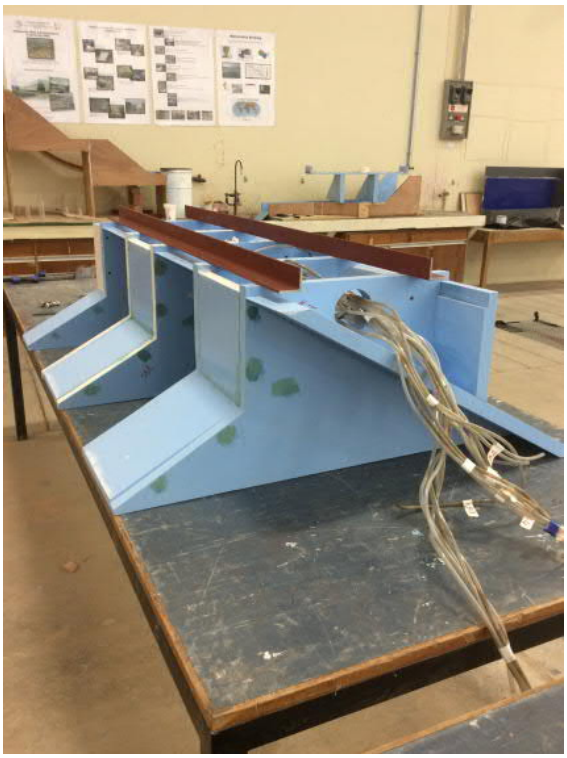

Figure C2.4: Model 2 construction (Denys, 2019)

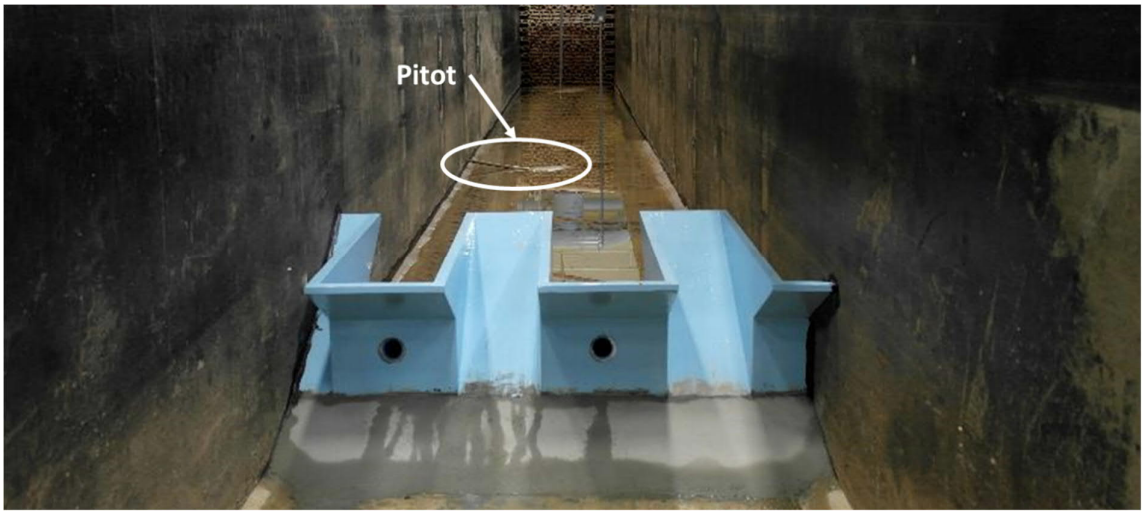

Figure C2.5: Model 2 view from downstream (aeration pipes open)

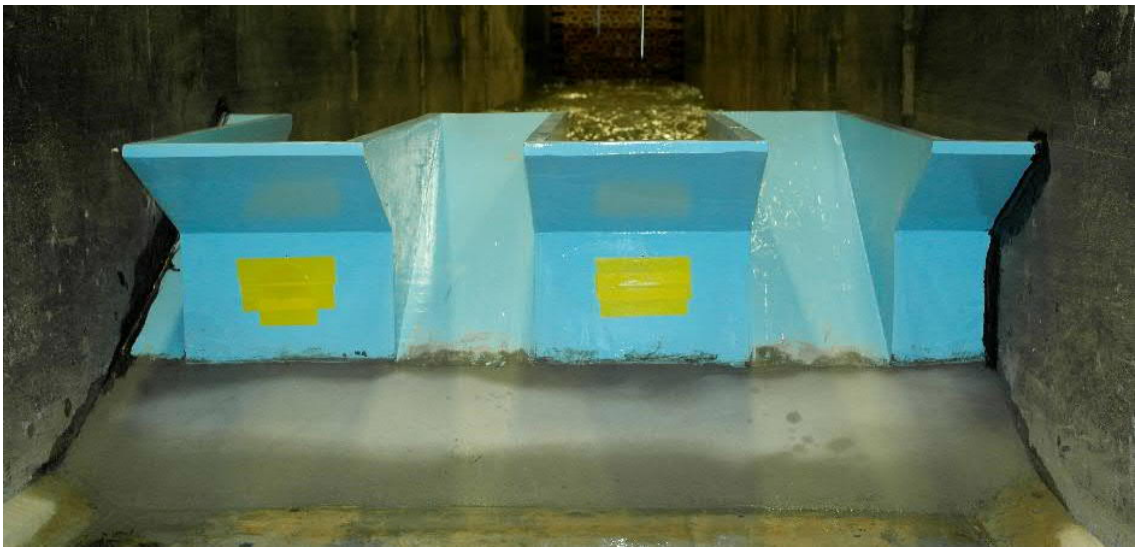

Figure C2.6: Model 2 view from downstream (aeration pipes closed)

Figure C2.7: Small aeration pipe installed into large aeration pipe

Appendix D

Experimental data and results

D.1 DISCHARGE DATA

Table D.1 Model 1 Physical model discharge results

P (m)	1.1	W (m)	0.75
Wi (m)	0.72	Ts (m)	0.006
Wo (m)	0.72	Bi = Bo (m)	0.66
Pt (m)	1.1	Bb (m)	1.32

Q (m^3/s)	H (m)	H/P	Cd	Aeration
0.0503	0.0600	0.055	1.611	None
0.1023	0.0850	0.077	1.941	
0.1494	0.1050	0.095	2.065	
0.1516	0.1050	0.095	2.096	
0.1483	0.1050	0.095	2.050	
0.2057	0.0850	0.077	3.903	
0.2009	0.1250	0.114	2.138	
0.2511	0.1420	0.129	2.207	
0.2544	0.1450	0.132	2.167	
0.2529	0.1425	0.130	2.211	
0.2999	0.1550	0.141	2.311	
0.3006	0.1575	0.143	2.262	
0.3507	0.1700	0.155	2.353	
0.3522	0.1700	0.155	2.363	
0.3547	0.1800	0.164	2.184	
0.3995	0.2000	0.182	2.101	
0.3981	0.2000	0.182	2.093	
0.3989	0.1900	0.173	2.265	
0.0498	0.0550	0.050	1.816	32 mm diameter aeration pipe
0.1018	0.0825	0.075	2.020	
0.1499	0.1025	0.093	2.149	
0.1997	0.1250	0.114	2.125	
0.2511	0.1400	0.127	2.255	
0.3020	0.1600	0.145	2.219	
0.3518	0.1800	0.164	2.167	
0.4005	0.1975	0.180	2.146	
0.0509	0.0580	0.053	1.713	105 mm diameter aeration pipe
0.0509	0.0580	0.053	1.713	
0.0500	0.0575	0.052	1.705	
0.0947	0.0800	0.073	1.969	
0.0990	0.0825	0.075	1.966	
0.0990	0.0825	0.075	1.966	
0.1515	0.1050	0.095	2.095	
0.1499	0.1025	0.093	2.149	
0.2014	0.1250	0.114	2.143	
0.1991	0.1225	0.111	2.185	

Table D.1 Model 1 Physical model discharge results

Q (m^3/s)	H (m)	H/P	Cd	Aeration
0.2500	0.1400	0.127	2.245	105 mm diameter aeration pipe
0.2521	0.1400	0.127	2.264	
0.2995	0.1600	0.145	2.201	
0.3063	0.1650	0.150	2.150	
0.3006	0.1550	0.141	2.317	
0.3529	0.1825	0.166	2.129	
0.3500	0.1800	0.164	2.155	
0.4037	0.2000	0.182	2.123	
0.3895	0.1910	0.174	2.195	
0.4023	0.1950	0.177	2.197	

Table D.2 Model 2 Physical model discharge results

P (m)	0.4	W (m)	1.5
Wi (m)	0.3	Ts (m)	0.03
Wo (m)	0.24	Bi = Bo (m)	0.27
Pt (m)	0.45	Bb (m)	0.48

Q (m^3/s)	H (m)	H/P	Cd	Aeration
0.0509	0.0300	0.075	2.210	No air
0.1023	0.0430	0.108	2.590	
0.2019	0.0700	0.175	2.461	
0.2985	0.1030	0.258	2.039	
0.4056	0.1300	0.325	1.953	
0.5073	0.1600	0.400	1.790	
0.0503	0.0290	0.073	2.301	Complete aeration (Breaking nappe)
0.0980	0.0430	0.108	2.480	
0.2014	0.0720	0.180	2.354	
0.2993	0.1020	0.255	2.074	
0.4052	0.1330	0.333	1.886	
0.4798	0.1600	0.400	1.692	
0.0503	0.0290	0.073	2.301	20 mm diameter aeration pipe
0.1038	0.0440	0.110	2.538	
0.2014	0.0720	0.180	2.354	
0.2991	0.0980	0.245	2.201	
0.4052	0.1330	0.333	1.886	
0.5038	0.1600	0.400	1.777	
0.0514	0.0290	0.073	2.350	52 mm diameter aeration pipe
0.1033	0.0430	0.108	2.614	
0.2024	0.0700	0.175	2.467	
0.2995	0.1000	0.250	2.138	
0.4001	0.1320	0.330	1.884	
0.5073	0.1600	0.400	1.790	

D.2 FLOW CHARACTERISTICS

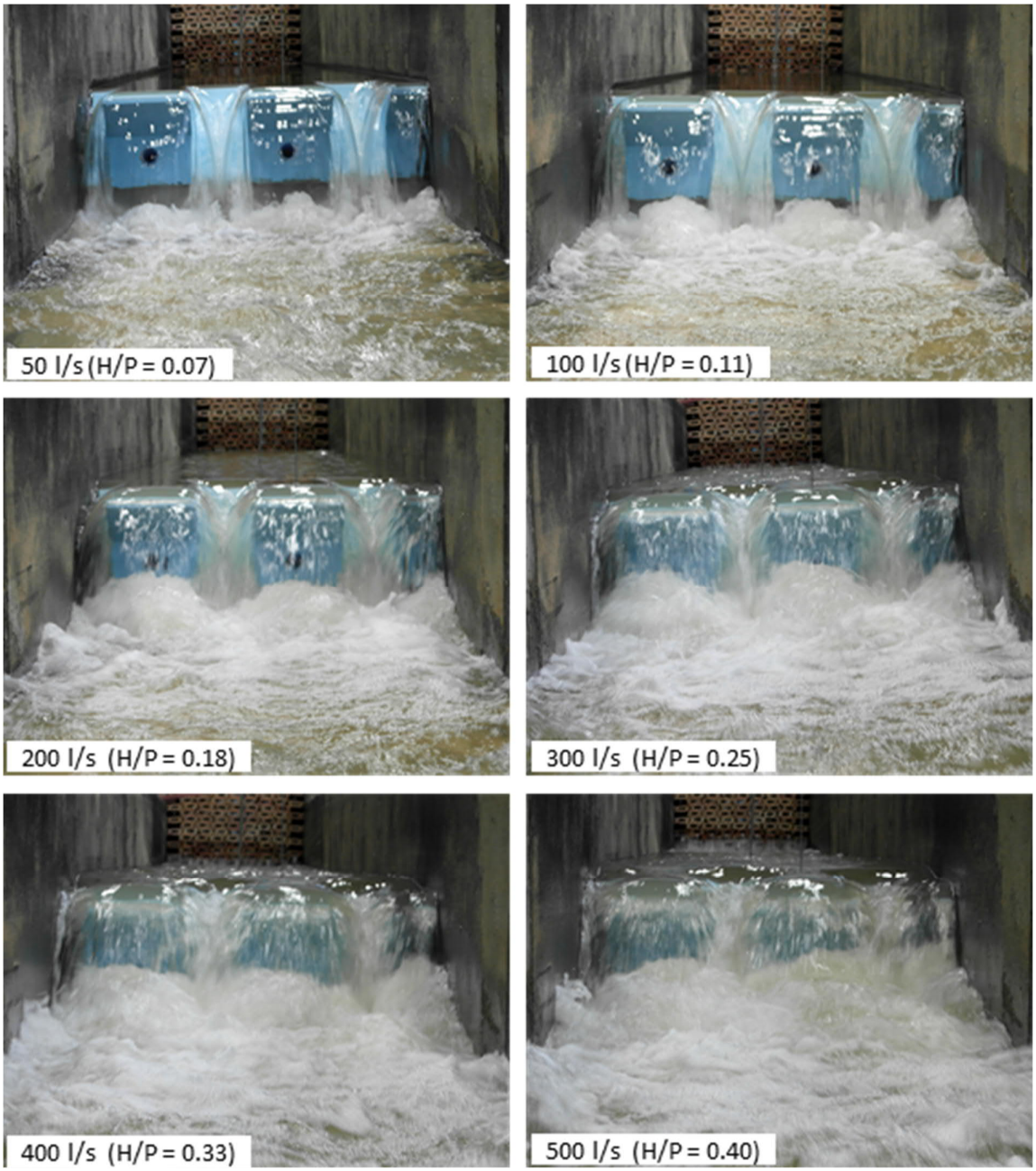

Figure D.2.1: Model 2 view from downstream for different discharges

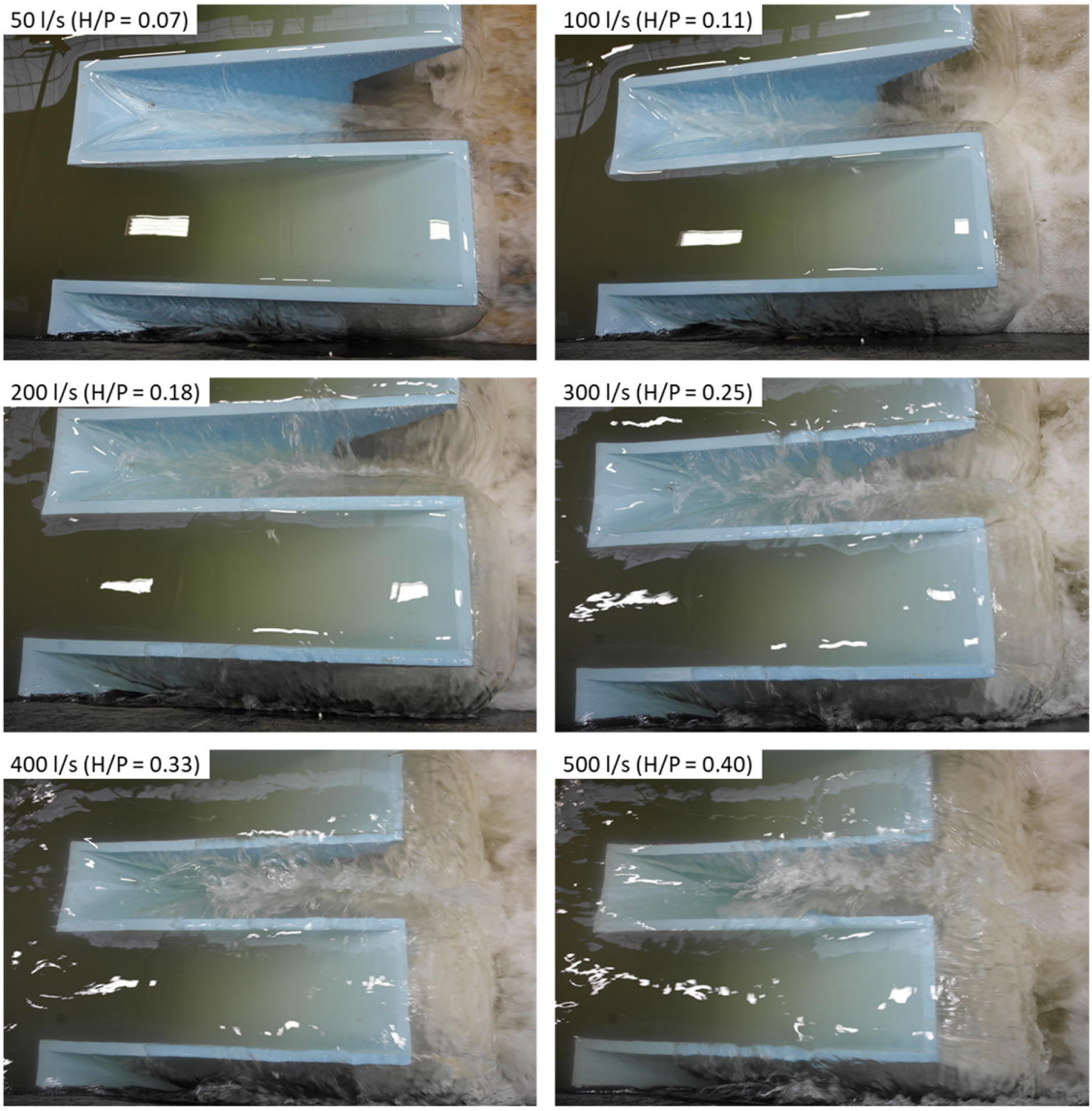

Figure D.2.2: Model 2 view from above for different discharges

D.3 WATER SURFACE PROFILES

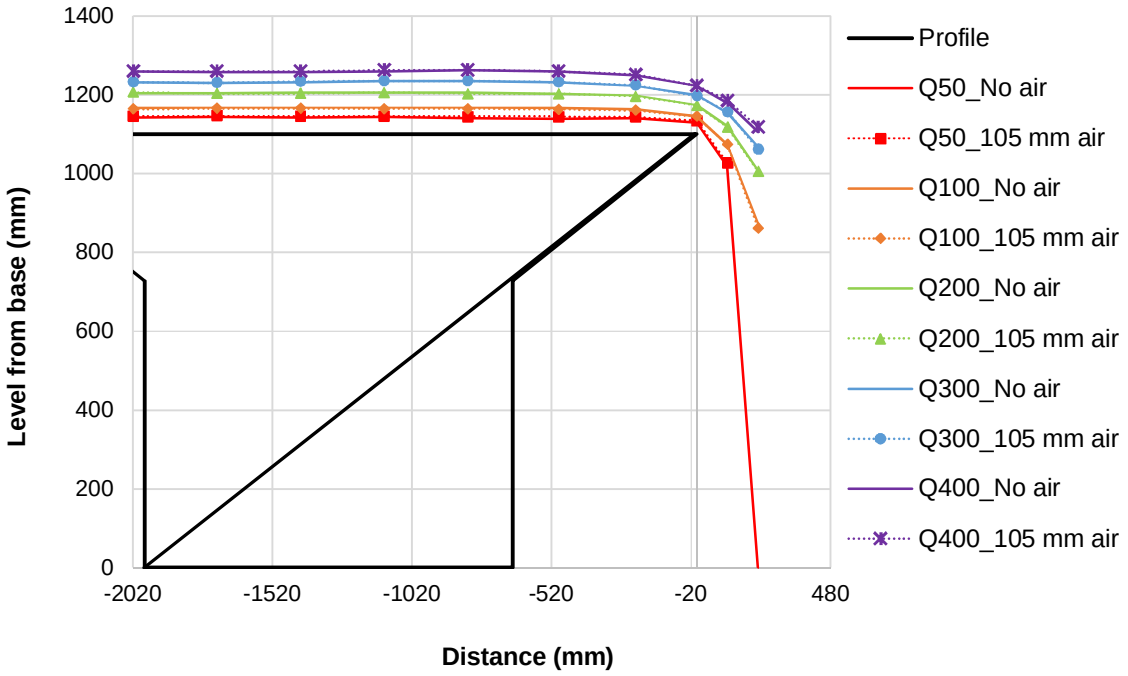

Figure D.3.1: Model 1 longitudinal water surface profile along centre of inlet key (No air vs. 105 mm diameter aeration pipe)

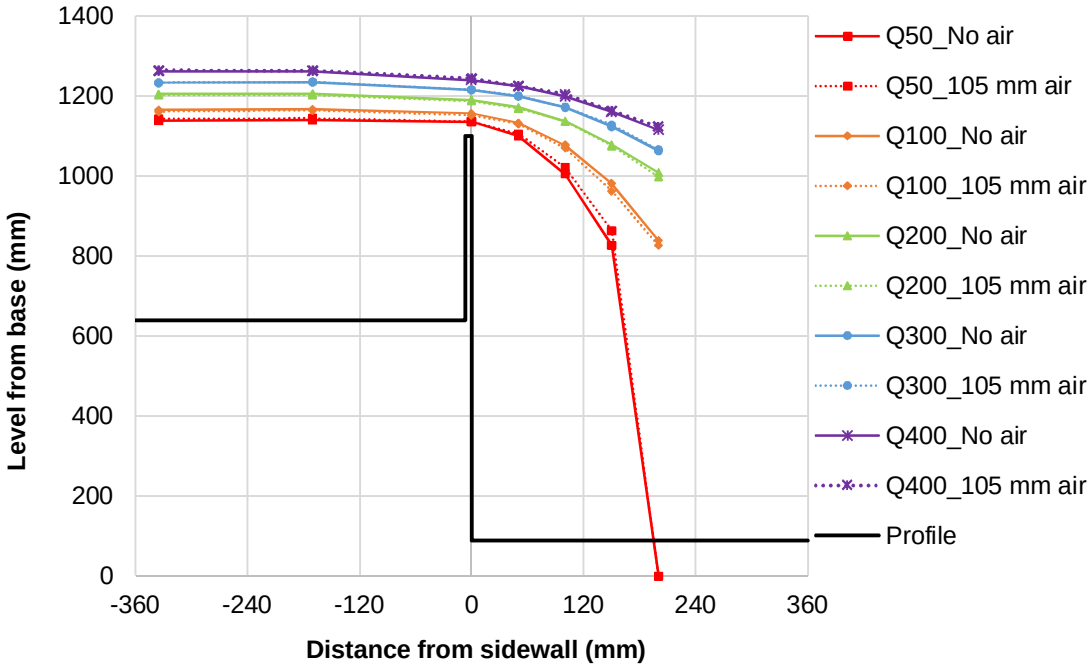

Figure D.3.2: Model 1 transverse water surface profile 820 mm from downstream inlet key crest (No air vs. 105 mm diameter aeration pipe)

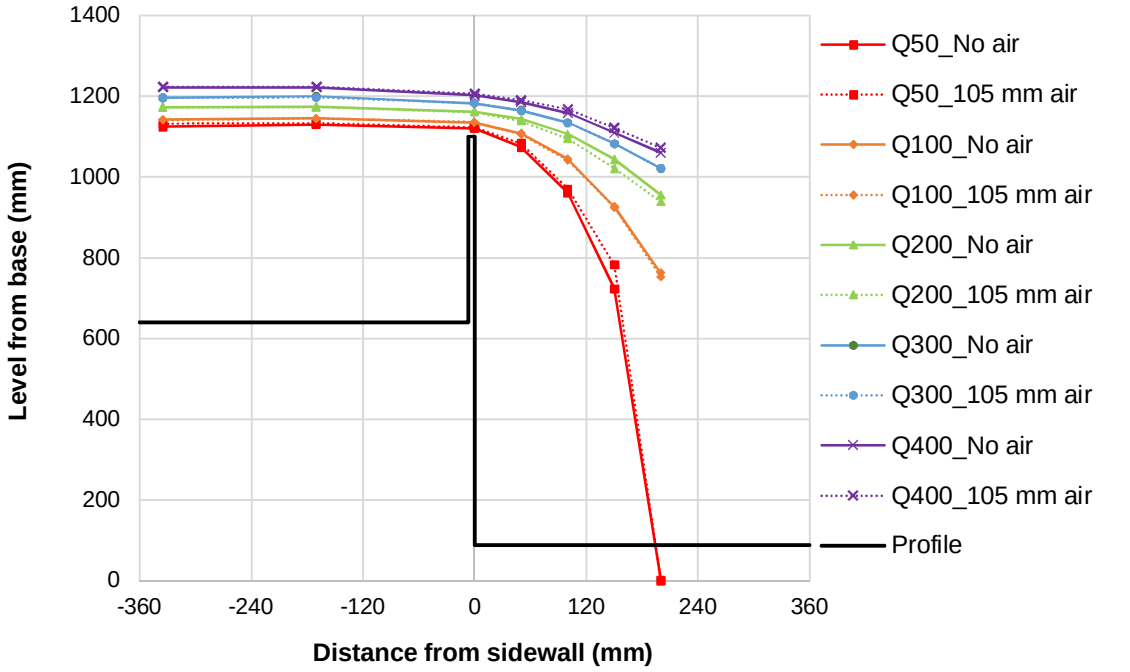

Figure D.3.3: Model 1 transverse water surface profile (No air vs. 105 mm diameter aeration pipe)

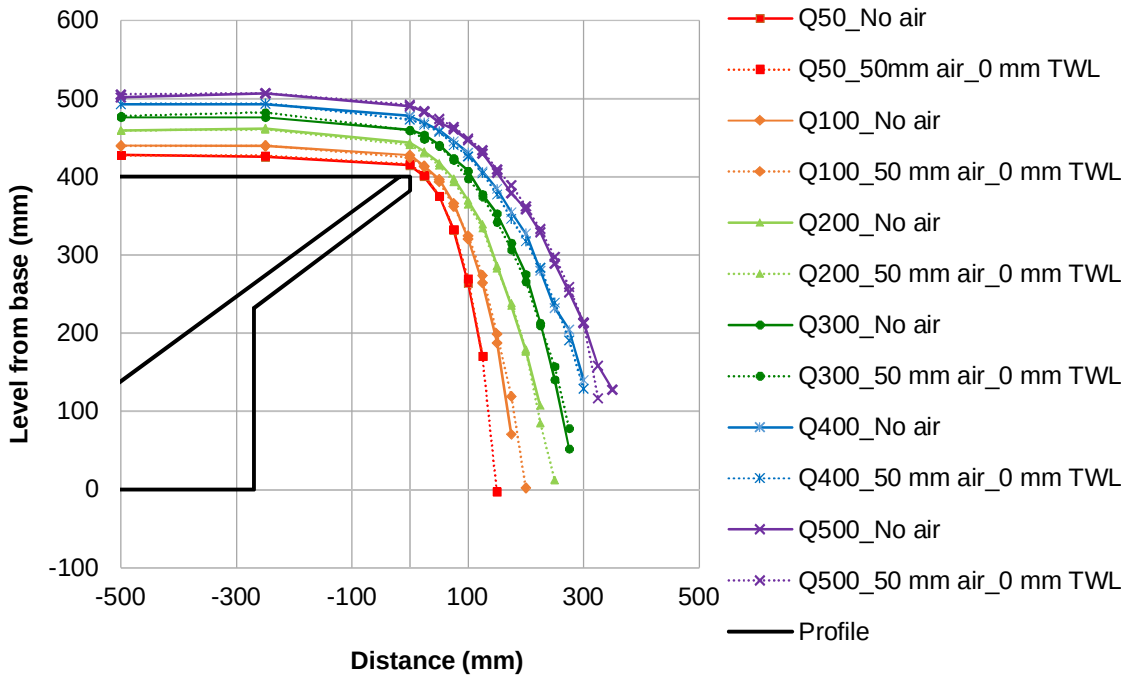

Figure D.3.4: Model 2 longitudinal water surface profile along centre of inlet key (No air vs. 52 mm diameter aeration pipe)

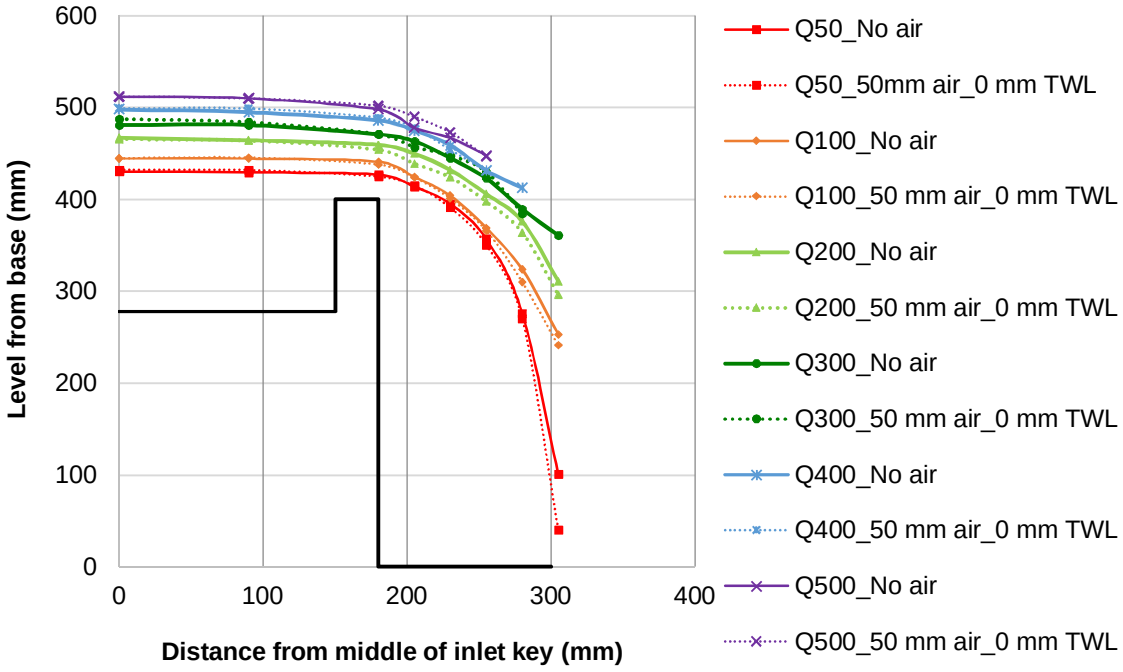

Figure D.3.5: Model 2 transverse water surface profile (No air vs. 52 mm diameter aeration pipe)

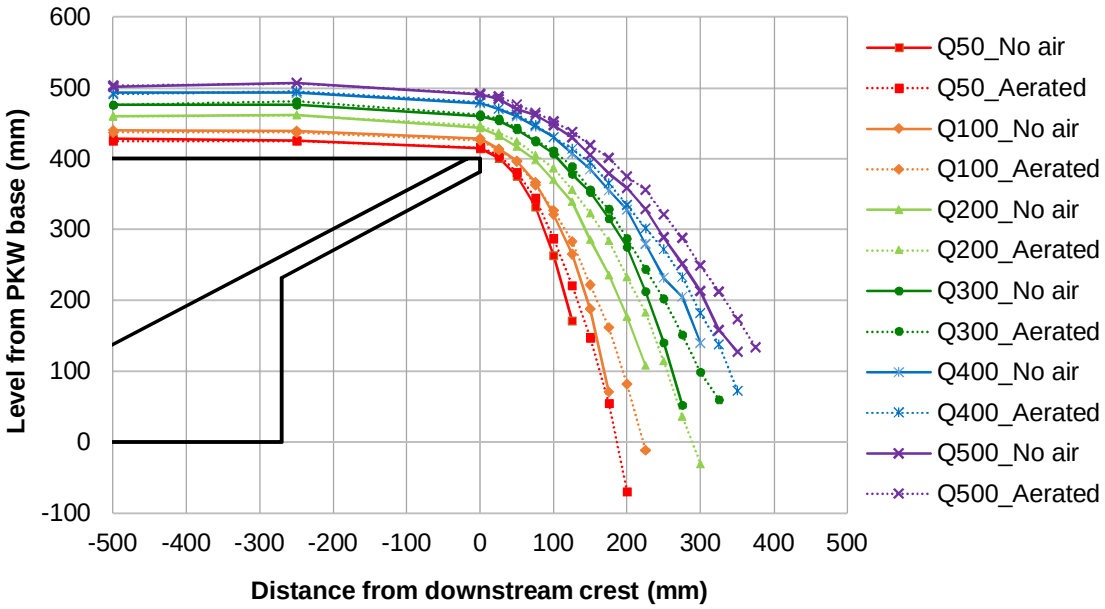

Figure D.3.6: Model 2 longitudinal water surface profile along centre of inlet key (No air vs. Completely aerated)

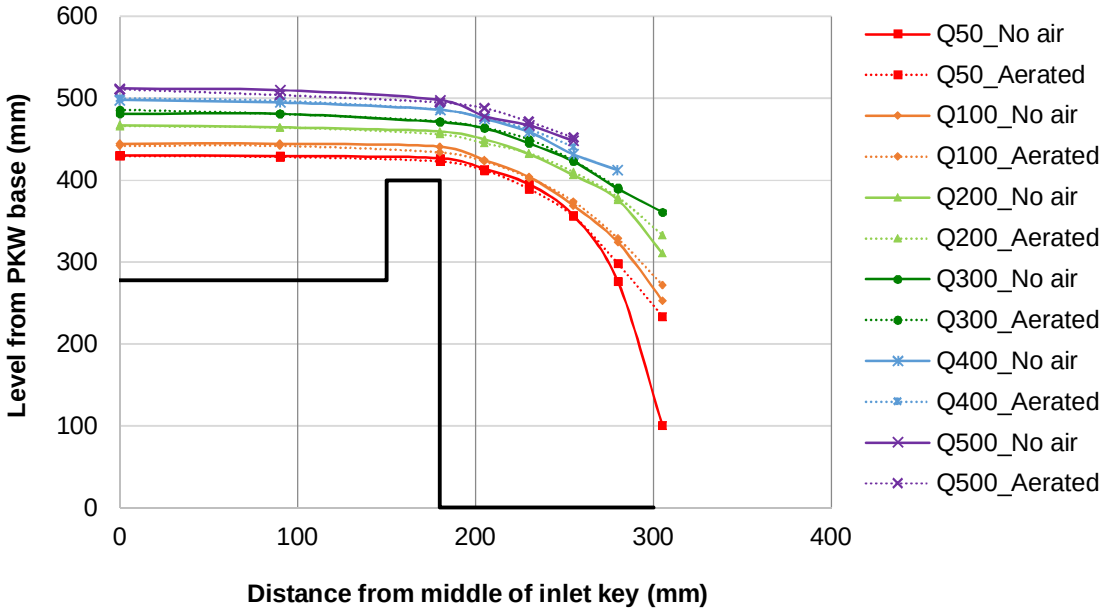

Figure D.3.7: Model 2 transverse water surface profile (No air vs. Completely aerated)

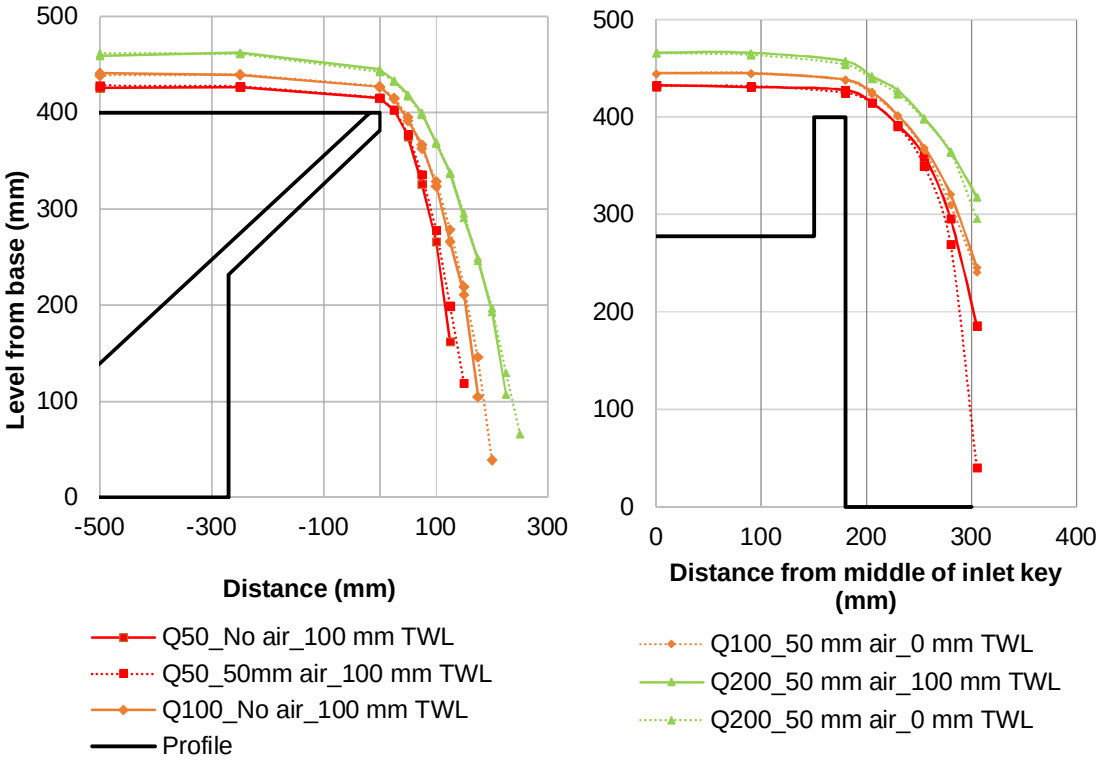

Figure D.3.8: Model 2 longitudinal (left) and transverse (right) water surface profile along centre of inlet key (No air vs. 52 mm diameter aeration pipe with 100 mm tail water level)

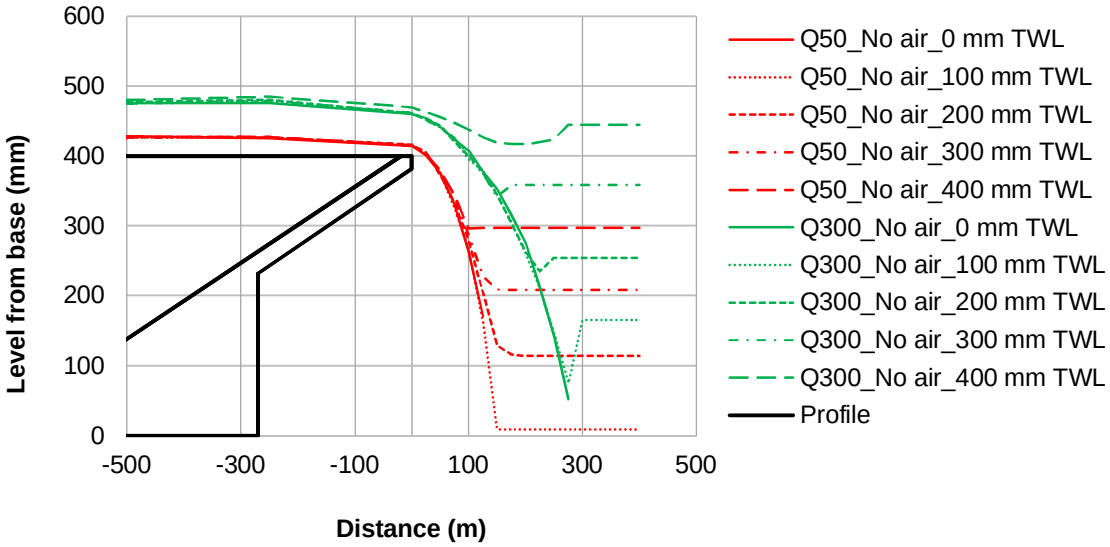

Figure D.3.9: Model 2 longitudinal water surface profile along centre of inlet key (Effect of tail water level)

D.4 PRESSURE PSD GRAPHS

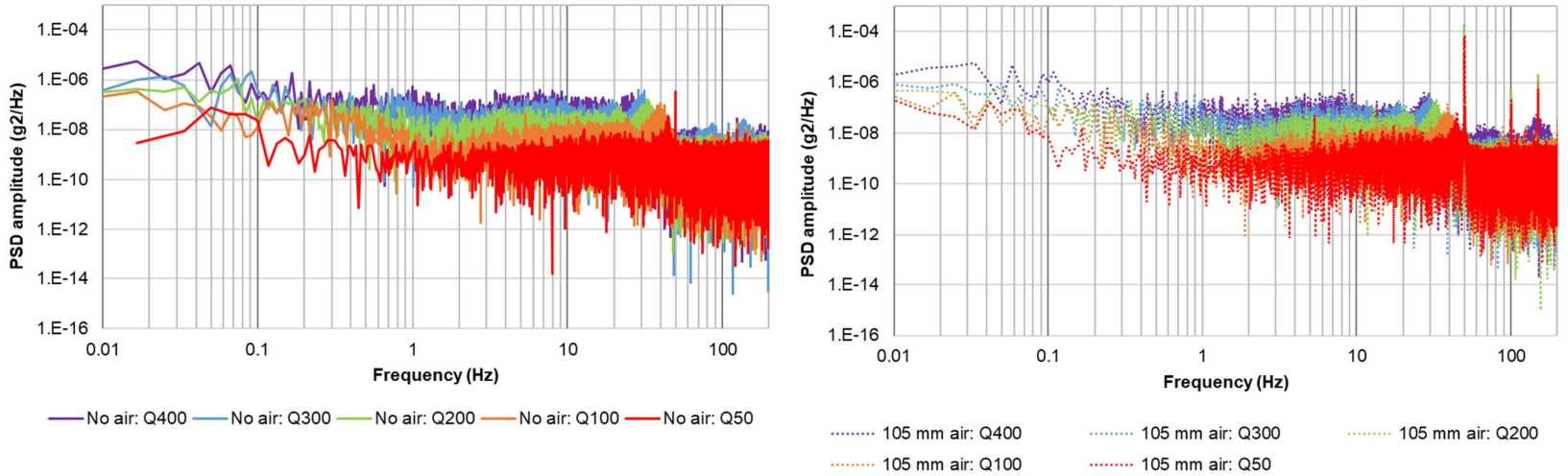

Figure D.4.1: Model 1 pressure PSD without aeration (left) with aeration (right) – 50, 100, 200, 300 and 400 l/s

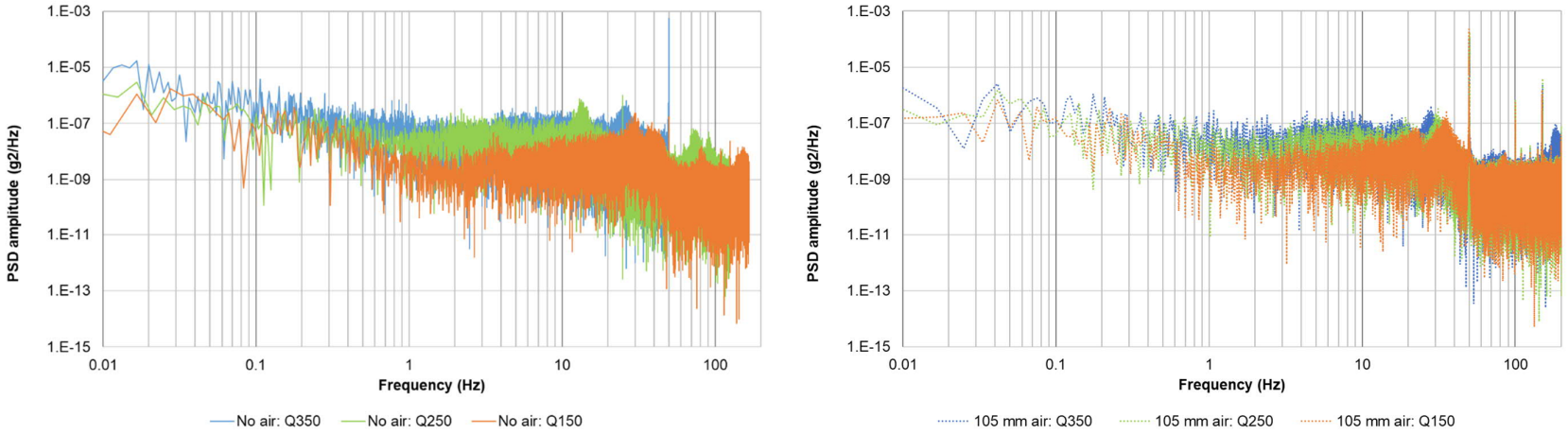

Figure D.4.2: Model 1 pressure PSD without aeration (left) with aeration (right) – 150, 250 and 350 l/s

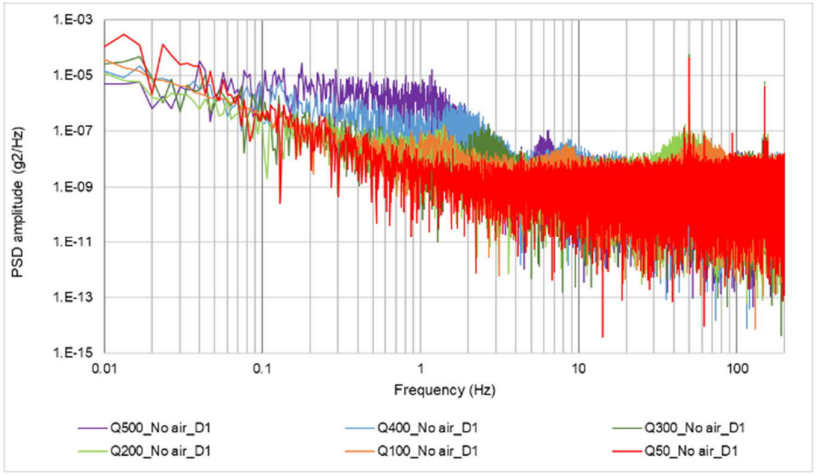

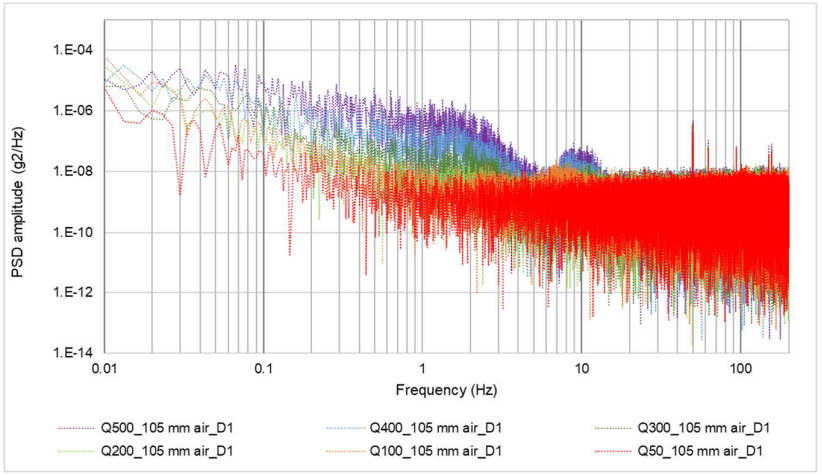

Figure D.4.3: Model 2 pressure PSD at pressure sensor D1 without aeration (left) with aeration (right)

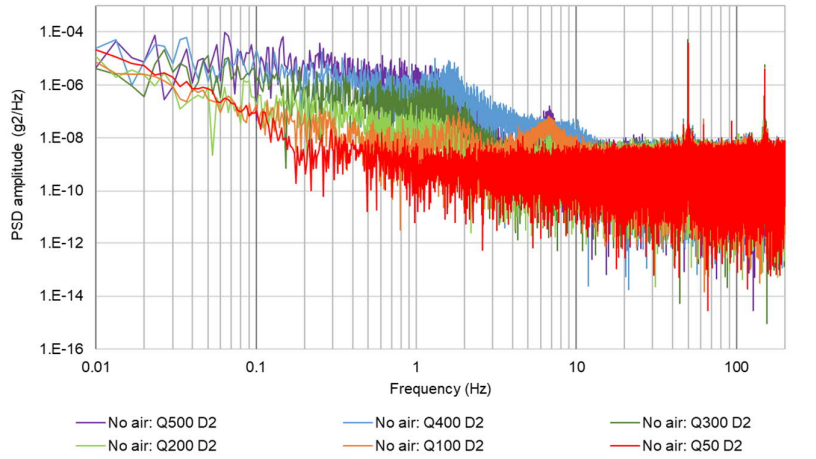

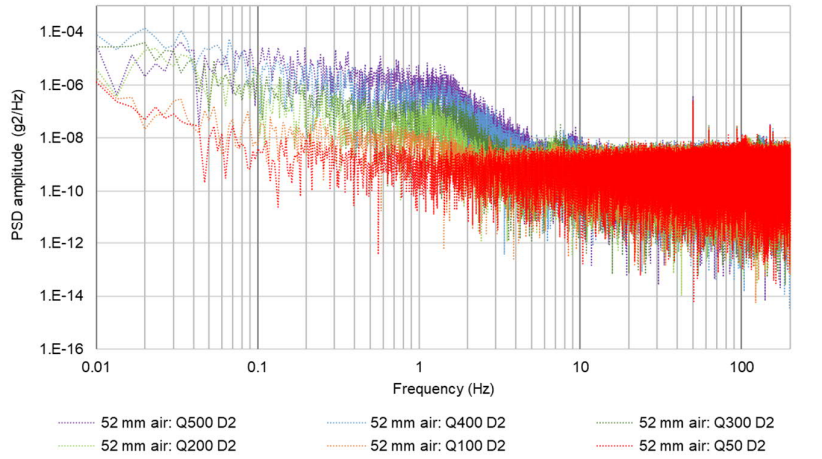

Figure D.4.4: Model 2 pressure PSD at pressure sensor D2 without aeration (left) and with aeration (right)

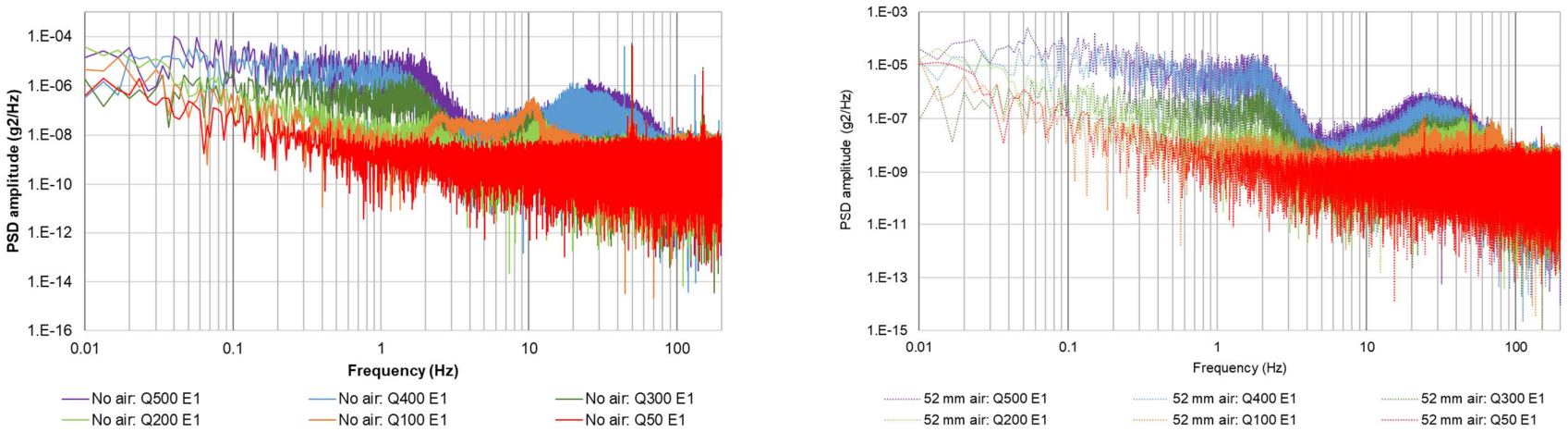

Figure D.4.5: Model 2 pressure PSD at pressure sensor E1 without aeration (left) and with aeration (right)

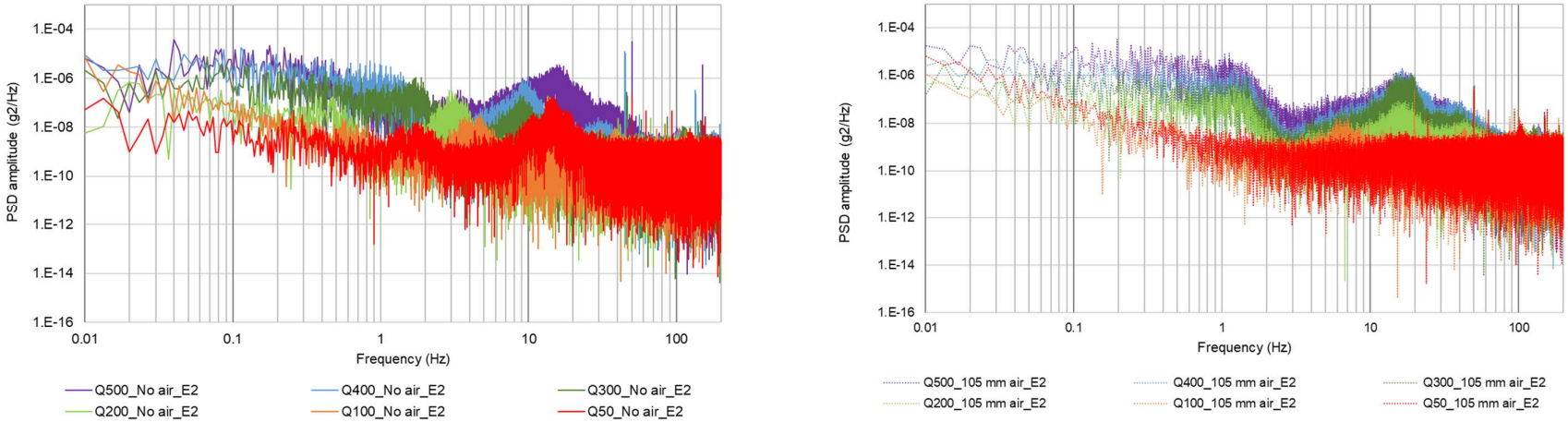

Figure D.4.6: Model 2 pressure PSD at pressure sensor E2 without aeration (left) and with aeration (right)

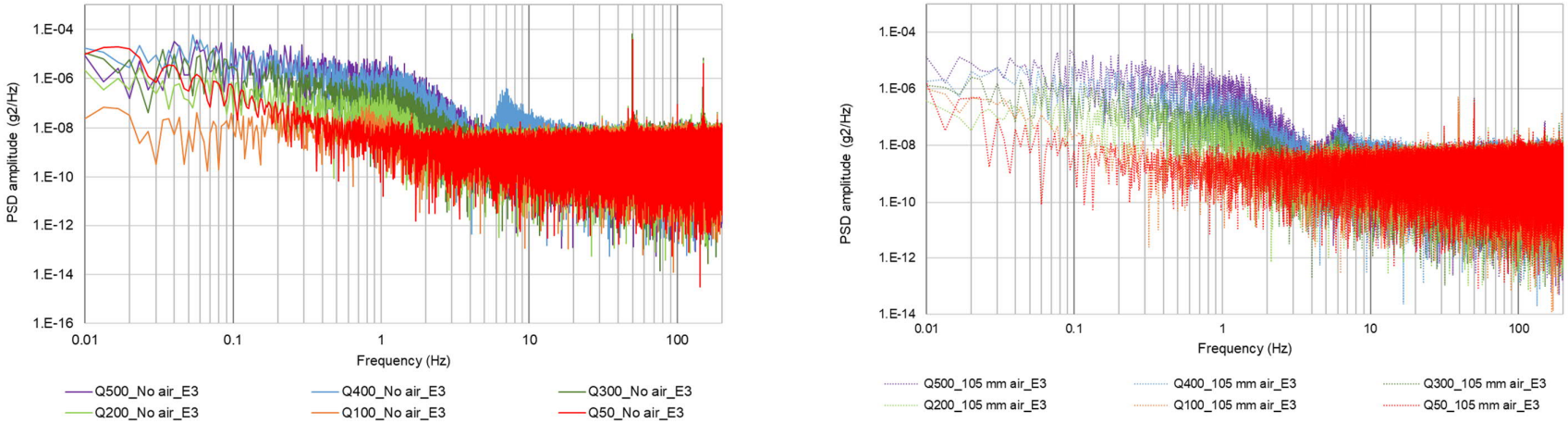

Figure D.4.7: Model 2 pressure PSD at pressure sensor E3 without aeration (left) and with aeration (right)

D.5 VIBRATION PSD GRAPHS

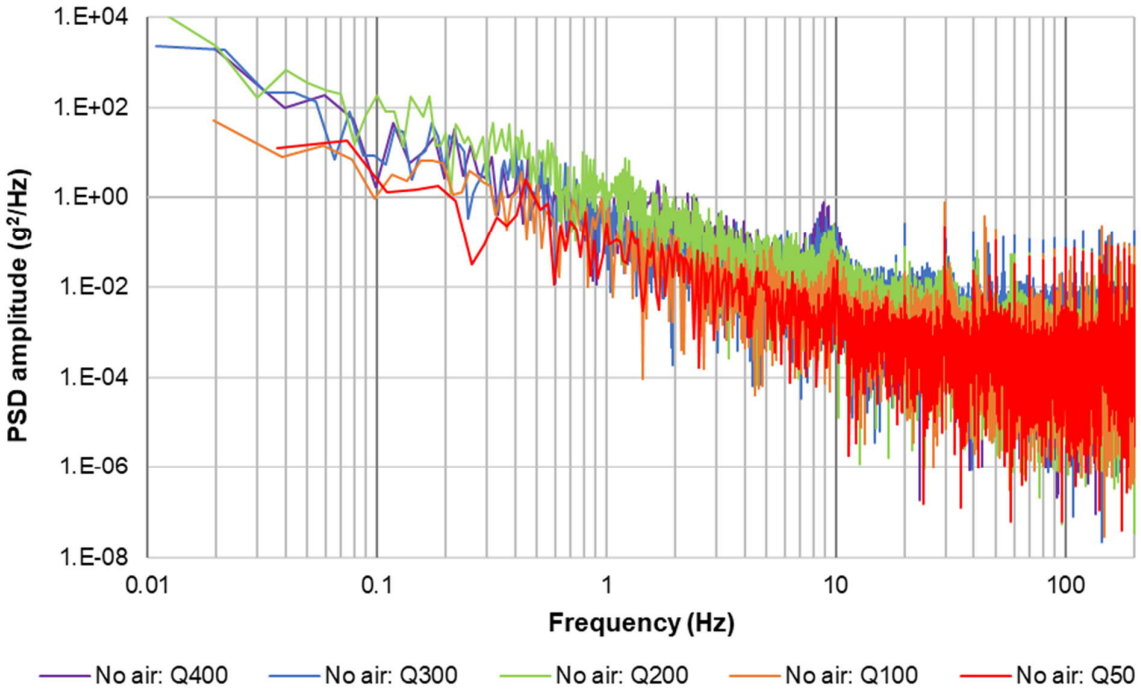

Figure D.5.1: Model 1 vibration PSD without aeration (Discharges 50, 100, 200, 300 and 400 l/s)

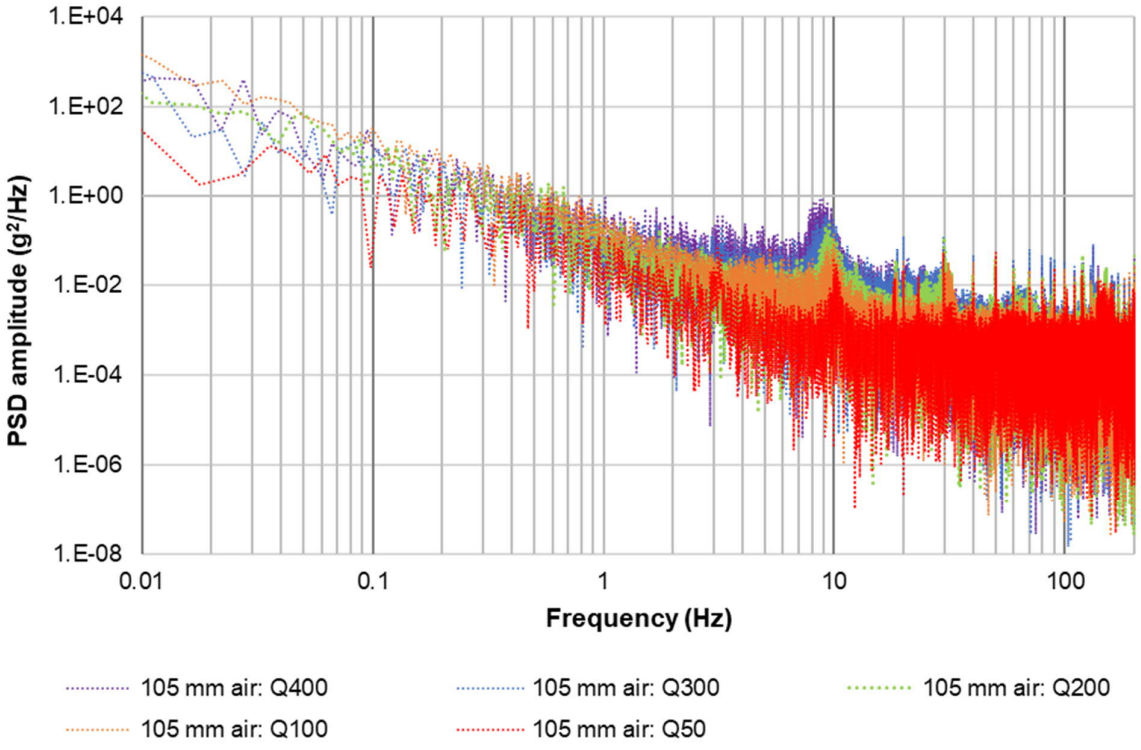

Figure D.5.2: Model 1 vibration PSD with aeration (Discharges 50, 100, 200, 300 and 400 l/s)

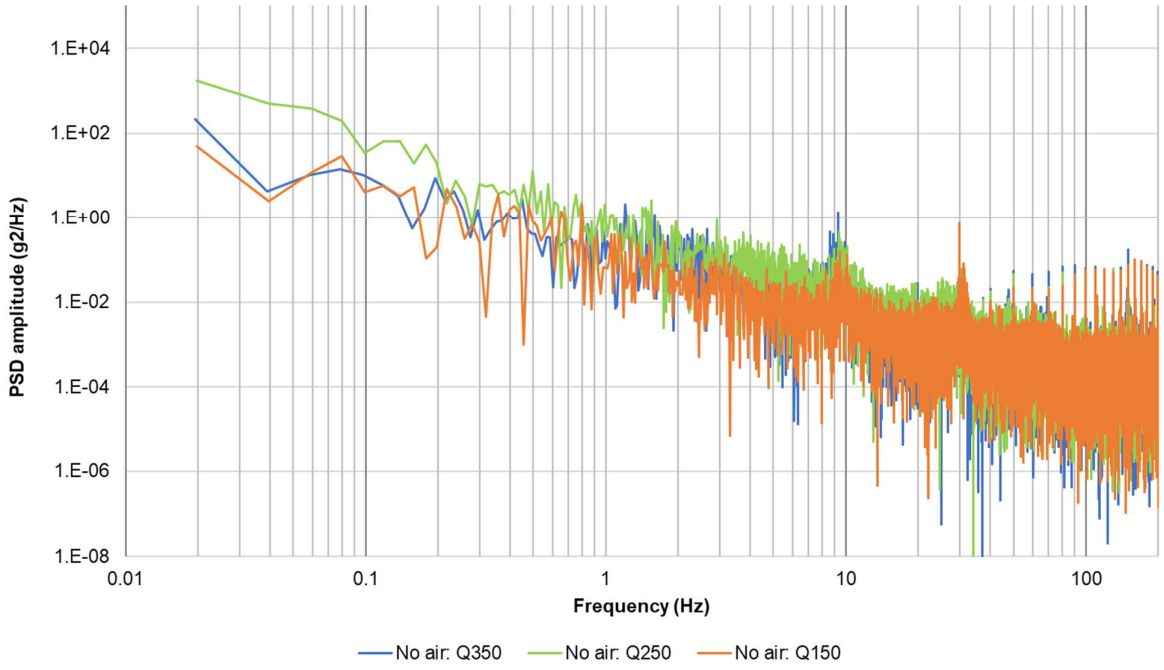

Figure D.5.3: Model 1 vibration PSD without aeration (Discharges 150, 250 and 350 l/s)

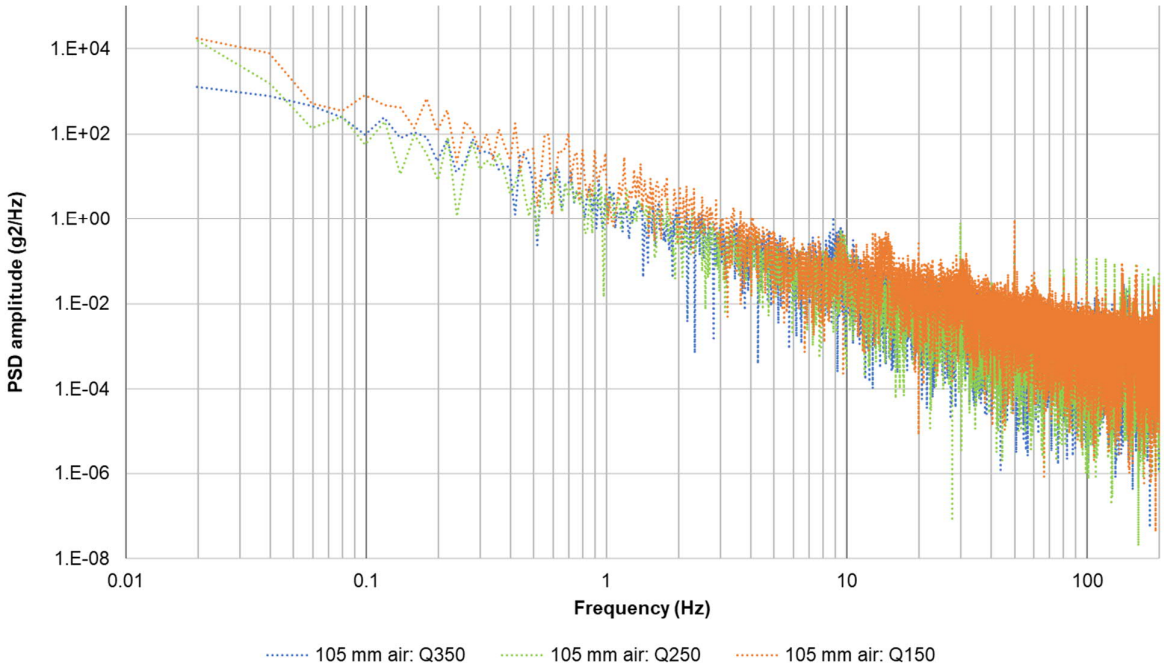

Figure D.5.4: Model 1 vibration PSD with aeration (Discharges 150, 250 and 350 l/s)